Applicability of the Restricted Active Space Self Consistent Field Methodology to Problems in Transition Metal and f-element Chemistry

Reece Beekmeyer
Chemistry
UCL

September 2017

I, Reece Beekmeyer confirm that the work presented in this thesis is my own. Where information has been derived from other sources, I confirm that this has been indicated in the thesis.

Abstract

Computational investigations of transition metal and f-element complexes, with their inherent multiconfigurational nature, can present significant challenges to the computational chemist. In this thesis the applicability of the Restricted Active Space Self Consistent Field (RASSCF) methodology to tackle these problems is investigated. This is initially used to investigate poprhyrin ring complexes, upon which there has been a great deal of experimental and computational literature. Calculations on free base porphyrin, regular transition metal porphryin and irregular transition metal porphyrins have been completed using the most commonly used and popular computational method, density functional theory (DFT) and its time-dependent extension, TDDFT. Ground state and vertical excitation energies have been compared and contrasted between DFT/TDDFT and RASSCF. Discrepancies in results between the methods have been identified for the irregular porphryin complexes, particularly in the manganese porphyrin complex where different ground states are predicted with different DFT $xc-$functionals. The significant covalency exhibited by transition metal complexes makes the selection of appropriate active spaces highly challenging using current methodologies and so this work expanded to investigate how the RASSCF methodology performs in inorganic complexes where there is less interaction between the metal and ligand, such as in f-element complexes. This began with a study of the unusual covalency observed experimentally in cerium and uranium hexachlorides where the bonding was further investigated through the use of the Quantum Theory of Atoms in Molecules (QTAIM) methodology. This was followed by an investigation into the newly synthesised family of divalent actinide and lanthanide complexes with three cyclopentadiene ligands (Cp_3) with the RASSCF methodology, the first of its kind using this methodology, again augmented with the use of the QTAIM methodology. Finally, having shown the effectiveness of the RASSCF methodology on f-element complexes this thesis returns to its initial theme with an investigation of lutetium texaphyrin - a f-element expanded porphyrin complex. Ultimately this thesis has demonstrated that the RASSCF methodology can be effectively applied to these systems to gain a deeper understanding of their electronic structure, although quantitatively

accurate descriptions sometimes remain out of reach.

Acknowledgements

There are too many people in my life who I need to thank for their help and support throughout not only this thesis but also my life.

My first thanks goes to my supervisor, Andy Kerridge, who has been not only an incredible supervisor from a scientific point of view but also a fantastic friend. I am thankful for the opportunity that he provided me as well as all of the help and guidance afforded. A special thanks must also go to my other primary supervisor, Helen Fielding, who not only 'adopted' and welcomed me into her group but was always available when I needed. I must also thank my second supervisor; Nik Kaltsoyannis for his aid and being so nice all the time!

I must also thank all the people I worked alongside at UCL; the members of G19 - Abi, Joe, Eszter, Nick and Eammon, the members of Helen's group - Mike, Jo, Bing-Xing and Jamie and all the support services provided at UCL and the NSCCS.

I thank my fiance Lauren for putting up with me being a student and all the support and love she has given me over the past years. I could not have achieved anything without her.

Finally I want to thank my family, unfortunately there are too many to name, but I want to thank every aunt, every uncle, every cousin, every grandparent, my parents and siblings. You are the greatest family in the world and I am grateful everyday for each and everyone of you. I would like to make special mentions to my two grandfathers; Peter Beekmeyer and Donald Clark to whom I dedicate this work to, without either of these two fantastic men I would not be the person I am today.

This thesis is based upon the following publications:

[1] R. Beekmeyer & A. Kerridge, *Investigating the electronic structure of Manganese Porphyrin using the RASSCF methodology*, **In Preparation**

[2] R. Beekmeyer & A. Kerridge, *Assessing Covalency in Cerium and Uranium Hexachlorides: A Correlated Wavefunction and Density Functional Theory Study*, Inorganics, **2015**, 3(4), 482-499;
DOI:10.3390/inorganics3040482

[3] E. McInnes, A. Formanuik, A.M. Ariciu, F. Ortu, R. Beekmeyer, A. Kerridge, F. Tuna & D. P. Mills, *Actinide Covalency measured by Pulsed Paramagnetic Resonance Spectroscopy*, Nature Chemistry, **2017**, 9, 578-583;
DOI:10.1038/nchem.2692

Other publications not included in this thesis:

[1] A. Formanuik, F. Ortu, R. Beekmeyer, A. Kerridge, R. W. Adams & D. P. Mills, *White Phosphorus Activation by a Th(III) Complex*, Dalton Transactions, **2016**, 45, 2390-2393;
DOI:10.1039/c5dt04528b

[2] R. Beekmeyer, M. A. Parkes, L. Ridgewell, J. W. Riley, J. Chen, A. Kerridge, B. L. Feringa & H. H. Fielding. *Unravelling the electronic structure and dynamics of an isolated molecular rotary motor in the gas-phase*, Chemical Science, **2017**
DOI:10.1039/C7SC01997A

Contents

List of Figures

List of Tables

Chapter 1

Introduction - A Brief Discussion of Computational Methods in Chemistry

Moore's law is the name given to the insight made by Gordon Moore in 1965 about the advancement of technology [20]. He observed and predicted a doubling in the processing power of computers year on year, a trend that has continued since 1965. It is not then unsurprising that the development of computational chemistry has progressed at a rate almost as rapid.

When Douglas Hartree first began developing the Hartree-Fock method in 1927 he began attempting to compute the properties of atomic physics using his own numerical ability [21]. However crucially Hartree had failed to obey the antisymmetry principle and so in 1930 Vladimir Fock (as well as John Slater) added the use of a Slater determinant to the wavefunction. The addition of the Slater determinant resulted in a further complication to the mathematics involved in calculating properties and thus the Hartree-Fock method was very rarely used until the dawn of computers in the 1950's and the application of the Roothan-Hall equations to the Hartree Fock method [22].

Since then many new and more advanced methods to describe atoms and molecules have been developed and as the computing power available has increased these methods have become more and more accessible for treating molecular systems. In the time-span of a generation computational chemists have gone from being restricted to cheap classical molecular mechanics methods on large systems (>100 atoms) to being able to run more accurate quantum calculation methods. At the rate technology continues to advance it surely can not be too long before computational methods are the first step in scientific discovery and used to guide scientists in obtaining solutions to problems.

In Density Functional Theory, which is discussed in detail later in Section 2.2, computational chemists have found a relatively quick and reliable tool with which to aid experimental results and guide conclusions. However DFT has its limitations and can be considered a semi-empirical method. This thesis has looked at expanding beyond DFT to a more powerful quantum mechanical methodology - the complete/restricted active space self consistent field method (CAS/RASSCF).

The need for more advanced and accurate computational methods is obvious. If experimental outcome and chemical properties could be accurately predicted the decrease in resources used would be remarkable. For example consider the scattergun approach often taken by pharmaceutical companies in development of new drugs - often a current drug that is known to have benefits is taken, modified chemically slightly and then tested and repeated until a viable solution is found [23]. This is an incredible waste of resources; human, energy and chemical. However because of the typically large size of drug molecules computational methods have been known to be relatively inaccurate.

Another example where the need for computational methods is a must is in nuclear energy.

Dealing with and disposing of nuclear waste is the one of the biggest problems with using nuclear energy (ignoring the security concerns about having a nuclear power station) [24, 25]. The difficulty in experimenting with nuclear waste is that it is toxic and radioactive and so raises serious health concerns. These concerns are immediately removed if simulated computationally, however, like with other potential applications, the need for accurate simulations is required.

This thesis follows the application of the Restricted Active Space Self Consistent Field (RASSCF) methodology through an investigation of the bonding and excited states of the bio-inorganic molecules, porphyrins. Then an investigation using the same methodology into the bonding, and particularly covalency, in small f-element complexes, namely hexachlorides. This is followed by an investigation into larger, novel divalent f-element complexes. This thesis then returns full circle to f-element expanded porphyrins using the RASSCF methodology.

Chapter 2

Methodology

2.1 Quantum Mechanics and the Schrödinger Equation

Methods for simulating chemical properties can be split broadly into classical and quantum methods. Classical methods include molecular mechanics and molecular dynamics and are based on Newton's classical laws of motion [26]. Quantum methods on the other hand are based upon the laws of quantum mechanics which describe the behaviour of very small particles, such as electrons. Perhaps one of the most used and famous equations in quantum mechanics is the Schrödinger Equation, which is shown in Eqn 2.1 [27].

$$\hat{H}\Psi = E\Psi \tag{2.1}$$

In the Schrödinger equation $\hat{H}$ is the Hamiltonian operator, E is the energy and Ψ is the wavefunction. A mathematical operator is simply a set of instructions to perform on a function, this can be as simple as multiplication, however in the case of the Hamiltonian operator it involves many more mathematical steps and is shown in Eqns 2.2 and 2.3.

$$\hat{H} = -\sum_i \frac{\hbar^2}{2m_e}\nabla_i^2 - \sum_k \frac{\hbar^2}{2m_k}\nabla_k^2 - \sum_i \sum_k \frac{e^2 Z_k}{4\pi\epsilon_0 r_{ik}} + \sum_{i<j} \frac{e^2}{4\pi\epsilon_0 r_{ij}} + \sum_{k<l} \frac{e^2 Z_k Z_l}{4\pi\epsilon_0 r_{kl}} \tag{2.2}$$

In quantum mechanics because of the scale on which things operate it can be much more useful to define equations in atomic units (au) rather than SI units, this also has the beneficiary effect of simplifying a lot of the constants that are used in the equations. In atomic units distance is in terms of the Bohr radius, energy in terms of Hartrees and charge in terms of elementary charge. Eqn 2.2 in au is therefore simplified to Eqn 2.3 [3];

$$\hat{H} = -\sum_i \frac{1}{2}\nabla_i^2 - \sum_k \frac{1}{2m_k}\nabla_k^2 - \sum_i \sum_k \frac{Z_k}{r_{ik}} + \sum_{i<j} \frac{1}{r_{ij}} + \sum_{k<l} \frac{Z_k Z_l}{r_{kl}} \tag{2.3}$$

In Eqns 2.2 and 2.3 the first two terms are the kinetic energy terms (often collectively referred to as $\hat{T}$), the first being the kinetic energy of the electrons, summed over i electrons and the second the kinetic energy of the nuclei summed over k nuclei. The third, fourth and fifth terms are then the potential energy terms (collectively known as $\hat{V}$); the third the electrostatic attraction between the electrons and nuclei, the fourth the repulsion between electrons and the fifth the repulsion between nuclei. ∇^2 is the Laplacian operator which is the sum of the second partial derivatives and is shown in Eqn 2.4 [3].

$$\nabla_i^2 = \frac{\partial^2}{\partial^2 x_i} + \frac{\partial^2}{\partial^2 y_i} + \frac{\partial^2}{\partial^2 z_i} \tag{2.4}$$

Solving the Schrödinger equation for a multi-particle system is not trivial and therefore approximations must be made. The key approximation made is the Born-Oppenheimer approximation which considers the position of nuclei fixed on the timescale of electron movement. This assumption is valid because of the differences in mass between nuclei and electrons. The Born-Oppenheimer (BO) approximation allows an electronic Hamiltonian to be written for a fixed

geometry [28]. The geometry can then be changed and the electronic Hamiltonian computed again to form what is known as a potential energy surface (PES) [3, 22].

$$\hat{H_{el}} = -\sum_i \frac{1}{2}\nabla_i^2 - \sum_i \sum_k \frac{Z_k}{r_{ik}} + \sum_{i<j} \frac{1}{r_{ij}} + \sum_{k<l} \frac{Z_k Z_l}{r_{kl}} \tag{2.5}$$

The electronic Hamiltonian is often written as [29];

$$\hat{H_{el}} = \hat{T} + \hat{V_{ee}} + \hat{V_{ext}} \tag{2.6}$$

where $\hat{T}$ is the electronic kinetic energy, $\hat{V_{ee}}$ is the electron-electron terms and $\hat{V_{ext}}$ contains the nuclear terms and any other terms including magnetic and electric fields.

Although the use of the BO approximation decouples the electronic motion from nuclear motion, it is still a differential equation in $3n$ co-ordinates (n= number of electrons) and further approximations must be made [3].

Another key approximation that can be made, known as the orbital approximation, is that a many electron wavefunction can be constructed as a product of n one-electron wavefunctions. This wavefunction is often referred to as the Hartree Product (HP) wavefunction [3].

$$\Psi_{HP}(r_1, r_2, ..., r_n) = \psi_1(r_1)\psi_2(r_2)...\psi_n(r_n) \tag{2.7}$$

The HP wavefunction is exact for a one electron system as it includes the kinetic energy of the electron and the attraction energy between the electron and nuclei. However for many electron systems it is not exact as it considers electrons indistinguishable and importantly does not obey the Pauli exclusion principle.

2.1.1 Electron Spin and Slater Determinants

So far electron spin has not been discussed, electrons can have two states of spin often referred to as alpha (positive) or beta (negative) spin. Electrons also obey the Pauli exclusion principle, which says that no two electrons can have the same set of quantum numbers [3, 22, 30]. Therefore in any given molecular orbital (MO) there can not be two electrons with the same spin.

Constructing a HP wavefunction for a system of two molecular orbitals with two electrons of alpha spin would be;

$$^3\Psi_{HP} = \psi_A(r_1)\alpha_1\psi_B(r_2)\alpha_2 \tag{2.8}$$

A result of the Pauli exclusion principle is that the electronic wavefunction is antisymmetric, this means that if two electrons are interchanged the sign of the wavefunction changes. This is not true of the HP wavefunction but can be achieved through the use of Slater determinants (SD).

$$^3\Psi_{SD} = \frac{1}{\sqrt{2}}[\psi_A(r_1)\alpha_1\psi_B(r_2)\alpha_2 - \psi_A(r_2)\alpha_2\psi_B(r_1)\alpha_1] \tag{2.9}$$

which can also been written in a matrix determinant format;

$$^3\Psi_{SD} = \frac{1}{\sqrt{2}}\begin{vmatrix}\psi_A(r_1)\alpha_1 & \psi_B(r_1)\alpha_1\\ \psi_A(r_2)\alpha_2 & \psi_B(r_2)\alpha_2\end{vmatrix} \tag{2.10}$$

For a more general wavefunction Slater determinants are written as;

$$\Psi_{SD} = \frac{1}{\sqrt{n!}}\begin{vmatrix}\chi_1(1) & \chi_2(1) & \cdots & \chi_n(1)\\ \chi_1(2) & \chi_2(2) & \cdots & \chi_n(2)\\ \vdots & \vdots & \ddots & \vdots\\ \chi_1(n) & \chi_2(n) & \cdots & \chi_n(n)\end{vmatrix} \tag{2.11}$$

where χ is a spin-orbital and n is the total number of electrons. The above notation can get very large for larger wavefunctions, so can be written more compactly in Dirac notation [3, 22, 31];

$$\Psi_{SD} = |\chi_1\chi_2\chi_3 \cdots \chi_N\rangle \tag{2.12}$$

Notice that the $1/\sqrt{n!}$ is assumed in Dirac notation. If χ_1 and χ_2 represented α and β spin-orbitals of the same molecular orbital and were both filled this can be represented as;

$$\Psi_{SD} = |\chi_1^2\chi_3 \cdots \chi_N\rangle \tag{2.13}$$

Eqns 2.12 and 2.13 show the use of Dirac ket notation which is a way of compactly labelling a quantum state. For every ket there is a corresponding bra which is the complex conjugate of the ket and is represented as "$\langle x|$". Combination of a bra and ket describes the overlap of states.

$$\langle\psi|\psi\rangle = \int \psi^*(r)\psi(r)dr \tag{2.14}$$

and

$$\langle\psi|\hat{H}|\psi\rangle = \int \psi^*(r)\hat{H}\psi(r)dr \tag{2.15}$$

describes the expectation value of ψ with respect to the Hamiltonian operator using Dirac notation.

2.1.2 Construction of Trial Wavefunctions and Linear Combination of Atomic Orbitals (LCAO)

A trial molecular wavefunction (ψ), which is a quantum mechanical concept that describes a molecule, can be constructed from molecular orbitals (φ).

$$\psi = |\varphi_1\varphi_2 \ldots \varphi_N\rangle \tag{2.16}$$

Molecular orbitals themselves can be constructed as a linear combination of atomic orbitals (LCAO) shown in Eqn 2.17.

$$\varphi(r) = \sum_i c_i \phi_i(r) \tag{2.17}$$

where φ is the molecular orbital, c_i is the coefficient that describes the degree that the atomic orbital contributes to the molecular orbital and ϕ_i is the atomic orbital. In this LCAO method the atomic orbitals constitute the basis set, which are described in more detail in Section 2.7.

2.1.3 The Variational Principle

The variational principle is a key concept in quantum mechanics, it states that any trial wavefunction (ψ) can not be lower in energy than the real wavefunction (Ψ). The energy of a trial wavefunction can be defined as the expectation value of the wavefunction, as in Eqn 2.18 [3, 32].

$$E_\psi = \frac{\langle \psi | \hat{H} | \psi \rangle}{\langle \psi | \psi \rangle} \tag{2.18}$$

The variational principle means that if we have two trial wavefunctions ψ_1 and ψ_2, the wavefunction which when acted upon by the Hamiltonian results in a lower energy is a better representation of the system as the the energy of a trial wavefunction can not be lower than the energy of the real wavefunction.

$$E_\Psi \leq E_\psi \tag{2.19}$$

This is obviously very important when it comes to optimisation of trial wavefunctions as it provides a basis for convergence.

2.1.4 Hartree-Fock Self Consistent Field

The Hartree-Fock method builds upon the HP wavefunction through the use of Slater determinants and the BO approximation to give an approximate solution to the Schrödinger equation.

The wavefunction is still built as a product of one electron wavefunctions however some electron-electron interactions are included.

The Fock operator ($\hat{f}$) acts on molecular orbitals (φ) which produces an energy for each orbital (ϵ).

$$\hat{f}_i\varphi_i(r) = \epsilon_i\varphi_i(r) \tag{2.20}$$

Eqn 2.21 shows the form of the Fock operator;

$$\hat{f}_i = \hat{h}_i + 2\sum_{j\neq i}\hat{J}_j - \sum_{j\neq i}\hat{K}_j \tag{2.21}$$

where $\hat{h}$ is the one electron Hamiltonian, $\hat{J}$ is the Coloumb operator and $\hat{K}$ is the exchange operator.

The only issue with this is that the exchange and Coloumb operators depend on knowledge of all other electrons, hence an iterative self consistent field (SCF) method was proposed by Hartree to remedy this problem [3, 22].

In the SCF method, the first step is to guess the wavefunctions, ψ , of the molecular orbitals, φ and use these to construct the one electron Fock equation, $\hat{f}$. Solving the set of one electron Schrödinger equations provides a new set of ψ. These wavefunctions can then be used to solve the one electron Schrödinger equations again and this process repeated until a convergence criteria, generally based around the overall energy, has been reached. This is the basis of the Hartree-Fock methodology, for a fuller overview the reader is directed to literature texts [3, 22].

2.2 Density Functional Theory (DFT)

Density Functional Theory (DFT) is perhaps the most widely used and most popular theory in computational chemistry because of its relative accuracy compared to its computational cost. The essential idea behind the theory is that the positions of nuclei and the ground state energy can be uniquely determined by the ground state electron density. In DFT the energy is obtained as a function of the density, which itself is a function of the electron coordinates. This is known as a functional, which take a function as input and returns a number (i.e. function of a function), hence the name Density Functional Theory. In mathematics functions are often denoted with parenthesis e.g. f($\mathbf{x}$) while functionals are denoted with square brackets e.g. F[f($\mathbf{x}$)].

As one of the key properties of the electronic wavefunction of a molecule is that its square modulus gives the probability of finding an electron at a particular position in space, it therefore follows that inspecting the electron density should allow us to obtain information about the molecule. For instance points of maximum electron density indicates the positions of nuclei in a molecule. In addition to this the total number of electrons (N) in the system can be determined by integrating the electron density ($\rho(\mathbf{r})$) over all space shown in Eqn 2.22;

$$N = \int \rho(\mathbf{r}) d\mathbf{r} \tag{2.22}$$

2.2.1 Using the Density of a System

DFT built upon the successes of Hartree-Fock (HF) theory whilst improving on its failings. The major failure of HF theory is the inability of the methodology to deal properly with electron correlation. Some correlation is included in HF theory, for instance Fermi correlation, that two electrons of the same spin cannot occupy the same point in space, is dealt with by the antisymmetric properties of the Slater determinant, discussed in Section 2.1.1. However, Coloumb correlation, which is the correlation in electron motion due to their electrostatic repulsion, is not properly accounted for by HF theory. Consider the simplistic example of He

below;

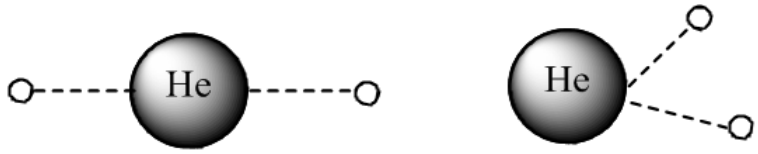

Figure 2.1: Electron correlation problem in HF theory. The case on the left is as likely as the case on the right in HF as each electron sees only an average electronic field.

HF theory does not distinguish between the two cases in Figure 2.1 above, when it would be expected that the probability of the case on the left to be more likely than the case on the right due to the electrostatic repulsion between the two electrons.

As mentioned previously the electron density of a molecule gives information about the position of electrons and nuclei. This, according to Hohenberg and Kohn, is all that is needed to build a unique Hamiltonian for the system, this is known as the first Hohenberg-Kohn Theorem (HK1) [33]. The proof is as follows;

Assume that there are two external potentials V_{ext} and V'_{ext} which can both be associated with the same ground state electron density, ρ. Two Hamiltonians corresponding to two ground state wavefunctions, $\hat{H}$ & $\hat{H}'$ and Ψ & Ψ', can be constructed in accordance with Eqn 2.6;

$$\hat{H} = T + V_{ee} + V_{ext} \tag{2.23}$$

$$\hat{H}' = T + V_{ee} + V'_{ext} \tag{2.24}$$

These two Hamiltonians give rise to two ground state energies, E_0 and E'_0 where $E_0 \neq E'_0$. As Ψ and Ψ' are different, Ψ' can be used as a trial wavefunction for $\hat{H}$ and therefore according to the variational principle;

$$E_0 < \langle \Psi' | \hat{H} | \Psi' \rangle = \langle \Psi' | \hat{H}' | \Psi' \rangle + \langle \Psi' | \hat{H} - \hat{H}' | \Psi' \rangle \tag{2.25}$$

$$E_0 < E_0' + \langle \Psi' | V_{ext} - V_{ext}' | \Psi' \rangle \tag{2.26}$$

Swapping the subscripts and repeating the above steps gives a second inequality for E_0'. Addition of these inequalities then produces the following;

$$E_0 + E_0' \neq E_0' + E_0 \tag{2.27}$$

which is clearly not mathematically correct. Therefore this proves a one-to-one correspondence between the electron density and the energy of the system as there can not be two different V_{ext} which produce the same electron density.

The importance of the HK1 theorem is best shown in comparison to wavefunction methods, if a wavefunction for an N-electron system is constructed then it contains $4N$ variables (3 spatial and 1 spin for each electron) which can not be probed experimentally. However the electron density depends only on three spatial variables and furthermore is an experimentally observable quantity. This means that as the number of electrons is increased the complexity of the wavefunction increases but the electron density has the same number of variables regardless [22, 3]. Therefore much faster computational results can be achieved by using the density of the system.

If the HK1 theorem is accepted as true then it follows that the ground state Hamiltonian is a functional of the ground state electron density and so:

$$E[\rho] = F_{HK}[\rho] + E_N[\rho] \tag{2.28}$$

Where $E[\rho]$ is the energy of the system, $F_{HK}[\rho]$ is the Hohenberg-Kohn (or Universal) functional acting on the density and $E_N[\rho]$ is the nuclear potential term. The Hohenberg-Kohn functional can be broken down further into;

$$F_{HK}[\rho] = T[\rho] + V_{ee}[\rho] \tag{2.29}$$

where $T[\rho]$ is the kinetic energy functional of the system, $V_{ee}[\rho]$ is the electron-electron functional.

The second Hohenberg-Kohn theorem (HK2) shows that this energy can be obtained variationally as it obeys the variational principle. These two theorems provide a basis for a method that is computationally cheaper than wavefunction methods whilst also giving comparable accuracy.

However, whilst the $F_{HK}[\rho]$ functional maps the ground state electron density exactly to the ground state Hamiltonian, it's form is not known. Furthermore although the HK2 theorem states that the energy obtained from the electron density can be minimised variationally, no indication is offered as to how to optimise the electron density so as to obtain a better representation of the system. Moreover orbital-free DFT struggles to describe the kinetic energy of the system correctly. This is where Kohn-Sham theory excels, which reintroduces orbitals generated in the same way as HF theory into DFT.

2.2.2 Kohn-Sham Theory

The Hohenberg-Kohn theorems show that the density can be used to calculate the energy however it offers no indication as to how the energy can be determined, this is where Kohn-Sham (KS) theory is utilised [33, 34]. The KS equations describe the KS system of non-interacting particles that generates the same density as the target system of interacting particles. In the non-interacting KS system, like in HF theory, the wavefunction is a single Slater determinant constructed from the KS orbitals. The KS density is then equal to the sum of the square modulus of the occupied KS orbitals (Eqn 2.30) [3, 34].

$$\rho^{KS}(r) = \sum^{i} |\varphi_i^{KS}(r)|^2 \tag{2.30}$$

The energy of the non-interacting (ni) KS system can be calculated very simply as the kinetic energy of the system (Eqn 2.31).

$$E^{KS(ni)}[\rho] = T^{ni}[\rho] \tag{2.31}$$

Interactions that map the non-interacting system onto the interacting system must then be added. These include interactions between the nuclei and the electrons ($V_{ne}[\rho]$), Coulombic interactions ($V_{ee}[\rho]$), kinetic energy changes due to the interaction of particles ($\Delta T[\rho]$) and exchange-correlation interactions between electrons ($\Delta V_{ee}[\rho]$).

$$E^{KS}[\rho] = T^{ni}[\rho] + V_{ne}[\rho] + V_{ee}[\rho] + \Delta T[\rho] + \Delta V_{ee}[\rho] \tag{2.32}$$

The last two terms in Eqn 2.32 are often collectively referred to as the exchange-correlation functional $E_{xc}[\rho]$.

$$E_{xc}[\rho] = \Delta T[\rho] + \Delta V_{ee}[\rho] \tag{2.33}$$

There are a lot of similarities between the equations of HF theory and KS-DFT, however the major difference is that KS-DFT is an exact method, provided that the form of $E_{xc}[\rho]$ is known, whereas HF is an approximate method. The difficulty in KS-DFT comes from the evaluation of the exchange-correlation functional, as its true form is an unknown quantity.

2.2.3 Approximating the Exchange-Correlation Functional

The development of exchange correlation approximations are shown on Jacobs Ladder (Figure 2.2), where the bottom is HF theory and the top being the exact form of the exchange correlation term (or heaven of chemical accuracy) [1, 2].

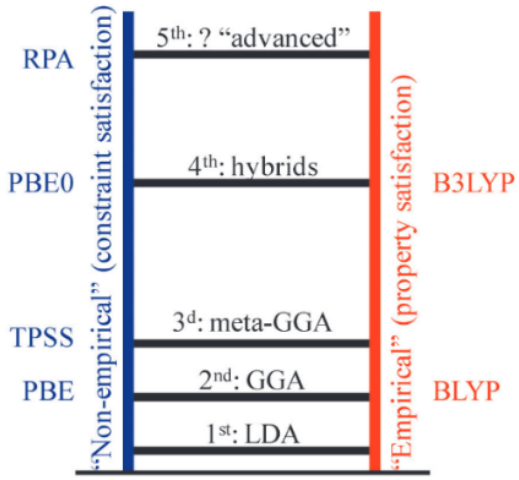

Figure 2.2: Jacob's Ladder of DFT exchange-correlation functionals. Adapted from [1, 2].

One of the first ways that computational chemists attempted to approximate the form of $E_{xc}[\rho]$ was through the local density approximation (LDA) (Rung 1 on Jacobs Ladder). The LDA attempts to calculate $E_{xc}[\rho]$ by assuming that it can be evaluated using only the magnitude of the electron density at specific points in space, as shown in the equation below. LDAs are based upon the idea of a Homogeneous or Uniform Electron Gas (UEG) [22, 3, **?**].

$$E_{xc}^{LDA}[\rho] = \int \rho(\mathbf{r})\epsilon_{xc}(\rho)d\mathbf{r} \tag{2.34}$$

In the above equation $\epsilon_{xc}(\rho)$ is the exchange correlation energy per particle of a UEG of density ρ.

The problem with LDA functionals is in the assumption that only the magnitude of the electron density matters which results in an overbinding of systems. This assumption is valid in the case of a UEG, and gives good results, however for many real systems LDA functionals cause errors greater than those obtained when HF theory is used. Nevertheless LDA functionals are still sometimes utilised for describing systems where there is little variation in the electron density such as in bulk metals [22].

In an attempt to remedy the problems of LDA functionals, the next rung of the Jacobs Ladder, Generalised Gradient Approximation (GGA) functionals were developed. These again take the ideas from a UEG but instead of using just the magnitude of the electron density they also use the gradient of the electron density. This is achieved partly through a correction parameter, one of the most successful and popular of these being the Lee-Yang-Parr (LYP) GGA functional which was parameterised based upon the helium atom [35]. This corrects the problem of overbinding that LDAs have, unfortunately these still do not give very accurate results when studying chemical processes and reactions. The problem with GGA functionals is that they overestimate the effect of the Coulomb interaction, effectively resulting in electrons avoiding each other too often [22, 3, 36]. Therefore one of the biggest issues when using GGA functionals to model chemical processes is that barrier heights obtained are generally too high [22, 3]. To further build upon GGA functionals, meta-GGA functionals (Rung 3) were introduced, which attempted to increase the accuracy of calculations by also using the second derivative of the density, an example of a m-GGA being the TPSS xc-functional [37]. However despite the extra correction of the second derivative of the density, m-GGA functionals still produce barrier heights which are too large. The mathematical form of both GGA and m-GGA functionals are shown below in Eqns 2.35 & 2.36.

$$E_{xc}^{GGA}[\rho] = \int \rho(\mathbf{r})\epsilon_{xc}(\rho, \nabla\rho)d\mathbf{r} \tag{2.35}$$

$$E_{xc}^{mGGA}[\rho] = \int \rho(\mathbf{r})\epsilon_{xc}(\rho, \nabla\rho, \nabla^2\rho)d\mathbf{r} \tag{2.36}$$

Hybrid Functionals

Hybrid functionals (Rung 4) are perhaps the most commonly used exchange correlation functionals, especially the Becke 3-parameter with LYP correlation (B3LYP) functional [38, 35, 39]. Hybrid functionals are constructed using a different approach than that taken in the construction of LDA, GGA and m-GGA functionals. Hybrid functionals are constructed by combining

percentages of the lower rung DFT functionals with exact exchange from the HF system.

Using the Hellman-Feynman theorem [40] it can be shown that the exchange correlation term can be calculated as [3]

$$E_{xc}[\rho] = \int_0^1 \langle \Psi(\lambda)|V_{xc}(\lambda)|\Psi(\lambda)\rangle d\lambda \tag{2.37}$$

where λ describes the degree of interelectronic interaction, a value of 0 describing the KS non-interacting system and a value of 1 describing the exact system. Evaluation of Eqn 2.37 is perhaps best shown graphically, as in Figure 2.3.

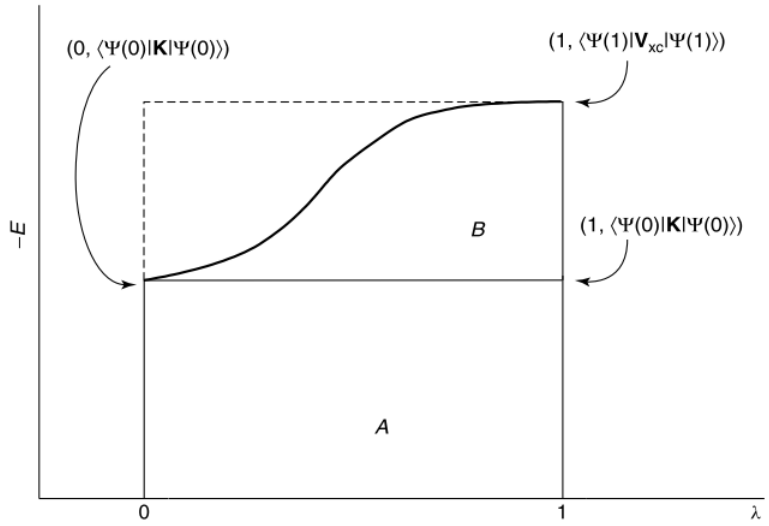

Figure 2.3: Graphical schematic of computation of Eqn 2.37 adapted from [3]. The area of rectangle A is calculated as the expectation value of the HF exchange operator acting on the non-interacting system, $\Psi(0)$.

The result of integrating Eqn 2.37 is that the area under the curve in Figure 2.3 is obtained. Whilst little is known about how Ψ and V_{xc} change with λ, what is known is the value at the

left hand limit. This is the value of exact exchange of the non-interacting system, rectangle A in Figure 2.3 therefore represents exact exchange. The area of rectangle B is $\langle\Psi(1)|V_{xc}(1)|\Psi(1)\rangle - E_x^{HF}$ and thus the area under the curve is some fraction z of this area. Although z is not known it can be optimised empirically as in Eqn 2.38.

$$E_{xc} = E_x^{HF} + z(E_{xc}^{DFT} - E_x^{HF}) \tag{2.38}$$

which is often displayed using the value $a = (1 - z)$ [3];

$$E_{xc} = (1 - a)E_{xc}^{DFT} + aE_x^{HF} \tag{2.39}$$

Eqns 2.38 & 2.39 are the simplified forms for hybrid functionals, the popular B3LYP functional, which contains three parameters (a, b, c), has the form;

$$E_{xc}^{B3LYP} = (1 - a)E_x^{LDA} + aE_x^{HF} + b\Delta E_x^B + (1 - c)E_c^{LDA} + cE_c^{LYP} \tag{2.40}$$

where *a, b* & *c* equal 0.20, 0.72 and 0.81 respectively [38, 39, 35].

Hybrid functionals improve upon GGAs and m-GGAs in the majority of cases as they include some HF exchange, 20% in the case of B3LYP. Including this HF exchange helps reduce the self-interaction error, discussed later in Section 2.4. In the case of modelling reactions, as pure DFT functionals tend to overestimate barrier heights and HF underestimates, hybrid functionals see almost a cancelling of these errors and give generally good agreement with experiment [22, 3].

The development of these different functionals, particularly rungs 3 & 4, has seen DFT become the most popular method amongst chemists and its importance was recognised by the award

of the 1998 Nobel Prize in Chemistry to W. Kohn for "*development of the Density Functional Theory and Computational Methods in Quantum Chemistry*" [22, 34, 41].

2.3 Time Dependent Density Functional Theory (TDDFT)

Density Functional Theory as described in Section 2.2 is only valid for stationary states and does not extend to how the wavefunction is affected by time. This is information that is required to predict the properties and behaviour of excited states. Furthermore as DFT is a ground state methodology the variational theorem means that all excited states will relax to the ground state unless it is restricted by spin or symmetry. Therefore to look at excited states, an extension of DFT, Time Dependent Density Functional Theory (TDDFT), was conceived.

Eqn 2.1 in Section 2.1 showed the form of the time-independent Schrödinger equation, however when investigating the effect of time on the evolution of the wavefunction the time-dependent Schrödinger equation must be used which is shown in Eqn 2.41.

$$\hat{H}(r,t)\Psi(r,t) = i\frac{\partial}{\partial t}\Psi(r,t) \tag{2.41}$$

The time-depenedent Schrödinger equation is an example of an initial value problem where $\Psi_0(r) = \Psi(r,t_0)$, hence the wavefunction at time t is a functional of the wavefunction at time t_0, $\Psi[\Psi_0(r,t)]$ and so the energy can be calculated by;

$$E[\Psi_0(r,t)] = \langle\Psi[\Psi_0(r,t)]|H|\Psi[\Psi_0(r,t)]\rangle \tag{2.42}$$

At the heart of TDDFT is the Runge-Gross (RG) theorem which has been described as the time-dependent analogue of the HK1 theorem [42]. Similar to how the HK1 theorem showed that the ground state density uniquely determines the ground state Hamiltonian, the RG theorem showed that there is a unique relationship between the time-dependent external potential of a system and its time-dependent charge density when a ground stationary state is exposed to a time-dependent perturbation [42, 43].

TDDFT calculates excited states by determining the (time-dependent) Kohn-Sham system and approximating not only the exchange-correlation functional, as in DFT, but also the exchange correlation kernel [44] (the functional derivative of the exchange correlation potential). As with DFT the KS system is constructed using a single Slater determinant.

Often TDDFT, such as its implementation in computational packages, for example the Turbomole package, utilises linear response (LR) theory [45]. In the LR TDDFT approach, the KS orbitals evolve in time and the orbital energies can be calculated using the ground state KS system equations. TDDFT then considers the linear response of the ground state density to the time-dependent perturbation of the external potential, $\delta V_{ext}(t)$. The energy is then calculated as the original time-independent KS system plus the time-dependent perturbation [43].

Currently, TDDFT using the RG theorem is limited to applied electric fields and not magnetic fields, however generally this is sufficient for many problems as magnetic effects are often considerably smaller. It has also been noted that TDDFT performs better when the excitation energies under consideration are considerably lower than ionisation potential [43, 3].

2.4 Problems with DFT & TDDFT

The methodologies of DFT and TDDFT have been discussed in Sections 2.2 & 2.3, however, their limitations have not. This section details two of the main limitations with the DFT methodology; the failure to deal with static correlation and the self-interaction error.

2.4.1 Failure to Deal with Static Correlation

DFT is satisfactory for use in cases when there are no degenerate or near degenerate electron configurations. In the cases where there are near-degenerate electron configurations, DFT (and hence TDDFT) do not perform as well due to a failure to deal with static correlation (also known as non-dynamical correlation) in the system [3].

As mentioned in Section 2.2.2, DFT uses a single Slater determinant to build an approximate solution to the Schrödinger equation, this is unsatisfactory for systems containing near-degenerate configurations.

A prime example of this is in the computational simulation of the H_2 molecule. The two Hydrogen 1s orbitals can form two molecular orbitals (Figure 2.4), a bonding (φ_1) & an anti-bonding (φ_2) molecular orbital.

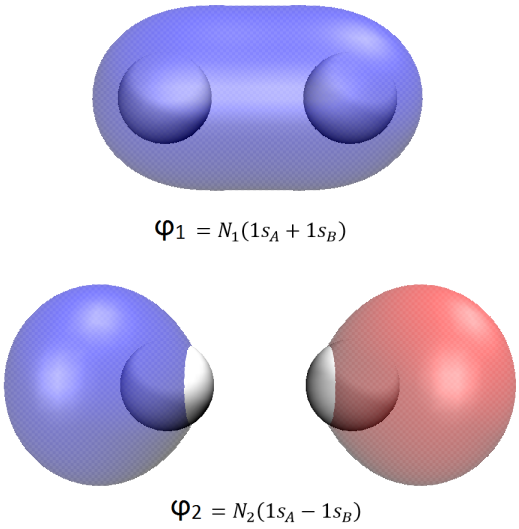

Figure 2.4: Hydrogen bonding and anti-bonding molecular orbitals generated with Hartree-Fock theory and minimal basis set at an isosurface of 0.03 a.u.

The ground state wavefunction has the bonding orbital, φ_1, doubly occupied, which at the equilibrium geometry is a good approximation (Eqns 2.43 & 2.44).

$$\psi_0 = |\varphi_{1\alpha}\varphi_{1\beta}| \tag{2.43}$$

$$\psi_0 = N_0(|1s_A\alpha 1s_B\beta| + |1s_B\alpha 1s_A\beta| + |1s_A\alpha 1s_A\beta| + |1s_B\alpha 1s_B\beta|) \tag{2.44}$$

However as the H-H bond is stretched this approximation becomes less valid. It can be seen in Eqn 2.44 that there are two types of terms; ionic, where both electrons occupy orbitals on the same Hydrogen, and covalent, where the two electrons occupy orbitals on different Hydrogens. The first two terms are covalent & the second two ionic, there is therefore a 50% chance of both $1s$ electrons being localised on one of the Hydrogens. At very large bond lengths (effectively dissociated) this would mean forming one H^+ ion and one H^- ion when in reality this would

not be the case

Consider now the doubly excited wavefunction where both electrons occupy φ_2 (Eqns 2.45 & 2.46).

$$\psi_2 = |\varphi_{2\alpha}\varphi_{2\beta}| \tag{2.45}$$

$$\psi_2 = N_2(|1s_A\alpha 1s_A\beta| + |1s_B\alpha 1s_B\beta| - |1s_A\alpha 1s_B\beta| - |1s_B\alpha 1s_A\beta|) \tag{2.46}$$

Combining wavefunctions ψ_0 & ψ_2 in a linear combination (Eqn 2.47) it can be seen that the ionic terms cancel (Eqn 2.48) and a better description of the H_2 system is obtained.

$$\Psi = \psi_0 - \psi_2 \tag{2.47}$$

$$\begin{aligned}\Psi = N((&|1s_A\alpha 1s_B\beta| + |1s_B\alpha 1s_A\beta| + |1s_A\alpha 1s_A\beta| + |1s_B\alpha 1s_B\beta|) \\ &- (|1s_A\alpha 1s_A\beta| + |1s_B\alpha 1s_B\beta| - |1s_A\alpha 1s_B\beta| - |1s_B\alpha 1s_A\beta|))\end{aligned} \tag{2.48}$$

The effect of static correlation is also particularly pronounced in excited states where many different electron configurations may be close in energy, as well as in open shell transition metals & heavier elements (i.e. complexes with the f-block), again because the metal orbitals may be close in energy. This is where multireference methods become useful such as Configuration Interaction (CI) or the Complete Active Space Self Consistent Field method (CASSCF), which consider multiple electron configurations and recover a lot of the static correlation that is not present in DFT, (see Section 2.5).

2.4.2 Self-Interaction Error

The self-interaction problem of KS-DFT is a result of, as the name suggests, the methodology including contributions of an electron interacting with itself. In HF theory this is not an issue as, although electrons interact with themselves in the Coloumb term, the effect of self-interaction is directly cancelled out by the exchange term.

In 'pure' DFT, although there is an exchange term, it does not cancel out the self-interaction error exactly and leads to DFT predicting impossible quantities such as a two electron energy for a Hydrogen atom [46, 47]. The effects of the self-interaction error can be reduced through the use of hybrid functionals which contain a percentage of HF exchange, see Eqns 2.39 and 2.40. However, despite the inclusion of HF exchange in hybrid functionals the self interaction error is still present in the methodology and can still cause issues when modelling complexes containing radicals or involving significant charge-transfer [46].

There have been attempts to remedy the problems of the self-interaction error within the KS-DFT framework, most notably by Perdew and Zunger [48]. However *xc*-functionals which account for the self-interaction energy whilst also providing accurate results for more general chemistry applications comparable to popular functionals such as B3LYP are few and far between.

2.5 CASSCF/RASSCF

The Complete Active Space Self Consistent Field (CASSCF) and its derivative Restricted Active Space Self Consistent Field (RASSCF) are methods that have been developed over the last 30 years to better describe the static correlation of a molecular system whilst attempting to keep the computational cost as low as possible [49].

The CASSCF method involves selecting chemically important 'active' orbitals with which to do a full Configuration Interaction (CI) calculation [50] upon; this involves building the wavefunction of the molecule as a linear combination of a series of configurations as shown in Eqn 2.49, where c_i are the CI coefficients.

$$|\Psi\rangle = c_0|\Psi_0\rangle + \sum c_i^a|\Psi_i^a\rangle + \sum c_{ij}^{ab}|\Psi_{ij}^{ab}\rangle + \sum c_{ijk}^{abc}|\Psi_{ijk}^{abc}\rangle + ... \tag{2.49}$$

In this equation the first term is the reference configuration, the second is a sum of the single excitations, the third is a sum of the double excitations and so on. The reference configuration is generally the Hartree-Fock wavefunction. The CASSCF (and RASSCF) approach is therefore an example of a multi-configurational wavefunction based method.

In the CASSCF methodology two parameters are optimised; firstly the CI coefficients, describing the mixing of each electron configuration to the overall wavefunction. Secondly, the CASSCF molecular orbitals are optimised using an SCF method similar to HF.

To illustrate how a multi-configurational wavefunction can be constructed consider the simple example of Benzene. Benzene has three π bonding & three π anti-bonding molecular orbitals, as illustrated in Figure 2.5.

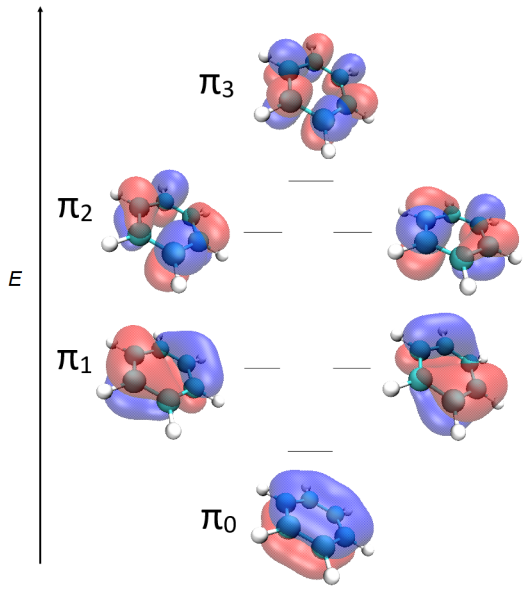

Figure 2.5: Energy ordering of Benzene π orbitals. Orbitals generated with CASSCF(6/6) active space with isosurface of 0.35 a.u.

A ground state reference wavefunction can be constructed by occupying the three lowest molecular orbitals with six electrons (Eqn 2.50), this is the same as a Hartree-Fock calculation.

$$\Psi_0 = |...\pi_0^2\pi_1^2\pi_1^2\pi_2^0\pi_2^0\pi_3^0\rangle \tag{2.50}$$

As per Eqn 2.49 we can further expand the molecular wavefunction beyond a simple Hartree-Fock calculation by the addition of single excitations, of which there are nine in this benzene example (Eqn 2.51), double excitations (Eqn 2.52) and so on.

$$\Psi_1^S = |...\pi_0^2\pi_1^2\pi_1^1\pi_2^1\pi_2^0\pi_3^0\rangle + |...\pi_0^2\pi_1^2\pi_1^1\pi_2^0\pi_2^1\pi_3^0\rangle + |...\pi_0^2\pi_1^2\pi_1^1\pi_2^0\pi_2^0\pi_3^1\rangle + |...\pi_0^2\pi_1^1\pi_1^2\pi_2^1\pi_2^0\pi_3^0\rangle + ... \tag{2.51}$$

$$\Psi_2^D = |...\pi_0^2\pi_1^2\pi_1^0\pi_2^2\pi_2^0\pi_3^0\rangle + |...\pi_0^2\pi_1^0\pi_1^2\pi_2^0\pi_2^2\pi_3^0\rangle + |...\pi_0^0\pi_1^2\pi_1^2\pi_2^0\pi_2^0\pi_3^2\rangle + |...\pi_0^2\pi_1^1\pi_1^1\pi_2^1\pi_2^1\pi_3^0\rangle + ... \tag{2.52}$$

The Benzene molecular wavefunction is then built as a linear combination of the configurations and the CI coefficients determined variationally, this is done by solving a series of CI secular equations, shown in Eqn 2.53.

$$\begin{pmatrix} \langle\Psi_0|\mathbf{H}|\Psi_0\rangle - E & 0 & \langle\Psi_0|\mathbf{H}|\Psi_2^D\rangle & 0 & ... \\ 0 & \langle\Psi_1^S|\mathbf{H}|\Psi_1^S\rangle - E & \langle\Psi_1^S|\mathbf{H}|\Psi_2^D\rangle & \langle\Psi_1^S|\mathbf{H}|\Psi_3^T\rangle & ... \\ \langle\Psi_2^D|\mathbf{H}|\Psi_0\rangle & \langle\Psi_2^D|\mathbf{H}|\Psi_1^S\rangle & \langle\Psi_2^D|\mathbf{H}|\Psi_2^D\rangle - E & \langle\Psi_2^D|\mathbf{H}|\Psi_3^T\rangle & ... \\ 0 & \langle\Psi_3^T|\mathbf{H}|\Psi_1^S\rangle & \langle\Psi_3^T|\mathbf{H}|\Psi_2^D\rangle & \langle\Psi_3^T|\mathbf{H}|\Psi_3^T\rangle - E & ... \\ ... & ... & ... & ... & \langle\Psi_n^N|\mathbf{H}|\Psi_n^N\rangle - E \end{pmatrix} \begin{pmatrix} c_0 \\ c_i^a \\ c_{ij}^{ab} \\ c_{ijk}^{abc} \\ c_n^N \end{pmatrix} = \begin{pmatrix} 0 \\ 0 \\ 0 \\ 0 \\ 0 \end{pmatrix} \tag{2.53}$$

Some of the diagonal elements in the matrix presented in Eqn 2.53 can be set to zero in accordance with Brillouin's Theorem [51] and gives the CI matrix a block diagonal structure.

It can be seen even in the simple example of Benzene that the computational expense of a CASSCF calculation is dictated by not only the size of the system but also the number of electrons and orbitals that are included in the active space. As the number of active electrons and orbitals are increased the total number of configurations increases and can be calculated by Eqn 2.54 [3];

$$N = \frac{m!(m+1)!}{(\frac{n}{2})!(\frac{n}{2}+1)!(m-\frac{n}{2})!(m-\frac{n}{2}+1)!} \tag{2.54}$$

In Eqn 2.54; N is the total number of configurations, m is the number of orbitals and n is the number of electrons [3]. It can be seen that the total number of configurations (and hence the computational cost) increases factorially meaning that realistically only a limited number of electrons and orbitals may be considered. Unfortunately computer processing power has only progressed so far to the point that a rough maximum of 18 orbitals and 18 electrons can be practically considered within the active space, which is still a significant increase on the number that would have been able to be considered a decade ago. Fortunately the presence of symmetry within a molecule can help as this reduces the total number of configurations which are present

in the description of the wavefunction.

18 orbitals and electrons can often be an acceptable limit for examining smaller molecules, however for larger molecules, especially those with a large conjugated π-system, it can begin to affect the accuracy of simulations. This is where the Restricted Active Space Self Consistent Field (RASSCF) method can be effectively utilised.

In the RASSCF approach instead of the solitary CAS there are now three spaces; RAS1, RAS2 and RAS3 [49]. The RAS2 is similar to the CAS in that all excitations are permitted within this space (although a RAS2 typically, but not always, contains fewer orbitals and electrons than a CAS would). The RAS1 space is then chosen where all selected orbitals are doubly occupied and l excitations are allowed from the RAS1. The RAS3 is composed of formally unoccupied orbitals with m excitations permitted into the RAS3, thus in the RAS1 and RAS3 spaces a truncated CI calculation is performed. Generally up to triple excitations (l,m=3) are used as this recovers a lot of the static correlation that you would obtain from a Full CI calculation [52] but crucially cuts the computational cost. A schematic of the CAS/RASSCF partitioning is shown in Figure 2.6.

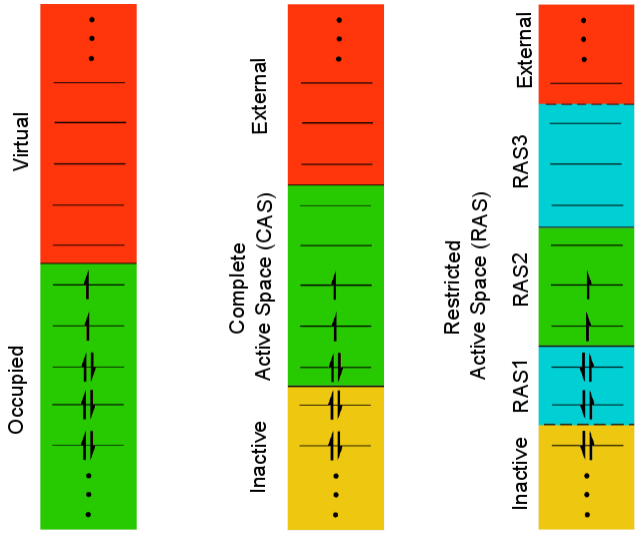

Figure 2.6: Schematic of orbital partitioning in the Hartree-Fock (left), CASSCF (middle) and RASSCF (right) methodologies.

2.5.1 Natural Orbital Occupancies

In the CAS/RASSCF method any particular active orbital can be occupied by 0, 1 or 2 electrons in each configuration. As a consequence of this, active orbitals do not have a unique eigenvalue, and hence an energy value, associated to them and so are instead often discussed in terms of their natural orbital occupation number. Natural orbitals are orbitals of maximum occupancy that are obtained when the first order density matrix is diagonalised [53]. The natural orbital occupation number is calculated as the occupation of the orbital in each configuration multiplied by the percentage contribution of that configuration to the total wavefunction.

2.5.2 Selection of Active Space Orbitals

The selection of orbitals to be included in an active space for a CASSCF calculation is dependent on what chemical property is being investigated. Including all electrons and orbitals from a molecule, i.e. in essence completing a Full CI calculation, would provide us with an almost perfect description of the static & dynamic correlation of the molecule. However Full CI is very computationally demanding to do with even a relatively small system hence the need to narrow down the active space to chemically important orbitals.

CAS/RASSCF is not a 'black box' method, often the most difficult part of the calculation can be in the selection of the orbitals which need to be included in the active space, again particularly for large π conjugated systems. In general chemical intuition can be used to decide which orbitals are important. The general guidelines for selecting orbitals for a CAS/RASSCF calculation, as described by Bjorn Roos, are [54];

- Have most active orbitals paired
- Include conjugated & aromatic orbitals
- Include bonding & antibonding orbitals of a bond that may be broken
- Generally including valence orbitals from main group elements, d-character orbitals for transition metals, 4f, 5d & 6s for lanthanides and 5f, 6d & 7s for actinides.

Should these general rules still not provide a good active space or, more commonly, provide too many orbitals for an active space, then sometimes it can be determined by trial & error. If instead a large RASSCF calculation (with an empty RAS2) is performed on the system in question, allowing only up to double excitations, then which orbitals should be included can be determined by an examination of their natural orbital occupation numbers (NOOs).

As mentioned in Section 2.5.1, CAS/RASSCF calculations sample over a number of different configurations and so the active orbitals of the system will no longer take integer values. The general guidelines to follow when selecting orbitals for an active space based on natural orbital occupation numbers are to;

- select any orbital with a natural orbital occupation which varies by more than 0.02 from either 2 or 0 in the CAS or RAS2 space
- any orbital with a natural orbital occupation which varies between 0.01 and 0.02 should be placed in the RAS1 or RAS3

However it should be noted that again these are only general guidelines and not strict rules [3] that describe a good active space.

Although CAS/RASSCF recovers a lot of the static correlation, dynamical correlation is not included. One of the most popular methods to recover this is to apply perturbation theory to the results of a CAS/RASSCF calculation. This is usually denoted CAS/RASPT2 where the PT2 stands for second order perturbation theory [3]. The details of perturbation theory is outlined in Section 2.6.

2.5.3 Notation

When reporting a CASSCF calculation the active space is normally denoted (n,m) or (n/m) where n is the number of electrons and m is the number of orbitals in the active space.

The notation of a RASSCF calculation is little more complicated but follows the same general format and is denoted (n,l,m;i,j,k) where n is again the total number of electrons in the active space, l the number of excitations permitted out of the RAS1 and m the number of excitations permitted into the RAS3). i, j and k are the number of orbitals included in the RAS 1, RAS2 & RAS3 spaces respectively [42, 43].

2.6 Perturbation Theory

Perturbation theory is a mathematical method of finding an approximate solution to a problem by perturbing an exact solution to a related simpler problem. This can be expressed in quantum mechanics in Eqn 2.55 where $\hat{H}$ is the Hamiltonian, $\hat{H}^{(0)}$ is the unperturbed Hamiltonian, $\hat{V}$ is the perturbing operator and λ is a parameter that varies from 0 to 1 [55].

$$\hat{H} = \hat{H}^{(0)} + \lambda\hat{V} \tag{2.55}$$

The Hamiltonian of our perturbed system can be expanded out to form Eqn 2.56 where higher powers indicate smaller and smaller perturbations to the unperturbed Hamiltonian $\hat{H}^{(0)}$.

$$\hat{H} = \hat{H}^{(0)} + \lambda\hat{H}^{(1)} + \lambda^2\hat{H}^{(2)} + ... \tag{2.56}$$

The same can also be applied to the wavefunction, Ψ, and the energy, E, as seen in Eqns 2.57 & 2.58.

$$\Psi = \Psi_0 + \lambda\Psi_0^{(1)} + \lambda^2\Psi_0^{(2)} + ... \tag{2.57}$$

$$E = E_0 + \lambda E_0^{(1)} + \lambda^2 E_0^{(2)} + ... \tag{2.58}$$

In Eqn 2.58 the terms $E_0^{(1)}$ & $E_0^{(2)}$ are known as the first order & second order correction energies respectively.

If Eqns 2.56-2.58 are inserted into the Schrödinger equation (Eqn 2.59) & like terms of λ are grouped Eqn 2.60 is obtained.

$$\hat{H}\Psi = E\Psi \tag{2.59}$$

$$\lambda^0(\hat{H}^{(0)}\Psi_0 - E_0\Psi_0) + \lambda^1(\hat{H}^0\Psi_0^{(1)} + \hat{H}^{(1)}\Psi_0 - E_0\Psi_0^{(1)} - E_0^{(1)}\Psi_0) + \lambda^2(\hat{H}^{(0)}\Psi_0^{(2)} + \hat{H}^{(1)}\Psi_0^{(1)} + \hat{H}^{(2)}\Psi_0 - E_0\Psi_0^{(2)} - E^{(1)}\Psi_0^{(1)} - E_0^{(2)}\Psi_0) + ... = 0 \quad (2.60)$$

λ is an arbitrary parameter and therefore the coefficient of each power of λ separately must equal zero, therefore Eqn 2.60 can instead be written as a series of equations (Eqns 2.61-2.63);

$$\hat{H}^{(0)}\Psi_0 = E_0\Psi_0 \quad (2.61)$$

$$\{\hat{H}^{(0)} - E_0\}\Psi_0^{(1)} = \{E_0^{(1)} - \hat{H}^{(1)}\}\Psi_0 \quad (2.62)$$

$$\{\hat{H}^{(0)} - E_0\}\Psi_0^{(2)} = \{E_0^{(2)} - \hat{H}^{(2)}\}\Psi_0 + \{E^{(1)} - \hat{H}^{(1)}\}\Psi_0^{(1)} \quad (2.63)$$

Eqn 2.61 is just the Schrödinger equation for the unperturbed system. The first order correction to the system can be written as a linear combination of the unperturbed wavefunctions [55] (Eqn 2.64).

$$\Psi_0^{(1)} = \sum_n a_n\Psi_n^{(0)} \quad (2.64)$$

Inserting this back into Eqn 2.62, it can be shown that;

$$E_0^{(1)} = \langle\Psi_0|\hat{H}^{(1)}|\Psi_0\rangle \quad (2.65)$$

The first order correction to the energy can therefore be calculated as the first order perturbation with respect to the unperturbed wavefunction. The matrix element $H_{00}^{(1)}$ from Eqn 2.65 is the average value of the perturbation with respect to the unperturbed state. Similarly the second order correction can be calculated using;

$$\Psi_0^{(2)} = \sum_n b_n\Psi_n^{(0)} \quad (2.66)$$

which can be inserted into Eqn 2.63 to form;

$$E_0^{(2)} = \langle \Psi_0 | \hat{H}_0^{(2)} | \Psi_0 \rangle + \sum_{n \neq 0} \frac{\hat{H}_{0n}^{(1)} \hat{H}_{n0}^{(1)}}{E_0 - E_n} \tag{2.67}$$

Eqn 2.67 shows that the first order correction is required to calculate the second order correction. In fact, if an n^{th} order perturbation of the wavefunction is known then $2n+1$ order perturbation energies can be calculated. However typically corrections beyond the second order are rarely computed, as they can be computationally very expensive and, in the case of Moller-Plesset (MP) perturbations can even diverge.

2.6.1 CASPT2

In the CASPT2 approach, the CASSCF wavefunction is used as the zeroth order reference wavefunction from which to calculate the perturbation energies. One of the limitations of perturbation theory is that for the perturbative corrections to the energy to be accurate the reference wavefunction must be a good approximation. This means that the choice of active space in the CASSCF approach is not only important for studying the system using CASSCF but also when it comes to calculating accurate energies with CASPT2 [56].

Other considerations when performing a CASPT2 calculation are intruder states and the inclusion of the Ionisation Potential and Electron Affinity (IPEA) shift. Intruder states occur when an orbital outside the CASSCF active space in the CASSCF reference wavefunction has a similar energy to an orbital inside the CASSCF active space. The best way to deal with intruder states is to expand the size of the CASSCF active space, however this is not often practical due to the increased computational demands. The second, and more commonly used, option is to instead introduce a imaginary level shift to the zeroth order Hamiltonian ($\hat{H}_0^{(0)}$). By introducing a level shift in $\hat{H}_0^{(0)}$ weak intruder states should be removed when calculating the first order correction, then with intruder states removed the second order correction can be calculated, following which a transformation can be computed to remove the level shift [57, 58].

The IPEA shift is another parameter that is implemented in the second order perturbation theory program of Molcas. It has been found that CASPT2 energies, particularly excitation energies are underestimated by the methodology [59, 60]. The systematic errors are due, according to Ghigo and coworkers, to an unbalanced description of the zeroth order Hamiltonian for unpaired electrons. This has been remedied, to a certain extent, by modification of the zeroth order Hamiltonian with a shift, which has been parameterised by the calculation of different properties of several diatomic molecules [56].

2.7 Basis Sets

In order to use different computational methods to derive approximate solutions to the Schrödinger equation, basis sets must be used. These are a set of functions which describe atomic orbitals that can be combined in a linear combination to form molecular orbitals (see Section 2.1.2).

There are two main types of functions available when studying molecular systems; Gaussian Type Orbitals (GTO) & Slater Type Orbitals (STO). The form of a GTO function is shown in Eqns 2.68 and 2.69 using polar and cartesian coordinates respectively [3].

$$\chi_{\zeta,n,l,m}(r,\theta,\varphi) = NY_{l,m}(\theta,\varphi)r^{2n-2-l}e^{-\zeta r^2} \tag{2.68}$$

$$\chi_{\zeta,l_x,l_y,l_z}(x,y,z) = Nx^{l_x}y^{l_y}z^{l_z}e^{-\zeta r^2} \tag{2.69}$$

In the GTO equations N is a normalisation constant, $Y_{l,m}$ are spherical harmonic functions & r is the distance from the nucleus. The sum of n, l and m give information about the type of orbital being constructed, for instance when the sum is 0 the orbital has spherical symmetry and is an s-type orbital.

Eqn 2.70 shows the form of an STO in polar form.

$$\chi_{\zeta,n,l,m}(r,\theta,\varphi) = NY_{l,m}(\theta,\varphi)r^{n-1}e^{-\zeta r} \tag{2.70}$$

The r^2 dependence in the exponential term in the GTO compared to only an r dependence in the exponential term in the STO results in some key differences between the two. At an atomic nucleus a GTO has a zero slope whilst a STO has a cusp, this results in GTOs struggling to properly model behaviour near the nucleus. Furthermore at large distances from the nucleus GTOs fall off far too rapidly compared to STOs [22, 36], this can be seen in Figure 2.7.

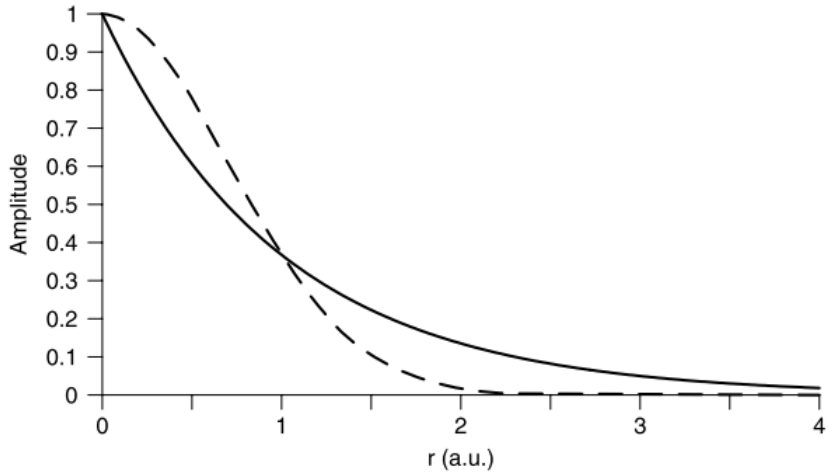

Figure 2.7: Solid line shows the form of e^{-r} (STO) whilst dashed line shows form of e^{-r^2} (GTO) - adapted from [3].

In terms of computational efficiency, GTOs are more favourable to use, however as discussed above STOs reproduce radial shape more accurately. Therefore in order to produce basis sets with the best properties of both, some of the first basis sets were constructed as linear combinations of GTOs to form the shape of an STO. When an STO basis set is formed from a linear combination of GTOs it is known as a contracted basis set and the GTOs from which it

is constructed are know as primitive Gaussians [3].

After considering which type of functions to use for a basis set, the second consideration is how many functions to use. The minimum number of functions that can be used, which has just enough to contain all the electrons of the system under investigation, is known as a minimal basis (MB) set [22]. Minimal basis sets generally do not give accurate results, and so the next step up is a doubling of all functions included in a minimal basis set to form a double zeta (DZ) basis set, where the zeta refers back to ζ in Eqns 2.68, 2.69 and 2.70. Similarly a triple zeta (TZ) basis set is a tripling of the number of functions in a minimal basis set and a quadruple zeta (QZ) is a quadrupling and so on.

A minimal basis will include one s function for hydrogen and helium, two s and one set of p functions for a first row element and for a second row element three s and two sets of p functions. A double zeta for Carbon therefore contains four s and two p functions, however doubling the number of functions for a 1s orbital in Carbon is rather unnecessary as it is buried deep in the core and so the use of a single s function is sufficient to describe the orbital and the electrons that occupy it. Therefore a variation on the double zeta (and above) basis set(s) has been produced in which only the valence orbital functions are doubled, this is known as a split valence basis set (e.g. VDZ means split valence double zeta, VTZ means split valence triple zeta and so on). As increasing the number of basis functions in your basis set increases the computational cost, the advantage of split valence basis sets is that increased accuracy can be obtained whilst the computational cost is kept as low as possible.

2.7.1 Polarisation & Diffuse Functions

To further increase the accuracy of calculations, polarisation & diffusion functions can be added to basis sets. Polarisation functions are included by the addition of higher angular momentum functions, for instance adding a p-function to a Hydrogen or a d-function to a first row element

and as the name suggests polarises the orbitals that are formed from the basis set. Adding polarisation functions to a VDZ basis set forms a VDZP basis set (split valence double zeta plus polarisation). Similarly if two sets of polarisation functions are added, it is denoted as a VDZ2P basis set.

However adding more and more polarisation functions not only increases the computational cost but also may unbalance the basis set. A general guideline is that the number of functions of certain angular momentum should be at most one less than the number of functions with one lower angular momentum. For instance a 2s2p2d basis set would be considered overpolarised for Carbon but not a 3s2p1d basis set.

Diffuse functions are often utilised in simulations where there are loosely bound electrons, such as in anions or excited states. Diffuse functions have a low value of ζ (Eqns 2.68 - 2.70), which means that they better describe asymptotic behaviour at large distances from the nucleus.

2.8 Quantum Theory of Atoms in Molecules (QTAIM)

The Quantum Theory of Atoms in Molecules (hereafter referred to as QTAIM) is a methodology developed by Bader [61, 62, 63, 64] to describe the quantum nature of molecules, from which many properties can be quantitatively described. QTAIM relies heavily on quantum observables such as the electron density in order to do this.

2.8.1 Critical Points

In QTAIM a Critical Point (CP) is the point at which the first derivative (i.e. the gradient) of the electron density, $\rho(\mathbf{r})$, is zero. There are many different types of CPs which are distinguished from each other by the direction of second derivative of the electron density. In 3-D space there are nine second derivatives of $\rho(\mathbf{r})$ which can be arranged in the Hessian Matrix (Eqn 2.71).

$$H = \begin{pmatrix} \frac{\partial^2\rho}{\partial x^2} & \frac{\partial^2\rho}{\partial x\partial y} & \frac{\partial^2\rho}{\partial x\partial z} \\ \frac{\partial^2\rho}{\partial y\partial x} & \frac{\partial^2\rho}{\partial y^2} & \frac{\partial^2\rho}{\partial y\partial z} \\ \frac{\partial^2\rho}{\partial z\partial x} & \frac{\partial^2\rho}{\partial z\partial y} & \frac{\partial^2\rho}{\partial z^2} \end{pmatrix} \tag{2.71}$$

The Hessian matrix is real and symmetric and can therefore be diagonalised, which is equivalent to rotating the coordinate system $\mathbf{r}(x,\ y,\ z) \rightarrow \mathbf{r}(x',\ y',\ z')$ where the new axes x', y', z' are the principal curvature axes of the CP [64]. The Hessian in its diagonal form (Λ) is shown in Eqn 2.72 where λ_1, λ_2 & λ_3 are eigenvalues.

$$\Lambda = \begin{pmatrix} \frac{\partial^2\rho}{\partial x'^2} & 0 & 0 \\ 0 & \frac{\partial^2\rho}{\partial y'^2} & 0 \\ 0 & 0 & \frac{\partial^2\rho}{\partial z'^2} \end{pmatrix} = \begin{pmatrix} \lambda_1 & 0 & 0 \\ 0 & \lambda_2 & 0 \\ 0 & 0 & \lambda_3 \end{pmatrix} \tag{2.72}$$

In addition to being eigenvalues of the Hessian, λ_1, λ_2 & λ_3 are also the curvatures of the density with respect to the principle axes, *x', y'* & *z'* at the Critical Point.

CPs are classified by their rank (ω), which is the number of non-zero curvatures of $\rho(r)$, & signature (σ), the sum of the signs of the curvatures; denoted CP(ω, σ) [64]. The value of the rank of a CP is nearly always 3 for a stable system. In total there are four types of stable CPs; Nuclear Critical Point (NCP), Bond Critical Point (BCP), Ring Critical Point (RCP) & Cage Critical Point (CCP). NCPs (3,-3) are found at local maxima of the electron density (negative curvatures along the principle axis x', y' & z') and correspond to the position of atoms, whilst CCPs (3,+3) are found at the opposite, at a local minimum. Perhaps of most interest is the BCP (3,-1) where the second derivative is negative in two directions and positive in the third, perpendicular to the bond path.

The Poincaré-Hopf (PH) relationship [62] (Eqn 2.73) outlines the number and type of critical points that can coexist in a molecule or crystal:

$$n_{NCP} - n_{BCP} + n_{RCP} - n_{CCP} = \begin{cases} 1 & \text{(Isolated molecules)} \\ 0 & \text{(Infinite Crystals)} \end{cases} \tag{2.73}$$

Figure 2.8 shows an example of different critical points in the Ce(II)Cp_3 system. If the PH relationship is applied to the system in Figure 2.8 where there are 45 BCPs, 18 RCPs, 3 CCPs & 31 NCPs it can be seen that the relationship is satisfied as an isolated molecule.

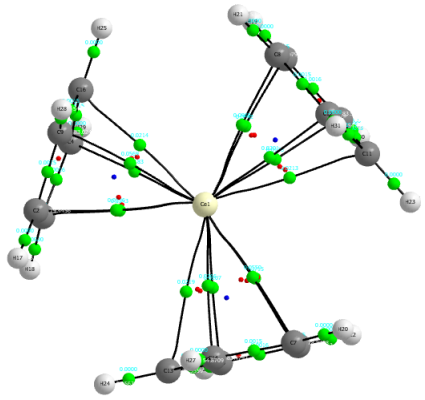

Figure 2.8: Critical Points in the $[Ce(II)Cp_3]^-$ system, green spheres indicate BCPs, red spheres RCPs and blue spheres CCPs.

The electron density at critical points can yield some important properties about a molecule. Attention is now focused on BCPs, generally speaking a bond can be considered to be covalent if the electron density at the BCP, ρ_{bcp}, is 0.20 a.u. or higher, whilst lower than 0.10 a.u. is indicative of ionic bonding. Furthermore it has been shown that ρ_{bcp} can be directly related to the binding energy of the bond [64].

There are many other properties that can be obtained from a QTAIM analysis, these can be categorised as topological properties, those obtained as a result of the deformations of the electron density, or as integrated properties, calculated through the integration of the electron density.

2.8.2 Topological Properties

The value of the electron density at a critical point (ρ_{bcp}) is an example of a topological property obtained from QTAIM analysis. Other useful topological properties include the Laplacian at

the critical point ($\nabla^2\rho_{bcp}$) & the bond path.

The Laplacian is a second order differential operator defined as the divergence of the gradient, in this case, of the electron density. In section 2.8.1 the Hessian was defined (Eqn 2.71), The Laplacian of the electron density at the critical point can be defined using the eigenvalues of the Hessian (Eqn 2.74).

$$\nabla^2\rho(\mathbf{r}) = \frac{\partial^2\rho(\mathbf{r})}{\partial x^2} + \frac{\partial^2\rho(\mathbf{r})}{\partial y^2} + \frac{\partial^2\rho(\mathbf{r})}{\partial z^2} = \lambda_1 + \lambda_2 + \lambda_3 \tag{2.74}$$

$\nabla^2\rho_{bcp}$ is therefore the sum of the curvatures of the density at the critical point. At a BCP(3,-1), two of these are negative whilst the third is positive. The magnitude of these numbers presents information about the bonding associated with that particular BCP. In a covalent bond, the two negative curvatures tend to be larger than the one positive curvature and so $\nabla^2\rho_{bcp} < 0$, conversely in a bond considered ionic the positive curvature is dominant and $\nabla^2\rho_{bcp} > 0$. However it should be noted that this is a guide rather than a rule, for instance in strongly polar bonds because of the accumulation of electron density in all directions the Laplacian can be either sign.

The bond path is a line of locally maximum density which connects two nuclei. It is important to note that in QTAIM the bond path is not necessarily the same as a bond. The point along the bond path where the electron density is at a minimum is the BCP.

2.8.3 Integrated Properties

In addition to topological properties, more information can be obtained by also calculating the integrated properties. For instance, integrating the electron density over an atomic basin of atom A gives the number of electrons localised on A, N_A [65]. N_A can be related back to the atomic charge of atom A, $q(A)$, which is the difference between the atomic number, Z_A, and N_A and is shown in Eqn 2.75.

$$q(A) = Z_A - N_A \tag{2.75}$$

N_A & $q(A)$ provide information about where the electrons are located in the molecules.

Further useful properties can also be obtained by integrating the electron pair density over an atomic basin to calculate the localisation index, $\lambda(A)$, or integrating over a pair of atomic basins to obtain the delocalisation index, $\delta(A, B)$.

$\lambda(A)$ is a measure of the number of electrons localised on atom A, whilst $\delta(A, B)$ is a measure of the number of electrons shared between atoms A & B. When A & B are bonded, and in the absence of charge transfer, then $\delta(A, B)$ can be considered as the bond order or index.

2.9 Software Packages Used

2.9.1 GaussView

All molecular structures, before geometry optimisations and when not taken from experiment, have been built using GaussView [66].

2.9.2 Turbomole

All Density Functional Theory and Time Dependent Functional Theory calculations have been completed using version 6.6 of the Turbomole program [67] unless otherwise indicated. Turbomole calculations have employed the Ahlrichs style basis sets of polarised triple-zeta quality (def2-TZVP) [68].

2.9.3 Molcas

All CASSCF and RASSCF calculations have been completed using the Molcas 8.0 program [69] and employed the relativistically contracted atomic natural orbital (ANO-RCC) basis sets [70]

of polarised triple-zeta quality. Scalar relativistic effects were included via the use of the 2nd order Douglas-Kroll-Hess Hamiltonian in all calculations [71].

Where second order perturbation theory calculations (PT2) have been completed, these have been performed on the converged CAS/RASSCF wavefunctions and adds in the effect of dynamical correlation. All perturbation theory calculations included an imaginary level shift of 0.2 a.u. which was included to reduce the effect of intruder states. Additionally all perturbation calculations have also been performed both with the standard IPEA shift of 0.25 a.u.

2.9.4 Aimall

All QTAIM data presented in this thesis has been obtained using the Aimall package on wavefunctions obtained from the programs described above [72].

Chapter 3

Porphyrin Complexes

3.1 Introduction

3.1.1 Overview

Porphyrin ring complexes are some of the most widely studied and investigated molecules in the chemical world. Their necessity to life, in processes such as photosynthesis in plants and oxygen transport in the human body, and the colourful complexes they form have earned them the nickname The Pigments of Life [73], in fact the word Porphyrin is derived from the Greek word for purple, *porphura*.

The simplest porphyrin molecule, porphine, is shown in Figure 3.1, the backbone structure consists of four pyrrole rings joined together by four methine bridges. Porphyrins can be easily substituted at the eight β positions on the four pyrrolic rings as well as at the four meso positions of the methine bridge. This wide range of potential substitution positions on the porphyrin ring backbone, in addition to the vast number of groups which can be substituted, gives rise to a huge number of potential molecules which can be synthesised.

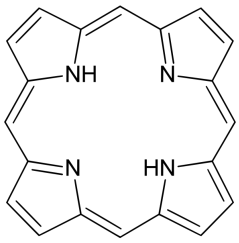

Figure 3.1: Porphine - the simplest free base porphyrin (FBP) consisting of four pyrrole joined together by four methyne bridges.

Porphine is an example of a Free Base Porphyrin (FBP), a porphyrin ring that is not complexed to a metal. Complexation of porphyrin rings to metals can occur when the porphyrin ring is deprotonated and an anion with a -2 charge is formed. If the many different metals which can complex to the ring are included, the total number of potential porphyrin molecules increases even further. By differing the metal and the substitution on the basic porphyrin backbone structure the electronic energy gap between occupied and unoccupied orbitals can be altered. By varying this energy gap we can fine tune potentially useful porphyrin molecules for various applications, including but not limited to photosensitisers for cancer therapy and dye sensitised solar cells (DSSC), described later in Section 3.1.4.

3.1.2 Gouterman's Four Orbital Model

The optical absorption spectra of porphyrins has been rationalised by Goutermans four orbital model [74], which considers the main electronic transitions of porphyrin complexes to be between the HOMO (highest occupied molecular orbital) and HOMO-1 to the LUMO (lowest unoccupied molecular orbital) and LUMO+1 of the porphyrin ring, shown in Figure 3.2 (right).

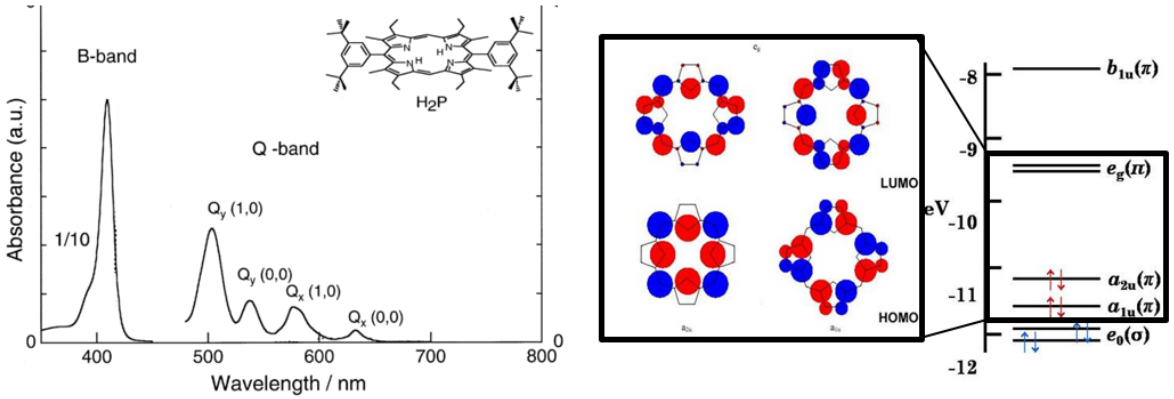

Figure 3.2: Absorption Spectra of a FBP showing the difference in intensity of the Q and B bands (left) & Energy level diagram of Gouterman Orbitals and molecular orbital pictures (right). Adapted from [4, 5, 6].

The main transitions seen in the absorption spectra of porphyrin complexes are called the Q and B bands. The B band is a very intense absorption band which is characterised by its large oscillator strength and is commonly referred to as the Soret Band (or Peak). The Q band is weaker than the B band and exists as two separate components for porphine due to its D_{2h} symmetry. Figure 3.2 above shows an example absorption spectra of a FBP (left) and the Gouterman orbitals and their energies (right) for a D_{4h} porphyrin.

The problem with considering only these four 'Gouterman' orbitals is that it is a very simplistic view of what is a highly conjugated and complex molecule. In truth the electronic transitions of porphyrin molecules are composed of transitions from the entire conjugated π-system. This is why when the substitution on the ligand backbone is altered or the metal complexed changed, the excitation energies obtained from an absorption spectra are also altered. For example if a conjugated chain were to be added to one or more of the meso or β positions on the Porphyrin ring then the number of π electrons in the system and the overall conjugation of the molecule would be increased. This in turn would affect the energy levels of the Gouterman orbitals

and hence also the excitation energies. Generally speaking it can be predicted what would happen if an electron donating or withdrawing group is added to the porphyrin backbone, however synthesising the molecule and experimentation is the only way to quantify the change in excitation energies.

3.1.3 The Need for Computational Models

Obviously not every porphyrin molecule will have the potential for useful applications, so how can the screening of every potential molecule without the waste of time, effort and resources be achieved? To efficiently test for potentially useful molecules it is wise to utilise computational chemical simulations and calculations. In order to assess the effect of different metals and substitutions on the electronic energy gap and the absorption spectrum, excited states of the molecules in question also need to be simulated. Excited states can be simulated using Time Dependent Density Functional Theory (TDDFT) or by using multiconfigurational methods (such as CASSCF), an overview of both of these methods is given in Section 2.

But what is the most accurate and efficient way of describing the electronic structure of both free base and metal porphyrins? Can an accurate generic description of the frontier orbitals of a metal porphyrin be defined which can be transposed onto any metal porphyrin system that is to be investigated? The aim of this section of the thesis is to develop an understanding of the transitions that comprise the excitations of porphryin system and consequently a method of selecting orbitals that is not particular to one transition metal porphryin system.

3.1.4 Potential Uses of Porphyrin Complexes

As mentioned previously the substitution on the ring and complexation to different metals affects the electronic energy gap. This is evident in the very different colours of haemoglobin (Fe) and chlorophyll (Mg), both of which are porphyrinLOL complexes (both shown in Figure 3.3).

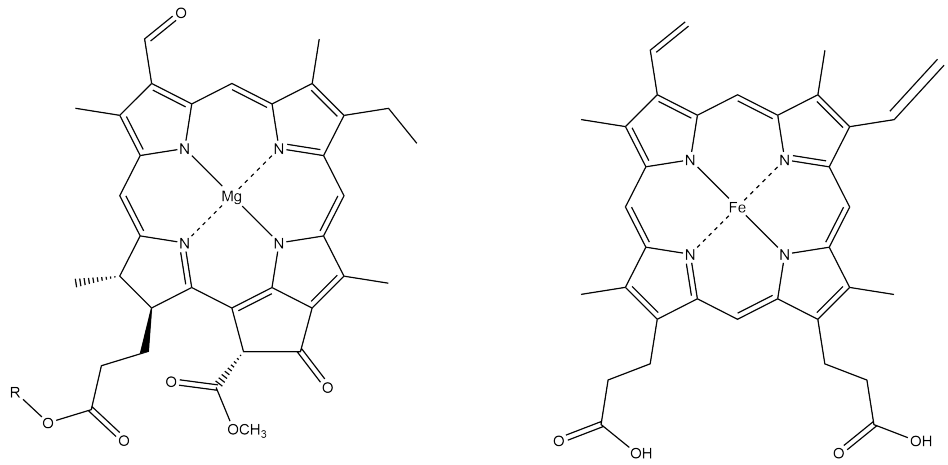

Figure 3.3: Chemical structures of Chlorophyll (Left) and Haemoglobin (Right) showing the porphryin ring backbone structure.

Recently uses of porphyrins have expanded into molecular electronics, specifically as dye-sensitised solar cells (DSSC). A dye sensitised solar cell is a variation of thin-film solar cells, they are a semi-conductor formed between the photo-sensitised anode and an electrolyte. DSSCs are potential sources of renewable energy as although they typically possess low conversion rates they are cheap to make, very tunable and easily fabricated [75]. Typically porphyrin based DSSCs contain zinc porphyrin as the photosensitised dye [75, 76, 77] but there are also a great deal of other transition metals that have been used in the literature including but not limited to Ruthenium [78, 79] and Cobalt [80].

Another use of porphyrins molecules is in medical imaging and photodynamic therapy (PDT). Photodynamic therapy is the use of light-sensitive molecules to kill abnormal cells. Porphyrin molecules are ideal molecules for photodynamic therapy because they are soluble in water, meaning that they can be administered intravenously, as well as having an energy gap that is tunable, as has been mentioned previously. Porphyrins as photosensitisers in PDT will be revisited in Chapter 5.

3.2 Free Base Porphyrin

3.2.1 Introduction

Free Base Porphyrins (FBP) are porphyrin molecules which have no metal complexed. They are porphyrin molecules that are very well reported in the literature, an overview of which is given in Section 3.2.2. As mentioned previously, the simplest FBP is porphine (hereafter referred to as FBP unless otherwise indicated) shown in Figure 3.1, its electronic structure and excitation energies have been studied extensively. This is why FBP has been selected as the starting molecule that will be used to test different TDDFT functionals as well as CAS/RASSCF active spaces. Considering that the Q and B bands are composed of mainly of ligand-ligand transitions, even in metal porphyrins, functionals that perform well for FBP should also perform well for regular metal porphyrins.

3.2.2 Summary of previous computational FBP work

A full table summarising excitation energies and methods compared to experimental values is presented at the end of this section in Table 3.1.

When it comes to simulating the optical absorption spectrum of FBP the vast majority of papers use the TDDFT methodology. One of the most comprehensive papers examining the singlet excitation energies of FBP using TDDFT was published in 2000 by D. Sundholm [81]. In his paper, Sundholm reports the singlet excitation energies of FBP calculated with two different functionals with varying basis sets. Sundholms structures were optimised using DFT with the BP (Becke-Perdew) functional [82] and a split valence basis set with polarisation functions (SVP). Singlet excitation energies were then calculated with four different combinations of functionals and basis sets; BP/SVP, BP/SVP and diffuse basis functions, BP/TZVP (triple zeta valence plus polarization basis set) and B3LYP (the Becke three parameter exchange-correlation functional incorporating Lee-Yang-Parr correlation)/SVP [38].

Sundholms results showed that there is little variation on the excitation energies by changing the basis set used (0.01 eV), which is slightly surprising as larger basis sets should describe the more diffuse orbitals on an excited state better. However changing the functional used does result in a difference in calculated excitation energies. The results also showed that the BP functional predicted the value of the Q_x band excitation energy more accurately than the B3LYP functional, BP giving a value of 2.13 eV compared to the B3LYP value of 2.24 eV (Experimentally observed at 1.98 - 2.12 eV) [11]. On the other hand the B3LYP functional performs much better in the calculation of the Q_y and B band excitation energies; 2.39 & 3.27 eV with B3LYP and 2.26 & 2.95 eV with BP (Experimentally 2.42 and 3.33 eV [11]).

B3LYP is one of the most popular functionals used by computational chemists and it is not a surprise to see many papers in the literature reporting the singlet excitation energies of FBP using B3LYP. Another paper where B3LYP is used was published by Parusal & Ghosh in 2000 who looked at the excitation energies of FBP, FBC (Free Base Chlorin) and FBBC (Free Base Bacteoriochlorin) using DFT/SCI (Density Functional Theory/Single Excitation Configuration Interaction) [83]. This method involves optimising the ground state using DFT, to obtain eigenvalues and molecular orbitals, and then performing a CI calculation [84]. Their structures were optimised using DFT B3LYP/TZP model chemistry and the symmetry was restricted to D_{2h}. The singlet excitation energies were calculated to be 2.03, 2.29, 3.54 eV for the Q_x, Q_y and B band respectively. These results are remarkably close for the Q_x band which is significant considering that TDDFT can struggle to reproduce the value for the Q_x band, even with a hybrid functional (such as B3LYP). The values for the Q_y and B band show a similar error to that seen for TDDFT when non-hybrid functionals are used. If these results are compared to Sundholms using B3LYP it can be seen that DFT/SCI produces a better value for the Q_x band but not the Q_y or B band excitation energies.

Another paper published in 2006 by Petit *et al*, like Parusal & Ghoshs, calculated the singlet excitation energies of FBP, FBC and FBBC. However in addition to calculating energies in the gas phase they also implicitly modelled solvation effects [85]. Structures were optimised with DFT using the PBE0 (Perdew-Burke-Erzenrhof) hybrid functional [86] and the 6-31G(d) basis set. Structures were optimised both in the gas phase, whilst constrained to the correct symmetry (D_{2h} in the case of porphine), and also explicitly including solvating water molecules (with no symmetry restrictions). Excitation energies were then calculated using TDDFT and the PBE0 functional employing the 6-31+G(d) basis set. Bulk solvation effects were included by use of the conductor like polarisable continuum model (C-PCM) for excited state calculations.

Petit *et al* calculated the singlet excitation energies *in vacuo* to be 2.33, 2.49 and 3.43 eV for the Q_x Q_y and B band respectively. When modelled including a C-PCM the singlet excitations were calculated to be 2.36, 2.50 and 3.34 eV. If the values for both the gas phase and in solution are compared to the experimental values of 1.98, 2.42 and 3.33 eV it can be seen that the aqueous model gives excitation energies that are further away from the experimental values for the two Q bands (especially the Q_x) but almost exact for the B band excitation energies. It is important to note that the Q_x band experimental excitation energy was measured in the gas phase.

A more recent paper examining the use of TDDFT was published in 2012 by Valiev *et al* [87] which simulated the singlet and triplet excitation energies of three different free base porphyrins; porphine, tetraphenylporphin (H_2TPP) and tetrabenzoporphin (H_2TBP). The structures used by Valiev were optimised using DFT B3LYP/def2-TZVP model chemistry. Using these optimised structures the singlet and triplet excitation were calculated with TDDFT using the same model chemistry and also using Second Order Coupled-Cluster theory (CC2) (for a description of this methodology please see the literature) [3].

Valiev's calculations found that the singlet excitation energy of the Q_x band of free base por-

phine, using both CC2 and TDDFT, were overestimated when compared to the experimental energies by about 0.3 eV. However, like Sundholms calculations, TDDFT was able to accurately give a value for the Q_y and B band which was comparable to experiment (2.42 and 3.31 eV respectively). This agreement was not seen in the calculations completed with CC2 which overestimated the energies to the same degree as it did with the Q_x band.

As with porphine a similar result is seen for H_2TPP and H_2TBP with CC2 overestimating every excitation energy and TDDFT calculating values which were comparable to experiment, with the exception of the Q_x band which is overestimated by both. It is worth noting that Valievs calculations show that the TDDFT results are not as close to experiment for H_2TPP and H_2TBP as they are for porphine, although still in good agreement.

One of the first papers which reported the use of a multiconfigurational method was a paper published in 1994 by Merchan and Roos which employed the Complete Active Space Self Consistent Field method with Perturbation Theory (CASPT2) [88]. The CASSCF reference wavefunction contained four electrons in the four Gouterman orbitals (denoted as 4/4 electrons/orbitals) which was then treated with perturbation theory to correlate the remaining π electrons in one calculation and also the π and σ electrons in another. In the absence of perturbation theory the CASSCF calculation gives excitation energies which are wildly different to experimental values (3.99, 4.56, 5.76 eV) however when the π electrons are correlated with perturbation theory the value for Q_x band is almost predicted correctly (1.85 eV) however the Q_y and B band excitation energies (3.48 and 4.69 eV) are again very different to the experimental excitation energies. Finally correlating both the π and σ electrons gets the predicted Q_y and B band excitation energies closer (2.74 and 3.74 eV) to experimental excitation energies but the Q_x band is greatly underestimated (1.20 eV). Merchan & Roos then began to increase the number of active orbitals and electrons in the active space which gradually brought the excitation energies for the Q_x, Q_y and B band closer to the experimental values. This trend makes

sense as although Goutermans four orbital model is partially correct it is also essentially too simplistic and the electronic transitions of porphine should be considered to have contributions from the entire π conjugated ring (i.e. 26 electrons in 24 orbitals).

In 1998 another paper using CASPT2 to calculate the singlet excitation energies was published by Serrano-Andres and Roos [89]. The structures used for the CASPT2 calculations were optimised using DFT with the B3PW91 (Becke three-parameter exchange functional with Perdew Wang 91 correlation) functional [38] using the 6-31G* basis set whilst restricting the structure to D_{2h} symmetry. Serrano-Andres and Roos used two different active spaces for calculating the singlet excitation energies, one which included 14 electrons in 13 orbitals (14/13) and the other including 16 electrons in 14 orbitals (16/14). The authors claim that the CASPT2 results do not depend on the size of the active space but the orbitals which are selected to be included in the active space. Roos computational results gave a good agreement with experiment for the singlet excitation energies with an error of around 0.2 eV for the Q_x, Q_y and B bands when using the (16, 14) active space (1.63 eV, 2.11 eV and 3.12 eV respectively).

A study using RASSCF, which is a method derived from CASSCF where the active space is split into three smaller sections, was published by Sauri *et al* in 2011 which calculated the excitation energies of FBP [90]. Structures were optimised using DFT (B3LYP) with the TZVP basis set. Excited states were then calculated using RASPT2, the active space used contained 26 electrons and 24 orbitals. Understandably the best results were obtained when single, double and triple excitations were permitted which simulated the Q_x, Q_y and B band to be 1.91, 2.16 and 3.16 eV respectively. These results obtained are remarkably close to the experimental values, however a slight underestimation is seen for the Q_y band.

Like the paper published by Sauri *et al*, RASSCF was also used by A. Kerridge in 2013 to compare the results of the singlet excitation energies of FBP, MgP and ZnP to experimental

results [59]. Structures were optimised using DFT (B3LYP) using the def2-TZVP basis set whilst restricting to D_{2h} symmetry. Two different active spaces were used in the RASPT2 calculations of the singlet excitation energies, the first containing 16 electrons in 14 orbitals and the second containing 26 electrons in 24 orbitals active space.

The eight lowest excitation energies were compared to experiment, for the 16 electron active space the error is around 0.4 eV regardless of the number of excitations permitted between the RAS1 and RAS3 spaces. The best result is seen for the 26 electron active space which allows triple excitations and 4 excitations between the RAS1 and RAS3 spaces and has an overall average error of 0.3 eV.

Table 3.1 below summarises the paper, method and excitation energies calculated for FBP. (Note (s) indicates modelled in solution).
The literature all seems to agree upon the error given by TDDFT for the singlet excitation energies of FBP, which is in the range of 0.1-0.4 eV, regardless of the functional used. When considering the relative low computational cost of TDDFT, especially compared to more computationally demanding methods, the deviation from experimental values is not a bad result. Furthermore looking at the results it is clear that the hybrid functionals (i.e. B3LYP and PBE0) perform better in calculating excitation energies. This is most likely because DFT functionals perform poorly for long range interactions which become more important for excited states due to the more diffuse orbitals. However hybrid functionals contain some Hartree-Fock exchange which helps correct some of the long range errors and hence we see better results for hybrid functionals.

The CASPT2 results vary greatly for the Q and B bands depending on the active space used. One of the biggest problems when it comes to using CASPT2 is that even modern day computer processors have not advanced far enough yet that more than 16 electrons and 16 orbitals can be considered in a CAS wavefunction calculation. This is a problem as when considering the

Lead Author (Year)	**Method**	**Other Details**	**Qx**	**Qy**	**B**
-	Experiment [74]	-	1.98	2.42	3.33
Sundholm (2000)	TDDFT	BP,SVP	2.13	2.25	2.94
		BP, SVP+diff	2.13	2.25	2.94
		BP,TZVP	2.13	2.26	2.95
		B3LYP, SVP	2.24	2.39	3.27
Parusal (2000)	DFT/SCI	B3LYP, TZP	2.03	2.29	3.54
Petit (2006)	TDDFT	PBE0, 6-31G(d)	2.33	2.49	3.43
			2.36 (s)	2.50 (s)	3.36(s)
Valiev (2012)	TDDFT	B3LYP, TZVP	2.27	2.42	3.31
	CC2	-	2.37	2.70	3.51
Merchan (1994)	CASPT2(4/4)	Correlating π electrons	1.85	3.48	4.69
		Correlating π and σ electrons	1.20	2.74	3.74
Roos (1998)	CASPT2(14/13)	ANO-S, TZVP	1.67	2.14	3.04
	CASPT2(16/14)		1.63	2.11	3.08
Sauri (2011)	RASPT2 (26,3,3;11,4,9)	ANO-S, TZVP	1.91	2.16	3.16
Kerridge (2013)	RASPT2 (16,3,3;6,4,4)+IPEA	ANO-RCC, TZVP	2.35	2.68	3.75
	RASPT2 (16,3,3;6,4,4)		1.65	1.97	2.95
	RASPT2 (26,3,3;11,4,9)+IPEA		2.28	2.57	3.59
	RASPT2 (26,3,3;11,4,9)		1.95	2.21	3.13

Table 3.1: Summary of calculated FBP Singlet Excitation Energies (in eV) using a variety of methodologies from the literature.

electronic transitions of porphyrins, all 26 π electrons (and potentially the entire valence space) should really be included due to the conjugated nature of the porphyrin ring. This is perhaps the source of the error in CASPT2 calculations on FBP which have been reported. As can be seen in the RASPT2 (which can include more electrons and orbitals) calculations, performed by A. Kerridge, calculated values which are closer to the experimental values are achieved.

3.2.3 Computational Details

The structure of FBP was constructed using GaussView [66] and optimised with Density Functional Theory (DFT). DFT structure optimisations were performed using version 6.6 of the Turbomole program [67] employing the Ahlrichs style basis sets of polarised triple-zeta quality (def2-TZVP) [68]. Five different exchange correlation ($xc-$) functionals were used, the hybrid $xc-$functionals; BHLYP [91, 35, 38], PBE0 [86], B3LYP [91, 35, 92], TPSSh [93, 94] which contain 50%, 25%, 20% and 10% exact Hartree Fock (HF) exchange respectively and the meta-GGA (generalised gradient approximation) $xc-$functional TPSS [37] which includes no exact HF exchange. Structures were constrained to D_{2h} symmetry and frequency analysis performed to ensure that structures were at a minima by ensuring there are no negative frequencies.

Following the structure optimisations of FBP, singlet excitation energies were calculated using Time Dependent-DFT (TDDFT) using the same functional that was used for optimisation and maintaining D_{2h} symmetry, again completed with Turbomole version 6.6 and def2-TZVP basis sets.

The structure of FBP was also optimised using a COSMO continuum solvation model with the relative permittivity of the model chosen so as to model a solvent such as water. The same basis sets and xc-functionals were used as for the gas phase calculations.

CAS/RASSCF calculations were also completed and employed the relativistically contracted

atomic natural orbital (ANO-RCC) basis sets [70] of polarised triple-zeta quality on B3LYP-DFT optimised structures, (14s9p4d3f2g)/[4s3p2d1f] for C and N and (8s4p3d1f)/[3s2p1d] for H. Scalar relativistic effects, although expected to be small, were included via use of the 2nd order Douglas-Kroll-Hess Hamiltonian [71]. All CAS/RASSCF calculations were constrained to D_{2h} symmetry and calculated using Molcas 8.0 [69].

3.2.4 Description of Active Spaces

CASSCF calculations were performed considering three different active spaces. The simplistic four orbital model proposed by Gouterman considers the electronic transitions of FBP to be composed of excitations from the HOMO and HOMO-1 to the LUMO and LUMO+1 (see Section 3.1.1), therefore the first, most simplistic, active space incorporated the four electrons and orbitals, known in porphyrin systems as the Gouterman orbitals [74, 95, 11], and is denoted CASSCF(4/4). This active space, although severely restricted, should provide a fairly good description of the lower excited states if these 'Gouterman' orbitals do indeed comprise the lower electronic transitions.

It should be noted that as the labels Highest Occupied Molecular Orbital (HOMO) and Lowest Occupied Molecular Orbital (LUMO) do not hold in the CAS/RASSCF methodology, the Gouterman orbitals will therefore be referred to as GO1-4 hereafter where GO1 and GO2 are the formal Gouterman HOMO-1 and HOMO (a_u and b_{1u} symmetries respectively) whilst GO3 and GO4 are the formal Gouterman LUMO and LUMO+1 (b_{2g} and b_{3g} symmetries respectively).

The second active space was larger and included sixteen electrons and fourteen orbitals (inclusive of the Gouterman orbtials) from the conjugated π system, in accordance with many previous works in the literature [59, 88] and is denoted CASSCF(16/14). The orbitals included in this active space span the 2-5 b_{2g}, 2-5 b_{3g}, 3-6 b_{1u} and 2-3 a_u irreps. The final active space included

two further orbitals (6 b_{2g} and 6 b_{3g}) to pair up corresponding orbitals in the active space, in accordance with guidelines set out by Roos (see Section 2.5.2), and is denoted CASSCF(16/16).

The benefit of the RASSCF over the CASSCF methodology is the ability to include more orbitals and electrons whilst keeping the computational cost relatively low, the potential downside is the effect that the truncation of the CI wavefunction could have upon the accuracy of simulated excitation energies. This has been investigated with respect to the Free Base Porphyrin system by performing RASSCF calculations on the two larger active spaces described above.

In all RASSCF calculations the Gouterman orbitals have been placed in the RAS2. In the RASSCF calculation analogous to the CASSCF with the (16/14) active space, six orbitals that could be considered formally occupied were placed in the RAS1 (2-3 b_{2g}, 2-3 b_{3g} and 3-4 b_{1u}) and four formally unoccupied in the RAS3 (5 b_{2g}, 5 b_{3g}, 6 b_{1u} and 3 a_u). Both double and triple excitations between the RAS1 and RAS3 were permitted and therefore this active space has been denoted RASSCF(16,l,m;6,4,4). Similarly, the second RASSCF active space based upon the CASSCF(16/16) active space, again filled the RAS1 with six formally occupied π-orbitals but the RAS3 with six instead of four orbitals. A schematic of all orbitals included in both the CASSCF and RASSCF active spaces is shown in Figure 3.4.

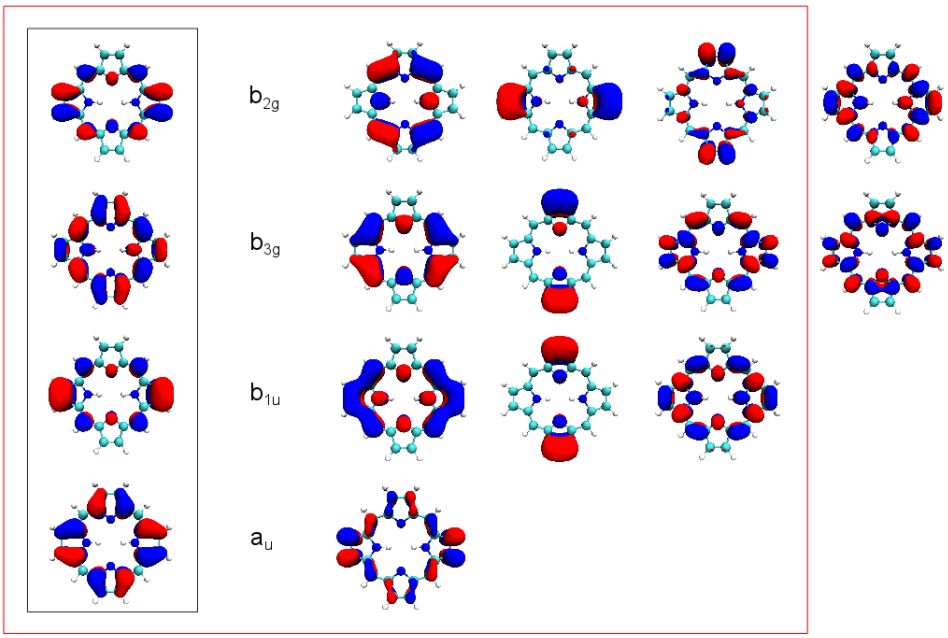

Figure 3.4: Orbitals included in CAS/RASSCF calculations of FBP. Orbitals in the black box are Gouterman Orbitals of FBP, whilst the red box indicates orbitals included in (16/14) active spaces. Orbitals generated with an isosurface of 0.03 a.u.

The effects of dynamic correlation were included via the addition of second order pertubation theory (PT2) to all converged CASSCF/RASSCF wavefunctions. An imaginary level shift of 0.2 a.u. was added to avoid the effects of intruder states. All pertubative calculations were completed both with and without the standard IPEA (Ionisation Potential and Electron Affinity) shift of 0.25 a.u. (see Section 2.6.1), as this standard shift has been shown to overestimate porphyrin excited states.

3.2.5 Structure Optimisations

Table 3.2 gives the details of key coordinates in FBP, calculated with a range of *xc*-functionals, based upon the numbering scheme in Figure 3.5. For comparison, literature data of experimentally determined bond lengths and angles are also provided [96].

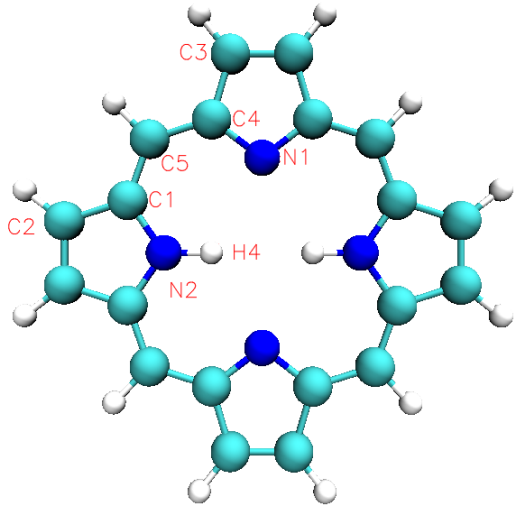

Figure 3.5: DFT-optimised (B3LYP/def2-TZVP) Free Base Porphyrin structure showing the labeling of atoms (Dark Blue=N, Teal=C, White=H) for Table 3.2.

Scrutiny of the bond lengths listed in Table 3.2 shows that using all five *xc*-functionals provides very good agreement with experiment; reproducing bond lengths to within 0.02 Å and angles to within 0.7°, with the B3LYP and TPSSh *xc*−functionals performing exceptionally well. Structures were also optimised incorporating a continuum solvation model, as described in section 3.2.3, and the results are presented in Table 3.3.

After the addition of a continuum solvation model, again all five *xc*-functionals reproduce experimental data accurately, again to within 0.02 Å for bond lengths and within 0.6° for angles. In fact, there is almost no difference between the DFT-simulated gas phase results with

Co-ordinate	**BHLYP**	**PBE0**	**B3LYP**	**TPSSh**	**TPSS**	**Experiment [96]**
R(C1-C5)	1.38	1.39	1.39	1.39	1.40	1.38
R(N2-C1)	1.36	1.36	1.37	1.37	1.37	1.38
R(N1-C4)	1.34	1.35	1.37	1.36	1.37	1.37
A(C1-C5-C4)	126.8	127.0	127.3	127.2	127.3	127.1
A(N2-C1-C5)	125.8	125.6	125.6	125.6	125.6	125.1

Table 3.2: Calculated bond lengths in Angstroms (Å) (indicated by R) and angles in degrees (°) (indicated by A) for Free Base Porphyrin in the Gas Phase calculated using DFT with different $xc-$functionals.

Co-ordinate	**BHLYP**	**PBE0**	**B3LYP**	**TPSSh**	**TPSS**	**Experiment [96]**
R(C1-C5)	1.39	1.39	1.39	1.39	1.40	1.38
R(N2-C1)	1.36	1.36	1.37	1.37	1.37	1.38
R(N1-C4)	1.35	1.36	1.36	1.36	1.37	1.37
A(C1-C5-C4)	126.8	126.9	127.1	127.1	127.2	127.1
A(N2-C1-C5)	125.7	125.6	125.5	125.5	125.4	125.1

Table 3.3: Calculated bond lengths in Angstroms (Å) (indicated by R) and angles in degrees (°) (indicated by A) for Free Base Porphyrin in the solution phase, modeled using continuum solvation model ($\epsilon_r = \infty$), as determined by DFT with different xc-functionals.

the DFT-simulated solution phase results.

3.2.6 Calculation of Excited States by TDDFT

The TDDFT-calculated gas phase singlet excitation energies of FBP simulated using the five *xc*-functionals that were used for geometry optimisation are presented in Table 3.4. In addition to the TDDFT-calculated energies, gas phase experimental results are presented for comparison purposes. Furthermore root mean squared (RMS) errors for calculated energies compared to experiment are also presented for (a) all excitations for each functional and (b) for the Q and B Bands (both x and y components) for each functional.

Transition	**BHLYP**	**PBE0**	**B3LYP**	**TPSSh**	**TPSS**	**Exp.** [11]
$1\ ^1B_{2u}$ (Q_y)	2.47	2.48	2.42	2.40	2.32	2.42
$2\ ^1B_{2u}$ (B_y)	3.77	3.56	3.47	3.36	3.09	3.33
$3\ ^1B_{2u}$	4.62	3.91	3.74	3.61	3.46	3.65
$4\ ^1B_{2u}$	5.17	4.53	4.36	4.16	3.85	4.68
$1\ ^1B_{3u}$ (Q_x)	2.31	2.33	2.27	2.27	2.19	1.98
$2\ ^1B_{3u}$ (B_x)	3.67	3.42	3.32	3.23	3.03	3.33
$3\ ^1B_{3u}$	4.40	3.95	3.82	3.72	3.53	3.65
$4\ ^1B_{3u}$	5.48	4.67	4.46	4.22	3.86	4.25
RMS Error	0.76	0.26	0.19	0.43	0.20	-
RMS Error (Q & B)	0.33	0.22	0.16	0.28	0.23	-

Table 3.4: Eight lowest TDDFT-calculated singlet excitation energies for FBP in the gas phase, experimental results [11] and deviations from experiment, all values given in eV.

The best performing *xc*-functionals, those with the lowest RMS error, are B3LYP, TPSS and

PBE0, which reproduce the experimental excitation energies of FBP to within an RMS error of 0.19, 0.20 and 0.26 eV respectively. When only the RMS error of the Q and B bands are considered, the deviation from experiment decreases for all *xc*-functionals apart from TPSS; however despite this TPSS is still the third most accurate functional investigated here. A closer inspection of the excitation energies shows that the main contribution to the RMS error of the Q and B bands comes from the $1\ ^1B_{3u}$ (Q_x) excitation which is overestimated by $\sim$0.3 eV with all of the hybrid *xc*-functionals, and 0.21 eV by TPSS, a pure functional.

Functional	HF Exchange (%)	$1\ ^1B_{3u}$ (Q_x)		$1\ ^1B_{2u}$ (Q_y)	
		$5\ b_{1u} \rightarrow 4\ b_{2g}$	$2\ a_u \rightarrow 4\ b_{3g}$	$5\ b_{1u} \rightarrow 4\ b_{2g}$	$2\ a_u \rightarrow 4\ b_{3g}$
BHLYP	50	48.3	50.1	46.0	52.8
PBE0	25	56.0	43.2	53.0	46.5
B3LYP	20	57.2	42.1	53.4	46.1
TPSSh	10	59.7	39.7	55.7	43.7
TPSS	0	62.1	37.1	57.5	41.5

Table 3.5: Contributions to the TDDFT-calculated $1\ ^1B_{3u}$ (Q_x) and $1\ ^1B_{2u}$ (Q_y) excitations as weight percentages for each $xc-$functional.

Table 3.5 shows the contributions to the Q_x and Q_y excitations which are both composed of two transitions, from $5\ b_{1u}$ (GO2) $\rightarrow 4\ b_{2g}$ (GO4) and $2\ a_u$ (GO1) $\rightarrow 4\ b_{3g}$ (GO3).

It can be seen in Table 3.5 that there is clear correlation between the percentage of HF-exchange included in the xc-functional and the weightings of the two transitions that form the $1\ B_{3u}$ excitation. As the percentage decreases, so does the contribution from the $2\ a_u \rightarrow 4\ b_{3g}$ transition. Conversely, the contribution from the $5\ b_{1u} \rightarrow 4\ b_{2g}$ transition increases as the percentage of HF-exchange decreases.

A similar pattern is also seen in the contributions to the $1\ B_{2u}$ (Q_y) excitation, also shown in Table 3.5, where a decrease in HF-exchange decreases the contribution from the $2\ a_u \rightarrow 4\ b_{3g}$ transition and an increase in the $5\ b_{1u} \rightarrow 4\ b_{2g}$ transition. The Q_y transition, unlike the Q_x transition, is well modelled by the five xc-functionals, particularly B3LYP and TPSSh. It is therefore unlikely that the cause of the error in the Q_x band is a result of the changing in the contributions from the two transition.

To further investigate the excited states of FBP, higher level CAS/RASSCF calculations were undertaken.

3.2.7 Calculation of Excited States by CAS/RASPT2

The CASSCF, RASSCF, CASPT2 and RASPT2 excitation energies are shown in Table 3.6 below. For a description of the active spaces see Section 3.2.4.

Although CASSCF and RASSCF energies without perturbation theory are generally not accurate due to a limited description of the dynamical correlation of the system, they are presented in the table below to evaluate the effect of the truncation of the CI wavefunction going from triple to double excitations. The CASPT2 energies marked by * are excitation energies calculated without the standard Ionisation Potential and Electron Affinity (IPEA) shift of 0.25 a.u. included in the perturbation calculations.

Effect of Truncating the CI Wavefunction

Looking at the first section of Table 3.6, it can be seen that reducing the number of excited configuration state functions (CSFs), i.e. going from a CASSCF(16/14) active space to a RASSCF(16,2,2;6,4,4) active space, has a greater effect on the simulated energies of higher excited states. For instance, the 1 $^1B_{2u}$ excitation energy varies by only 0.09 eV between CASSCF(16/14) and RASSCF(16,2,2;6,4,4), which is then reduced to a difference of 0.01 eV between RASSCF and CASSCF when triple excitations are considered. However, for the 3 $^1B_{2u}$ excitation energy there is a difference of 0.58 eV, reduced to 0.16 eV when triple excitations are considered.

Comparison of Excitation Energies corrected by Perturbation Theory

This section focuses on the values presented in the second section of Table 3.6 which includes excitation energies corrected via the use of second order perturbation theory.

Method	$1\ ^1B_{2u}$	$2\ ^1B_{2u}$	$3\ ^1B_{2u}$	$4\ ^1B_{2u}$	$1\ ^1B_{3u}$	$2\ ^1B_{3u}$	$3\ ^1B_{3u}$	$4\ ^1B_{3u}$
CASSCF(4/4)	4.02	5.05	11.81	13.94	3.81	5.00	11.67	13.91
CASSCF(16/14)	3.32	4.78	5.16	5.47	2.68	4.25	5.05	5.48
CASSCF(16/16)	3.58	5.09	5.41	5.77	2.49	4.53	5.26	5.49
RASSCF(16,2,2;6,4,4)	3.41	4.97	5.74	6.29	2.83	4.89	5.68	6.02
RASSCF(16,3,3;6,4,4)	3.33	4.79	5.32	5.75	2.72	4.36	5.13	5.55
RASSCF(16,2,2;6,4,6)	3.59	5.10	6.23	6.61	2.81	4.87	6.12	6.55
RASSCF(16,3,3;6,4,6)	3.45	4.86	5.59	5.87	2.55	4.58	5.36	5.58
CASPT2(4/4)	2.88	3.84	7.16	6.77	2.46	3.77	6.91	6.83
CASPT2(16/14)	2.72	3.42	4.47	4.85	2.40	3.65	4.11	5.35
CASPT2(16/16)	2.57	3.64	4.02	4.53	2.19	3.70	4.02	4.99
RASPT2(16,2,2;6,4,4)	2.75	3.68	4.36	4.88	2.34	3.64	4.41	5.22
RASPT2(16,3,3;6,4,4)	2.54	3.52	3.92	4.39	2.27	3.62	3.68	4.93
RASPT2(16,2,2;6,4,6)	2.64	3.58	4.46	5.04	2.22	3.57	4.65	5.22
RASPT2(16,3,3;6,4,6)	2.57	3.50	4.03	4.78	2.15	3.60	4.01	4.98
CASPT2(4/4)*	1.71	2.56	5.25	4.91	1.16	2.47	5.02	4.99
CASPT2(16/14)*	2.01	2.91	3.32	3.78	1.73	2.99	2.94	4.22
CASPT2(16/16)*	1.86	2.80	3.15	3.77	1.48	2.90	3.18	4.14
RASPT2(16,2,2;6,4,4)*	2.07	2.82	3.54	4.21	1.66	2.77	3.56	4.34
RASPT2(16,3,3;6,4,4)*	1.83	2.64	3.04	3.62	1.50	2.73	2.66	3.96
RASPT2(16,2,2;6,4,6)*	2.02	2.83	3.76	4.43	1.60	2.85	3.94	4.40
RASPT2(16,3,3;6,4,6)*	1.97	2.79	3.32	4.18	1.56	2.91	3.27	4.19
Experiment [11]	**2.42**	**3.33**	**3.65**	**4.68**	**1.98**	**3.33**	**3.65**	**4.25**

Table 3.6: Eight lowest optically allowed singlet vertical excitation energies of FBP at DFT (B3LYP/TZVP)-optimised structure using CASSCF, RASSCF, CASPT2 and RASPT2. * indicates perturbation energies evaluated without the standard IPEA shift of 0.25. a.u. All values given are in eV.

The small and simplistic (4/4) active space provides a constant overestimation of both components of the Q ($1B_{2u}$ and $1B_{3u}$) and B ($2B_{2u}$ and $2B_{3u}$) bands by ∼0.5 eV compared to experimental results even after the addition of second order perturbation theory to incorporate dynamical correlation effects. For higher excited states the energies calculated using the (4/4) active space deviate from experiment by more than 2 eV, this is not surprising as only the Q and B bands are, according to Gouterman, composed of transitions between the four Gouterman orbitals. Therefore this active space incorporating only Gouterman orbitals should not be expected to model states that involve transitions from or to orbitals not included in the active space. Considering the small size of this active space and the extremely low computational cost, the relative accuracy means that the Q and B Bands can be considered to be fairly well simulated.

Increasing the size of the active space from the (4/4) to the (16/14) active space improves the agreement with experiment for the 1 $^1B_{2u}$ (Q_y) state by nearly 0.2 eV. However, the increased active space only improves the accuracy of the predicted 1 $^1B_{3u}$ (Q_x) by 0.06 eV, still leaving an error of 0.42 eV from experiment. The performance of the (16/14) active space in predicting the B band compared to the (4/4) active space follows a similar pattern to that of the Q band, the accuracy of the prediction of the y component is greatly improved whilst the x component is only slightly improved, by 0.42 and 0.12 eV respectively. Furthermore, as expected, prediction of higher excited states is greatly improved by using the (16/14) active space.

Moving from the CASPT2 methodology with a (16/14) active space to the analogous (16,2,2;6,4,4) active space with the RASPT2 methodology has very little effect on the simulated first and second excited states of $^1B_{2u}$ and $^1B_{3u}$ symmetry. Typically only a few hundredths of an eV difference is found between the two methodologies, with the exception of the 2 $^1B_{2u}$ excitation where there is an increase in the excitation energy by 0.26 eV. Inclusion of triple excitations rather than double in the active space, RASPT2(16,3,3;6,4,4), decreases the deviation from

experiment of 1 $^1B_{2u}$ and 2 $^1B_{2u}$ excitations by $\sim$ 0.2 eV compared to the energies obtained with RASPT2(16,2,2;6,4,4). There is also a slight decrease in the excitation energies of the 1 $^1B_{3u}$ and 2 $^1B_{3u}$ excitations but to a much smaller degree (<0.1 eV).

Increasing the size of the active space from CASPT2(16/14) to CASPT2(16/16) also increases the accuracy of the 1 $^1B_{2u}$ and 1 $^1B_{3u}$ excitations, improving agreemenet with experiment, by 0.21 eV and 0.15 eV respectively, to the point where both calculated values are within 0.2 eV of the experimental value. However using the larger (16/16) active space also results in a decrease in the accuracy of the 2 $^1B_{2u}$, with the simulated excitation energy 0.22 eV larger than predicted by using the (16/14) active space.

Effect of Removal of the IPEA Shift

The standard IPEA shift of 0.25 a.u. was parametrised to perform well for a test set of molecules [57]. The test set consisted of 49 dimer complexes and it therefore reasonable to question whether this can be expected to perform well for a large more complicated molecule such as a porphyrin.

It can be seen from the results presented in Table 3.6 that when the IPEA shift is removed from the perturbation calculations there is a constant underestimation of the Q and B bands, particularly with the (4/4) active space.

Natural Orbital Occupations

Table 3.7 shows the natural orbital occupation numbers of the Gouterman orbitals of the FBP ground state (^1A_g) as well as the four lowest optically allowed excited states, 1 $^1B_{2u}$, 2 $^1B_{2u}$, 1 $^1B_{3u}$ and 2 $^1B_{3u}$ (Q and B bands), calculated using all of the active spaces described above.

Excluding the CASSCF(4/4) active space results, there is a great deal of similarity in the natural occupation numbers of the ground state, 1 ^1A_g, between the CASSCF(16/14) active space,

CASSCF(16,16) active space and their RASSCF counterparts, with occupancies differing by a maximum of 0.02. This suggests that all active spaces presented in the table model the ground state in the same way. Furthermore the values of the natural orbital occupation numbers show that this is a multiconfigurational system, with significant occupation of the so-called Gouterman 'LUMOs' in the ground state.

The 1 $^1B_{2u}$ state also displays similar natural orbital occupation numbers across the active spaces, albeit with a slightly larger range than that of the ground state. There is a similar degree of deoccupation from GO1 and GO2 orbitals (a_u and b_{1u}) which is mirrored by the similar occupation of the GO3 and GO4 orbitals (b_{2g} and b_{3g}). Interestingly the RASSCF active spaces seem to indicate a more even loss/gain of electrons than the CASSCF active spaces do. This is a pattern that is also seen in the 2 $^1B_{2u}$ state.

Again in the lowest two B_{3u} states, we see a similarity in occupation numbers across the active spaces similar to the B_{2u} states. It is interesting to note that when the CASSCF active spaces are compared with their RASSCF counterparts, for the B_{3u} states, the natural orbital occupation numbers of the triple excitations correspond more closely to the CASSCF natural orbital occupation numbers than the double excitations do. This is perhaps to be expected given the greater number of excitations permitted in the triple excitations, but may also suggest that the B_{3u} states contain a greater contribution from higher excited CSFs.

Root	Active Space	a_u	b_{1u}	b_{2g}	b_{3g}
	CASSCF(4/4)	1.91	1.93	0.08	0.08
	CASSCF(16/14)	1.88	1.89	0.12	0.14
	CASSCF(16/16)	1.87	1.88	0.13	0.15
1 A_g	RASSCF(16,2,2;6,4,4)	1.89	1.89	0.11	0.13
	RASSCF(16,3,3;6,4,4)	1.88	1.89	0.12	0.13
	RASSCF(16,2,2;6,4,6)	1.88	1.89	0.12	0.13
	RASSCF(16,3,3;6,4,6)	1.88	1.87	0.13	0.14
	CASSCF(4/4)	1.35	1.61	0.65	0.39
	CASSCF(16/14)	1.39	1.56	0.62	0.49
	CASSCF(16/16)	1.40	1.55	0.61	0.50
1 B_{2u}	RASSCF(16,2,2;6,4,4)	1.45	1.48	0.55	0.55
	RASSCF(16,3,3;6,4,4)	1.47	1.46	0.54	0.57
	RASSCF(16,2,2;6,4,6)	1.42	1.52	0.58	0.51
	RASSCF(16,3,3;6,4,6)	1.43	1.52	0.58	0.53
	CASSCF(4/4)	1.55	1.30	0.45	0.71
	CASSCF(16/14)	1.49	1.39	0.45	0.77
	CASSCF(16/16)	1.59	1.32	0.37	0.85
2 B_{2u}	RASSCF(16,2,2;6,4,4)	1.48	1.37	0.52	0.66
	RASSCF(16,3,3;6,4,4)	1.52	1.35	0.49	0.70
	RASSCF(16,2,2;6,4,6)	1.48	1.35	0.52	0.67
	RASSCF(16,3,3;6,4,6)	1.51	1.33	0.50	0.69
	CASSCF(4/4)	1.55	1.40	0.60	0.45
	CASSCF(16/14)	1.52	1.40	0.65	0.50
	CASSCF(16/16)	1.47	1.44	0.59	0.55
1 B_{3u}	RASSCF(16,2,2;6,4,4)	1.42	1.51	0.52	0.58
	RASSCF(16,3,3;6,4,4)	1.51	1.41	0.63	0.50
	RASSCF(16,2,2;6,4,6)	1.47	1.46	0.57	0.54
	RASSCF(16,3,3;6,4,6)	1.47	1.45	0.58	0.55
	CASSCF(4/4)	1.50	1.35	0.65	0.50
	CASSCF(16/14)	1.63	1.36	0.93	0.34
	CASSCF(16/16)	1.53	1.38	0.75	0.49
2 B_{3u}	RASSCF(16,2,2;6,4,4)	1.54	1.37	0.74	0.46
	RASSCF(16,3,3;6,4,4)	1.62	1.37	0.89	0.35
	RASSCF(16,2,2;6,4,6)	1.46	1.42	0.64	0.56
	RASSCF(16,3,3;6,4,6)	1.53	1.38	0.74	0.49

Table 3.7: Natural Orbital Occupation Numbers of Gouterman Orbitals in FBP for the A_g ground state and four lowest optically allowed excited states using five different active spaces.

3.2.8 Summary of TDDFT and CAS/RASPT2 Results

Table 3.8 compares and contrasts the simulated values of the Q and B bands of FBP using both TDDFT (various functionals) and CAS/RASPT2 (various active spaces) together with experimental values.

Method	Method Details	Q_x	Q_y	B_x	B_y
Experiment	-	1.98	2.42	3.33	3.33
TDDFT	BHLYP	2.31	2.47	3.67	3.77
	PBE0	2.33	2.48	3.42	3.56
	B3LYP	2.27	2.42	3.32	3.47
	TPSSh	2.27	2.40	3.23	3.36
	TPSS	2.19	2.32	3.03	3.09
CASPT2	(4/4)	2.46	2.88	3.77	3.84
	(16/14)	2.40	2.72	3.65	3.42
	(16/16)	2.19	2.57	3.70	3.64
	(4/4)*	1.71	2.56	1.16	2.47
	(16/14)*	2.01	2.91	1.73	2.99
	(16/16)*	1.86	2.80	1.48	2.90
RASPT2	(16,2,2;6,4,4)	2.31	2.72	3.61	3.64
	(16,3,3;6,4,4)	2.27	2.54	3.62	3.52
	(16,2,2;6,4,6)	2.22	2.64	3.57	3.58
	(16,3,3;6,4,6)	2.15	2.57	3.60	3.50
	(16,2,2;6,4,4)*	2.07	2.82	1.66	2.77
	(16,3,3;6,4,4)*	1.83	2.64	1.50	2.73
	(16,2,2;6,4,6)*	2.02	2.83	1.60	2.85
	(16,3,3;6,4,6)*	1.97	2.79	1.56	2.91

Table 3.8: Comparison of TDDFT and CAS/RASPT2 calculated singlet excitation energies of FBP with experimental values given in eV [11]. * indicates CAS/RASPT2 in absence of IPEA.

In general all methods, except the CASPT2 using the (4/4) active space, perform well, reproducing the experimental energies to within ~ 0.3 eV. This is not all that surprising considering

this is a closed shell system, albeit one that presents fairly significant multiconfigurational character, evident in the natural occupation numbers, shown in Table 3.7.

The TDDFT results are fairly consistent between the different *xc*-functionals for the Q band (both components), however they show significant deviation for both components of the B band with a range of just over 0.6 eV between the values obtained employing BHLYP (containing 50% HF-exchange) and TPSS (containing no HF-exchange).

On the other hand all CAS/RASPT2 active spaces (ignoring the CASPT2(4/4) active space) produce fairly similar results for both components of the B band excitation. Truncating the CI wavefunction by moving from the CASPT2 to RASPT2 methodology has little effect on the calculated excitation energies, even when only double excitations are permitted. Comparing the results between the (16/14) and (16/16) active space shows that addition of two further orbitals to balance the active space produces more accurate excitations energies for both components of the Q band whilst increasing the deviation from experiment of simulated of the B band excitations energies.

Having looked at the simplest example of a porphyrin, attention is now turned to the effect of complexing a metal to the porphyrin ring.

3.3 Regular Porphyrins

Regular porphyrins are those that have a closed electronic shell [95, 59], the most commonly reported regular porphyrins in the literature are Magnesium Porphyrin (MgP) and Zinc Porphyrin (ZnP). This is most likely due to them being the most stable. The stability of these regular porphyrins is because the size of the porphyrin cavity roughly matches the ionic radii of the Zn (57 pm) and Mg (60 pm) ions [97] as well as the fact that Mg and Zn form very stable 2+ ions.

MgP and ZnP are similar to free base porphyrins in the respect that they all have a closed shell electron configuration. The symmetry of MgP and ZnP is however different, where FBP is of D_{2h} symmetry, MgP and ZnP are D_{4h}. This increase in symmetry from 2-fold to 4-fold is a result of the deprotonation of the porphyrin ring and makes the x and y components of the Q and B bands of the electronic absorption spectrum degenerate, therefore MgP and ZnP simply have Q and B Bands.

MgP is the base component of chlorophyll, see Figure 3.3, whilst ZnP has been used in the literature as a dye in novel dye sensitised solar cells (see Section 3.1.4). These two molecules have also been heavily studied in the literature, both experimentally and theoretically (see Section 3.3.1), because of their interesting optical properties. In particular MgP and ZnP have raised significant interest to the theoretical chemist because of their high symmetry, interesting optical properties and the link they form between FBP and irregular porphyrins, which are discussed in Section 3.4.

3.3.1 Summary of previous works

An overview of methods and calculated excitation energies summarising the below paragraphs is provided in Tables 3.9 and 3.10 at the end of this section.

In 2001 work published by Nguyen and Patcher examined the electronic structure and absorption spectra of ZnP as well as some of its derivatives using TDDFT [98]. Structures were optimised using DFT B3LYP/6-31G(d) model chemistry, following which excitation energies were calculated using TDDFT and the same model chemistry used for the optimisation of the ground state structures. The singlet excitation energies were calculated to be 2.44 eV and 3.54 eV for the Q and B band respectively. The experimentally observed value varies depending on the solvent used but is in the range of 2.03-2.18 eV for the Q band and 2.95-3.13 eV for the B band [98, 99, 100]. In these results TDDFT overestimates the excitation energies by around

0.4 eV, which is slightly larger than the error seen for FBP using the same functional, reported in section 3.2.2.

Work published by Peralta *et al* in 2007 utilised TDDFT and calculated singlet excitation energies of MgP, ZnP and NiP [101]. Ground state structures were optimised using DFT with the BP86 functional [82, 39, 102] and excited states calculated using TDDFT with SAOP [103, 104] (statistical averaging of different orbital-dependent potentials). Peraltas calculations were found to be in reasonably good agreement for both ZnP and MgP (For NiP see section 3.c.). The Q and B bands being calculated at 2.28 and 3.25 eV for ZnP and 2.23 and 3.23 eV for MgP. This is unsurprising considering that the SAOP functional has been developed specifically for calculation of excited states using TDDFT by correcting the long range poor performance of many DFT functionals.

Like his paper on FBP, D. Sundholm, in 2000, also examined the electronic spectra of MgP using TDDFT [105]. The structures used by Sundholm were optimised using DFT BP/SVP model chemistry and also included polarisation functions. Singlet excitation energies of MgP were then obtained using TDDFT and the same model chemistry. Sundholm calculated the Q and B band to be 2.21 and 3.58 eV, which if we compare to the experimentally observed values of 2.14 and 3.18 eV 23 we see that the calculated Q band is very close whilst the B band shows an error of 0.4 eV. This B band error is similar to the error calculated by Nguyen using TDDFT (B3LYP) for ZnP 31. The fact that Nguyens error of 0.4 eV with a hybrid functional is the same as the error reported by Sundholm using a GGA is slightly surprising but not completely unexpected because of the inherent problems with DFT.

One of the first works to present results using a multiconfigurational methodology on a regular porphyrin was published by Roos and co-workers in 1999 which examined the electronic spectrum of MgP [106]. Structures were optimised using DFT B3PW91/6-31G* model chemistry

whilst restricting to D_{4h} symmetry. Excited states were calculated using the CASPT2 methodology, with symmetry restricted to only D_{2h} due to limitations in the computational software used. Ideally the CAS wavefunction should include all 26 π electrons across the 24 atom centres, as discussed previously, however this is computationally demanding to the point of impossible and so several smaller active spaces were instead tested. The five different active spaces used by Roos were 4/4, 12/16, 13/18, 14/16 and 15/18. As expected the 4/4 wavefunction performs the poorest and vastly underestimates the Q and B bands, 1.45 eV and 2.60 eV respectively, compared to the experimental values of 2.14 and 3.18 eV. Closer results are seen for the four larger active spaces for the Q band, although there is still a considerable underestimation of around 0.4-0.5 eV. However results for the B band do not show significant deviation on changing the active space and all show an error of approximately 0.5 eV. This result is to be expected as not enough electrons or orbitals are included in the calculation to sufficiently describe the electronic transitions.

Another paper involving the use of a multiconfigurational method was reported by Seda *et al* in 2005 comparing the excitation energies of MgP which they calculated using two different computational methods [107]. Ground state structures were optimised at the Hartree-Fock level of theory using the 6-31G(d) basis set whilst constraining to D_{4h} symmetry. Excited states were then calculated using SAC-CI (Symmetry Adapted Cluster-Configuration Interaction) and CASPT2 using the 6-31+G(d) basis set in D_{2h} rather than D_{4h} symmetry, due to limitations in the software. The active space used for the CASSCF reference wavefunction contained 16 electrons in 14 orbitals. Their results calculated the Q and B bands to be 1.68 and 3.29 eV respectively using SAC-CI and 2.15 and 3.41 eV using CASPT2. The SAC-CI results produce a better value for the B band however the CASPT2 results model the Q band more accurately.

Hirao *et al* examined the excitation energies of MgP and ZnP and their respective derivatives using CASSCF followed by Hirao's MRMP (Multi-reference Moller-Plesset)[108] pertubational

method in 1999 [109]. Structures were optimised using Hartree-Fock theory whilst constrained to D_{4h}. The active space for the CASSCF reference wavefunction included 8 electrons in 8 orbitals for both MgP and ZnP. The excitation energies were calculated as 2.00 and 3.07 eV for the Q and B bands for MgP and 2.11 and 3.21 eV for ZnP. These results are very close to the experimental values which is unexpected considering the relatively low number of orbitals and electrons included in the active space.

As mentioned in the previous section, work published by A. Kerridge in 2013 calculated the singlet excitation energies of regular porphyrins; MgP and ZnP using RASPT2 [59]. Identical to FBP two different active spaces were used; a 16/14 and a 26/24. Like FBP the best results are seen, for both MgP and ZnP, when the 26/24 active space is used and up to triple excitations are permitted. Kerridge's results calculated the Q and B band to be 2.53 and 3.59 eV for MgP and 2.58 and 3.62 eV for ZnP, which shows an error of around 0.4 eV, however removing the Ionisation Potential and Electron Affinity (IPEA) shift 44 gets the values almost exactly the same as experimental values. This small error shows the benefit for the active space to contain at least 26 electrons and 24 orbitals.

Lead Author (Year)	**Method**	**Other Details**	**Q**	**B**
-	Experiment	-	2.18	3.13
Nguyen (2001)	TDDFT	B3LYP, 6-31G(d)	2.44	3.54
Peralta (2007)	TDDFT	SAOP	2.28	3.25
Hirao (1999)	CASSCF(8/8)+MRMP	-	2.11	3.21
Kerridge (2013)	CASPT2(16/14)	ANO-RCC, TZVP	2.78	4.01
	RASPT2(26,3,3;11,4,9)+IPEA		2.58	3.62
	RASPT2(26,3,3,11,4,9)		2.20	3.13

Table 3.9: Summary of literature reported ZnP Singlet Excitation Energies (eV).

Lead Author (Year)	Method	Other Details	Q	B
-	Experiment	-	2.14	3.18
Sundholm (2000)	TDDFT	BP	2.21	3.15
Peralta (2007)	TDDFT	SAOP	2.23	3.23
Roos (1999)	CASPT2(4/4)	ANO-S, TZVP	1.45	2.60
	CASPT2(12/16)		1.62	2.66
	CASPT2(13/18)		1.71	2.59
	CASPT2(14/16)		1.66	2.66
	CASPT2(15/18)		1.78	2.65
Seda (2005)	SAC-CI	-	1.68	3.29
	CASPT2(16/14)	-	2.15	3.41
Hirao (1999)	CASSCF(8/8)+MRMP	-	2.00	3.07
Kerridge (2013)	CASPT2(16/14)	ANO-RCC, TZVP	2.72	4.00
	RASPT2(26,3,3;11,4,9)+IPEA		2.53	3.59
	RASPT2(26,3,3;11,4,9)		2.16	3.11

Table 3.10: Summary of literature reported MgP Singlet Excitation Energies (eV)

The most accurate calculations on ZnP have been performed by A. Kerridge. By inclusion of all 26 π electrons (using the RASPT2 methodology) the porphyrin system is described sufficiently to predict accurately the excitation energies, especially if you compare them to the values predicted by TDDFT, such as those reported by Nguyen. A similar result is also seen for MgP, with the most accurate excitation energies being calculated with RASPT2.

RASPT2 is clearly the most accurate method for calculating the excitation energies of regular porphyrins. However for its low computational cost, TDDFT provides excitation energies to a relatively good degree of accuracy, albeit with a slightly higher error than that seen for FBP.

3.3.2 Computational Details

Structures for MgP and ZnP were built with GaussView [66] and optimised with DFT using version 6.6 of the Turbomole program [67]. Five *xc*-functionals have been used, the hybrid functionals; BHLYP [91, 35, 38], PBE0 [86], B3LYP [91, 35, 92], TPSSh [93, 94] as well as the meta-GGA, TPSS [37]. Calculations employed Ahlrichs-style basis sets of polarised triple-zeta quality (def2-TZVP) [68]. Structures were constrained to D_{2h} symmetry rather than D_{4h} for consistency with higher level CAS/RASSCF calculations. All symmetry labels therefore refer to D_{2h} labels rather than D_{4h} (where the B_{2u} and B_{3u} symmetries are degenerate). Frequency analysis was also performed to ensure that minimum energy structures had been obtained.

Following DFT structure optimisations of MgP and ZnP, singlet excitation energies were calculated with TDDFT again with Turbomole 6.6. The same *xc*-functionals and basis sets as those that were used for structure optimisation were utilised again in the TDDFT calculations.

Like CAS/RASSCF calculations on FBP, CAS/RASSCF calculations on MgP and ZnP were also completed using the Molcas 8.0 code. As mentioned previously, the highest symmetry that can be imposed with the Molcas code is D_{2h} therefore MgP and ZnP calculations have been restricted to D_{2h} instead of D_{4h}. CAS/RASSCF calculations have been performed on B3LYP-DFT optimised structures and have employed relativistically contracted atomic natural orbital (ANO-RCC) basis sets [70] of polarised triple-zeta quality; (17s12p6d2f2g)/[6s3p2d] for Mg, (21s15p10d6f4g2h)/[6s5p3d2f] for Zn, (14s9p4d3f2g)/[4s3p2d] for C and N and (8s4p3d1f)/[3s2p] for H. Scalar relativistic effects, although expected to be small, have been included via the use of the 2nd order Douglas-Kroll-Hess Hamiltonian and the Cholesky decomposition has been used to reduce the computational cost of computing the two electron integrals [110].

The active spaces used for MgP and ZnP CASSCF calculations were the same as those employed for FBP in Section 3.2.3. The first CASSCF active spaces was the small, simplistic (4/4)

active space which includes only four electrons and the four Gouterman orbitals (labelled GO1-4 as in FBP - see Section 3.2.3). Like with FBP this active space is not expected to perform quantitatively well. The second CASSCF active space considered, like FBP, included orbitals from the porphyrin conjugated π system to form a (16/14) active space. The final active space included two further π^* orbitals to form a (16/16) active space.

RASSCF calculations were completed to investigate the effect of the truncation of the CI wavefunction. The first RASSCF active space includes all the orbitals of the (16/14) active space where, like FBP, the RAS2 has been filled with the Gouterman orbitals, the RAS1 with six formally occupied π-orbitals and the RAS3 with four formally unoccupied π orbitals. Up to triple excitations have been considered for using this RASSCF actvive space and are so is denoted RASSCF(16,l,m;6,4,4) where $l = m = 2/3$.

As Zinc is a 3d transition metal, attempts were made to include the Zn 3d-orbitals in the active space. However because Zn has a full 3d-shell, these orbitals are core like and rotate themselves out of the active space in favour of porphyrin π orbitals.

A schematic of the orbitals that have been included in the described active spaces above are presented in Figure 3.6.

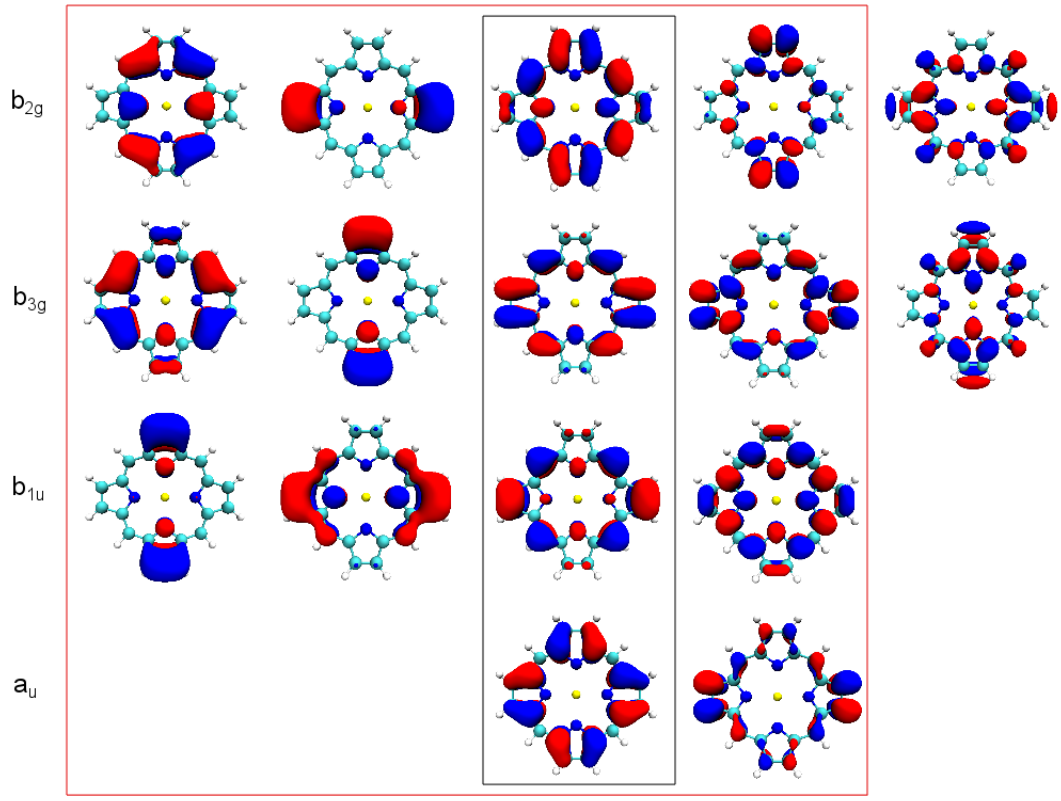

Figure 3.6: Orbitals included in MgP/ZnP CAS/RASSCF calculations by symmetry. Black box indicates four Gouterman orbitals included in (4/4) active space whilst red box indicates orbitals included in (16/14) active space. All orbitals generated at an isosurface of 0.03 a.u.

Second order perturbation theory calculations (PT2) have been added to all converged CAS/ RASSCF wavefunctions in order to add dynamical correlation effects. Perturbation theory calculations included an imaginary level shift of 0.2 a.u. which was included to reduce the effect of intruder states. Perturbation calculations have also been performed both with and without the standard IPEA shift of 0.25 a.u. similar to calculations of FBP.

3.3.3 Magnesium Porphyrin (MgP)

3.3.4 Structure Optimisation

Table 3.11 gives the details of key coordinates in MgP, calculated using DFT with five different *xc*-functionals, based upon the numbering scheme in Figure 3.7. For comparison, literature data of experimentally determined bond lengths and angles are also provided.

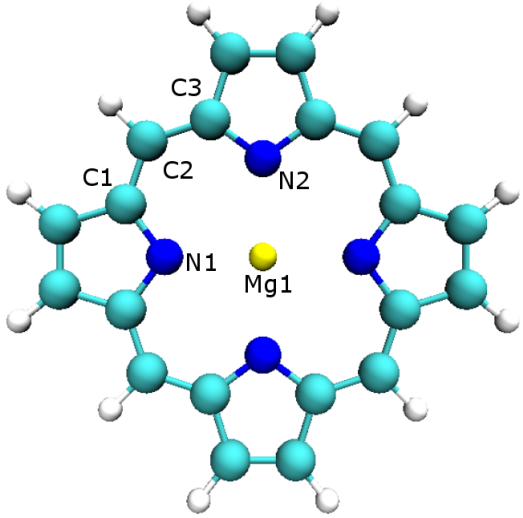

Figure 3.7: DFT(B3LYP/def2-TZVP)-optimised structure of MgP and labeling of atoms (Yellow=Mg, Dark Blue=N, Teal=C, White=H) for Table 3.11.

It can be seen in Table 3.11 that all five *xc*-functionals reproduce experimental bond lengths to within a reasonable degree of accuracy, particularly the TPSS *xc*-functional (which produces bond lengths within 0.004 Å). The biggest deviation, although still accurate, (∼0.02 Å) is obtained when using the BHLYP functional, which coincidentally contains the largest percentage of HF-exchange.

Coordinate	**BHLYP**	**PBE0**	**B3LYP**	**TPSSh**	**TPSS**	**Experiment** [12]
R(Mg1-N1)	2.041	2.049	2.057	2.055	2.061	2.065
R(Mg1-C2)	3.402	3.416	3.429	3.430	3.440	3.438
R(C1-C2)	1.386	1.389	1.396	1.397	1.401	1.401
R(C1-N1)	1.354	1.361	1.368	1.370	1.376	1.373
A(C1-C2-C3)	126.7	127.5	127.1	127.1	127.3	126.0

Table 3.11: DFT-calculated bond lengths (indicated by R) and angles (indicated by A) for MgP in the gas phase. All bond lengths given in Angstroms (Å) and angles in degrees (°).

3.3.5 MgP TDDFT Results

The TDDFT-calculated gas phase singlet excitation energies of MgP simulated using the five *xc*-functionals that have been used for the above geometry optimisations are presented in Table 3.12. Additionally gas phase experimental excitation energies and a root mean squared error (RMS) are also presented in Table 3.12 for comparison purposes.

Functional	$1\ ^1B_{2u}$ (Q)	$2\ ^1B_{2u}$ (B)	$3\ ^1B_{2u}$	$4\ ^1B_{2u}$	RMS
BHLYP	2.41 (0.009)	3.75 (2.394)	4.53 (0.076)	5.14 (0.420)	0.811
PBE0	2.42 (0.002)	3.55 (2.020)	3.94 (0.070)	4.41 (0.424)	0.434
B3LYP	2.37 (0.002)	3.47 (1.893)	3.77 (0.084)	4.23 (0.438)	0.334
TPSSh	2.35 (0.002)	3.43 (1.627)	3.58 (0.163)	4.03 (0.526)	0.275
TPSS	2.27 (0.001)	3.34 (0.568)	3.25 (0.126)	3.71 (0.361)	0.253
Experiment [12]	2.07	3.05	-	3.97	-

Table 3.12: Gas phase TDDFT-simulated singlet excitation energies for MgP using a variety of *xc*-functionals, experimental values and root mean squared (RMS) errors. All excitation energies are given in eV and calculated oscillator strengths are presented in parenthesis.

Table 3.12 shows a distinct functional dependence on the excitation energies obtained from TDDFT, seen very clearly in root mean squared (RMS) error. Those calculated with higher percentages of HF-exchange deviate further from experiment than functionals that have lower percentages. This may be partly explained by the fact that functionals with lower HF-exchange reproduce experimental structures better (Table 3.12), however as the difference in bond lengths between the functionals containing the highest and lowest percentage of HF-exchange (BHLYP and TPSS respectively) is $\sim$0.02 Å it is unlikely that this is the sole cause or indeed even the major cause.

In Table 3.12 it can also be seen that there is a much greater range of excitation energies calculated for the $2\ ^1B_{2u}$ excitation than for the $1\ ^1B_{2u}$. Tables 3.13 and 3.14 provide details of the composition of the $1\ ^1B_{2u}$ and $2\ ^1B_{2u}$ excitations respectively with the five different *xc*-functionals and provide a possible explanation for the differences in the range of calculated energies.

Functional	HF-Exchange (%)	Transitions	Weight (%)
BHLYP	50	$2\ a_u \rightarrow 4\ b_{2g}$	54.6
		$6\ b_{1u} \rightarrow 4\ b_{3g}$	44.0
PBE0	25	$6\ b_{1u} \rightarrow 4\ b_{3g}$	51.1
		$2\ a_u \rightarrow 4\ b_{2g}$	48.2
B3LYP	20	$6\ b_{1u} \rightarrow 4\ b_{3g}$	50.9
		$2\ a_u \rightarrow 4\ b_{2g}$	48.5
TPSSh	10	$6\ b_{1u} \rightarrow 4\ b_{3g}$	53.9
		$2\ a_u \rightarrow 4\ b_{2g}$	45.4
TPSS	0	$6\ b_{1u} \rightarrow 4\ b_{3g}$	55.4
		$2\ a_u \rightarrow 4\ b_{2g}$	43.6

Table 3.13: TDDFT Composition of 1 $^1B_{2u}$ (Q) excitation of MgP with five different *xc*-functionals with varying amounts of HF-exchange.

There is a clear pattern in the 1 $^1B_{2u}$ excitation with the percentage contribution of the $2\ a_u \rightarrow 4\ b_{2g}$ transition decreasing and $6\ b_{1u} \rightarrow 4\ b_{3g}$ transition increasing with decreased percentages of HF-exchange in the functional used. However, there is still only two transitions which comprise the excitation and the weight percentages of these transitions are relatively similar still.

Furthermore all *xc*-functionals support the work of Gouterman whose seminal paper on porphyrins suggested that the Q band was composed entirely of transitions involving the GO1 ($2\ a_u$), GO2 ($6\ b_{1u}$), GO3 ($4\ b_{2g}$) and GO4 ($4\ b_{3g}$) orbitals [74, 11].

Functional	HF-Exchange (%)	Transition	Weight (%)
BHLYP	50	6 $b_{1u} \rightarrow 4\ b_{3g}$	52.7
		2 $a_u \rightarrow 4\ b_{2g}$	42.9
PBE0	25	2 $a_u \rightarrow 4\ b_{2g}$	48.1
		6 $b_{1u} \rightarrow 4\ b_{3g}$	43.9
B3LYP	20	2 $a_u \rightarrow 4\ b_{2g}$	47.5
		6 $b_{1u} \rightarrow 4\ b_{3g}$	43.6
TPSSh	10	2 $a_u \rightarrow 4\ b_{2g}$	45.6
		6 $b_{1u} \rightarrow 4\ b_{3g}$	35.0
		5 $b_{1u} \rightarrow 4\ b_{3g}$	9.9
TPSS	0	2 $a_u \rightarrow 4\ b_{2g}$	35.5
		6 $b_{1u} \rightarrow 4\ b_{3g}$	32.0
		5 $b_{1u} \rightarrow 4\ b_{3g}$	15.6
		4 $b_{1u} \rightarrow 4\ b_{3g}$	14.1

Table 3.14: TDDFT Composition of 2 $^1B_{2u}$ (B) excitation of MgP with five different *xc*-functionals with varying amounts of HF-exchange.

If the transitions comprising the 1 $^1B_{2u}$ excitation are compared to those that comprise the 2 $^1B_{2u}$ excitation then it can be seen that the 2 $^1B_{2u}$ excitation involves more transitions as the percentage of HF-exchange is decreased. When the percentage of HF-exchange decreases below 20%, contributions from the 5 $b_{1u} \rightarrow 4\ b_{3g}$ transition appear as part of the 2 $^1B_{2u}$ excitation. When HF-exchange is removed completely from the *xc*-functional, contributions appear from the 4 $b_{1u} \rightarrow 4\ b_{3g}$ transition.

Despite MgP having a closed shell electron configuration the composition of the TDDFT excitations suggests that a higher level of theory should be used to investigate these excitations.

3.3.6 Simulation of Excited States with CAS/RASPT2

Higher level CAS/RASSCF calculations have also been performed to investigate the composition of excitations and simulate excitation energies. Table 3.15 details the vertical singlet excitation energies as calculated with CASSCF, RASSCF, CASPT2 and RASPT2 using a variety of active spaces.

Method	$1\ ^1B_{2u}$	$2\ ^1B_{2u}$	$3\ ^1B_{2u}$	$4\ ^1B_{2u}$
CASSCF(4/4)	3.96	5.12	11.88	14.11
CASSCF(16/14)	3.15	4.80	5.09	5.48
CASSCF(16/16)	3.20	4.96	5.34	5.92
RASSCF(16,2,2;6,4,4)	3.26	5.24	5.66	5.96
RASSCF(16,3,3;6,4,4)	3.21	4.82	5.14	5.96
CASPT2(4/4)	2.75	3.84	7.16	6.91
CASPT2(16/14)	2.43	3.46	4.12	5.06
CASPT2(16/16)	2.35	3.57	4.13	4.62
RASPT2(16,2,2;6,4,4)	2.52	3.51	4.45	5.15
RASPT2(16,3,3;6,4,4)	2.23	3.63	3.69	4.21
CASPT2(4/4)*	1.55	2.57	5.29	5.06
CASPT2(16/14)*	1.60	2.39	3.26	4.21
CASPT2(16/16)*	1.60	2.69	3.45	3.82
RASPT2(16,2,2;6,4,4)*	1.98	2.87	3.90	4.10
RASPT2(16,3,3;6,4,4)*	1.38	2.40	2.95	3.67
Experiment [12]	2.07	3.05	-	3.97

Table 3.15: Four lowest optically allowed singlet vertical excitation energies of MgP at DFT (B3LYP/TZVP)-optimised structure using CASSCF, RASSCF, CASPT2 and RASPT2 * indicates excitation energies corrected by perturbation theory without the standard IPEA shift of 0.25. a.u. All excitation energies are given in eV.

Effect of truncating the CI wavefunction

The first section of Table 3.15 gives the simulated excitation energies without perturbation theory. Similar to observations for FBP, the (4/4) active space performs poorly giving a difference from experiment of close to 2 eV for both the simulated Q ($1\ ^1B_{2u}$) and B ($2\ ^1B_{2u}$) band excitation energies. Increasing from the (4/4) active space to the (16/14) active space by inclusion of further ligand orbitals decreases the discrepancy from experiment of the simulated Q and B band excitation energies to just over 1 eV for the Q band but still 1.5 eV for the B band. Inclusion of two further unoccupied orbitals to form a (16/16) active space does not decrease the error but instead increases the error by ∼0.1 eV.

If we look at the effect of moving from a CASSCF(16/14) active space to a RASSCF(16,2,2;6,4,4) active space we see that the simulated Q band excitation energy increases slightly (by 0.06 eV) whilst higher excited states increase by around 0.5 eV each. Increasing the number of excitations allowed between the RAS1 and RAS3 from double to triple decreases the deviation of the RASSCF active space from the results of CASSCF(16/14) active space for the first three excitation energies but not at all for the 4th.

Comparison of perturbation corrected excitation energies

As previously mentioned CAS/RASSCF excitation energies tend not to be very accurate due to a severe lack of dynamical correlation, attention is now turned to the second section of Table 3.15 which contains the calculated excitation energies corrected by second order perturbation theory. Addition of second order perturbation theory decreases the deviation from experiment of the excitation energies obtained with the (4/4) active space by more than one eV, however still leaves a sizeable error of ∼0.7-0.8 eV for the simulated Q and B band excitation energies. This error is similar to that which was observed for FBP using the same active space. Even with the addition of second order perturbation theory higher excited states beyond the Q and B bands are simulated very poorly by the (4/4) active space, with errors of ∼3 eV. Again, like

FBP, this is understandable as this active space provides a severely limited description of the electronic strutcure of the excited states of MgP.

Expanding the active space from a (4/4) active space to a (16/14) active space decreases the error of all excitations, as is to be expected upon inclusion of more orbitals from the ligand. There is a decrease in the deviation from experiment of the excitation energy of the Q band of ∼0.3 eV going from the (4/4) active space to the (16/14) active space leaving an error of ∼0.35 eV from experiment. A similar decrease is seen for the simulated B band excitation energy. If the active space is expanded further to the (16/16) there is a decrease in the simulated Q band excitation energy of ∼ 0.3 eV but a slight increase in the simulated B band excitation energy (∼ 0.1 eV).

Finally if we look at the effect of the removal of the IPEA shift (third section in Table 3.15) it is seen that the standard value of 0.25 a.u. again results in an overestimation of the excitation energies compared to experiment. Whereas removal of the standard IPEA shift again also results in an underestimation of the excitation energies. Furthermore the degree to which the removal of the IPEA shift alters the excitation energies is almost identical to that which was observed for FBP.

Natural Orbital Occupations

Table 3.16 shows the natural orbital occupations of the Gouterman orbitals of the MgP ^1A_g ground state as well as those of the Q ($1\ ^1B_{2u}$) and B ($2\ ^1B_{2u}$) excited states.

The TDDFT results presented in Section 3.3.5 appeared to indicate that the B band excitation was not solely composed of transitions between the Gouterman orbitals, therefore the natural orbital occupations of the other orbitals included in the (16/14) active space are presented in Table 3.17.

Root	Active Space	$2a_u$	$6b_{1u}$	$4b_{2g}$	$4b_{3g}$
$1\ ^1A_g$	CASSCF(4/4)	1.92	1.93	0.08	0.08
	CASSCF(16/14)	1.90	1.91	0.12	0.11
	CASSCF(16/16)	1.90	1.91	0.12	0.11
	RASSCF(16,2,2;6,4,4)	1.91	1.92	0.10	0.10
	RASSCF(16,3,3;6,4,4)	1.91	1.91	0.11	0.11
$1\ ^1B_{2u}$	CASSCF(4/4)	1.31	1.64	0.69	0.36
	CASSCF(16/14)	1.39	1.56	0.63	0.47
	CASSCF(16/16)	1.43	1.53	0.60	0.52
	RASSCF(16,2,2;6,4,4)	1.35	1.58	0.64	0.45
	RASSCF(16,3,3;6,4,4)	1.44	1.50	0.57	0.53
$2\ ^1B_{2u}$	CASSCF(4/4)	1.59	1.26	0.41	0.74
	CASSCF(16/14)	1.67	1.32	0.34	0.91
	CASSCF(16/16)	1.48	1.37	0.55	0.67
	RASSCF(16,2,2;6,4,4)	1.52	1.34	0.49	0.71
	RASSCF(16,3,3;6,4,4)	1.56	1.40	0.41	0.81

Table 3.16: Natural orbital occupation numbers of Gouterman orbitals in MgP for the ^1A_g ground state and two lowest optically allowed excited states using five different active spaces at DFT (B3LYP/TZVP)-optimised geometries.

Like for FBP, Table 3.16 shows that the ground state $1\ ^1A_g$ has very similar natural occupation numbers for the four Gouterman orbitals across all the active spaces, suggesting that all active spaces model the ground state similarly. Furthermore the strong occupation of the formally unoccupied 4 b_{2g} and 4 b_{3g} orbitals (of around 0.1) also suggests that this is a strongly multi-configurational system.

Although the ground state has similar occupation numbers for all active spaces, the same is not

quite true of the excited states. The natural orbital occupations differ by roughly 0.1, if the (4/4) active space is ignored, for all Gouterman orbitals in the 1 $^1B_{2u}$ state. An even larger range is observed for the second excited state however it should be noted that qualitatively all active spaces give the same answer.

Looking now at the natural occupation numbers of the other orbitals included in the (16/14) active space, presented in Table 3.17, it can be seen that for the ground state 1 ^1A_g there are similar natural orbital occupation numbers between the three different active spaces. This is also seen for the 1 $^1B_{2u}$ excited state where the maximum difference between the same orbital in different active spaces in terms of its natural occupation is 0.03. However for the second excited state deviation from this behaviour can be seen. The $3b_{2g}$ orbital has an occupation of 1.84 when calculated using CASSCF but when RASSCF is used and only double excitations allowed this occupation increases to 1.95. An occupation of 1.85 is obtained again when up to triple excitations are allowed within the RAS space which suggests that there are higher excited CSFs contributing to the B band excitation. This would also explain why the RASSCF energy for the 2 $^1B_{2u}$ state is much closer to the CASSCF energy (4.80 eV) when triple excitations (4.82 eV) are permitted rather than double (5.24 eV).

Finally looking at the natural occupation numbers of the 4 and $5b_{1u}$ orbitals for the 2 $^1B_{2u}$ excited state, it can be seen that there is deoccupation of these orbitals as calculated by CASSCF and RASSCF when triple excitations are allowed. This is in agreement with the behaviour seen in the TDDFT calculations with *xc*-functionals containing less than 20% HF exchange.

The natural orbital occupation numbers which are presented in Tables 3.16 and 3.17 show how complex the electronic structure of the excited states of conjugated π systems can be, even for a closed shell system.

Root	Orbital	CASSCF(16/14)	RASSCF(16,2,2;6,4,4)	RASSCF(16,3,3;6,4,4)
$1\ ^1A_g$	$2b_{2g}$	1.99	1.99	1.99
	$3b_{2g}$	1.94	1.95	1.94
	$5b_{2g}$	0.01	0.01	0.01
	$2b_{3g}$	1.99	1.99	1.99
	$3b_{3g}$	1.96	1.97	1.97
	$5b_{3g}$	0.05	0.04	0.04
	$4b_{1u}$	1.97	1.98	1.98
	$5b_{1u}$	1.95	1.96	1.96
	$7b_{1u}$	0.04	0.03	0.04
	$3a_u$	0.07	0.05	0.06
$1\ ^1B_{2u}$	$2b_{2g}$	1.98	1.99	1.97
	$3b_{2g}$	1.94	1.96	1.93
	$5b_{2g}$	0.06	0.04	0.03
	$2b_{3g}$	1.92	1.93	1.95
	$3b_{3g}$	1.97	1.98	2.00
	$5b_{3g}$	0.02	0.02	0.04
	$4b_{1u}$	1.98	1.99	2.00
	$5b_{1u}$	1.94	1.96	1.93
	$7b_{1u}$	0.05	0.03	0.05
	$3a_u$	0.09	0.08	0.07
$2\ ^1B_{2u}$	$2b_{2g}$	1.97	1.96	1.96
	$3b_{2g}$	1.84	1.95	1.85
	$5b_{2g}$	0.05	0.03	0.03
	$2b_{3g}$	1.93	1.96	1.96
	$3b_{3g}$	1.98	1.98	2.00
	$5b_{3g}$	0.02	0.01	0.04
	$4b_{1u}$	1.94	1.98	1.98
	$5b_{1u}$	1.90	1.95	1.89
	$7b_{1u}$	0.05	0.03	0.05
	$3a_u$	0.08	0.06	0.07

Table 3.17: Natural orbital occupation numbers of orbitals included in (16/14) active space excluding Gouterman orbitals which are presented in Table 3.16, at DFT(B3LYP/def2-TZVP) optimised structure.

3.3.7 Comparison of TDDFT with CAS/RASPT2 excitation energies

The simulated excitation energies of the Q and B bands of MgP using both TDDFT (BHLYP, PBE0, B3LYP, TPSSh and TPSS *xc*-functionals) and CAS/RASPT2 are presented in Table 3.18 as well as experimental values [12].

Method	Method Details	1 B_{2u} (Q)	2 B_{2u} (B)
Experiment	-	2.07	3.05
TDDFT	BHLYP	2.41	3.75
	PBE0	2.42	3.55
	B3LYP	2.37	3.47
	TPSSh	2.35	3.43
	TPSS	2.27	3.34
CASPT2	(4/4)	2.75	3.84
	(16/14)	2.43	3.46
	(16/16)	2.35	3.57
	(4/4)*	1.55	2.57
	(16/14)*	1.60	2.39
	(16/16)*	1.60	2.69
RASPT2	(16,2,2;6,4,4)	2.64	3.70
	(16,3,3;6,4,4)	2.33	3.63
	(16,2,2;6,4,4)*	1.98	2.87
	(16,3,3;6,4,4)*	1.38	2.40

Table 3.18: Comparison of TDDFT and CAS/RASPT2 calculated singlet excitation energies of MgP with experimental values given in eV [12].

Agreement with experiment using the computational methods in Table 3.18 is less good for MgP than it is for FBP. This is a little surprising as it is expected that the electronic excitations should be predominantly described by transitions between ligand orbitals. It can also be seen in Table 3.18 that the predicted excitation energies by the (16/14) and (16/16) active spaces are comparable to those obtained from TDDFT using functionals containing 25% of HF-exchange or less with an average error of ∼0.4 eV.

3.3.8 Zinc Porphyrin (ZnP)

3.3.9 Structure Optimisation

Table 3.19 shows DFT-optimised bond lengths and angles using the five different *xc*-functionals previously used, based upon the numbering of atoms in Figure 3.8. Additionally experimental bond lengths and angles are provided for comparison purposes in Table 3.19.

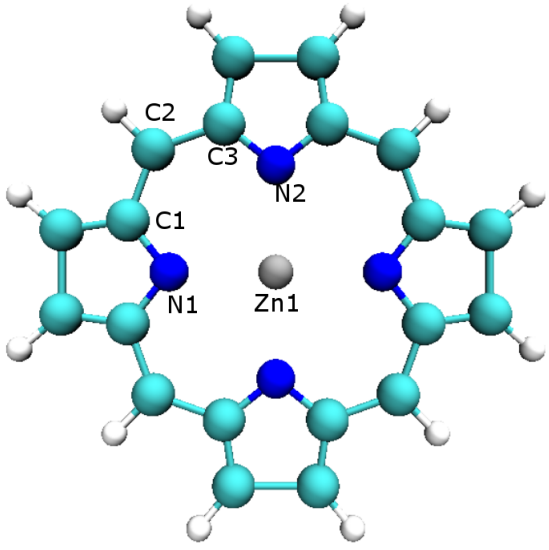

Figure 3.8: DFT (B3LYP/def2-TZVP)-optimised structure of ZnP and labeling of atoms (Grey=Zn, Dark Blue=N, Teal=C, White=H) for Table 3.19.

Coordinate	**BHLYP**	**PBE0**	**B3LYP**	**TPSSh**	**TPSS**	**Experiment** [11]
R(Zn1-N1)	2.039	2.041	2.053	2.046	2.051	2.053
R(Zn1-C2)	3.400	3.412	3.426	3.425	3.435	3.429
R(C1-C2)	1.384	1.389	1.393	1.393	1.397	1.403
R(C1-N1)	1.353	1.361	1.367	1.370	1.375	1.361
A(C1-C2-C3)	126.6	126.7	126.8	126.8	126.9	126.7

Table 3.19: DFT-calculated bond lengths (indicated by R) and angles (indicated by A) for ZnP in the gas phase. All bond lengths given in Angstroms (Å) and angles in in degrees (°).

Table 3.19 shows very similar results for the DFT-structural optimisation of ZnP as that what was seen for MgP and FBP, with very good agreement obtained using all functionals particularly B3LYP, TPSSh and TPSS. The biggest deviation again occurs when the BHLYP functional is used but this is relatively small at $\sim$ 0.01 - 0.02 Å.

3.3.10 TDDFT Results

The TDDFT-calculated gas phase singlet excitation energies of ZnP simulated using the five *xc*-functionals that were utilised in DFT geometry optimisations are presented in Table 3.20. Additionally experimental values and root mean squared (RMS) errors are presented for comparison purposes.

Functional	$1\ ^1B_{2u}$ (Q)	$2\ ^1B_{2u}$ (B)	$3\ ^1B_{2u}$	$4\ ^1B_{2u}$	RMS
BHLYP	2.45	3.78	4.58	5.19	0.80
PBE0	2.47	3.58	3.99	4.47	0.45
B3LYP	2.42	3.50	3.81	4.27	0.34
TPSSh	2.41	3.46	3.64	4.07	0.30
TPSS	2.33	3.29	3.38	3.75	0.27
Experiment [11]	2.09	3.05	-	4.06	-

Table 3.20: TDDFT-calculated singlet excitation energies of ZnP using five different *xc*-functionals and experimental values [11]. All values given in eV.

Similar to MgP, a functional dependence on the calculated excitation energies is visible in Table 3.20. As the percentage of HF-exchange included in the functional is decreased so is the value of the calculated excitation energy. This results in *xc*-functionals with lower HF-exchange predicting more accurate excitation energies whilst functionals containing higher percentages of HF-exchange give fairly large errors, particularly for higher excited states. Again, like MgP, this may be partly due to *xc*-functionals with higher HF-exchange producing structures which are slightly different from experiment. Also like MgP there is a larger range of excitation energies calculated with the five different *xc*-functionals for the B band excitation than the Q band excitation.

Functional	HF-Exchange (%)	Transitions	Weight (%)
BHLYP	50	2 $a_u \rightarrow 5\ b_{2g}$	56.3
		7 $b_{1u} \rightarrow 5\ b_{3g}$	42.0
PBE0	25	2 $a_u \rightarrow 5\ b_{2g}$	50.6
		7 $b_{1u} \rightarrow 5\ b_{3g}$	48.7
B3LYP	20	2 $a_u \rightarrow 5\ b_{2g}$	50.0
		7 $b_{1u} \rightarrow 5\ b_{3g}$	49.4
TPSSh	10	7 $b_{1u} \rightarrow 5\ b_{3g}$	51.1
		2 $a_u \rightarrow 5\ b_{2g}$	48.2
TPSS	0	7 $b_{1u} \rightarrow 5\ b_{3g}$	52.7
		2 $a_u \rightarrow 5\ b_{2g}$	46.3

Table 3.21: Composition of TDDFT-simulated 1 $^1B_{2u}$ (Q) excitation for ZnP with five different *xc*-functionals containing varying amounts of HF-exchange.

The pattern that can seen for the 1 $^1B_{2u}$ excitation is identical to MgP; the percentage contribution of the 2 $a_u \rightarrow 5\ b_{2g}$ transition decreases whilst the 7 $b_{1u} \rightarrow 5\ b_{3g}$ transition increases with decreased percentages of HF-exchange in the *xc*-functional used. Also like MgP there are still only two transitions which comprise the 1 $^1B_{2u}$ excitation and the weight percentages of these transitions have a discrepancy in the range of $\sim 10\%$. Furthermore the four orbitals that are involved in the two transitions are again the four 'Gouterman' orbitals.

Functional	HF-Exchange (%)	Transition	Weight (%)
BHLYP	50	$7\ b_{1u} \rightarrow 5\ b_{3g}$	54.5
		$2\ a_u \rightarrow 5\ b_{2g}$	41.3
PBE0	25	$7\ b_{1u} \rightarrow 5\ b_{3g}$	46.6
		$2\ a_u \rightarrow 5\ b_{2g}$	46.2
B3LYP	20	$2\ a_u \rightarrow 5\ b_{2g}$	46.1
		$7\ b_{1u} \rightarrow 5\ b_{3g}$	44.9
TPSSh	10	$2\ a_u \rightarrow 5\ b_{2g}$	45.2
		$7\ b_{1u} \rightarrow 5\ b_{3g}$	39.8
		$6\ b_{1u} \rightarrow 5\ b_{3g}$	7.7
TPSS	0	$7\ b_{1u} \rightarrow 5\ b_{3g}$	33.3
		$2\ a_u \rightarrow 5\ b_{2g}$	32.1
		$6\ b_{1u} \rightarrow 5\ b_{3g}$	23.2
		$5\ b_{1u} \rightarrow 5\ b_{3g}$	7.9

Table 3.22: Composition of TDDFT-simulated 2 $^1B_{2u}$ (B) excitation of ZnP with five different *xc*-functionals containing varying amounts of HF-exchange.

Again, like the 1 $^1B_{2u}$ excitation, the ZnP TDDFT-calculated 2 $^1B_{2u}$ excitation has a very similar composition to the TDDFT-calculated 2 $^1B_{2u}$ excitation of MgP in that as the the percentage of HF-exchange is decreased the number of transitions comprising the excitation increases. Identical to MgP, the transitions from the lower energy orbitals of symmetry b_{1u} begin to appear when *xc*-functionals containing less than 20% HF exchange are used.

3.3.11 Simulation of excited states with CAS/RASPT2

The ground state and the four lowest excited states of ZnP were also investigated using the CAS/RASSCF methodology, the excitation energies using these methodologies at the DFT(B3LYP/TZVP)-optimised structures are presented in Table 3.23.

4 Method	$1\ ^1B_{2u}$ (Q)	$2\ ^1B_{2u}$ (B)	$3\ ^1B_{2u}$	$4\ ^1B_{2u}$
CASSCF(4/4)	3.99	5.18	12.02	14.27
CASSCF(16/14)	3.31	4.87	5.34	7.22
CASSCF(16/16)	3.24	4.84	5.27	7.17
RASSCF(16,2,2;6,4,4)	3.58	5.62	6.05	6.33
RASSCF(16,3,3;6,4,4)	3.52	5.31	5.54	5.85
CASPT2(4/4)	2.79	3.85	7.21	6.90
CASPT2(16/14)	2.59	3.52	4.61	6.20
CASPT2(16/16)	2.56	3.47	4.56	6.17
RASPT2(16,2,2;6,4,4)	2.60	3.66	4.62	4.84
RASPT2(16,3,3;6,4,4)	2.48	3.76	3.94	4.88
CASPT2(4/4)*	1.59	2.57	5.33	5.05
CASPT2(16/14)*	1.75	2.54	3.78	5.00
CASPT2(16/16)*	1.73	2.53	3.75	4.98
RASPT2(16,2,2;6,4,4)*	1.87	2.78	3.95	5.44
RASPT2(16,3,3;6,4,4)*	1.78	2.43	3.77	5.07
Experiment [12]	2.09	3.05	-	4.06

Table 3.23: Four lowest optically allowed singlet vertical excitation energies of ZnP at DFT (B3LYP/TZVP)-optimised structure using CASSCF, RASSCF, CASPT2 and RASPT2 * indicates excitation energies corrected with PT2 completed without standard IPEA shift of 0.25. a.u. All excitation energies are given in eV.

Effect of truncation of the CI wavefunction

The (4/4) active space, as to be expected, performs poorly giving errors of approximately 2 eV for the Q and B band excitation energies and upwards of 10 eV errors for higher excited states. The (16/14) and (16/16) active spaces perform better than the (4/4) active space but still give errors of over 1 eV. Comparing the values obtained with a RASSCF(16,2,2;6,4,4) active space with its CASSCF counterpart it can be seen that there is a difference in the calculated values of the Q band excitation energy of 0.27 eV whilst the difference between the B band excitation energy is larger at 0.75 eV. If the results of the RASSCF active space allowing triple excitations instead of double are compared to the CASSCF(16/14) active space it can be seen that the difference in the excitation energy of the Q band is 0.21 eV (0.06 eV lower than the double excitations) and 0.44 eV for the B band excitation energy (0.31 eV lower than the double). This suggests that the B band excitation is composed at least partly by highly excited CSFs.

Comparison of excitation energies corrected with perturbation theory

As has been mentioned previously excitation energies calculated using the CAS/RASSCF methodology suffer from a severe lack of dynamical correlation and so are generally not accurate. Attention is now turned to the second section of Table 3.23 which details the excitation energies calculated with the addition of second order perturbation theory. The (4/4) active space gives an error from experiment of $\sim$0.75 eV for the Q and B band excitation energies, an almost identical error to that obtained for FBP and MgP using the same active space. However even with the addition of second order perturbation theory, higher excited states are simulated poorly as to be expected with such a restricted active space.

Looking now at the values obtained for the (16/14) and (16/16) active spaces it can be seen that the two similar active spaces provide almost identical excitation energies. Furthermore they improve the accuracy of the calculated Q and B band excitation energies by roughly 0.3 eV compared to the (4/4) active space, leaving a deviation from experiment of $\sim$0.45 eV. For

higher excited states excitation energies calculated with the (16/14) and (16/16) active spaces are more accurate by more than 2 eV.

Finally looking at the effect of removing the standard IPEA shift, it is seen that the excitation energies are underestimated by ∼0.2-0.3 eV compared with experiment, similar to the observations made for FBP and MgP.

Natural Orbital Occupations

Table 3.24 presents the natural occupation numbers of the Gouterman orbitals in ZnP using the active spaces described previously for the ground state and two lowest excited states.

As has been seen for FBP and MgP the ground state of ZnP, 1 ^1A_g, is modelled by all active spaces almost identically, particularly if the (4/4) active space is discounted. Similarly the first excited state, 1 $^1B_{2u}$ state, also has very similar natural orbital occupation numbers across all active spaces. Although a small difference it should be noted that the RASSCF(16,3,3;6,4,4) active space is closer in terms of occupation numbers than when only double excitations are permitted.

The question of double excitations vs triple excitations in the RASSCF active space becomes more important for the second excited state. Whilst the CASSCF (16/14), CASSCF (16/16) and RASSCF (16,3,3;6,4,4) active spaces have very similar natural orbital occupations the RASSCF (16,2,2;6,4,4) active space presents values that differ from the CASSCF(16/14) active space in the range of 0.04-0.10. Indicating, as had been suggested by the excitation energies produced, that higher excited CSFs play a role in the B band excitation. This has been further investigated through examination of the natural occupation numbers of the ZnP orbitals included in CASSCF(16/14) active space which are presented in Table 3.25.

Root	Active Space	a_u	b_{1u}	b_{2g}	b_{3g}
1 A_g	CASSCF(4/4)	1.92	1.93	0.08	0.08
	CASSCF(16/14)	1.90	1.91	0.12	0.11
	CASSCF(16/16)	1.90	1.91	0.12	0.11
	RASSCF(16,2,2;6,4,4)	1.91	1.92	0.11	0.10
	RASSCF(16,3,3;6,4,4)	1.90	1.91	0.12	0.11
1 B_{2u}	CASSCF(4/4)	1.31	1.64	0.69	0.36
	CASSCF(16/14)	1.39	1.56	0.63	0.47
	CASSCF(16/16)	1.40	1.55	0.63	0.48
	RASSCF(16,2,2;6,4,4)	1.37	1.58	0.64	0.44
	RASSCF(16,3,3;6,4,4)	1.39	1.56	0.63	0.46
2 B_{2u}	CASSCF(4/4)	1.59	1.26	0.41	0.74
	CASSCF(16/14)	1.45	1.41	0.54	0.67
	CASSCF(16/16)	1.45	1.41	0.54	0.67
	RASSCF(16,2,2;6,4,4)	1.52	1.31	0.49	0.71
	RASSCF(16,3,3;6,4,4)	1.45	1.40	0.53	0.68

Table 3.24: Natural orbital occupation numbers of Gouterman Orbitals in ZnP for the A_g ground state and two lowest optically allowed excited states using five different active spaces.

Similar to that which was observed for MgP, it can be seen in Table 3.25 that the orbitals included in the active space have almost identical natural orbital occupation numbers for the ground state and first excited state across the CASSCF (16/14), RASSCF (16,2,2;6,4,4) and RASSCF (16,3,3;6,4,4) active spaces. However there are small differences in the natural orbital occupations of the Gouterman orbitals between the CASSCF (16/14) and RASSCF (16,2,2;6,4,4) active spaces. These differences are not as pronounced as they are between the CASSCF (16/14) and RASSCF(16,3,3;6,4,4) active spaces, concurrent with the excitation energies predicted by the different active spaces. The fact that the RASSCF(16,3,3;6,4,4) active space produces natural orbital occupation numbers closer to the CASSCF (16/14) active space than the (16,2,2;6,4,4) active space does tells us that the triply excited CSFs play a part in the Q and B band excitations.

Root	Orbital	CASSCF(16/14)	RASSCF(16,2,2;6,4,4)	RASSCF(16,3,3;6,4,4)
$1\ ^1A_g$	$2b_{2g}$	2.00	2.00	2.00
	$3b_{2g}$	1.99	1.99	1.99
	$5b_{2g}$	0.05	0.04	0.04
	$2b_{3g}$	1.93	1.94	1.93
	$3b_{3g}$	1.97	1.97	1.97
	$5b_{3g}$	0.02	0.02	0.02
	$4b_{1u}$	1.93	1.95	1.94
	$5b_{1u}$	1.98	1.98	1.98
	$7b_{1u}$	0.05	0.04	0.04
	$3a_u$	0.07	0.05	0.06
$1\ ^1B_{2u}$	$2b_{2g}$	2.00	2.00	2.00
	$3b_{2g}$	1.95	1.96	1.95
	$5b_{2g}$	0.05	0.04	0.05
	$2b_{3g}$	1.92	1.94	1.93
	$3b_{3g}$	1.96	1.97	1.97
	$5b_{3g}$	0.05	0.02	0.04
	$4b_{1u}$	1.92	1.95	1.93
	$5b_{1u}$	1.98	1.99	1.98
	$7b_{1u}$	0.05	0.04	0.05
	$3a_u$	0.09	0.07	0.08
$2\ ^1B_{2u}$	$2b_{2g}$	1.99	2.00	1.99
	$3b_{2g}$	1.96	1.97	1.96
	$5b_{2g}$	0.06	0.04	0.06
	$2b_{3g}$	1.89	1.94	1.90
	$3b_{3g}$	1.96	1.97	1.97
	$5b_{3g}$	0.03	0.02	0.03
	$4b_{1u}$	1.90	1.94	1.91
	$5b_{1u}$	1.97	1.99	1.98
	$7b_{1u}$	0.05	0.04	0.05
	$3a_u$	0.06	0.06	0.06

Table 3.25: ZnP Natural orbital occupation numbers of orbitals included in (16/14) active space excluding Gouterman orbitals, which are presented in Table 3.24, at DFT(B3LYP/def2-TZVP) optimised structure.

3.3.12 Comparison of TDDFT with CAS/RASPT2

Table 3.26 compares and contrasts the simulated excitation energies of the Q and B bands of ZnP using both TDDFT (BHLYP, PBE0, B3LYP, TPSSh and TPSS *xc*-functionals) and CAS/RASPT2 with experimental values [12].

Method	Method Details	1 B_{2u} (Q)	2 B_{2u} (B)
Experiment [11]	-	2.09	3.05
TDDFT	BHLYP	2.45	3.78
	PBE0	2.47	3.58
	B3LYP	2.42	3.50
	TPSSh	2.41	3.46
	TPSS	2.33	3.29
CASPT2	(4/4)	2.79	3.85
	(16/14)	2.59	3.52
	(16/16)	2.56	3.47
	(4/4)*	1.59	2.57
	(16/14)*	1.75	2.54
	(16/16)*	1.73	2.53
RASPT2	(16,2,2;6,4,4)	2.60	3.66
	(16,3,3;6,4,4)	2.48	3.76
	(16,2,2;6,4,4)*	1.87	2.78
	(16,3,3;6,4,4)*	1.78	2.43

Table 3.26: Comparison of TDDFT and CAS/RASPT2 calculated singlet excitation energies of ZnP with experimental values [11]. All values given in eV.

Table 3.26 shows that TDDFT simulates a more accurate excitation energy for the Q band excitation than CAS/RASPT2 does. However for the B band excitation, which from investigation of the natural orbital occupation appears to be a highly multiconfigurational excitation, CAS/RASPT2 predicts excitation energies which are comparable to TDDFT.

3.3.13 Comparison of FBP, MgP and ZnP

Tables 3.27 and 3.28 compare and contrast the Q and B band excitation energies determined experimentally as well as calculated using the variety of methods discussed in this chapter for FBP, MgP and ZnP.

Method	Method Details	FBP		MgP	ZnP
		Q_x ($1\ ^1B_{3u}$)	Q_y ($1\ ^1B_{2u}$)	Q ($1\ ^1B_{2u}$)	Q ($1\ ^1B_{2u}$)
Experiment [12, 11]	-	1.98	2.42	2.07	2.09
TDDFT	BHLYP	2.31	2.47	2.41	2.45
	PBE0	2.33	2.48	2.42	2.47
	B3LYP	2.27	2.42	2.37	2.42
	TPSSh	2.27	2.40	2.35	2.41
	TPSS	2.19	2.32	2.27	2.33
CASPT2	(4/4)	2.46	2.88	2.75	2.79
	(16/14)	2.40	2.72	2.43	2.59
	(16/16)	2.19	2.57	2.35	2.56
RASPT2	(16,2,2;6,4,4)	2.34	2.75	2.64	2.60
	(16,3,3;6,4,4)	2.27	2.54	2.33	2.48

Table 3.27: Comparison of Q band excitation energies of FBP, MgP and ZnP calculated with DFT(BHLYP, PBE0, B3LYP, TPSSh and TPSS) and CAS/RASPT2 as well as experimental values [12, 11]. All values given in eV.

Method	Method Details	FBP		MgP	ZnP
		B_x ($2\ ^1B_{3u}$)	B_y ($2\ ^1B_{2u}$)	B ($2\ ^1B_{2u}$)	B ($2\ ^1B_{2u}$)
Experiment [12, 11]	-	3.33	3.33	3.05	3.05
TDDFT	BHLYP	3.67	3.77	3.75	3.78
	PBE0	3.42	3.56	3.55	3.58
	B3LYP	3.32	3.47	3.47	3.50
	TPSSh	3.23	3.36	3.43	3.46
	TPSS	3.03	3.09	3.34	3.29
CASPT2	(4/4)	3.77	3.84	3.84	3.85
	(16/14)	3.65	3.42	3.46	3.52
	(16/16)	3.70	3.64	3.57	3.47
RASPT2	(16,2,2;6,4,4)	3.61	3.64	3.70	3.66
	(16,3,3;6,4,4)	3.62	3.52	3.63	3.76

Table 3.28: Comparison of B band excitation energies of FBP, MgP and ZnP calculated with DFT(BHLYP, PBE0, B3LYP, TPSSh and TPSS) and CAS/RASPT2 as well as experimental values [12, 11]. All values given in eV.

It is very clear in Tables 3.27 and 3.28 that when the computational method is kept constant excitation energy predicted is very similar between the three different molecules. This is not entirely surprising considering that the Q and B band excitations are considered to be composed of transitions between the ligand orbitals. Furthermore FBP, MgP and ZnP have very similar structures, with Mg^{2+} and Zn^{2+} also having an almost identical ionic radii.

Having considered both free base and regular porphyrins which have a closed electronic shell and shown the similarities between the two, focus now switches to the more complex and interesting irregular porphyrins.

3.4 Irregular Transition Metal Porphyrins

So far only porphyrin systems which have a closed shell electronic structure have been discussed and it has been seen that even in these systems where static correlation may be expected to be fairly small, a great deal of multiconfigurational character has been observed, as evidenced by natural orbital occupation numbers presented in Tables 3.7, 3.16 and 3.24.

Attention is now turned to more complicated porphyrin systems which have an open shell electronic structure, known as irregular porphyrins [111]. This section focuses on two irregular porphyrins, namely Manganese Poprhyrin and Iron Porphyrin, hereafter referred to as MnP and FeP respectively.

MnP and FeP are of principal interest because of the high number of 3d-electrons, giving rise to some very interesting behaviour and properties, but also because of their key roles in photosystem II [112].

3.4.1 Summary of previous works

Irregular porphyrins are porphyrins that do not have a closed electronic shell, i.e. the metal centre contains a partially filled d shell. Because irregular porphyrins have a partially filled shell they contain a great deal of static correlation and hence TDDFT would not be expected to accurately predict excitation energies. It is therefore understandable that the majority of papers computationally examining the absorption spectra of irregular porphyrins are based on NiP and CuP as they contain 8 and 9 d electrons respectively, meaning that their absorption spectra should be easier to simulate as it is closer to a closed shell.

One example is the computational simulation of Nickel Porphyrin (NiP) which is reported by E. J. Baerends *et al* [113] in which they used TDDFT to calculate the singlet excitation energies. Structures were optimised with DFT followed by excited state calculations performed

with TDDFT using the SAOP functional. The results obtained are in good agreement with the experimental results with the Q and B band calculated to be 2.40 and 3.23 eV compared to experimental values of 2.28 and 3.11 eV [114]. As mentioned previously the SAOP functional has been developed specifically with the aim of accurately predicting excited states so it is not surprising to see it perform well.

As described earlier; Peralta *et al* paper in 2007 also calculated the excitation energies of NiP. Like the MgP and ZnP structures, NiP was optimised using DFT with the BP86 functional, following which excited states were calculated using TDDFT with SAOP. The Q and B bands were calculated at 2.37 and 3.21 eV respectively. These results are very close to the experimental results as well as being almost identical to the results published by E. J. Baerends *et al*, which is expected as they have both used the SAOP functional. The slight deviation arising from the use of different basis sets with Peralta *et al* using more polarisation functions in the basis set than Baerends *et al* explaining the slightly more accurate results obtained by Peralta.

A paper which computationally simulated the absorption spectrum of NiOEP (Nickel octaethylporphyrin), a molecule very similar to NiP, was published in 2010 by Kovalenko *et al* [115]. Structures were optimised using a variety of different methods, including DFT with different functionals. The optimised structures with the greatest accuracy (when compared with experiment) were found with the PW91 and PBE functionals. Excited states were then calculated using TDDFT (PBE0) with the 6-31G* basis set. The Q and B bands were calculated to be 2.43 and 3.04 eV for NiOEP, which are extremely close to the experimental energies for NiP. Because ethyl chains are simple hydrocarbon chains with no conjugation it is unlikely that they will greatly affect the excitation energies, we can therefore compare these calculated energies to the experimental energies reported above. The high level of accuracy with which Kovalenko *et al* calculated excitation energies for NiOEP is very surprising considering that it was achieved with TDDFT and a hybrid functional.

Moving away from NiP, the simulated absorption spectrum of Copper Porphyrin (CuP) was reported in 1995 by Stavrev and Zerner [116]. To optimise structures, the authors used the Intermediate Neglect of Differential Overlap (INDO) model, which is a semi-empirical method, followed by a Configuration Interaction (CI) calculation. The Q and B band of CuP are calculated to be 1.97 and 3.54 eV* . If we compare the calculated Q and B band values to experimental CuOEP (see paragraph above) excitation energies which place the Q and B band at 2.19 and 3.20 eV respectively [12], we see that the simulated values show a small error of around 0.2 eV. This result is incredibly close for a semi-empirical method such as INDO.

The reported values for NiP and CuP simulated using TDDFT show a small error which is comparable to the error seen for ZnP. This is not completely unexpected as the electron configuration of NiP and CuP is 2 and 1 electrons away from ZnP respectively. As mentioned previously due to space constraints other irregular porphyrins have not been discussed here however the TDDFT results show a larger error, which is perhaps indicative of multiconfigurational character.

*Results were reported in nm in the literature and have been converted to eV for comparison purposes

3.4.2 Manganese Porphyrin (MnP)

The main attention of this work on irregular transition metals has been completed on Manganese porphyrin. Managanese (II) poprhyrin is of principal interest because it has a half full d shell and so it would be expected that a great deal of multiconfigurational behaviour will be observed. It is also an important molecule biologically, playing a key role in the body in the photosystem II process [112, 117, 118, 119].

3.4.3 Computational Details

Simulations were performed using both wavefunction- and density-based methodologies: Complete/Restricted Active Space Self Consistent Field (CASSCF/RASSCF) theory and Density Functional Theory (DFT). Excited states were calculated using both State Averaged (SA)-CASSCF/RASSCF & Time Dependent Density Functional Theory (TDDFT). DFT-based structural optimisations were performed using version 6.6 of the Turbomole program [67] employing the Ahlrichs-style basis sets of polarised triple-zeta quality (def2-TZVP) [68]. Five different exchange correlation ($xc-$) functionals were used, the hybrid $xc-$functionals; BHLYP [91, 35, 38], PBE0 [86], B3LYP [91, 35, 92], TPSSh [93, 94] which contain 50%, 25%, 20% & 10% components of exact Hartree Fock (HF) exchange respectively. The pure meta generalised gradient approximation (meta-GGA) xc-functional TPSS [37] was also considered. Optimisations were performed on the four irreducible representations (irreps) that can be formed by the occupation of Manganeses five d orbitals with five electrons; the states A_g, B_{1g}, B_{2g} & B_{3g} and frequency analysis performed.

TDDFT simulations were also performed with Turbomole using the same basis sets and functionals; BHLYP, PBE0, B3LYP, TPSSh & TPSS. TDDFT calculations were simulated from each functionals respective optimised geometry at the ^6A_g state and the lowest 5 B_{2u}/B_{3u} states calculated.

Although MnP has D_{4h} symmetry, DFT optimisations (and TDDFT simulations) were constrained to the lower D_{2h} point group for consistency with subsequent CAS/RASSCF calculations, which were performed using version 8.0 of the Molcas software package.

CAS/RASSCF calculations employed the relativistically contracted atomic natural orbital (ANO-RCC) basis sets [70] of polarised triple-zeta quality on DFT-optimised structures. Scalar relativistic effects, although expected to be small, were included via use of the 2nd order Douglas-Kroll-Hess Hamiltonian [71]. Second order perturbation theory (PT2) calculations were performed on the CAS/RASSCF converged wavefunctions in order to incorporate dynamical correlation effects. In these PT2 calculations an imaginary level shift of 0.2 a.u. was included in order to reduce the effect of intruder states. Perturbation calculations were performed both with and without the standard IPEA shift of 0.25, as inclusion of the IPEA shift has been shown to incorrectly model porphyrin excited state energies.

CASSCF calculations were performed using an active space which incorporated the four Gouterman orbitals as well as the transition metal d-orbitals to form a 9 electron, 9 orbital, denoted as (9/9), active space. The molecular orbitals included in the CAS span the 24-25 a_g, 4-5 b_{2g}, 15 b_{1g}, 4-5 b_{3g}, 2 a_u and 7 b_{1u} irreps and are shown in Figure 3.9. It should be noted that this CASSCF(9/9) active space is minimal in size and so is used only to provide a largely qualitative description of the electronic structure in this system.

RASSCF calculations were also performed using a larger active space which included the orbitals defined above in the RAS2, but additionally included six orbitals in the RAS1 & four orbitals in the RAS3, based upon an active space developed by Roos and coworkers [88, 59] to describe Free Base Porphyrin. Hereafter the RASSCF active space will use the standard notation $(n, l, m; i, j, k)$, where n is the number of electrons, l and m are the number of excitations permitted from/to the RAS1/RAS3 respectively and i, j and k are the number of orbitals

in RAS1, RAS2 and RAS3 respectively. The active space is therefore RASSCF(21,2,2;6,9,4). The molecular orbitals in the RAS1, RAS2 and RAS3 are also shown in Figure 3.9 and span the 24-25 a_g, 2-6 b_{2g}, 15 b_{1g}, 2-6 b_{3g}, 2-3 a_u, 5-8 b_{1u} irreps. For both CASPT2(9/9) and RASPT2(21,2,2;6,9,4) calculations were performed on the ^6A_g, ^4A_g, $^4B_{1g}$ & $^4B_{2g}$ states.

Vertical excitation energies (VEEs) were also calculated with the CASPT2 (9/9) and RASPT2 (21,2,2;6,9,4) active spaces by simulation of the $^6B_{2u}/B_{3u}$ excited states, with the 7 lowest states calculated. In addition to these two active spaces, one CASPT2 & two further RASPT2 active spaces were used for calculation of excited states. The additional CASPT2 active space was a CASPT2(9/14) which includes the same orbitals as the CASPT2(9/9) but additionally includes a second set of Mn d-orbitals , allowing us to investigate the so-called double shell effect [120, 121]. Both additional RASPT2 calculations attempt to balance the active space by inclusion of corresponding bonding and antibonding orbitals. The first active space was a reduction of the RASPT2 (21,2,2;6,9,4) to RASPT2 (17,l,m;4,9,4), one orbital from each of the b_{2g} and b_{3g} subspaces was removed, and because of the smaller size of the active space, both double and triple excitations could be considered. The second additional active space was an expansion to a RASPT2 (21,2,2;6,9,6) via inclusion of a further orbital each from the b_{2g} and b_{3g} subspace. Through evaluation of these active spaces the dependence of the calculated excitation energies on the active space can be investigated.

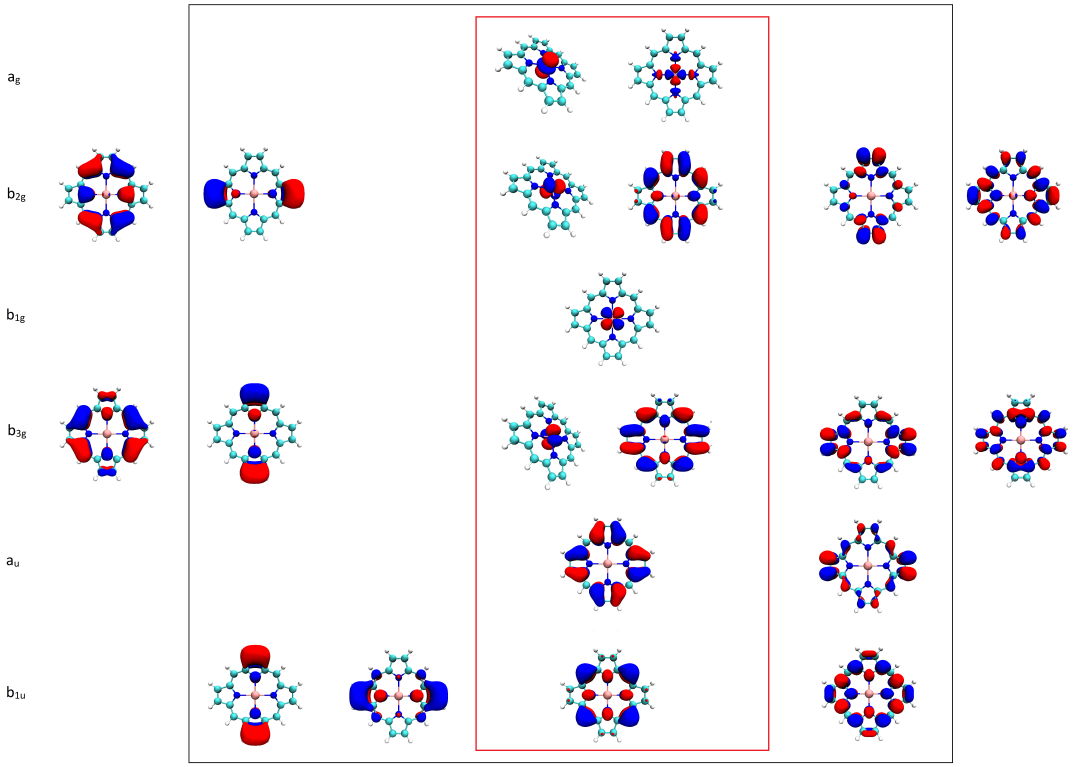

Figure 3.9: MnP Active Space Diagram. Red box indicates orbitals included in CASSCF (9/9) and RAS2 of all active spaces. Black box indicates orbitals included in RASSCF (17,n, m;4,9,4), Orbitals to left of black box included in RASSCF (21,2,2;6,9,4) and all orbitals in diagram included in RASSCF (21,2,2;6,9,6). All orbitals generated with an isosurface of 0.30 a.u.

Again like for other porphyrin systems examined previously in this thesis, the Gouterman orbitals are referred to as GO1-4 where GO1 and GO2 are the formal Gouterman HOMO-1 and HOMO (a_u and b_{1u} symmetries respectively) whilst GO3 and GO4 are the formal Gouterman LUMO and LUMO+1 (b_{2g} and b_{3g} symmetries respectively).

3.4.4 Structure Optimisation

As mentioned previously manganese porphyrin is an interesting case of a metal porphyrin as it contains a half full 3d-shell. Experimental electron paramagnetic resonance (EPR) studies have previously been utilised to show that in MnP, the ground state is a sextet [122]. In these calculations electronic and geometrical structures of MnP have been optimised, using a selection of different DFT *xc*-functionals that contain various amounts of Hartree-Fock exchange, considering the experimentally determined ^6A_g ground state, in addition to the lowest quartet states, of ^4A_g, $^4B_{1g}$ and $^4B_{2g}/B_{3g}$ symmetry. These four states correspond to the following 3d-occupations:

^6A_g - $((d_{xz})^1(d_{yz})^1(d_{xy})^1(d_{z^2})^1(d_{x^2-y^2})^1)$
^4A_g - $((d_{z^2})^2(d_{xy})^1(d_{xz})^1(d_{yz})^1)$
$^4B_{1g}$ - $((d_{xy})^2(d_{xz})^1(d_{yz})^1(d_{z^2})^1)$
$^4B_{2g}/^4B_{3g}$† - $((d_{xz})^2(d_{yz})^1(d_{xy})^1(d_{z^2})^1)/((d_{xz})^1(d_{yz})^2(d_{xy})^1(d_{z^2})^1)$.

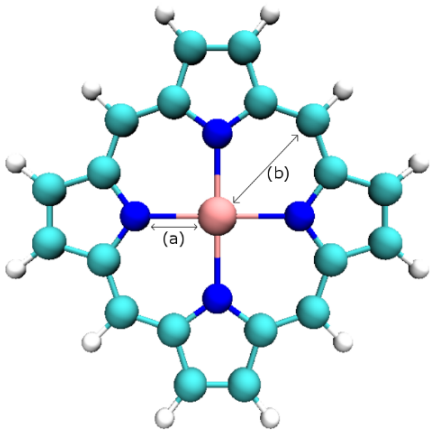

Figure 3.10: Coordinates (a) Mn-N bond length and (b) Mn-C(Methyne) of MnP detailed in Table 3.29.

†The $^4B_{2g}$ & $^4B_{3g}$ states are degenerate since calculations are performed in D_{2h} rather than D_{4h} symmetry

Table 3.29 gives the details of two key coordinates in MnP, the Mn-N bond distance and the Mn-C (Methyne) distance ((a) and (b) respectively in Figure 3.10) calculated for the various electronic states with a range of xc-functionals and compares to experimental values.

Bond	State	BHLYP	PBE0	B3LYP	TPPSh	TPSS	Exp [122]
Mn-N	^6A_g	2.080	2.078	2.089	2.080	2.082	2.084
	^4A_g	2.017	2.009	2.021	2.010	2.011	
	$^4B_{1g}$	2.022	2.011	2.024	2.012	2.011	
	$^4B_{2g}$	2.019	2.001	2.012	2.001	2.003	
Mn-C (Methyne)	^6A_g	3.413	3.425	3.438	3.437	3.447	3.464
	^4A_g	3.395	3.406	3.419	3.418	3.427	
	$^4B_{1g}$	3.397	3.407	3.420	3.419	3.428	
	$^4B_{2g}$	3.35	3.408	3.421	3.420	3.430	

Table 3.29: DFT-optimised and experimental bond lengths of Mn-N and Mn-C(Methyne) as shown in Figure 3.10 using five different *xc*-functionals for four different electron configurations of MnP.

Table 3.29 shows that there is very little change (<0.01) in the Mn-N bond distance between states with equivalent spin, particularly when using the same functional. However there is a difference in the optimised length of the Mn-N bond between the sextet & quartet states of 0.07 Å. This can be attributed to the forced occupation of the $d_{x^2-y^2}$ orbital in the ^6A_g state. This orbital has lobes which lie in the plane of, and are anti-bonding with respect to, the Mn-N bond and thus its occupation increases the bond length.

If the simulated Mn-N bond lengths are compared to the experimental Mn-N bond length, presented in Table 3.29, it can be seen that the bond length generated by all xc-functionals for the ^6A_g state provides excellent agreement, particularly with the B3LYP and TPSS xc-

functionals (deviating by 0.005 and 0.002 Å respectively).

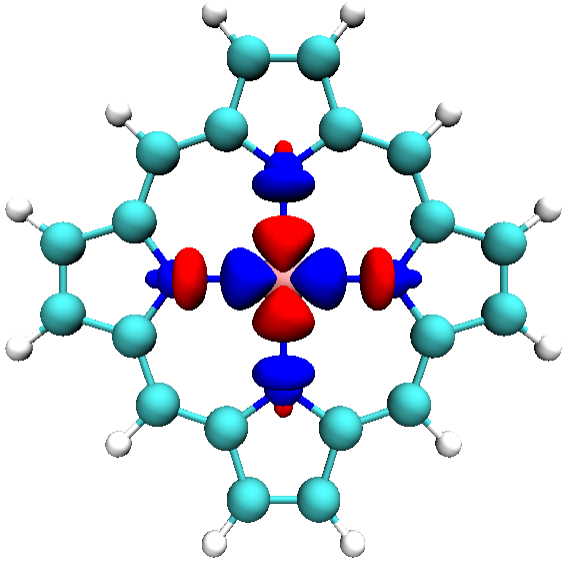

Figure 3.11: $d_{x^2-y^2}$ orbital of MnP generated using CASSCF (14/9) active space at DFT (B3LYP/def2-TZVP)-optimised geometry. Orbital generated using an isosurface of 0.03 a.u.

Conversely to the trend seen for the Mn-N bond there is a change in the Mn-C (Methyne) distance between states with equivalent spin on changing the functional, however this is fairly minimal with 0.03 Å difference between the minimum and maximum values. This trend is evidence that there is a dependence on the amount of HF-exchange included in the xc-functional. Finally, there is a much smaller difference in the Mn-C (Methyne) distance between the sextet and the quartet states with the same functional of 0.02 Å.

Although the agreement of the simulated Mn-C (Methyne) distance with experiment is not as close as it is for the Mn-N bond, we still see relatively good agreement (< 0.05 Å) and again particularly for the B3LYP and TPSS functionals (< 0.03 Å).

3.4.5 Comparison of Relative Ground State Energetics

If the relative energies of each state are now compared, shown in Table 3.29, it is found that there is a strong functional dependence on the relative stabilities.

Functional	Hartree-Fock Exchange	$^4B_{1g}$	^4A_g	$^4B_{2g}/B_{3g}$	^6A_g
BHLYP	50%	0.70	1.00	0.94	0.00
PBE0	25%	0.35	0.58	0.35	0.00
B3LYP	20%	0.14	0.31	0.14	0.00
B3LYP*	20%	0.33	0.52	0.42	0.00
TPSSh	10%	-0.03	0.12	-0.16	0.00
TPSS	0%	-0.28	-0.18	-0.21	0.00

Table 3.30: Relative energy differences of different MnP spin states at respective optimised geometries * indicates all spin states calculated at constant ^6A_g geometry. All values given in eV.

Table 3.30 highlights the uncertainty that stems from the choice of different xc-functionals in the simulation of MnP; it can be clearly seen that there is a variety of different solutions obtained using different xc-functionals. Use of the BHLYP functional, which includes the highest percentage of HF-exchange at 50%, results in the relative stabilisation of the ^6A_g state, in which the 3d-shell is half-filled, by 0.70 eV compared to the $^4B_{1g}$ state. Conversely the TPSS functional which includes no HF exchange predicts the $^4B_{1g}$ state to be relatively more stable by 0.28 eV than the ^6A_g. This corresponds to a change in a stabilisation of 0.98 eV when changing from an xc-functional containing no HF-exchange to one which contains a 50% HF contribution. Whether the most stable spin state is a sextet or a quartet depends on whether it is more energetically favourable to singly occupy the high energy $d_{x^2-y^2}$ orbital than to doubly occupy one of the lower energy 3d-orbitals.

In order to further understand the ground state of MnP, the relative stabilities of different states using the CASPT2 and RASPT2 methodologies have also been calculated. Table 3.30 reveals that there is little functional dependence on the optimal structure for a given electronic state, therefore the B3LYP-optimised ^6A_g and $^4B_{1g}$ geometries have been used for all CAS/RASPT2 calculations.

Method	$^4B_{1g}$	^4A_g	$^4B_{2g}/B_{3g}$	^6A_g
CASPT2(9/9)*	1.57	1.69	1.72	0.00
CASPT2(9/9)‡	1.14	1.24	1.29	0.00
RASPT2(21,2,2;6,9,4)*	1.82	1.66	1.71	0.00
RASPT2(21,2,2;6,9,4)‡	1.41	1.24	1.87	0.00

Table 3.31: Relative energy differences of different MnP spin states * indicates all spin states calculated at constant ^6A_g DFT(B3LYP/def2-TZVP) geometry ‡ indicates all spin states calculated at constant $^4B_{1g}$ DFT(B3LYP/def2-TZVP) optimised geometry. All values given in eV.

There is no ambiguity as to which is the most stable spin state when the CAS/RASPT2 methodology is used, regardless of whether it is performed at the ^6A_g or $^4B_{1g}$ optimised geometry - Table 3.31 shows that it is clearly the ^6A_g state which is stable by more than 1 eV. It is encouraging that our minimal active space, CASPT2(9/9), qualitatively agrees with the larger RASPT2 calculation.

3.4.6 Analysis of the CAS/RAS wavefunction and comparisons with DFT

Table 3.32 presents the natural orbital occupation numbers of the five metal d-orbitals and the four Gouterman orbitals from calculations using the CASSCF (9/9) and RASSCF(21,2,2;6,9,4) active spaces.

Orbital	^6A_g	^4A_g	$^4B_{1g}$	$^4B_{2g}/B_{3g}$
$d_{x^2-y^2}$	1.00 (1.00)	0.11 (0.11)	0.04 (0.04)	0.08 (0.08)
d_{xy}	1.00 (1.00)	1.00 (1.00)	1.96 (1.96)	1.03 (1.03)
d_{xz}	1.00 (1.00)	1.00 (1.00)	1.00 (1.00)	0.97 (0.97)
d_{yz}	1.00 (1.00)	1.00 (1.00)	1.00 (1.00)	1.91 (1.91)
d_{z^2}	1.00 (1.00)	1.89 (1.89)	1.00 (1.00)	1.01 (1.01)
GO1	1.92 (1.90)	1.92 (1.89)	1.91 (1.90)	1.92 (1.90)
GO2	1.93 (1.91)	1.93 (1.91)	1.93 (1.95)	1.93 (1.91)
GO3	0.08 (0.11)	0.08 (0.11)	0.08 (0.10)	0.08 (0.11)
GO4	0.08 (0.11)	0.08 (0.11)	0.08 (0.10)	0.08 (0.12)

Table 3.32: Natural orbital occupations at ^6A_g DFT(B3LYP/def2-TZVP) optimised geometry using CASSCF(9/9) active space. Values given in parenthesis are obtained from using RASSCF(21,2,2;6,9,4) active space.

In all three of the quartet spin states there is significant occupation (>0.02) of the $d_{x^2-y^2}$ orbital, particularly in the ^4A_g state. The occupation numbers of the Gouterman orbitals is largely constant across the four different configurations. There is very little change in the natural occupations of the metal orbitals upon increasing the size of the active space from CAS(9/9) to RAS(21,2,2;6,9,4) via inclusion of more ligand-based π orbitals. Conversely there is a more pronounced change in the natural occupations of the Gouterman orbitals, specifically a decrease of the occupied orbitals of ∼0.01 and an increase in the (formally) unoccupied orbitals of ∼0.03.

A comparison of DFT-derived molecular orbitals with CAS/RASSCF natural orbitals highlights some significant variation, particularly for the (formally) unoccupied Gouterman orbitals and the metal-based $3d_{xz}$ and $3d_{yz}$ orbitals, which have the same symmetry. These orbitals are shown in Figures 3.12 and 3.13.

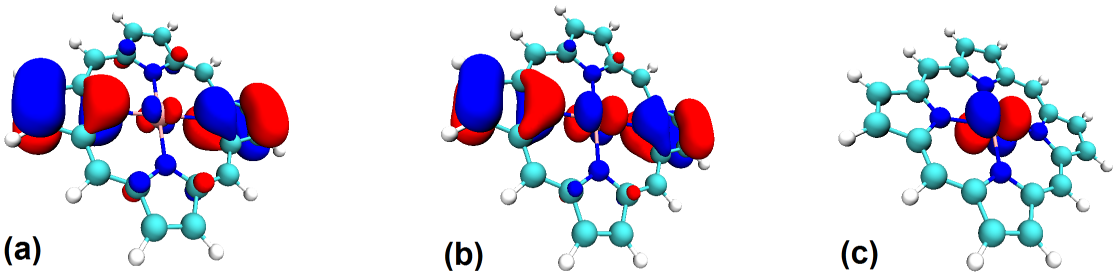

Figure 3.12: d_{xz} orbital of the ^6A_g state generated by (from left to right) (a) DFT(TPSS) (b) DFT(BHLYP) and (c) RASSCF(21,2,2;6,9,4) at an Isosurface of 0.03 a.u.

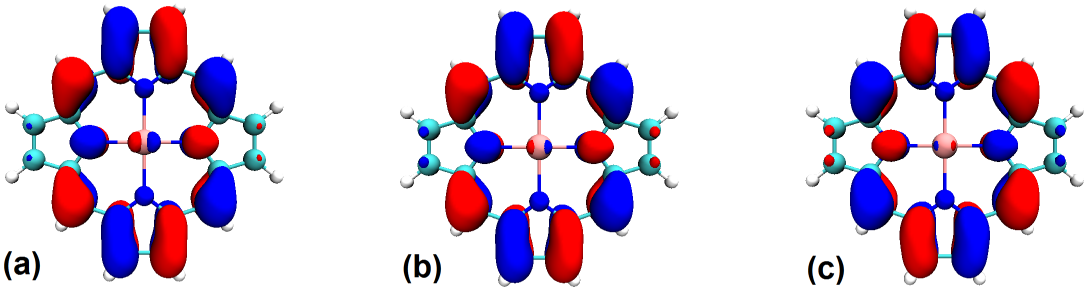

Figure 3.13: GO3 orbital of the ^6A_g state generated by (from left to right) (a) DFT(TPSS) (b) DFT(BHLYP) and (c) RASSCF(21,2,2;6,9,4) at an Isosurface of 0.03 a.u.

It can be clearly seen in Figure 3.12 that there is significant mixing of a ligand-based π orbital with the metal-based $3d_{xz}$ orbital in the DFT simulations, however the RASSCF(21,2,2;6,9,4)-derived $3d_{xz}$ orbital displays no mixing of the porphyrin ligand. Similar behaviour is found for the Gouterman LUMO, although the effect is less pronounced.

3.4.7 QTAIM Analysis

In order to investigate the bonding in MnP, and in particular the Mn-N bond, we have used the Quantum Theory of Atoms in Molecules (QTAIM) approach as devised by Bader and coworkers [61, 62, 63]. Within the context of QTAIM we can define the bond critical point (BCP) as the point on the uniquely defined line of maximum density between two atoms where the gradient of the electron density vanishes.

Table 3.33 shows the magnitude of the electron density (ρ) at the M-N BCP, derived from densities calculated using the five DFT $xc-$functionals at their respective sextet-optimised structures, as well as from CAS/RASSCF derived densities, obtained at the B3LYP-optimised ^6A_g structure.

Method	^6A_g	^4A_g	$^4B_{1g}$	$^4B_{2g}/B_{3g}$
BHLYP	0.079	0.089	0.082	0.085
PBE0	0.081	0.093	0.086	0.095
B3LYP	0.079	0.090	0.083	0.091
B3LYP*	0.079	0.078	0.072	0.075
TPSSh	0.080	0.092	0.086	0.093
TPSS	0.080	0.092	0.086	0.093
CASSCF(9/9)*	0.076	0.072	0.066	0.068
RASSCF(21,2,2;6,9,4)*	0.076	0.072	0.066	0.068
CASSCF(9/9)‡	0.087	0.083	0.076	0.078
RASSCF(21,2,2;6,9,4)‡	0.087	0.083	0.076	0.077

Table 3.33: Value of the electron density (ρ) at the BCP of Mn-N bond * indicates all spin states calculated at constant ^6A_g DFT(B3LYP/def2-TZVP) geometry ‡ indicates all spin states calculated at constant $^4B_{1g}$ DFT(B3LYP/def2-TZVP) optimised geometry. All values given in a.u.

Table 5 shows that there is a dependence of ρ_{bcp} on the spin states. Lowering the multiplicity has the effect of increasing the value of ρ_{bcp}, commensurate with a shortening of the optimised Mn-N bond length. In the case of B3LYP simulations, when the geometry is kept constant at that of the ^6A_g state it can be seen that the value of ρ_{bcp} for the sextet is slightly greater than for all of the quartet states.

This behaviour can also be seen in the CAS/RASSCF data (which was obtained by evaluating states at a constant geometry). Furthermore, when the geometry for the CAS/RASSCF calculations is changed from the B3LYP-optimised ^6A_g geometry to the B3LYP-optimised $^4B_{1g}$ geometry, the value of ρ_{bcp} increases for all states by an almost identical amount ($\sim$0.01 a.u.), commensurate with the reduction in the Mn-N bond length. It is also worth noting that there is minimal difference between the CASSCF and RASSCF results at the same geometry for the same spin state. There is a small yet consistent difference in the value of ρ_{bcp} between the quartet states in that it is systematically higher in the ^4A_g and $^4B_{2g}/B_{3g}$ states than in the $^4B_{1g}$ state. This may be explained by the natural occupations presented in Table 3.32, where the ^4A_g and the $^4B_{2g}/^4B_{3g}$ states show more pronounced occupation of the $3d_{x^2-y^2}$ orbital than the $^4B_{1g}$ state, which as can be seen in Figure 3.11 has orbital lobes which point along the Mn-N bond.

Finally, while there is a slight functional dependence on the values of ρ_{bcp} for a given state, there appears to be no pronounced correlation with the percentage of exact HF exchange included in the functional, although BHLYP values appear to be lower than all other xc-functionals.

	^6A_g	^4A_g	$4B_{1g}$	$^4B_{2g}$
BHLYP	0.402	0.497	0.507	0.504
PBE0	0.435	0.551	0.565	0.596
B3LYP	0.440	0.555	0.565	0.589
B3LYP*	0.440	0.519	0.529	0.538
TPSSh	0.452	0.572	0.586	0.607
TPSS	0.470	0.597	0.612	0.626
CASPT2(9/9)*	0.467	0.527	0.538	0.524
RASPT2(21,2,2;6,9,4)*	0.464	0.528	0.531	0.525
CASPT2(9/9)	0.499	0.575	0.581	0.566
RASPT2(21,2,2;6,9,4)	0.495	0.525	0.573	0.515

Table 3.34: Delocalisation indices of Mn-N Bond (δ(Mn-N)) * indicates all spin states calculated at constant ^6A_g DFT(B3LYP/def2-TZVP) geometry ‡ indicates all spin states calculated at constant $^4B_{1g}$ DFT(B3LYP/def2-TZVP) optimised geometry. All values given in a.u.

Table 3.34 shows the delocalisation indices of the Mn-N bond (δ(Mn-N)), which is a measure of the number of electrons shared between two atoms in a molecule. There is a significant increase in δ(Mn-N) on going from the ^6A_g state to each of the quartet states. Furthermore the difference in δ(Mn-N) between the ^6A_g state and the quartet spin states decreases as the percentage of HF-exchange present in the functional increases.

Turning attention to the CAS/RASSCF derived delocalisation indices it can be seen that as for ρ, both approaches give near identical values at the same geometry. However changing from the B3LYP-optimised ^6A_g geometry to the B3LYP-optimised $^4B_{1g}$ geometry results in an increase in the value of δ(Mn-N) commensurate with the ρ_{bcp} data presented in Table 3.33.

3.4.8 Optically Active Excited States

Table 3.35 presents simulated vertical excitation energies, in eV, as predicted by TDDFT with the same five *xc*-functionals used previously for structure optimisation; BHLYP, PBE0, B3LYP, TPSSh & TPSS. Calculations were performed at the ^6A_g state geometry obtained with each functional. The fifth B_{2u}/B_{3u} transition (which are degenerate due to lowering of symmetry) has been assigned as the experimentally observed B band due to its large oscillator strength, particularly in comparison to those of the other transitions presented here.

Transition	BHLYP	PBE0	B3LYP	TPSSh	TPSS
$1\ ^6B_{2u}$	1.06 (0.000)	1.60 (0.000)	1.67 (0.000)	1.67 (0.000)	1.68 (0.001)
$2\ ^6B_{2u}$	2.11 (0.003)	2.04 (0.003)	2.00 (0.004)	1.99 (0.004)	1.95 (0.005)
$3\ ^6B_{2u}$	2.39 (0.012)	2.40 (0.001)	2.34 (0.002)	2.33 (0.000)	2.24 (0.001)
$4\ ^6B_{2u}$	3.45 (0.001)	3.24 (0.000)	3.18 (0.000)	3.04 (0.000)	2.85 (0.001)
$5\ ^6B_{2u}$	3.67 (2.172)	3.45 (1.674)	3.33 (1.434)	3.26 (1.124)	2.98 (0.515)

Table 3.35: TDDFT calculated excitation energies using a variety of different *xc*-functionals at DFT-optimised structures. Oscillator strengths given in parenthesis. All excitation values given in eV.

The experimentally determined B band absorption energy is 2.84 eV [123]. Although all *xc*-functionals overestimate the excitation energy, it can be seen that as the amount of HF exchange included in the *xc*-functional decreases so does the deviation from experiment. This is in contrast to what was found when DFT was used to predict the most stable spin state.

These TDDFT simulations reveal that the calculated B band absorption ($5\ ^6B_{2u}$) is composed of four main orbital transitions which are; α HOMO ($2\ a_u$) $\rightarrow$ α LUMO ($5\ b_{2g}/b_{3g}$), α HOMO-1 ($7\ b_{1u}$) $\rightarrow$ α LUMO, β HOMO $\rightarrow$ β 3 d_{xz} ($4\ b_{2g}$) and β HOMO-1 $\rightarrow$ β 3 d_{yz} ($4\ b_{3g}$).

As with the calculated B band absorption energy, there is also a dependence of the relative contributions of the two transitions involving the HOMO on the percentage of HF-exchange in the *xc*-functional, this is summarised in Table 3.36.

Functional	HF Exchange	GO2 $\alpha \rightarrow$ GO3 α	GO2 $\beta \rightarrow 3d_{xz}$ β
BHLYP	50	27.0	23.3
PBE0	25	22.9	18.6
B3LYP	20	21.7	17.2
TPSSh	10	18.9	15.1
TPSS	0	11.8	10.7

Table 3.36: Table to show changing percentage contributions to MnP B band excitation as calculated by TDDFT using five different *xc*-functionals.

The molecular orbitals involved in the B band transition when employing the BHLYP and TPSS *xc*-functionals (the two extremes in terms of HF-exchange considered here) are visualised in Figure 6. The BHLYP-calculated excitation involves only the four orbital transitions described above, however when using the TPSS *xc*-functional (and indeed for *xc*-functionals with 20% HF or less considered here) there is also a contribution from the transition between the β 5 b_{1u} and β 4 b_{3g} orbitals (6.1% for B3LYP, 11.6% for TPSSh and 12.0% for TPSS).

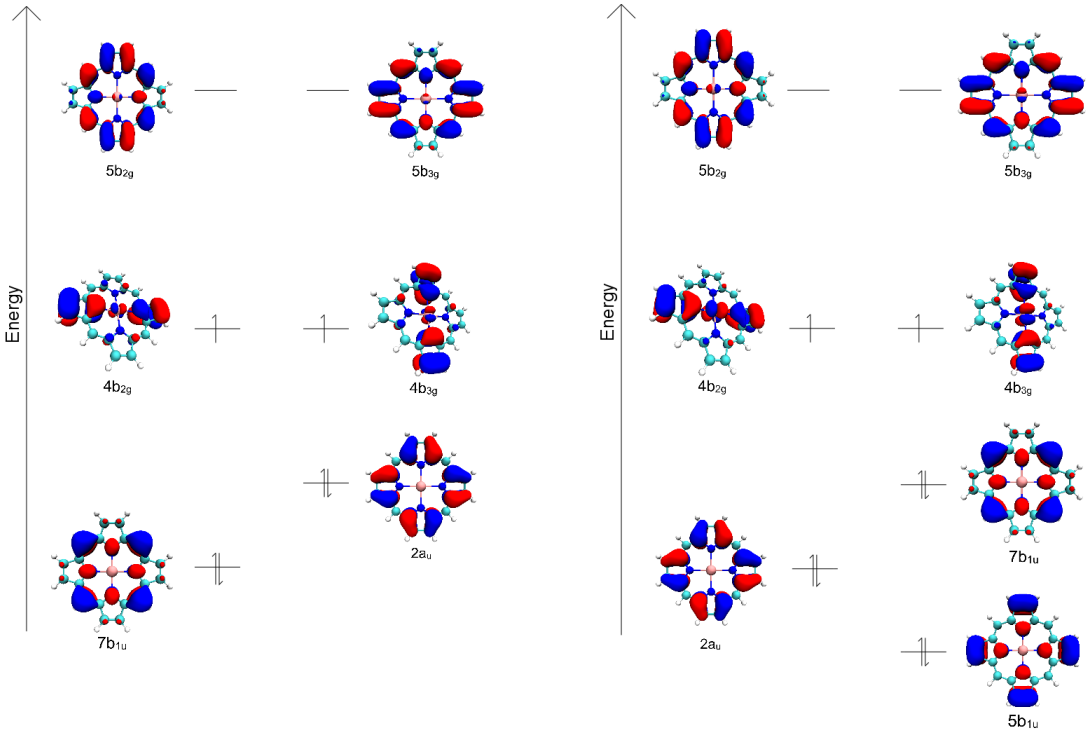

Figure 3.14: Orbitals involved in MnP B band excitation as simulated by TDDFT using the *xc*-functionals BHLYP (Left) and TPSS (Right).

Table 3.37 compares the TDDFT-calculated values of the B band absorption energies to those obtained using a variety of different active space; CASPT2(9/9), CASPT2(9/14), RASPT2(17,2,2;4,9,4), RASPT2(17,3,3;4,9,4), RASPT2(17,2,2;4,14,4), RASPT2(21,2,2;6,9,4), RASPT2(21,3,3;6,9,4) and RASPT2(21,2,2;6,9,6) simulations, with the experimental value.

Method	HF-Exchange (%)	Excitation Energy (eV)	Oscillator Strength
BHLYP	50	3.67	2.172
PBE0	25	3.45	1.674
B3LYP	20	3.33	1.434
TPSSh	10	3.26	1.124
TPSS	0	2.98	0.515
CASPT2(9/9)	100	4.16 (3.54)	1.711
CASPT2(9/14)	100	3.71 (3.33)	1.220
RASPT2(17,2,2;4,9,4)	100	3.71 (3.39)	1.687
RASPT2(17,3,3;4,9,4)	100	3.68 (3.41)	1.264
RASPT2(17,2,2;4,9,9)	100	3.99 (3.52)	1.503
RASPT2(21,2,2;6,9,4)	100	4.07 (3.84)	1.645
RASPT2(21,3,3;6,9,4)	100	4.07 (3.81)	1.548
RASPT2(21,2,2;6,9,6)	100	3.57 (3.36)	1.529
Experiment [123]	-	2.84	∼1.5

Table 3.37: Vertical Excitation Energies in eV of MnP B Band calculated by TDDFT with various *xc*-functionals and different CAS/RASPT2 active spaces. Values given in parenthesis for CAS/RASPT2 results are those obtained without the standard IPEA shift of 0.25 a.u.

It can be seen from Table 3.37 that the two CASPT2 simulations both overestimate the value of the B band absorption energy. This is not surprising considering the small number of orbitals from the ligand that are considered in these active spaces, although it should be noted that this overestimation is reduced upon removing the standard IPEA shift of 0.25 a.u., as previously found for free base porphyrin [59]. The larger RASPT2(21,2,2;6,9,4) simulation performs similarly despite the inclusion of six occupied and four unoccupied ligand orbitals, presumably due to the fact that only doubly excited configurations between RAS1 and RAS3 were included. It

should be noted that this RASPT2(21,2,2;6,9,4) was based upon a similar active space used for free base porphyrin, RASPT2(16,3,3;6,4,4), which performed relatively well in the calculation of excitation energies [88, 59].

Balancing the number of occupied and unoccupied orbitals (i.e. by setting the size of the RAS1 and RAS3 spaces to be equal) results in a similar, and improved, absorption energies. This suggests that there is a benefit to balancing the porphyrin active space with corresponding π and $\pi*$ orbitals.

Because the RASPT2(17,2,2;4,9,4) simulation contains fewer orbitals than the RASPT2(21,2,2;6,9,4) it is possible to consider triple excitations. It can be seen in Table 3.37 that including triple excitations rather than double between the RAS1 and RAS3 decreases the excitation energy by $\sim$0.03 eV, whilst removal of the IPEA shift from both double and triple excitations results in almost identical excitation energies.

Examination of the CAS/RASSCF natural orbital occupation numbers, which are shown in Table 3.38, reveals some very interesting behaviour in terms of the simulation of the B band.

CASSCF(9/9)				**CASSCF(9/14)**			
Orbital	^6A_g	$4\ ^6B_{3u}$	Δ Occ.	Orbital	^6A_g	$4\ ^6B_{3u}$	Δ Occ.
d_{z^2}	1.00	1.00	0.00	d_{z^2}	1.00	1.00	0.00
d_{xy}	1.00	1.96	+0.96	d_{xy}	1.00	1.96	+0.96
$d_{x^2-y^2}$	1.00	0.04	-0.96	$d_{x^2-y^2}$	1.00	0.03	-0.97
d_{xz}	1.00	1.00	0.00	d_{xz}	1.00	1.00	0.00
d_{yz}	1.00	1.00	0.00	d_{yz}	1.00	1.00	0.00
GO1	1.92	1.87	-0.05	GO1	1.93	1.86	-0.07
GO2	1.93	1.07	-0.86	GO2	1.92	1.08	-0.84
GO3	0.08	0.13	+0.05	GO3	0.08	0.14	+0.06
GO4	0.08	0.93	+0.85	GO4	0.08	0.92	+0.84
RASSCF(17,3,3;4,9,4)				**RASSCF(17,2,2;4,9,9)**			
Orbital	^6A_g	$4\ ^6B_{3u}$	Δ Occ.	Orbital	^6A_g	$4\ ^6B_{3u}$	Δ Occ.
d_{z^2}	1.00	1.00	0.00	d_{z^2}	1.00	1.00	0.00
d_{xy}	1.00	1.97	+0.97	d_{xy}	1.00	1.96	+0.96
$d_{x^2-y^2}$	1.00	0.03	-0.97	$d_{x^2-y^2}$	1.00	0.03	-0.97
d_{xz}	1.00	1.00	0.00	d_{xz}	1.00	1.00	0.00
d_{yz}	1.00	1.00	0.00	d_{yz}	1.00	1.00	0.00
GO1	1.91	1.89	-0.02	GO1	1.89	1.77	-0.12
GO2	1.90	1.02	-0.88	GO2	1.89	1.15	-0.74
GO3	0.11	0.12	+0.01	GO3	0.11	0.24	+0.13
GO4	0.09	0.98	+0.89	GO4	0.11	0.85	+0.74
RASSCF(21,3,3;6,9,4)				**RASSCF(21,2,2;6,9,6)**			
Orbital	^6A_g	$4\ ^6B_{3u}$	Δ Occ.	Orbital	^6A_g	$4\ ^6B_{3u}$	Δ Occ.
d_{z^2}	1.00	1.00	0.00	d_{z^2}	1.00	1.00	0.00
d_{xy}	1.00	1.96	+0.96	d_{xy}	1.00	1.97	+0.97
$d_{x^2-y^2}$	1.00	0.04	-0.96	$d_{x^2-y^2}$	1.00	0.03	-0.97
d_{xz}	1.00	1.00	0.00	d_{xz}	1.00	1.00	0.00
d_{yz}	1.00	1.00	0.00	d_{yz}	1.00	1.00	0.00
GO1	1.91	1.91	0.00	GO1	1.91	1.84	-0.07
GO2	1.90	1.03	-0.87	GO2	1.90	1.12	-0.78
GO3	0.12	0.12	0.00	GO3	0.10	0.17	+0.07
GO4	0.11	0.99	+0.88	GO4	0.11	0.90	+0.79

Table 3.38: Natural Orbital Occupation Numbers of the Ground State (^6A_g) and B band excited state ($5\ ^6B_{3u}$) as simulated by various active spaces and the change in occupation (ΔOcc) between the two states.

From the natural occupation numbers it appears that the excitation into the B band involves a lowering of the metal spin state from a sextet to a quartet, with the oxidation state remaining constant. In order to preserve the overall spin of the molecule there is a corresponding increase in the ligand spin from singlet to triplet, resulting in an overall sextet spin. Furthermore the excited state is a relatively singly configurational state, shown by the weightings in Table 3.39.

Active Space	Main Transitions	Weight (%)
CASSCF(9/9)	GO2 $\rightarrow d_{xy}$ $d_{x^2-y^2} \rightarrow$ GO4	85.7
CASSCF(9/14)	GO2 $\rightarrow d_{xy}$ $d_{x^2-y^2} \rightarrow$ GO4	79.1
RASSCF(17,3,3;4,9,4)	GO2 $\rightarrow d_{xy}$ $d_{x^2-y^2} \rightarrow$ GO4	76.8
RASSCF(17,3,3;4,9,9)	GO2 $\rightarrow d_{xy}$ $d_{x^2-y^2} \rightarrow$ GO4	69.0
RASSCF(21,3,3;6,9,4)	GO2 $\rightarrow d_{xy}$ $d_{x^2-y^2} \rightarrow$ GO4	82.2
RASSCF(21,2,2;6,9,6)	GO2 $\rightarrow d_{xy}$ $d_{x^2-y^2} \rightarrow$ GO4	74.0

Table 3.39: Main transition contribution and weighting for the various active spaces used in investigation of MnP.

As this appears to be a two electron process, according to CASSCF/RASSCF, this will not be modeled accurately by TDDFT as it is a linear response method, see section 2.3. Therefore excitation energies have also been simulated for the B band excitation using a ΔSCF method by calculating the DFT energy of the CAS/RASPT2-predicted B band configuration

(a d-occupation of $(d_{xy})^2$ $(d_{z^2})^2$ $(d_{xz})^2$ $(d_{yz})^2$ and a Gouterman occupation of $(GO1)^2$ $(GO2)^1$ $(GO3)^1$ $(GO4)^0$ and the sextet ground state (^6A_g). The energy difference between these two states are presented below in Table 3.40.

Functional	HF-Exchange (%)	TDDFT Excitation Energy	ΔSCF
BHLYP	50	3.67	2.81
PBE0	25	3.45	2.64
B3LYP	20	3.33	2.41
TPSSh	10	3.26	2.26
TPSS	0	2.98	2.01

Table 3.40: Vertical excitation energy of B band as calculated by TDDFT and ΔSCF using five different *xc*-functionals. All energies are given in eV.

Table 3.40 shows the same pattern as the TDDFT results in that decreasing the HF-exchange percentage decreases the energy of the excitation. Whereas the most accurate excitation energy predicted by TDDFT was obtained with the TPSS *xc*-functional, using this ΔSCF method the most accurate prediction was obtained with the BHLYP functional. Furthermore there is a fairly constant energy difference between the TDDFT excitation energy and the ΔSCF energy (0.86 - 1.00 eV).

Further weight is lent to the argument that the ΔSCF method is more accurate than TDDFT by visualisation of the density difference between the ground state and excited state in question, which is shown in Figure 3.15.

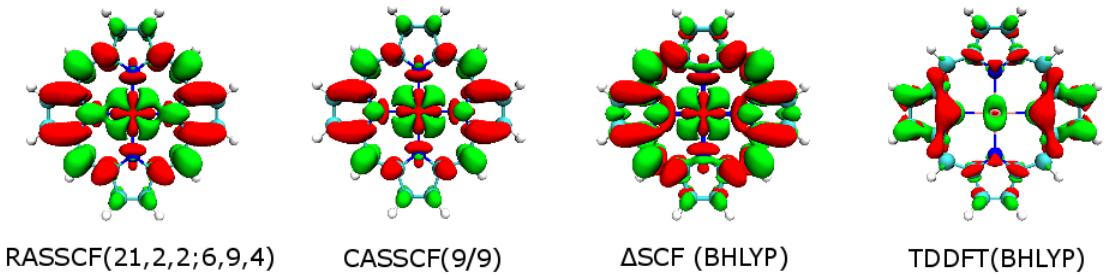

Figure 3.15: Density Difference Plots between Ground State and B band excitated state calculated using a variety of methods. Areas of green indicate gain of electron density from the ground state to excited state whilst red indicates loss of electron density.

It would appear from Figure 3.15 that TDDFT is modeling an entirely different state than CAS/RASSCF. From Figure 3.15 the fact that TPSS predicts a value close to the experimental value would appear to be more by accident than design.

3.4.9 Iron Porphyrin (FeP)

Iron Porphyrin (FeP), like MnP, is an important molecule in biological systems. FeP is the basic unit of haemoglobin in blood which is key to oxygen transport around the body.

There has been much debate over the electronic structure of Iron (II) porphyrin [refs], which contains six d-electrons and can have low (S=0), intermediate (S=1) or high spin (S=2). It is also well documented in the literature that addition of further ligands to FeP, both above and below the plane of the porphyrin ligand, can further influence the spin state [refs]. In this section focus has been on the planar Fe(II)P molecule with no further ligands complexed, so as to investigate the effect of just the metal and the porphyrin ring on the electronic structure, consistent with the work done in previous sections on other porphyrin molecules. As there are six d-electrons and numerous ways of filling the d-orbitals DFT geometry optimisations have been performed based upon the following rules:

- $d_{x^2-y^2}$ orbital (25 a_g) not to be doubly occupied
- $d_{x^2-y^2}$ orbital (25 a_g) only singly occupied if all other orbitals have been at least singly occupied first
- d_{xz} and d_{yz} orbitals (4 b_{2g} and 4 b_{3g}) to have same occupation, which enforces the degeneracy that would occur in D_{4h} symmetry

These rules have been applied so to reduce the number of configurations upon which to carry out geometry optimisations in an effort to reduce the total computational cost. The first rule is chemically significant because the $d_{x^2-y^2}$ in planar porphyrin systems is high in energy and therefore incredibly unlikely to be doubly occupied before the other metal d orbitals. Similarly the second rule is also chemically significant for the same reason. Finally the third rule is a result of the restrictions of the Molcas program which can only constrain to a symmetry of D_{2h} rather than D_{4h} - therefore geometry optimisations have been constrained to the same

symmetry for comparison purposes.

Applying these rules leaves six d-electron configurations to be investigated, two low spin states, two intermediate spin states and two high spin states. For convenience these d-electron configurations will be named; 1a, 1b, 3a, 3b, 5a and 5b, as shown in Table 3.41.

Name	2S+1	d_{z^2} (24 a_g)	$d_{x^2-y^2}$ (25 a_g)	d_{xy} (15 b_{1g})	d_{xz} (4 b_{2g})	d_{yz} (4 b_{3g})
1a	1	2	0	0	2	2
1b	1	0	0	2	2	2
3a	3	2	0	2	1	1
3b	3	1	0	1	2	2
5a	5	1	1	2	1	1
5b	5	2	1	1	1	1

Table 3.41: Naming of different FeP d-electron configurations investigated using DFT with a variety of different *xc*-functionals, numbers in the table correspond to number of electrons in orbital.

3.4.10 Computational Details

In the previous section on MnP (Section 3.4.2) it had been shown that DFT can produce wildly different results depending on the *xc*-functional used. Therefore this study on FeP has also been investigated with DFT using five different *xc*-functionals.

DFT structural optimisations were performed using version 6.6 of the Turbomole program [67] employing the Ahlrichs-style basis sets of polarised triple-zeta quality (def2-TZVP). Five different exchange correlation *xc*-functionals were used, the hybrid *xc*-functionals; BHLYP

[91, 35, 38], PBE0 [86], B3LYP [91, 35, 92], TPSSh [93, 94] which contain 50%, 25%, 20% and 10% components of exact Hartree Fock (HF) exchange respectively. The meta generalised gradient approximation (meta-GGA) pure xc-functional TPSS [37] was also considered. Optimisations were performed on the six d-electron configurations outlined in Table 3.41.

Although FeP has D_{4h} symmetry, DFT optimisations were constrained to the lower D_{2h} point group for consistency with subsequent CAS/RASSCF calculations, which were performed using version 8.0 of the Molcas software package.

CAS/RASSCF calculations employed the relativistically contracted atomic natural orbital (ANO-RCC) basis sets [70] of polarised triple-zeta quality on DFT-optimised structures. Scalar relativistic effects, although expected to be small, were included via use of the 2nd order Douglas-Kroll-Hess Hamiltonian [71]. Second order perturbation theory (PT2) calculations were performed on the CAS/RASSCF converged wavefunctions in order to incorporate dynamical correlation effects. In these PT2 calculations an imaginary level shift of 0.2 a.u. was included in order to reduce the effect of intruder states.

CASSCF calculations were performed using an active space which incorporated the four Gouterman orbitals (labelled as GO1-4 in accordance with previous sections) as well as the transition metal d-orbitals to form a 10 electron, 9 orbital, denoted as (10/9), active space. The molecular orbitals included in the CAS span the 24-25 a_g, 4-5 b_{2g}, 15 b_{1g}, 4-5 b_{3g}, 2 a_u and 7 b_{1u} irreps and are shown in Figure 3.16. It should be noted that this CAS(10/9) active space is a very minimal active space and so realistically only qualitative and not quantitative conclusions can be reached.

RASSCF calculations were also performed using a larger active space which included the orbitals defined above in the RAS2, but additionally included six orbitals in the RAS1 and four orbitals in the RAS3, based upon an active space developed by Roos and coworkers [88, 59] to describe

Free Base Porphyrin and previously used in calculation in Sections 3.2.1, 3.3.3 and 3.3.8 on FBP, MgP, ZnP and MnP. The RASSCF active space will use the standard notation $(n, l, m; i, j, k)$, where n is the number of electrons, l and m are the number of excitations permitted from/to the RAS1/RAS3 respectively and i, j and k are the number of orbitals in RAS1, RAS2 and RAS3 respectively. Our active space is therefore RAS(22,2,2;6,9,4). The molecular orbitals in the RAS1, RAS2 and RAS3 are also shown in Figure 3.16 and span the 24-25 a_g, 2-6 b_{2g}, 15 b_{1g}, 2-6 b_{3g}, 2-3 a_u, 5-8 b_{1u} irreps.

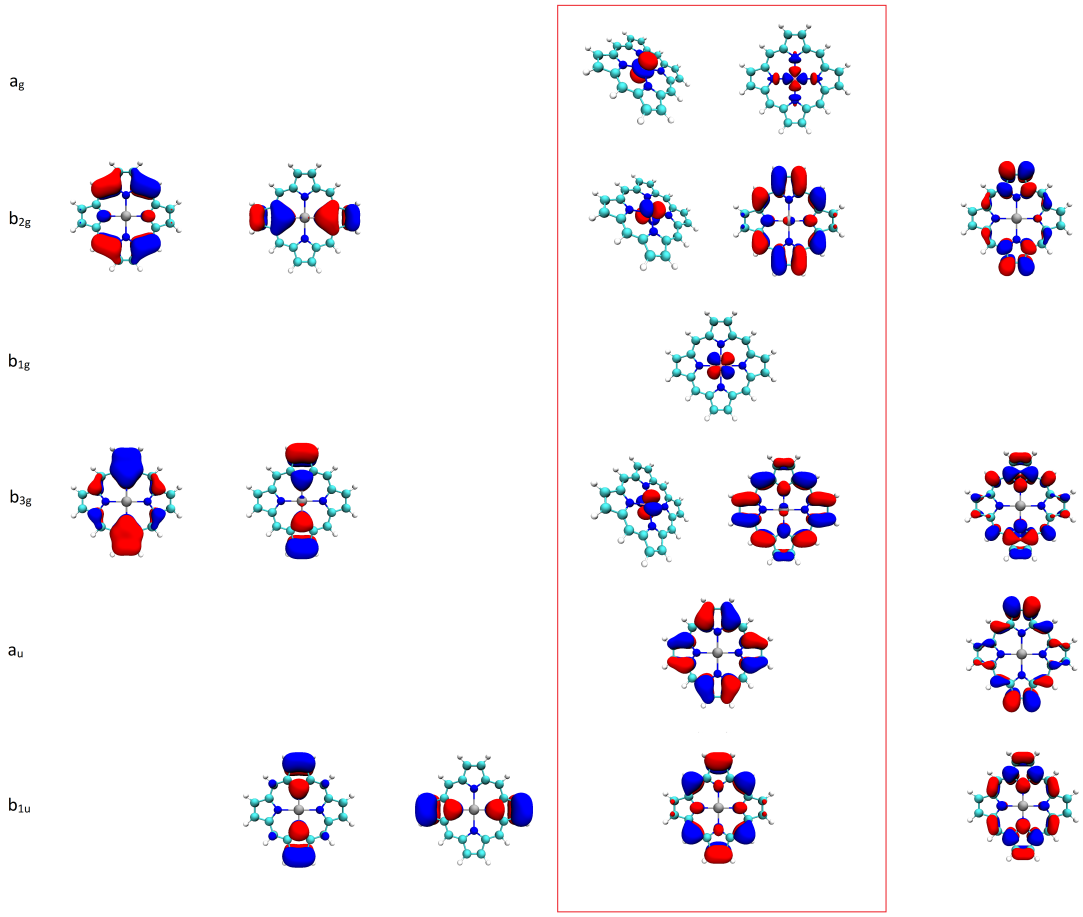

Figure 3.16: Natural orbitals included in FeP active spaces. Red box indicates molecular orbitals included in RAS2/CAS. All orbitals generated from RAS(22,2,2;6,9,4) active space with an isosurface of 0.03 a.u.

3.4.11 Structure Optimisation

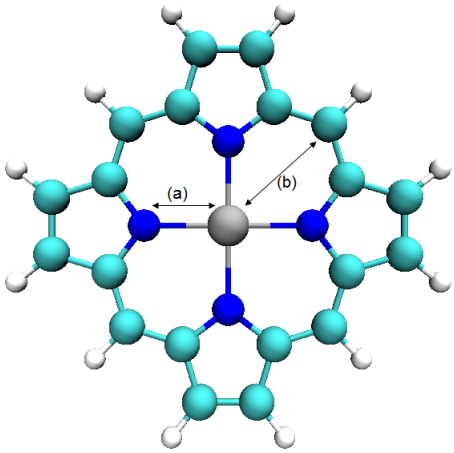

Figure 3.17: Key Coordinates in FeP (a) Fe-N and (b) Fe-C(Methyne).

Table 3.42 gives the details of two key coordinates in FeP, the Fe-N bond distance and the Fe-C (Methyne) distance ((a) and (b) respectively in Figure 3.17) calculated for the various electronic states with a range of *xc*-functionals and compared to experimental values.

Bond	State	1a	1b	3a	3b	5a	5b
Fe-N	BHLYP	1.990	2.004	2.000	2.002	2.056	2.055
	PBE0	1.977	1.990	1.990	1.989	2.052	2.053
	B3LYP	1.990	2.005	2.003	2.002	2.064	2.063
	TPSSh	1.975	1.991	1.992	1.989	2.055	2.055
	TPSS	1.974	1.991	1.991	1.990	2.056	2.057
	Exp	1.981-2.001 [124]		1.972 [125]		2.057 [126]	
Fe-C	BHLYP	3.386	3.390	3.390	3.389	3.406	3.406
	PBE0	3.396	3.399	3.400	3.399	3.417	3.417
	B3LYP	3.409	3.413	3.414	3.413	3.431	3.430
	TPSSh	3.408	3.411	3.412	3.411	3.430	3.430
	TPSS	3.417	3.421	3.422	3.422	3.440	3.439
	Exp	-		-		3.435-3.460 [126]	

Table 3.42: DFT-optimised bond lengths of key co-ordinates indicated in Figure 3.17 using five different *xc*-functionals along with experimentally determined bond lengths. All values given in Angstoms (Å). Naming convention as per Table 3.41.

Table 3.42 shows consistent results between the different *xc*-functionals at the same spin state, with a maximum range of 0.015 Å for the Fe-N bond. Comparing between the different spin states it can be seen that the Fe-N bond length of the quintet states is larger than for the triplet or singlet states. This is a trend that was also seen in MnP in the previous section, where occupation of the high energy and anti-bonding $d_{x^2-y^2}$ orbital results in a larger bond length. The triplet states have very similar bond lengths to the 1b singlet state (within 0.004 Å of each other). Comparing the results obtained with the various *xc*-functionals to the experimentally determined Fe-N bond length it can be seen that all *xc*-functionals reproduce the Fe-N bond lengths within 0.02 Å, with bond lengths reproduced particularly well, < 0.01 Å, for the quintet states.

Unlike DFT geometry optimisation calculations performed on other porphyrin molecules in previous sections there does not appear to be a functional dependence on the value of the predicted Fe-N bond length. However there is a pattern for the predicted value of the Fe-C bond which shows an increased value as the percentage of Hartree Fock exchange included in the functional decreases.

3.4.12 Analysis of Ground State Electronic Structure

It was shown in Section 3.4.2 that the predicted relative energy states of MnP are dependent on the method used. Relative energy of different electron states have been investigated for FeP using DFT and CAS/RASPT2 and the results are presented in Table 3.43. Spin state 3a has been selected as the reference energy ground state as the intermediate spin state is that most commonly reported to the be the ground state in the literature for numerous FeP complexes. Table 3.43 shows that, like for MnP, the predicted most stable spin state is dependent on the method used. Use of the BHLYP xc-functional, containing the highest percentage of HF-exchange, favours the 5b d-orbital occupation whilst the TPSS xc-functional favours the 3a d-orbital occupation. Unlike the MnP results presented in the previous section out of the five $xc-$functionals investigated, only the BHLYP functional predicts relative energies that are similar to those obtained from the higher level CAS/RASPT2 calculations. This can perhaps be rationalised by considering the stability afforded by including more exact exchange in the functional. The high spin state of MnP has five unpaired electrons (a half full shell) compared to the to the four unpaired electrons in the high spin state of FeP, therefore the energy of exchanging electrons in FeP is higher as not every exchange of pairs of electrons are equal considering that there is a doubly occupied metal orbital.

In terms of d-orbital occupations the only difference between the 3a and 5b electron configurations is that in the 5b electron configuration both the $d_{x^2-y^2}$ and d_{xy} orbitals are singly

Method	HF-Exchange (%)	1a	1b	3a	3b	5a	5b
TPSS	0	3.94	1.40	0.00	0.29	1.11	0.73
TPSSh	10	4.28	1.45	0.00	0.39	0.84	0.48
B3LYP	20	4.26	1.49	0.00	0.48	0.66	0.24
PBE0	25	4.41	1.57	0.00	0.44	0.39	0.04
BHLYP	50	5.05	1.50	0.00	0.65	0.05	-0.34
CASPT2(10/9)*	100	-	1.35	0.00	0.54	-0.28	-0.58
CASPT2(10/9)‡	100	-	1.36	0.00	0.43	-1.75	-0.91
CASPT2(10/14)*	100	-	-	0.00	0.52	-0.21	-0.56
RASPT2(22,2,2;6,9,4)*	100	-	-	0.00	0.51	0.04	-0.43
RASPT2(22,2,2;6,9,4)‡	100	-	-	0.00	0.45	-0.47	-0.94

Table 3.43: Relative energies of low (1a and 1b), intermediate (3a and 3b) and high spin (5a and 5b) states using DFT (five different $xc-$functionals) and CAS/RASPT2. * indicates DFT (B3LYP/def2-TZVP)-optimised 3a geometry ‡ indicates DFT (B3LYP/def2-TZVP)-optimised 5b geometry. All energies given in eV. Naming convention as per Table 3.41.

occupied whereas in the 3a electron configuration d_{xy} is doubly occupied and $d_{x^2-y^2}$ is unoccupied. This again is very similar to what was seen for MnP where xc-functionals which contain higher percentages of HF-exchange favourably occupy the high energy $d_{x^2-y^2}$ orbital over pairing electrons in the d_{xy} orbital.

Looking at the CAS/RASPT2 results all of the active spaces predict that the lowest energy configuration has high spin. Whether the most stable spin state is 5a or 5b depends on the geometry used for the CAS/RASSCF calculation, when the geometry is high spin the most stable spin state is 5b whilst if an intermediate spin state geometry is used the most stable spin state is 5a.

All of the methods; all DFT $xc-$functionals and all CAS/RASSCF active spaces, agree that the low spin states (1a and 1b) are much higher in energy than any of the intermediate or high spin states. In fact the 1a spin state was not among the lowest 10 roots of symmetry A_g for any of the CAS/RASSCF active spaces. Therefore in the subsequent discussion the low spin states have been omitted.

Orbital	CASSCF(10/9)				RASSCF (22,2,2;6,9,4)			
	3a	3b	5a	5b	3a	3b	5a	5b
d_{z^2}	1.96	1.00	1.00	2.00	1.96	1.00	1.00	2.00
$d_{x^2-y^2}$	0.06	0.17	1.00	1.00	0.06	0.16	1.00	1.00
d_{xy}	1.98	1.13	2.00	1.00	1.98	1.12	2.00	1.00
d_{yz}	1.00	1.85	1.00	1.00	1.00	1.86	1.00	1.00
d_{xz}	1.00	1.85	1.00	1.00	1.00	1.86	1.00	1.00
GO1	1.91	1.91	1.91	1.91	1.89	1.90	1.89	1.89
GO2	1.93	1.94	1.93	1.93	1.91	1.91	1.91	1.91
GO3	0.08	0.07	0.08	0.08	0.11	0.11	0.12	0.12
GO4	0.08	0.07	0.08	0.08	0.11	0.11	0.11	0.11

Table 3.44: Natural orbital occupation numbers of different FeP electron configurations at 5b DFT-optimised structure (B3LYP/def2-TZVP) using the CASSCF(10/9) and RASSCF(22,2,2;6,9,4) active spaces. GO1-4 refer to the Gouterman Orbitals as described in previous sections.

Table 3.44 shows the natural orbital occupation numbers of FeP for the 3a, 3b, 5a and 5b electron configurations calculated using the CAS(10/9) and RAS(22,2,2;6,9,4) active spaces. It can be seen in the table that there is effectively no difference between the natural orbital occupations of the Fe d-orbitals between the two different active spaces for the same electron configuration. There is a more pronounced difference, however, between the natural orbital occupations of the Gouterman orbitals between the two active spaces at the same electron configuration, although this difference is relatively small. Furthermore this difference in the natural orbital occupation of the Gouterman orbitals between the CASSCF and RASSCF active spaces is in line with the pattern seen for MnP, see Section 3.4.5.

If the natural orbital occupations of the Fe d-orbitals are now compared for the different d-electron configurations it can be seen that both the high spin electron configurations (5a and

5b) show no multiconfigurational character between the d-electrons, indicated by the d-orbitals having occupations of 1.00 or 2.00. This is not the case for the intermediate spin states (3a and 3b), particularly the 3b spin state. The consequence of this is that the relative energies of the different electron configurations presented above in Table 3.43 calculated with DFT may be untrustworthy for the intermediate spin states as DFT, as defined by its methodology, is a single configurational method.

3.4.13 QTAIM analysis

As with other Porphyrin systems investigated in this chapter, the QTAIM methodology has been applied to the different spin states of FeP to further characterise the Fe-N bond.

Method	3a	3b	5a	5b
BHLYP	0.088	0.088	0.080	0.084
PBE0	0.092	0.091	0.082	0.086
B3LYP	0.089	0.089	0.079	0.084
TPSSh	0.091	0.092	0.081	0.085
TPSS	0.092	0.093	0.081	0.085
CASSCF(10/9)*	0.082	0.080	0.088	0.091
RASSCF(22,2,2;6,9,4)*	0.083	0.080	0.088	0.091
CASSCF(10/9)‡	0.072	0.070	0.086	0.080
RASSCF(22,2,2;6,9,4)‡	0.072	0.070	0.081	0.079

Table 3.45: Value of the electron density (ρ) at the BCP of Fe-N (ρ_{BCP}(Fe-N)) bond at DFT-optimised geometry * indicates all spin states calculated at constant 3a B3LYP/def2-TZVP geometry ‡ indicates all spin states calculated at constant 5b B3LYP/def2-TZVP optimised geometry.

The data presented in Table 3.45 shows the value of the electron density at the BCP (ρ_{BCP}) of

the Fe-N bond. It can be seen in Table 3.45 that for each respective DFT xc-functional the value of ρ_{BCP} is higher for the triplet state than it is for the quintet state. However this is almost certainly because the quintet states have a significantly longer Fe-N bond length than the triplet states do, as seen in Table 3.42. This conclusion is further supported by the CAS/RASSCF QTAIM data, where the geometry is kept constant, which shows a higher value for the quintet states than the triplet states. This in keeping with what was observed for MnP, and is because of the occupation of the $d_{x^2-y^2}$ orbital in the higher spin state, whose orbital lobes lie in the plane of the Fe-N bond.

If comparisons between the CASSCF and RASSCF QTAIM data are now made it can be seen that at the same geometry there is no difference in the value of ρ_{BCP}, with the exception of spin state 5a where there is a difference at the quintet geometry of 0.005 a.u. or in percentage terms of 6%. It can also be seen in Table 3.45 that there is little variation between the value of ρ_{BCP} for the same spin state between the different DFT xc-functionals.

Method	3a	3b	5a	5b
BHLYP	0.522	0.521	0.442	0.421
PBE0	0.584	0.589	0.482	0.458
B3LYP	0.583	0.591	0.487	0.465
TPSSh	0.604	0.614	0.500	0.477
TPSS	0.631	0.637	0.523	0.498
CASPT2(10/9)*	0.809	0.781	0.741	0.695
RASPT2(22,2,2;6,9,4)*	0.813	0.790	0.745	0.702
CASPT2(10/9)‡	0.754	0.736	0.705	0.646
RASPT2(22,2,2;6,9,4)‡	0.756	0.736	0.695	0.660

Table 3.46: Delocalisation indices of Fe-N Bond (δ(Fe-N)) at DFT-optimised geometry * indicates all spin states calculated at constant 3a B3LYP/def2-TZVP optimised geometry ‡ indicates all spin states calculated at constant 5b B3LYP/def2-TZVP optimised geometry.

Looking now at the data in Table 3.46 which shows the value of the delocalisation index of the Fe-N bond (δ(Fe-N)) it can be seen that like with the values of ρ_{BCP} in Table 3.45, Table 3.46 shows a higher value for δ(Fe-N) for the triplet states than the quintet states. Again this can be attributed to the longer Fe-N bond length of the quintet states over the triplet states.

Comparing the values of δ(Fe-N) between the CASSCF and RASSCF QTAIM data it can again, like the values of ρ_{BCP}, be seen that there is very little difference in the values, if any.

However unlike the ρ_{BCP} data it can be seen that there is a significant difference between the different *xc*-functionals, although a general trend can be observed that as the degree of HF-exchange that is included in the *xc*-functional is decreased the value of δ(Fe-N) is increased. It is also very clear that the values of δ(Fe-N) as calculated by the various *xc*-functionals are significantly lower than those calculated with CASSCF or RASSCF. This indicates that

CAS/RASSCF predicts a greater degree of electron sharing between the Fe and N atoms than DFT does.

3.5 Conclusions

In this extensive work on various porphyrin systems the limitations of TDDFT have been highlighted and the potential uses of the CAS/RASSCF methodology to these systems demonstrated. It has been shown that whilst DFT predicts accurate structures when compared to experiment regardless of the $xc-$functional used, its excited state derivative struggles in systems where there is a great deal of multiconfigurational behaviour.

Gouterman's work on free base porphyrins which concluded that the main electronic transitions of porphyrins are between the HOMO, HOMO-1, LUMO and LUMO+1 has been shown by the CAS/RASSCF work in this section to be correct. However the CAS/RASSCF results have also shown that this is ultimately too simplistic a model for molecules with such a complex, conjugated π systems. This is shown by the fact that expanding the active space from one which contains just the Gouterman orbitals to an active space which contains more orbitals from the conjugated π system results in a more accurate prediction of the excitation energies of FBP. Furthermore it has been shown that accurate predictions with a lower computational cost can be obtained after truncating the CI wavefunction, the result of restricting the active space i.e. going from CASSCF to RASSCF.

When this work, and more importantly these active spaces, are used for modeling metal porphryin systems it again is seen that the (4/4) active space is too simplistic and extending the active space to include more orbitals from the π system results in more accurate excitation energies. The regular porphyrins investigated here, whose active spaces were almost identical to those used for FBP, have shown very similar results to FBP in that truncating the CI wavefunction, moving from a complete active space to a restricted active space has little effect if the

appropriate number of excitations are permitted in the truncated active space.

In this work these active spaces have also been applied to irregular porphyrins, open shell systems. This work has shown that whilst TDDFT can sometimes provide excitation energies which are close to experiment this can be dependent on the functional chosen and even then its accuracy is partly down to luck. In the particular case of manganese poprhyrin it was shown that DFT with different $xc-$functionals predicts different ground spin states, with a clear correlation between the degree of exact Hartree Fock exchange included in the functional and the most stable spin state. This ambiguity is removed when the CAS/RASSCF methodology is used, even with the most minimal of active spaces. A similar observation has been made for iron porphyrin, where again DFT predicts a different ground state depending on the functional used.

However it has also been seen that whilst the CAS/RASSCF methodology provides a qualitatively correct description of the electronic structure and excited states it is not always a quantitatively correct result. Ultimately the metal d orbitals are too similar in energy to the poprhyrin π system and so require more orbitals to be included in the active space to correlate them correctly, as suggested by Bjorn's rules. Unfortunately computer processors have not advanced to the point where it is viable to include more orbitals in the active space to correlate the metal d-orbitals.

In the next section attention is turned to the heavier actinide and lanthanide complexes whose metal valence orbitals are widely accepted in the literature to not be involved in bonding. Attempts will be made to apply the same principles that have been applied here to d-block complexes.

Chapter 4

Actinide and Lanthanide Simulations

4.1 Overview

Actinide and lanthanide elements are collectively known as the 'f-block' elements and are situated in a modern day periodic table off from the rest of the elements. The lanthanides include all elements from cerium (Ce) to lutetium (Lu) whilst the actinides include thorium (Th) to lawrencium (Lr). The parent atoms, lanthanum (La) and actinium (Ac), after which the two series of the f-block elements are named, are strictly speaking group III elements, however are often also discussed as part of the chemistry of the f-block elements [17].

Computational simulations of the f-block elements and their compounds poses many interesting problems. The first of these is that f-block elements have considerable mass and therefore the effects of relativity, both on physical and electronic properties, must be considered. Eqn 4.1 displays the effect of relativity on the mass of a particle which has resting mass, m_0, and is traveling at velocity, v.

$$m = \frac{m_0}{\sqrt{1 - (v/c)^2}} \tag{4.1}$$

The radial velocity, $< v_{rad} >$, for an electron in the 1s orbital can be approximately equated to the atomic charge, Z, this is shown in Eqn 4.2 [17]. The effect of relativity can therefore be approximated as $\frac{Z}{137}$ (137 being the speed of light, c, in atomic units). This means that there is a relativistic mass increase of 1.10 for Ce to 1.17 for Lu and 1.33 for Th to 1.52 for Lr of an electron in the 1s orbital [17].

$$\frac{< v_{rad} >}{c} \approx \frac{Z}{137} \tag{4.2}$$

The result of this relativistic mass increase is a contraction and stabilisation of the s and p orbitals, an effect known as the *direct relativistic orbital contraction*. However the opposite is true for the d and f orbitals which relativistically expand and destabilise in comparison to that which would be expected of their non-relativistic counterparts, this is known as the *indirect relativistic orbital expansion*. The result of the combination of these effects is the lanthanide contraction which occurs because of the poor shielding of the 4f electrons of the nuclear charge, drawing in the 6s electrons.

The expansion of the f orbitals plays a huge role in explaining the chemistry of the f block elements and particularly in explaining the differences between the actinides and lanthanides. The actinide's 5f orbitals are more affected by relativity, due to their larger mass, than the lanthanide's 4f orbitals, as a result the 5f actinide orbitals bind more weakly than the corresponding 4f lanthanides orbitals meaning that they are more chemically active. This explains why the actinides (in general) take on a greater number of oxidation states than the lanthanides, as the lanthanide 4f orbitals are often considered to be core like. In addition the greater availability of the actinide 5f orbitals means that they typically participate more in bonding than the lathanide 4f orbitals, resulting in the formation of more covalent bonds in actinide complexes than in lanthanide complexes.

Furthermore, partly as a result of relativity, the lanthanide and actinide compounds present

a great deal of multiconfigurational character due to significant dynamic electron correlation. The problem of multiconfigurational behaviour in computational simulations has already been discussed in Chapter 2.4. The result of these effects is a highly complicated electronic structure which can be difficult to comprehend and deal with when using lower level theoretical methods.

4.2 Applications of Lanthanide and Actinides

Complexes of lanthanides have many useful applications; one of the main and most prominent applications is their use as contrast agents in magnetic resonance imaging of which gadolinium complexes have been commonly reported in the literature for this purpose [127, 128, 129]. Lanthanide complexes' interesting optical properties as well as their magnetic properties are exploited when used in magnetic resonance imaging. Gadolinium for example is paramagnetic and although the Gd ion is toxic it forms strong ionic bonds to chelating ligands with a high co-ordination number and so can be safely used inside the human body. The magnetic properties of lanthanides have been further exploited to create energy efficient lighting components [130], parts in hybrid electric cars [131, 65] and in rechargeable batteries [132, 133]. The oxide of Cerium, Ceria, has been widely used for catalysis because of the equilibrium that it exists in between the (III) and (IV) oxidation state.

The application of actinide complexes is heavily dominated by uranium, which is the main fuel source in nuclear fission in nuclear power plants. The fission of uranium in nuclear power plants leads to the formation of other actinides, particularly plutonium. Separation of plutonium from uranium in nuclear waste has proved to be a difficult challenge due to their similar chemical properties. Plutonium has also found uses in pacemakers and a fuel source in deep space probes [134].

This chapter focuses on the two lanthanide and actinide projects that have been completed, which are a study of the covalency in Ce and U hexachlorides and a theoretical investigation

of low valent actinide and lanthanide complexes. In both these investigations the bonding and question of covalency in lanthanide and actinide complexes will be discussed. Section 4.3 below gives a brief overview of publications where covalency in lanthanide and actinide complexes has been discussed.

4.3 Summary of previous works investigating bonding in actinide and lanthanide complexes

It has long been accepted in the literature that the actinide f-orbitals are more available for bonding than the lanthanide f-orbitals. This is a result of the short radial distribution function of the 4f orbitals which can be seen in Figure 4.1. The consequence of this is that it has been considered that actinide complexes form more covalent bonds than lanthanide complexes do [7, **?**, 135, 136, 137, 138, 139, 140, 141].

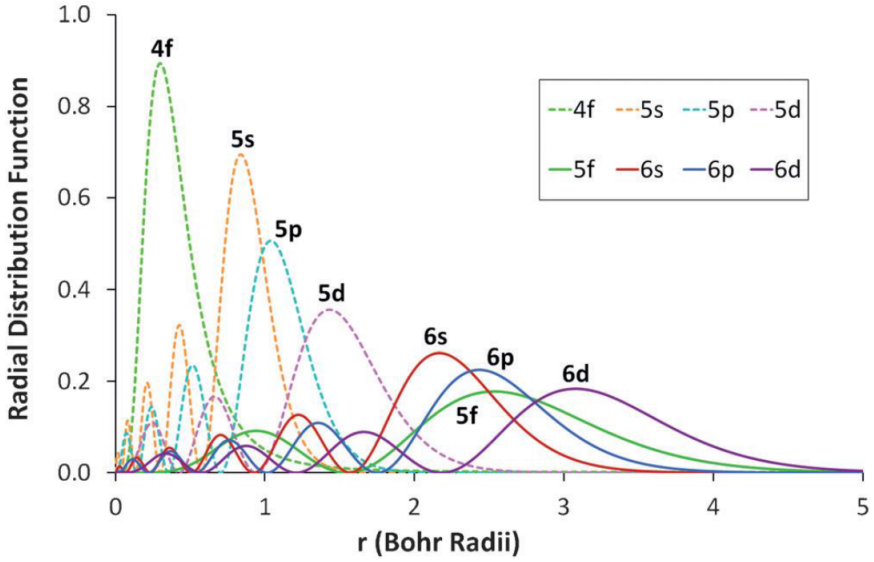

Figure 4.1: Radial distribution function of actinide and lanthanide frontier orbitals. Adapted from [7].

The covalency of f-element complexes was debated by Martin *et al* in their 2013 paper. They concluded from their K-edge X-ray absorption spectroscopy (XAS) studies that typically higher oxidation states of the actinides form more covalent bonds, particularly the lighter actinides [138]. In terms of bonding they concluded that the covalent interactions of actinide complexes comes as a result of donation from ligand lone pairs into the empty 6d orbitals with minimal contribution from the 5f orbitals. However they also claim that the contribution from the 5f orbitals to covalency does increase for heavier actinides. This shows, as claimed by Martin *et al*, that there are two kinds of covalency in f-element complexes, firstly covalency from the ligand donating into the 6d orbitals and secondly covalency from donation from the 5f orbitals.

Two studies from Kaltsoyannis on actinide triscyclopentadiene complexes also revealed interesting duality in covalency across the actinide series [**?**, 137]. In both studies computational results revealed, by means of density examination using the Quantum Theory of Atoms in Molecules (QTAIM) methodology, that for the early actinides (Th, Pa and U) that there is a relatively consistent degree of covalency, which then begins to decrease for heavier actinides. However examination of molecular orbital compositions and atomic populations suggests the opposite, that covalency increases along the actinide series.

A CASSCF study completed by Kerridge in 2013 on Ce, Th and Pu metallocenes ($MCOT_2$, COT = η^8-C_8H_8) revealed, with the aid of the QTAIM methodology, that there is greater degree of covalency, as evidenced by the ρ_{BCP}(M-C) and δ(M-C) data, in $ThCOT_2$ than $CeCOT_2$, however only by roughly 5% [65]. It was also shown that $PuCOT_2$ displays more covalency than either the thorium or cerium complex as determined by QTAIM indicators. A second CASSCF study completed by Kerridge in 2014 on seven actinocenes ($AnCOT_2$) showed that there was stong multiconfigurational character in these complexes, which the author suggested means that orbital-based analysis of covalency are unreliable [139]. Therefore to aid the discussion of covalency the QTAIM methodology was also employed here, which revealed the trend that

there is greater covalency in the earlier actinides with the exception of the thorium complex. The author suggests is a result of an empty 5f shell in the tetravalent oxidation state. The author concludes that this indicates that the origin of covalency in these complexes is from 5f contributions [65].

A ground breaking paper by Kozimor *et al*, published in 2015, was perhaps one of the first experimental papers to demonstrate that levels of covalency in some f-block complexes is comparable between the lanthanides and actinides [14]. In their paper they published the results of a K-edge X-ray Absorption Near Edge Spectroscopy (XANES) of Ce and U hexachlorides (among other lanthanide complexes) which showed mixing of the Ce 4f orbitals with the Cl 3p. Furthermore they observed that increasing the oxidation state from (III) to (IV) resulted in increased mixing of the Ce 4f orbitals with the Cl 3p. Kozimor *et al* also reported that the degree of Ce 4f mixing with the Cl 3p orbitals was higher than the mixing of U 5f with Cl 3p, which they attribute to the lower energy mismatch of Ce 4f orbitals with Cl 3p orbitals.

It is this paper by Kozimor where attention is focused for the first study of this Chapter, with an investigation of covalency in cerium and uranium hexachlorides.

4.4 Covalency in Ce and U Hexachlorides

4.4.1 Introduction

As has been discussed in the literature summary above, due to the contracted and core-like nature of the f-orbitals it has long been considered that the bonding in lanthanide and actinide complexes is almost completely ionic [7, **?**, 135, 137, 138, 139, 140, 141]. Furthermore whilst it has also been accepted that although both are predominantly ionic, the degree of covalency is larger in actinide complexes than lanthanide as a result of poorer shielding from the 4f-orbitals of the lanthanides compared with that of the 5f-orbitals in actinides [17]. However recently advanced experimental techniques such as X-ray Absorption Near Edge Spectroscopy (XANES)

has shown that this is not completely true. Kozimor *et al* have shown that although bonding is predominantly ionic there is a non-zero and significant degree of covalency in some lanthanide and actinide complexes, such as their hexachlorides [14].

Complexes of f-elements, due to their relatively large mass, display strong relativistic effects and significant static and dynamical electron correlation and therefore ideally requires a high level computational method to model, such as CAS/RASSCF.

4.4.2 Computational Details

Quantum chemical simulations were performed using version 7.6 of the Molcas code, employing the relativistically contracted atomic natural orbital (ANO-RCC) basis sets of polarised triple-zeta quality (TZVP) [70]; (26s23p17d13f5g3h)/[9s8p6d4f2g] for U, (25s22p15d11f4g2h)/[8s7p4d3f2g] for Ce and (17s12p5d4f2g)/[5s4p2d] for Cl. Scalar relativistic effects were included with the use of the 2nd order Douglas-Kroll-Hess Hamiltonian, whilst computational time decreased by using the Cholesky decomposition.

CAS/RASSCF calculations were performed using two different active spaces, a large RASSCF active space and a smaller CASSCF active space (Figure 4.2). The large RASSCF active space included the eighteen Cl valence 2p orbitals in the RAS1, seven Ce/U 4/5f orbitals in the RAS2 and five Ce/U 5/6d orbitals in the RAS3 based upon the active space employed by Pierloot and co-workers [142]. By definition all configurations within the RAS2 subspace were allowed in the CI expansion of the wavefunction, whilst only double excitations were permitted from (to) RAS1 (RAS3). This active space is therefore denoted (36+n,2,2;18,7,5) (where n ranges from 0 to 3 based upon the number of f electrons in the system).

The second, smaller CASSCF active space was utilised to investigate the effects of truncation of the wavefunction implicit in the RASSCF methodology. This CASSCF active space originally

included the 4/5f orbitals and the linear combination of Cl 2p orbtials which contribute to σ and δ bonding in addition to the one non-bonding f-orbital. However it was found that for the lower oxidation state complexes of Ce and U it became impossible to stabilise such an active space and was therefore enlarged to incorporate three additional orbitals which led to comparable active spaces between systems. This resulted in a CASSCF (18+n,16) where again n ranges from 0 to 3 and is dependent on the number of f electrons in the system.

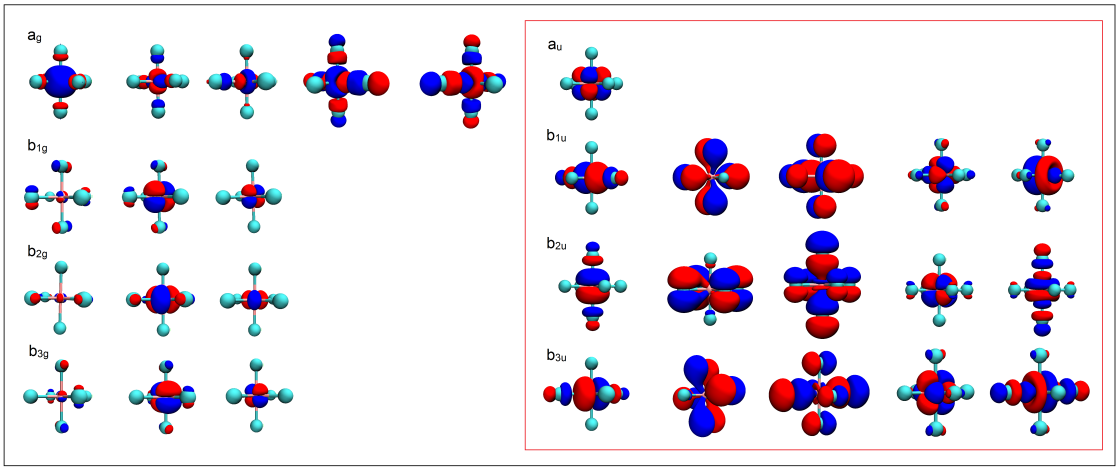

Figure 4.2: Orbitals included in RASSCF (black box) and CASSCF (red box) active spaces in calculations of MCl_6. Orbital generated at an isosurface of 0.02 a.u.

The effects of dynamic correlation were included via the addition of second order pertubation theory (PT2) to all converged CASSCF/RASSCF wavefunctions. An imaginary level shift of 0.2 a.u. was added to avoid the effects of intruder states [57, 58]. All pertubative calculations also were completed with the standard IPEA (Ionisation Potential and Electron Affinity) shift of 0.25 a.u.

The high symmetry of these molecules, in addition to them containing only seven atoms, means that it is possible to optimise their structures at a high level of theory using a numerical method of completing a series of single point calculations whilst stretching the Ce/U-Cl bond in all di-

rections. The RASSCF active space was used for the geometry optimisation of the six complexes both in the gas phase and in solution phase, using a polarizable continuum solvation (PCM) model simulating water. The CASSCF active space was used for geometry optimisation only in aqueous phase. In addition to this DFT calculations were performed with the Molcas code using the same numerical optimisation method described with the hybrid-GGA B3LYP and GGA PBE exchange-correlation functionals, both in the gas phase and including a PCM simulating water. All structures were restricted to D_{2h} symmetry due to limitations in the Molcas code and all symmetry labels refer to this point group.

Finally to validate the numerical geometry optimisations that are described above, analytical geometry optimisations using Turbomole 6.6 with the B3LYP exchange correlation functional were also performed. These calculations employed the Alrichs basis set of polarised triple-zeta quality (def-TZVP for U, def2-TZVP for Ce and Cl) along with associated relativistic effective core potentials in order to include scalar relativistic effects. Solvation effects were also modelled using the COSMO continuum solvent model simulating water and again all calculations were restricted to D_{2h} symmetry for consistency with Molcas.

Furthermore the Quantum Theory of Atoms in Molecules (QTAIM) methodology, described in Section 2.8, was applied to electron densities obtained from both wavefunction- and density-based methods to obtain information about the bonding in the molecules in question.

4.4.3 Investigation of ground state electronic structure and structural characterisation

As has been mentioned previously, the actual symmetry of these molecules is O_h however the highest symmetry that can be implemented in the Molcas code is D_{2h}. In the O_h point group the f-orbitals span the triply degenerate t_{1u} and t_{2u} orbitals as well as the a_{2u} irreducible representations (irreps). Upon lowering the symmetry to D_{2h} the three t_{1u} and three t_{2u} orbitals

transform to two b_{1u}, two b_{2u} and two b_{3u} orbitals whilst the a_{2u} orbital becomes an orbital of a_u symmetry.

For the U(VI)Cl_6 and $[Ce(IV)Cl_6]^{2-}$ systems, where there are formally no electrons in the f-orbital manifold, we have a non-degenerate ground state, ^1A_g. However as electrons are added to the f-orbital manifold it becomes more complicated and the number of possible ground state symmetries increases, therefore calculations to investigate the ground state symmetry have been completed using the RASSCF active space described above.

U(VI)Cl_6 and $[Ce(IV)Cl_6]^{2-}$

Both the U(VI)Cl_6 and $[Ce(IV)Cl_6]^{2-}$ complexes are closed shell systems with formally no electrons in the f-orbital manifold, therefore their ground state is of symmetry ^1A_g. Table 4.1 shows the calculated bond lengths using all the methods outlined in section 4.4.2.

Method	U(VI)Cl_6		$[Ce(IV)Cl_6]^{2-}$	
	Gas Phase	Aqueous Phase	Gas Phase	Aqueous Phase
RASPT2	2.51	2.48	2.68	2.64
CASPT2	-	2.45	-	2.62
DFT (PBE)	2.48	2.48	2.67	2.65
DFT (B3LYP)	2.49	2.47	2.67	2.66
DFT (B3LYP)*	-	2.47	-	2.65

Table 4.1: Optimised bond lengths in Angstroms (Å) of Ce/U-Cl bond in U(VI) and Ce(IV) complexes using RASPT2(36,2,2;18,7,5)/CASPT2(18,16)/DFT(B3LYP/PBE) with Molcas in both gas and aqueous phase * indicates DFT-geometry optimisation completed analytically with Turbomole 6.6.

All methods produce similar bond lengths for both systems with a maximum deviation of 0.03

Å between methods. Aqueous phase structures are found to produce shorter bond lengths than the gas phase. Furthermore the difference between gas and aqueous phase bond lengths is larger when using the RASPT2 methodology (∼0.04 Å) over DFT (∼0.02 Å). Encouragingly both analytical and numerical optimisations produce values within 0.01 Å of each other (and identical in the case of U(VI)Cl_6).

$[U(V)Cl_6]^-$ and $[Ce(III)Cl_6]^{3-}$

The electronic structure of these molecules becomes more complicated as you move to Ce(III) and U(V) as an unpaired electron is introduced. Therefore there becomes more than one way of filling the f-orbital manifold. In D_{2h} there are four different irreps (and seven states in total) that can be formed. The relative energies (in eV) as calculated by RASSCF and RASPT2 of these states are shown below in Tables 4.3 and 4.2 (where only lowest energy root of each symmetry is shown).

Symmetry	Rel. Energy (RASSCF)	Rel. Energy (RASPT2)
^2A_u	0.00	0.00
$^2B_{1u}$	0.35	0.32
$^2B_{2u}$	0.34	0.33
$^2B_{3u}$	0.34	0.33

Table 4.2: Relative energies of different $[U(V)Cl_6]^-$ symmetry states (in eV) as calculated by RASSCF and RASPT2 at experimental geometry [13].

Table 4.2 shows that the A_u symmetry state is clearly the lowest in energy and corresponds to the occupation of the non-bonding f-orbital of symmetry a_u. Both the relative energies obtained using the RASSCF level and those obtained after correction by perturbation theory agree and provide almost exactly the same value.

Symmetry	Rel. Energy (RASSCF)	Rel. Energy (RASPT2)
^2A_u	0.00	0.04
$^2B_{1u}$	0.39	0.00
$^2B_{2u}$	0.39	0.00
$^2B_{3u}$	0.39	0.00

Table 4.3: Relative energies of different $[Ce(III)Cl_6]^{3-}$ symmetry states (in eV) as calculated by RASSCF and RASPT2 at experimental geometry [14].

However the situation is more complicated for Ce(III) which is clearly evident in Table 4.3 where the relative energies obtained from RASSCF disagree with perturbation corrected energies over which is the lowest energy state. As perturbation theory approximately accounts for dynamical correlation that is missing from the RASSCF methodology the $^2B_{1u}/^2B_{2u}/^2B_{3u}$ degenerate states have been used for structural optimisation.

Method	$[U(V)Cl_6]^-$		$[Ce(III)Cl_6]^-$	
	Gas Phase	Aqueous Phase	Gas Phase	Aqueous Phase
RASPT2	2.56	2.54	2.92	2.85
CASPT2	-	2.53	-	2.85
DFT (PBE)	2.55	2.55	2.86	2.79
DFT (B3LYP)	2.56	2.55	2.88	2.82
DFT (B3LYP)*	-	2.54	-	2.80

Table 4.4: Optimised bond lengths in Angstroms (Å) of Ce/U-Cl bond in U(V) and Ce(III) complexes using RASPT2(36,2,2;18,7,5)/CASPT2(18,16)/DFT(B3LYP/PBE) with Molcas in both gas and aqueous phase * indicates DFT-geometry optimisation completed analytically with Turbomole 6.6.

For the U(V) system it can be seen that there is very good agreement between the different methods and addition of a solvation model only decreases the calculated bond lengths by a maximum of 0.02 Å if at all. For the Ce(III) system there is more deviation in the calculated bond lengths with CAS/RASPT2 giving longer bond lengths than DFT (both *xc*-functionals) does. Furthermore the difference between the CAS/RASPT2 and DFT bond lengths is constant (∼0.05 Å) regardless of whether simulated in the gas phase or aqueous phase.

$[\mathbf{U(IV)Cl_6}]^{\mathbf{2-}}$ and $[\mathbf{U(III)Cl_6}]^{\mathbf{3-}}$

The filling of the f-orbital manifold becomes complicated further for $[U(IV)Cl_6]^{2-}$ and $[U(III)Cl_6]^{3-}$ which have 2 and 3 electrons to fill the f-orbital manifold respectively. Tables 4.5 and 4.6 show the relative energies of the lowest root of each state in eV as calculated by RASSCF and RASPT2.

Symmetry	Rel. Energy (RASSCF)	Rel. Energy (RASPT2)
^3A_g	0.26	0.27
$^3B_{1g}$	0.00	0.00
$^3B_{2g}$	0.00	0.00
$^3B_{3g}$	0.00	0.00

Table 4.5: Relative energies of different $[U(IV)Cl_6]^{2-}$ symmetry states (in eV) as calculated by RASSCF and RASPT2 at experimental geometry [15].

Table 4.5 shows that both RASSCF and RASPT2 predict a triply-degenerate ground state by 0.26 and 0.27 eV respectively.

Symmetry	Rel. Energy (RASSCF)	Rel. Energy (RASPT2)
^4A_u	0.00	0.00
$^4B_{1u}$	0.03	0.03
$^4B_{2u}$	0.03	0.03
$^4B_{3u}$	0.03	0.03

Table 4.6: Relative energies of different $[U(III)Cl_6]^{3-}$ symmetry states (in eV) as calculated by RASSCF and RASPT2 at experimental geometry [14].

The relative energies of the different symmetry states is much closer for U(III) than any of the complexes discussed here, shown in Table 4.6. Both RASSCF energies and energies corrected by perturbation theory predict the four states to be within 0.03 eV of each other.

Comparing the results for all the uranium systems it can be seen that as the number of f electrons in the system increases the energy gap between the different states decreases to the point where for the $[U(III)Cl_6]^{3-}$ system there is almost no difference in energy between the different states.

Method	$[U(IV)Cl_6]^{2-}$		$[U(III)Cl_6]^{3-}$	
	Gas Phase	Aqueous Phase	Gas Phase	Aqueous Phase
RASPT2	2.70	2.69	2.90	2.89
CASPT2	-	2.65	-	2.86
DFT (PBE)	2.66	2.66	2.87	2.80
DFT (B3LYP)	2.69	2.66	2.90	2.83
DFT (B3LYP)*	-	2.66	-	2.81

Table 4.7: Optimised bond lengths in Angstroms (Å) of U-Cl bond in $[U(IV)Cl_6]^{2-}$ and $[U(III)Cl_6]^{3-}$ complexes using RASPT2 (36,2,2;18,7,5)/CASPT2 (18,16)/DFT (B3LYP/PBE) with Molcas in both gas and aqueous phase * indicates DFT-geometry optimisation completed analytically with Turbomole 6.6.

Table 4.7 shows that for U(IV) there is very little difference between the gas phase and aqueous phase optimised structures. Whilst again it can be seen that RASPT2 predicts a longer bond length than DFT, CASPT2 predicts a bond length that is 0.01 Å shorter than that predicted by DFT.

For U(III) RASPT2-predicted bond are significantly longer than DFT in aqueous phase but not in the gas phase. Addition of the PCM reduces the bond length by only 0.01 Å when using RASPT2 but decreases by 0.07 Å when DFT (both functionals) is used.

Comparison with Experiment

The aqueous phase optimised structures using DFT (Both B3LYP and PBE), RASPT2 and CASPT2 are presented below in Table 4.8 along with, for comparison purposes, literature data of experimentally determined structures.

Molecule	B3LYP	PBE	RASPT2	CASPT2	Experiment
$[U(VI)Cl_6]$	2.47	2.48	2.48	2.45	2.47 [16]
$[U(V)Cl_6]^-$	2.55	2.55	2.54	2.53	2.52 [13]
$[U(IV)Cl_6]^{2-}$	2.66	2.66	2.69	2.65	2.62/2.65 [15]
$[U(III)Cl_6]^{3-}$	2.83	2.80	2.89	2.86	-
$[Ce(IV)Cl_6]^{2-}$	2.66	2.65	2.64	2.62	2.60/2.62 [14]
$[Ce(III)Cl_6]^{3-}$	2.82	2.79	2.85	2.85	2.77/2.79 [14]

Table 4.8: Optimised bond lengths in Angstroms (Å) of U/Ce-Cl bond in all complexes using RASPT2(36+n,2,2;18,7,5)/CASPT2(18+n/16)/DFT(B3LYP/PBE) in aqueous phase and comparison with experimental (XRD/EXAFS [16, 13, 15, 14]) bond lengths.

For the closed shell $U(VI)Cl_6$ complex all methodologies reproduce the XRD-derived bond lengths to within ± 0.02 Å. In the $[U(V)Cl_6]^-$ complex again structures are reproduced to a good degree of accuracy, with only a slight overestimation of bond lengths by DFT, using both functionals, (0.03 Å) whilst the RASPT2 and, in particular, CASPT2 provide better agreement. $[U(IV)Cl_6]^{2-}$ structures are reproduced well by CASPT2 and DFT however there is a significant overestimation of the bond length by RASPT2. No experimental data could be found for the $[U(III)Cl_6]^{3-}$ complex, however the ionic radii of the U(III) ion is 0.14 Å greater than that of U(IV) ion [97]. Predicting a value for the bond length in line with the ratio of ionic radii to bond length would produce an estimated value of roughly 2.80 Å. The significantly longer U-Cl bond for both $[U(III)Cl_6]^{3-}$ and $[U(IV)Cl_6]^{2-}$ found at the RASPT2 level may suggest that the larger RASSCF active space employed has reduced the effect of the PT2 correction, which would normally account for the bond length overestimation found in the absence of dynamical correlation.

Looking at the closed shell $[Ce(IV)Cl_6]^{2-}$ complex the same very close agreement that was seen for $[U(IV)Cl_6]^{2-}$ is not observed with DFT and RASPT2, however the CASPT2 does reproduce the EXAFS-derived bond lengths. For $[Ce(III)Cl_6]^{3-}$ both CASPT2 and RASPT2 overestimate

the experimental bond length, whereas DFT, particularly with the PBE *xc*-functional, give much better agreement with experiment.

4.4.4 Natural Orbital Occupations of U and Ce Complexes

Natural orbital occupations have been used in the literature as a means of justifying the multiconfigurational nature of a system [143, 144]. This multiconfigurational character typically manifests itself in correlating 'strongly occupied' (occupation number close to 2) and 'weakly occupied' orbitals (occupation number close to 0) where, as a rule of thumb, deviation of 0.02 away from 2 or 0 is an indication of multiconfigurational character.

Of the seven f-orbitals available for occupation in Ce and U hexachlorides, three have σ-antibonding character (f_σ), three δ-antibonding character (f_δ) and one has non-bonding character (f_{NB}). The natural orbital occupations of these orbitals are shown below in Table 4.9. As mentioned previously the symmetry of these molecules is O_h where there are two triply degenerate set of f-orbitals. As these calculations have been completed in D_{2h} symmetry it is possible to break this symmetry, where this has occurred in Table 4.9 the occupation of the orbital that breaks the degeneracy is given in parenthesis.

Complex	Method	f-orbital occupation		
		f_σ	f_δ	f_{NB}
$[U(VI)Cl_6]$	CASSCF(18/16)	0.06	0.03	0.01
	RASSCF(36,2,2;18,7,5)	0.01	0.01	0.01
$[U(V)Cl_6]^-$	CASSCF(19/16)	0.03	0.01	1.00
	RASSCF(37,2,2;18,7,5)	0.01	0.01	1.00
$[U(IV)Cl_6]^{2-}$	CASSCF(20/16)	0.01 (1.00)	0.01	1.00
	RASSCF(38,2,2;18,7,5)	0.01 (1.00)	0.01	1.00
$[U(III)Cl_6]^{3-}$	CASSCF(21/16)	0.09	0.92	0.00
	RASSCF(39,2,2;18,7,5)	0.01	0.99	0.00
$[Ce(IV)Cl_6]^{2-}$	CASSCF(18/16)	0.00	0.00	0.00
	RASSCF(36,2,2;18,7,5)	0.01	0.01	0.01
$[Ce(III)Cl_6]^{3-}$	CASSCF(19/16)	0.00 (1.00)	0.00	0.00
	RASSCF(37,2,2;18,7,5)	0.01 (1.00)	0.01	0.01

Table 4.9: Natural orbital occupations of f-orbitals using CASSCF (18+n/16) and RASSCF (36+n,2,2;18,7,5) active spaces. Where f-occupation breaks degeneracy natural orbital occupation number is given in parenthesis.

Table 4.9 shows significant multiconfigurational character in the $[U(III)Cl_6]^{3-}$ system at the CASSCF level. The electron configuration of $[U(III)Cl_6]^{3-}$ can be approximated to f_δ^3 however the formal value is 0.92 which deviates from unity by almost 0.1, indicative of multiconfigurational character. Multiconfigurational character is also manifested as well as in the $[U(IV)Cl_6]^{2-}$ and $[U(V)Cl_6]^-$ complexes looking at the natural orbital occupancies in Table 4.9. It is interesting that this behaviour is not manifested in the RASSCF results but may be due to having a smaller complete active space (or RAS2). In the RASSCF methodology excitations are not permitted between the RAS1(/RAS3) and the RAS2, the Cl 2p orbitals which form linear combinations with the Ce/U f-orbitals which have been placed in the RAS1 in the RASSCF active

space and therefore can not be excited to their corresponding anti-bonding pair which have been placed in the RAS2. On the other hand in the CASSCF active space these excitations are allowed evidenced by the natural orbital occupation numbers. This can be further investigated by examining the natural occupation numbers of these Cl 2p orbitals to those of the f-orbitals presented in Table 4.9. The natural orbital occupancies of these orbitals are shown in Table 4.10 calculated using CASSCF and RASSCF.

Complex	σ		δ	
	CASSCF	RASSCF	CASSCF	RASSCF
$[U(VI)Cl_6]$	1.938 (0.061)	1.997 (0.009)	1.973 (0.033)	1.999 (0.007)
$[U(V)Cl_6]^-$	1.973 (0.030)	2.000 (0.007)	1.993 (0.012)	2.000 (0.007)
$[U(IV)Cl_6]^{2-}$	1.999 (0.008)	2.000 (0.007)	2.000 (0.006[a])	2.000 (0.006)
$[U(III)Cl_6]^{3-}$	2.000 (0.091)	2.000 (0.007)	2.000[b]	2.000 (0.999)
$[Ce(IV)Cl_6]^{2-}$	1.999 (0.004)	2.000 (0.007)	2.000 (0.004)	2.000 (0.007)
$[Ce(III)Cl_6]^{3-}$	2.000 (0.004[a])	2.000 (0.007)	2.000 (0.003)	2.000 (0.007)

Table 4.10: Natural orbital occupation of σ and δ bonding (anti-bonding) orbitals calculated using CASSCF (18+n/16) and RASSCF (36+n,2,2;18,7,5) active spaces. Occupation values are averaged over three equivalent orbitals except where f-orbital occupation breaks degeneracy. [a] average taken over two weakly occupied orbitals [b] no weakly unoccupied orbitals.

Looking at Table 4.10 it can be seen that moving these Cl 2p orbitals from the CAS into a RAS1 appears to remove the multiconfigurational character seen in the U(VI) and U(V) systems. This is evident by the fact that the occupation increases for the 'strongly occupied' orbitals from below 1.98 to 2.00 (to 2 dp) and from above 0.02 to 0.01 for the 'weakly occupied' orbitals going from the CASSCF to the RASSCF.

Looking at the data in Table 4.10 it can be seen that there is decreasing multiconfigurational

character with decreasing oxidation state, particularly so in the CASSCF results. The multiconfigurational character is particularly pronounced in the σ orbitals for U(VI) and U(V). However for the U(IV), U(III) and both Ce systems the multiconfigurational character is no longer manifested.

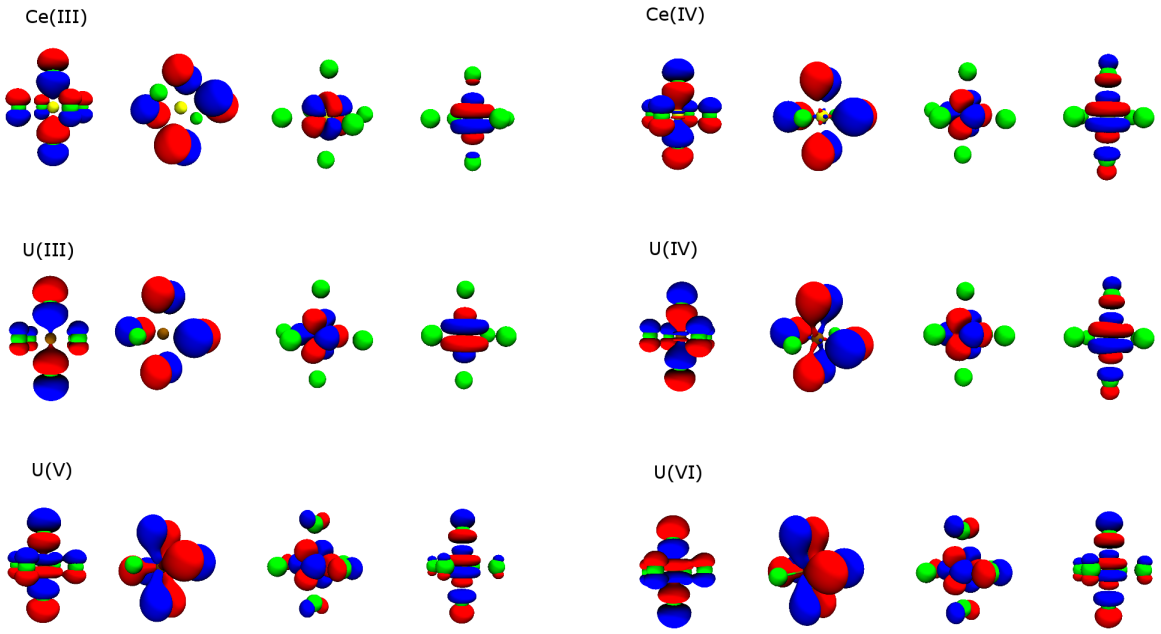

Figure 4.3: CASSCF-calculated σ and δ bonding and anti-bonding natural orbitals for each complex (generated using isosurface of 0.02 a.u.).

Inspecting the molecular orbitals, which are shown in Figure 4.3, reveals increased localisation on the chloride ligands as the oxidation of the metal increases. U(VI) and U(V) exhibit significant f-orbital contribution in both the σ and δ-bonding orbitals. U(IV) presents some f-orbital contribution particularly in the σ-bonding orbital. In the δ-bonding orbital the f character isn't as pronounced but is still present. U(III), at this isosurface, shows essentially no f-orbital contribution in the δ bonding orbital and very little in the σ-bonding orbital.

What is very clear from inspection of the molecular orbitals is the similarities between the U(IV) and Ce(IV) and U(III) and Ce(III) bonding orbitals. This suggests that the covalency in Ce may be comparable to their U counterparts and was further investigated through the use of the QTAIM methodology.

4.4.5 QTAIM Data

The similarities in the bonding orbitals of the U and Ce complexes seen in Figure 4.3 may point to covalency but does not provide quantitative insight. Therefore in order to further investigate the covalency of these systems the Quantum Theory of Atoms in Molecules (QTAIM) was employed. QTAIM is a robust method to measure the degree of covalency, a more in depth overview is provided in section 2.8. The properties obtained from QTAIM can be split into two categories, topological and integrated.

Topological Properties

One of the key properties that is obtained from QTAIM analysis is the magnitude of the electron density (ρ_{BCP}) at the bond critical point (BCP), which is shown in Table 4.11. This property has been used extensively in the literature to quantify the degree of covalency in a bond [65, 145, 139, 146, 147, 148]. Generally speaking values of greater than 0.2 indicate a covalent bond whilst less than 0.1 indicates predominantly ionic character. The Laplacian ($\nabla^2\rho$), which is also shown in Table 4.11, can be used in tandem with the magnitude to further quantify the covalency of a bond.

Complex	ρ_{BCP}				$\nabla^2\rho_{BCP}$			
	CASSCF	RASSCF	B3LYP	PBE	CASSCF	RASSCF	B3LYP	PBE
$U(VI)Cl_6$	0.105	0.102	0.099	0.096	+0.148	+0.126	+0.156	+0.159
$[U(V)Cl_6]^-$	0.086	0.084	0.082	0.081	+0.148	+0.126	+0.156	+0.159
$[U(IV)Cl_6]^{2-}$	0.064	0.059	0.063	0.065	+0.154	+0.150	+0.145	+0.146
$[U(III)Cl_6]^{3-}$	0.038	0.037	0.041	0.044	+0.121	+0.111	+0.119	+0.124
$[Ce(IV)Cl_6]^{2-}$	0.064	0.061	0.058	0.060	+0.144	+0.141	+0.122	+0.128
$[Ce(III)Cl_6]^{3-}$	0.037	0.036	0.040	0.044	+0.105	+0.104	+0.101	+0.107

Table 4.11: Values of the electron density (ρ_{BCP}) and its Laplacian ($\nabla^2\rho_{BCP}$) at the M-Cl bond critical point for all complexes at CASPT2-optimised geometries (CASSSCF/ RASSCF) and DFT-optimised geometries for DFT. All values given in a.u.

Table 4.11 shows very similar values of ρ_{BCP} regardless of the method employed, there is also a very clear decrease in covalency as measured by this property, with decreasing oxidation state of the metal. This reduction in ρ_{BCP} may be partly due to the increasing M-Cl bond with decreasing oxidation state. However Figure 4.3 shows that it also may be due to an increased energy mismatch between the metal and chloride ligand orbitals. However as expected all these systems are predominantly ionic, which is supported by the positive values of $\nabla^2\rho$.

Interestingly there are clear similarities between U(III) and Ce(III) and U(IV) and Ce(IV) systems. The values of ρ at the same oxidation states of U and Ce are almost identical, which is a clear indication of similar degrees of covalency. This is seen in all methods but it should be noted that the respective values of ρ for Ce(IV) and U(IV) are closer when calculated from CAS/RASSCF densities than they are for DFT densities.

Integrated Properties

Attention is now turned to integrated properties, which as the name suggests are obtained by the integration of a particular property (for more details see Section 2.8). Table 4.12 below presents a one-electron property, the atomic charge (q(A)), this is obtained by integrating the electron density over the atomic basins.

Complex	q(M)				q(Cl)			
	CASPT2	RASPT2	B3LYP	PBE	CASPT2	RASPT2	B3LYP	PBE
$U(VI)Cl_6$	+3.01	+3.25	+2.55	+2.36	-0.50	-0.54	-0.42	-0.39
$[U(V)Cl_6]^-$	+3.02	+3.23	+2.52	+2.33	-0.67	-0.71	-0.59	-0.55
$[U(IV)Cl_6]^{2-}$	+2.88	+2.95	+2.39	+2.24	-0.81	-0.82	-0.73	-0.71
$[U(III)Cl_6]^{3-}$	+2.38	+2.41	+2.11	+2.00	-0.90	-0.90	-0.85	-0.83
$[Ce(IV)Cl_6]^{2-}$	+2.81	+2.86	+2.26	+1.97	-0.80	-0.81	-0.71	-0.68
$[Ce(III)Cl_6]^{3-}$	+2.39	+2.41	+2.10	+2.07	-0.90	-0.90	-0.85	-0.83

Table 4.12: QTAIM derived atomic charges q(A) of U, Ce and Cl in all complexes at CASPT2-optimised geometry (CASSSCF/RASSCF) and DFT-optimised geometries for DFT. All values given in a.u.

There is a clear trend that with increased oxidation state there is an increased charge on the metal and reduced charge on the ligands, which would suggest greater covalency and is in direct agreement with the ρ data from Table 4.11. Again if the U(III) and Ce(III) as well as the U(IV) and Ce(IV) data are compared it can be seen again that there are remarkable similarities in the results.

Complex	λ(M)				Z(M)-λ(M)			
	CASPT2	RASPT2	B3LYP	PBE	CASPT2	RASPT2	B3LYP	PBE
$U(VI)Cl_6$	86.48	86.16	86.15	86.19	5.52 (6)	5.84 (6)	5.85 (6)	5.81 (6)
$[U(V)Cl_6]^-$	86.96	86.83	86.86	86.88	5.04 (5)	5.17 (5)	5.14 (5)	5.12 (5)
$[U(IV)Cl_6]^{2-}$	87.68	87.73	87.68	87.91	4.32 (4)	4.27 (4)	4.32 (4)	4.09 (4)
$[U(III)Cl_6]^{3-}$	88.65	88.69	88.60	88.55	3.35 (3)	3.31 (3)	3.40 (3)	3.45 (3)
$[Ce(IV)Cl_6]^{2-}$	53.74	53.79	53.79	53.78	4.26 (4)	4.21 (4)	4.21 (4)	4.22 (4)
$[Ce(III)Cl_6]^{3-}$	54.72	54.75	54.71	54.69	3.28 (3)	3.25 (3)	3.29 (3)	3.31 (3)

Table 4.13: QTAIM calculated localisation indices (λ) and Z(M)-λ(M), the number of electrons shared with the ligand at CASPT2-optimised geometry (CASSSCF/RASSCF) and DFT-optimised geometries for DFT. Parentheses indicates Z(M)-λ(M) rounded to nearest integer. All values in a.u.

The localisation index (λ(A)) is a two-electron property (presented in Table 4.13) and is a measure of the number of electrons localised on atom A. Previous work in the group on actinide and lanthanide complexes have shown there to be a close relationship between localisation index and oxidation state [65, 141, 145]. In a purely ionic system it would be expected that λ(M) would increase by one for each change in oxidation state. Looking at Table 4.13, this only occurs from U(IV) to U(III) but not between the other oxidation states. This suggest that the degree of covalency is decreasing with decreasing oxidation state.

In order to make a fair comparison between U and Ce it can be a more useful measure to use Z(M)-λ(M) which gives the number of electrons that are shared by the metal centre with the ligand. Table 4.13 shows that when rounded to the nearest integer Z(M)-λ(M) is equivalent to the oxidation state. Again there is also pronounced similarity between U and Ce complexes of the same oxidation state.

Table 4.14 shows the value of the delocalisation index between the U/Ce and Cl atoms (δ(M,Cl)). The delocalisation index is a two-electron property that can also be used as a measure of covalency [65, 149, 150], further details on the delocalisation index is given in Section 2.8 in the Methodology chapter. In Table 4.14 the 'Total' delocalisation index is given as well as the *gerade (g)* and *ungerade (u)* contribution to the δ(M,Cl). As d-orbitals have *gerade* parity and f-orbital *ungerade*, decomposing the total δ(M,Cl) into these two contributions allows an assessment of d- and f-orbital contribution to bonding.

Complex	δ(M,Cl)											
	CASPT2			RASPT2			B3LYP			PBE		
	Total	u	g	Total	u	g	Total	u	g	Total	u	g
$[U(VI)Cl_6]$	0.838	0.447	0.391	0.868	0.475	0.393	1.102	0.678	0.424	1.151	0.725	0.426
$[U(V)Cl_6]^-$	0.673	0.335	0.338	0.647	0.316	0.331	0.872	0.494	0.378	0.932	0.547	0.385
$[U(IV)Cl_6]^{2-}$	0.482	0.210	0.272	0.442	0.197	0.245	0.633	0.307	0.326	0.619	0.353	0.266
$[U(III)Cl_6]^{3-}$	0.324	0.145	0.179	0.300	0.138	0.162	0.432	0.193	0.239	0.487	0.224	0.263
$[Ce(IV)Cl_6]^{2-}$	0.485	0.202	0.283	0.450	0.184	0.266	0.651	0.435	0.216	0.716	0.482	0.234
$[Ce(III)Cl_6]^{3-}$	0.297	0.124	0.173	0.279	0.122	0.157	0.395	0.163	0.232	0.446	0.195	0.251

Table 4.14: QTAIM calculated delocalisation indices of U/Ce-Cl bond (δ(M-Cl)) as well as decomposed *gerade* (g) and *ungerade* (u) contributions at CASPT2-optimised geometries. All values in a.u.

Looking at the 'Total' column in Table 4.14 it is clear that as the oxidation state of the metal decreases so does δ(M,Cl) and hence the covalent interaction between the two atoms, in agreement with the ρ_{BCP} data. However unlike the ρ_{BCP} data there is disagreement between the correlated wavefunction methods and the two DFT functionals, with DFT predicting a larger value of δ(M,Cl).

Closer examination of the two contributions to the total δ(M,Cl) reveals that whilst the *ger-*

ade, the d-orbital contribution, is relatively constant between all methods for U(VI) and U(V), the *ungerade*, the f-orbital contribution, is much larger when simulated using DFT. For U(IV) and U(III) not only is there a disparity between the *ungerade* contribution but there is also a difference in the *gerade* contribution. One of the problems with KS-DFT is that it suffers from self-interaction error (see Section 2.4 of Methodology chapter). The self-interaction error can lead to apparent electron delocalisation which vanishes when a correlated wavefunction is used. The disparity in δ(M,Cl) between DFT and CAS/RASSCF is therefore most likely due to the self-interaction error. This hypothesis is supported by the fact that B3LYP, a hybrid *xc*-functional containing a percentage of Hartree-Fock exchange which reduces the self-interaction error, produces values closer to CAS/RASSCF than PBE does, a pure functional with no Hartree-Fock exchange and hence more susceptible to self-interaction error.

Now comparing the values of δ(M,Cl) between U and Ce of the same oxidation state it can be seen that, like the ρ_{BCP} data, there are very similar values particularly with CAS/RASSCF.

4.4.6 Conclusions

The bonding in several U and Ce hexachlorides has been optimised and analysed using a variety of different methods. It has been seen that contrary to previous studies and complimentary to the work of Kozimor [14] there is actually a great deal of similarity in the degree of covalency between Ce and U, in these hexachloride complexes.

The degree of multiconfigurational character exhibited by these systems was explored by examination of natural orbital occupancies. Whilst there was very little deviation from integer occupation in σ- and δ-type bonding/antibonding orbitals using the RASSCF methodology, CASSCF electronic structures displayed a degree of multiconfigurational character for higher oxidation states (U(VI), U(V)), particularly with respect to the σ-bonds. This multiconfigurational character effectively disappears for lower oxidation states (M(IV), M(III)). U(III)

provides an interesting case, where multiconfigurational character manifests itself not in the MCl bonds, but within the f-manifold itself: f_δ orbitals have natural orbital occupations of 0.913 and f_σ orbitals have occupations of 0.091. This can be attributed to a weakening of the ligand field, which results in near degeneracy with the f-manifold.

Both correlated wavefunction methods and DFT have been used and it has been seen that although DFT produces similar values for some metrics of covalency (such as ρ_{BCP}) for δ(M-Cl) there is a disparity between DFT and CAS/RASPT2. This has been further investigated and broken down into *gerade* and *ungerade* contributions, the source of the discrepancy has been shown to originate from the *ungerade* contribution in the DFT calculations. This error has been attributed to the self interaction error that the DFT methodology suffers from.

It has been shown that the RASSCF methodology can successfully and accurately describe bonding in relatively small f-element complexes. Furthermore it has been shown that a greater number of orbitals can be included in the active space in a RASSCF calculation allowing for a fuller picture of the electronic structure and bonding. The challenge is to now use what has been learnt in this section and apply to larger f-element systems. The next section of this thesis deals with low valent actinide and lanthanide systems where the ligand is a Cp ring.

4.5 Actinide and Lanthanide Cp_3 Complexes

4.5.1 Introduction

The chemistry of the actinide and lanthanide complexes is heavily dominated by the (III) oxidation state, as shown in Table 4.15. Accessibility of the (II) oxidation state has until recently had been limited exclusively to the heavier of the actinide complexes, a result of the lowering in energy of the 5f-orbitals when moving right across the actinide series. However as more advanced synthetic techniques have been developed divalent complexes of the earlier actinides have been discovered. The synthesis of many divalent actinide/lanthanide complexes

were first published in the literature by the Evans group [151, 19, 18], which has been achieved through the use of potassium and a cryptand as the reducing agent.

Element	Electron Configuration	Oxidation States
Thorium (Th)	$[Rn]6d^2 7s^2$	II, III, **IV**
Protactinium (Pa)	$[Rn]5f^2 6d^1 7s^2$	III*, IV, **V**
Uranium (U)	$[Rn]5f^3 6d^1 7s^2$	II, III, IV, V, **VI**
Neptunium (Np)	$[Rn]5f^4 6d^1 7s^2$	III, IV, **V**, VI, VII
Plutonium (Pu)	$[Rn]5f^6 7s^2$	III, **IV**, V, VI, VII
Americum (Am)	$[Rn]5f^7 7s^2$	II*, **III**, IV, V, VI
Curium (Cm)	$[Rn]5f^7 6d^1 7s^2$	**III**, IV
Berkelium (Bk)	$[Rn]5f^9 7s^2$	**III**, IV
Californium (Cf)	$[Rn]5f^{10} 7s^2$	II*, **III**, IV*
Einsteinium (Es)	$[Rn]5f^{11} 7s^2$	II*, **III**
Fermium (Fm)	$[Rn]5f^{12} 7s^2$	II, **III**
Mendelevium (Md)	$[Rn]5f^{13} 7s^2$	II, **III**
Nobelium (No)	$[Rn]5f^{14} 7s^2$	**II**, III
Lawrencium (Lr)	$[Rn]5f^{14} 6d^1 7s^2$	III

Table 4.15: Electron configuration and most stable oxidation states of the actinides. Bold indicates most stable oxidation state in solution * indicates oxidation state only found in solids [17].

In this work computational simulations have been carried out on the actinide complexes Th(II-IV)Cp_3, U(II-IV)Cp_3 and Pa(II)Cp_3 as well as the lanthanide complex Ce(II)Cp_3 using the RASSCF methodology. As far as the author is aware this is the most wide ranging computational study of the divalent actinide complexes using the RASSCF methodology.

4.5.2 Computational Details

Quantum chemical simulations using the RASSCF methodology have been performed using version 8.0 of the Molcas code on the divalent actinide and lanthanide complexes - $[Ce(II)Cp_3]^-$, $[Th(II)Cp_3]^-$, $[Pa(II)Cp_3]^-$ and $[U(II)Cp_3]^-$. Additionally to further investigate bonding and covalency in the lanthanide and actinide complexes the complexes $Th(III)Cp_3$, $U(III)Cp_3$, $[Th(IV)Cp_3]^+$ and $[U(IV)Cp_3]^+$ were also investigated with the RASSCF methodology. The calculations on these complexes employed the relativistically contracted atomic natural orbital (ANO-RCC) basis sets of polarised triple-zeta quality (TZVP) [70]; (26s23p17d13f5g3h) /[9s8p6d4f2g] for U, (14s9p4d3f2g)/[4s3p2d] for C and (8s4p3d1f)/[3s2p] for H. Scalar relativistic effects were included with the use of the 2nd order Douglas-Kroll-Hess Hamiltonian, whilst computational time decreased by using the Cholesky decomposition.

All RASSCF calculations were performed using an active space that consisted of six π-orbitals from the three Cp rings (two π_1 from each Cp) in the RAS1, thirteen metal orbitals (seven 5f, one 7s orbital and five 6d orbitals) in the RAS2 and six π^*-orbitals from the three Cp rings (two π_2 from each Cp), shown in Figure 4.4. This active space has been chosen based partly upon the work of R. Coates [152], who investigated $Ce(IV)Cp_3$. But also partly guided by the low valency of the compounds investigated, hence the need to include both the d- and f- orbitals in the active space as the occupation of these orbitals results in a change of the energy gap between the d- and f- orbitals.

By definition, all configurations within the RAS2 subspace were allowed in the CI expansion of the wavefunction, only configurations involving double excitations from (to) RAS1 (RAS3) were included and the active space is denoted (12+n,2,2;6,13,6) (where n ranges from 0 to 4 depending on the system and the number of f electrons). It should be noted that although the intention was to include the metal d- and f-orbitals as part of the RAS2, there were occasions where the metal d- and f- orbitals rotated out of the RAS2 and into the RAS3, switching places

with the π^* orbitals of the Cp rings. This is not considered to be an issue because these π^* orbitals are heavily correlated to the π orbitals of the Cp rings in the RAS1 and so it makes sense that they would rotate into the RAS2. Furthermore (as will be shown later) the natural orbital occupation of the metal orbitals are effectively zero, they therefore play no significant role in determining the correlation energy.

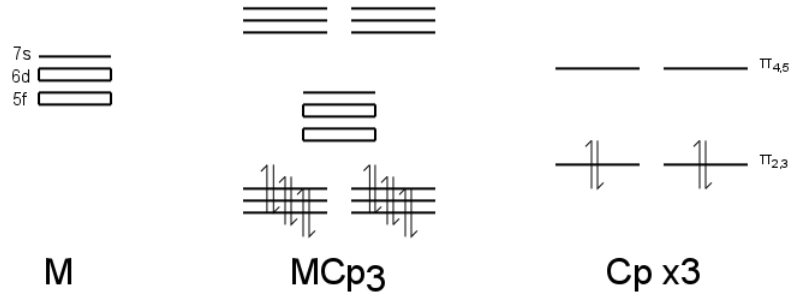

Figure 4.4: Qualitative $[M(n)Cp_3]^{n-3}$ $(n = 2 - 4)$ Molecular Orbital Diagram of Orbitals included in RASSCF Active Space where M contains 0 to 4 electrons.

4.5.3 Results

In this section, where available, experimental structures will be compared to DFT(PBE0/def2-TZVP) optimised structures. The optimised structures presented below have had the substituents on the Cp rings removed to reduce the computational cost of the optimisation calculations. The substituents that have been removed from the experimental structures are large bulky ^{t}Bu groups which have been introduced in the synthesis of these unique low valent complexes for steric and not electronic reasons. As the interest of these systems is in the bonding and covalency, the removal of these bulky substituents is considered justified, although the potential effects on bond lengths having removed the substituents will be borne in mind.

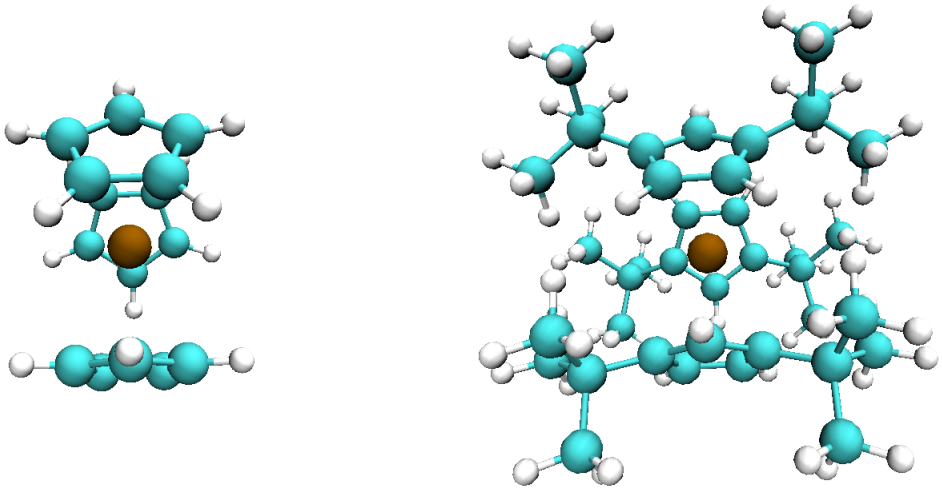

Figure 4.5: Difference in $[\mathrm{Th}(n)\mathrm{Cp}_3]^{n-3}$ structure with and without ^{t}Bu substituents.

4.5.4 Structural Comparison of Th and U Cp_3 Complexes

Tables 4.16 and 4.17 show the comparison between DFT(PBE0)-optimised and experimentally determined bond lengths for the Th and U systems investigated. Comparisons have been made between the different complexes, comparing the distances between the metal centre and the centre of the Cp ring as well as the average, highest and lowest bond lengths between the metal and each carbon of the Cp ring.

Bond	$[Th(II)Cp_3]^-$		$Th(III)Cp_3$		$[Th(IV)Cp_3]^+$	
	Exp	DFT	Exp	DFT	Exp	DFT
M-C (Average)	2.797	2.800	2.834	2.784	2.858	2.808
M-C (Highest)	2.854	2.824	2.881	2.799	2.943	2.817
M-C (Lowest)	2.739	2.769	2.765	2.771	2.737	2.799
M-Cp (Centre)	2.514	2.523	2.516	2.499	2.571	2.528

Table 4.16: Comparison of bond lengths in $[Th(II)Cp_3]^-$, $Th(III)Cp_3$ and $[Th(IV)Cp_3]^+$ between experimental structures [18] and DFT(PBE0/def2-TZVP)-optimised structures. All values are given in Å.

Table 4.16 shows that the DFT-optimised Th structures have a smaller range of M-C bond lengths than experimental structures. This is partly explained by the fact that the experimental structures contain bulky ^{t}Bu groups on the Cp rings which distort away from a symmetrical structure. These bulky ^{t}Bu groups have been omitted from calculations to reduce the computational cost.

If the average M-C bond lengths are compared between the DFT structures and the experimental structures it can be seen that there is remarkable agreement for the Th(II) structure whilst agreement is less good for Th(III) & Th(IV). Again this can be partly explained by a couple of very large M-C bonds, a result of the bulky ^{t}Bu groups on the Cp ring, skewing results.

Comparing the distances between the Th centre and the centre of the Cp ring, which is less affected by the range in the Th-C bond length, it can be seen that the difference between experimental and DFT structures increases with increased oxidation state.

Bond	U(II)		U(III)		U(IV)	
	Exp	DFT	Exp	DFT	Exp	DFT
M-C (Average)	2.794	2.787	2.836	2.766	2.803	2.735
M-C (Highest)	2.822	2.797	2.937	2.774	2.907	2.751
M-C (Lowest)	2.762	2.779	2.723	2.761	2.682	2.714
M-Cp (Centre)	2.521	2.541	2.565	2.482	2.549	2.444

Table 4.17: Comparison of bond lengths in $[U(II)Cp_3]^-$, $U(III)Cp_3$ and $[U(IV)Cp_3]^+$ between experimental structures [19] and DFT(PBE0/def2-TZVP)-optimised structures. All values are given in Å.

As with Thorium (Table 4.16), it can be seen in Table 4.17 that there is a wide range of U-C bond lengths in the experimental structures that is not replicated in the DFT-optimised structures. This is again a result of the ^{t}Bu groups on the Cp rings of the experimental structures which have not been included in calculations on these systems.

If the distances between the U and the centre of the Cp ring are now compared, a similar pattern to Th is observed. The DFT optimised distance is closer to the experimental distance for the U(II) structure than it is for U(III) and U(IV). In fact there is quite a discrepancy between the DFT and experimental distances between U and the centre of the Cp ring for U(III) and U(IV), much larger than that between the same coordinate for Th(III) and Th(IV).

4.5.5 Divalent Actinide and Lanthanide Cp_3 Complexes

Here the natural orbital occupation numbers and relative energies between different spin states that have been investigated with the RASSCF(n,2,2;6,13,6) active space are discussed for $[Ce(II)Cp_3]^-$, $[Th(II)Cp_3]^-$, $[Pa(II)Cp_3]^-$ and $[U(II)Cp_3]^-$. In the below paragraphs for brevity the complexes will be referred to by just their chemical symbol and oxidation state.

Ce(II)

RASSCF calculations have been performed on both singlet and triplet configurations, however regardless of the spin state the same two orbitals are populated by electrons when calculated with the RASSCF methodology using a (14,2,2;6,13,6) active space - a 4f orbital and a 5d orbital, which are shown in Figure 4.6. The occupation of these two orbitals is in agreement with experimental magnetic data which suggests that the Ce^{2+} ground state is a triplet with an electron configuration of [Xe]$5d^1 4f^1$ [151, 153].

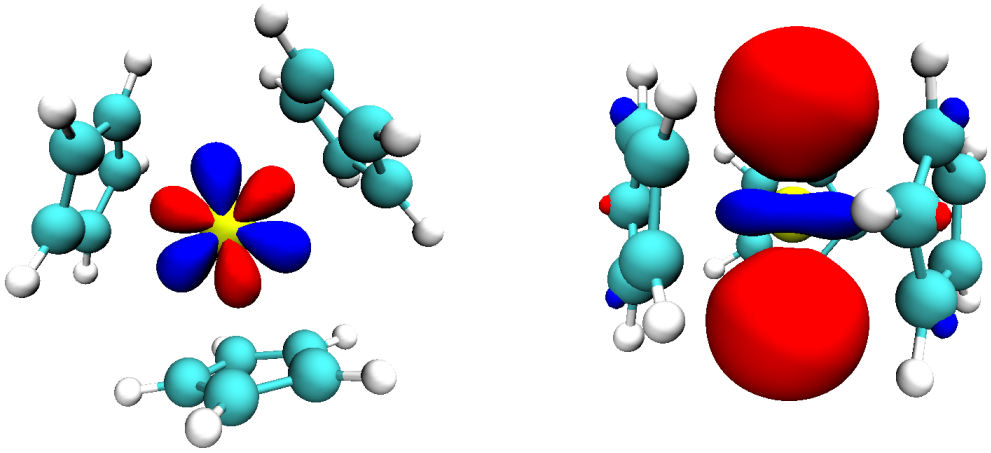

Figure 4.6: Strongly occupied natural molecular orbitals (4f orbital (left) and 5d orbital (right)) of triplet cerium at DFT(PBE0/def2-TZVP)-optimised structure. Natural orbitals generated with an isosurface of 0.035 a.u.

Table 4.18 shows the natural orbital occupation numbers of the orbitals included in the RASSCF (14,2,2;6,13,6) active space for both the singlet and triplet states. It is obvious to note that although the active space was planned so that it included the 7 4f orbitals, 5 5d orbitals and 1 6s orbital of Ce(II) it contains mainly orbitals of the Cp ring. As discussed above this is because the Ce(II) orbitals rotate out of the active space when included as they play little part

in the correlation energy whilst the Cp orbitals are more strongly correlated.

Natural Molecular Orbital No	Singlet	Triplet
82 Cp $\pi*$	0.031	0.031
83 **Ce 4f**	1.043	0.999
85 Cp $\pi*$	0.034	0.034
86 Cp $\pi*$	0.034	0.034
89 Cp $\pi*$	0.021	0.021
92 **Ce 5d**	0.951	0.995
Relative Energy (eV)	2.35	0.00

Table 4.18: Occupation numbers of natural orbitals included in RAS2 subspace of RASSCF (14,2,2;6,13,6) active space for both singlet and triplet spin states where occupation differs from integer value by greater than 0.02. Orbitals highlighted in bold are those that are 'strongly occupied', shown in Figure 4.6, as calculated using a RASSCF(14,2,2;6,13,6) active space at $[Ce(II)Cp_3]^-$ DFT(PBE0/def2-TZVP) optimised structure.

It can be seen in Table 4.18 that the natural orbital occupation numbers between the singlet and triplet states are very similar. There is, however, a small but significant difference of 0.04 in the natural orbital occupation numbers of the 92 Ce 5d orbital. This means that for the singlet state to maintain its spin multiplicity of 0 this would require that one of the electrons have spin alpha and the other beta.

When the singlet state is further investigated it is revealed that the singlet state is composed of two configurations; one configuration which has the 92 Ce 5d orbital doubly occupied and the other which has the 83 Ce 4f orbital doubly occupied instead, shown below in Table 4.19. Furthermore these two configurations have almost exactly the same weighting showing clear multiconfigurational character in the singlet state of the Ce(II) complex.

Configuration	Occupation	Weighting
9	22222202000000000000000	0.46541
24686	22222200000000020000000	0.42388

Table 4.19: Configurations of the $[Ce(II)Cp_3]^-$ singlet ground state as determined by RASSCF (14,2,2;6,13,6) active space. Doubly occupied orbitals correspond to orbitals shown in Figure 4.6.

Turning now to the energetics; it is clear that the Ce(II) triplet state is the ground state as it lies 2.35 eV (as calculated by RASSCF) lower in energy than the Ce(II) singlet state. This is a result of the energetic cost of doubly occupying electrons in either of Cerium's 4f/5d orbitals (the two main configurations of the singlet state) over singly occupying a 5d- and 4f-orbital. Also the fact that there is an equal weighting in configurations in the singlet state between doubly occupying the 5d sigma and the 4f phi suggests that the energy of the doubly occupied 5d sigma orbital is comparable to the energy of the doubly occupied 4f phi orbitals resulting in the multiconfigurational behaviour that is observed in the above RASSCF calculations.

Th(II)

Th(II) is the actinide analogue of Ce(II), the same RASSCF active space has therefore been used to simulate the singlet and triplet states of Th(II). It has been shown in the literature that although thorium is the actinide analogue of cerium the electronic structure of their complexes differ. An example of this is the difference in Th(III) and Ce(III) complexes [refs] where the electronic structure of Th(III) is typically $6\,d^1$ whilst Ce(III) is typically $4\,f^1$ - this is a result of the 4f orbitals being much lower in energy than the 5f, as discussed earlier in this chapter.

This difference in the chemistry of Cerium and Thorium is also evident in the +II oxidation state in the complexes investigated here. Whilst for Ce(II), the ground state is clearly the triplet state, the opposite is true for Th(II) where the ground state is a singlet, this has been

experimentally reported as the Thorium ground state by Evans et al [151]. Furthermore whilst the singlet state of Ce(II) is $4f^15d^1$ (although as a result of equal weighting of the $4f^2$ and $5d^2$ configurations) the singlet ground state of Th(II) is $6d^2$. The natural orbital occupation numbers for the singlet and triplet spin states are shown below in Table 4.20.

Natural Molecular Orbital	Singlet	Triplet
101 Cp $\pi*$	0.038	0.036
104 **Th 6d**	1.886	0.993
105 Cp $\pi*$	0.033	0.032
107 Th 6d	0.025	0.022
108 Cp $\pi*$	0.042	0.038
110 **Th 5f**	0.078	0.999
Relative Energy (eV)	0.00	0.67

Table 4.20: Occupation numbers of natural orbitals included in the RAS2 of active space for singlet and triplet states of $[Th(II)Cp_3]^-$ with significant occupation (differs from integer by more than 0.02). Orbitals in bold are 'strongly occupied' orbitals shown in Figure 4.7, as calculated using a RASSCF(14,2,2;6,13,6) active space at $Th(II)Cp_3$ DFT(PBE0/def2-TZVP) optimised structure.

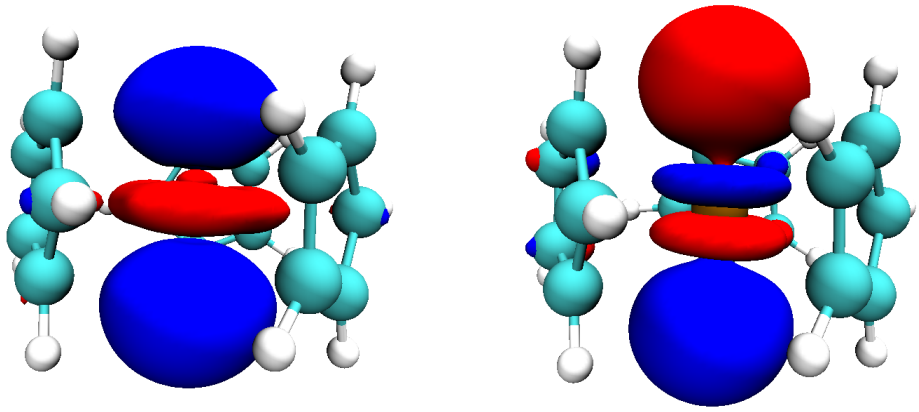

Figure 4.7: Strongly occupied natural molecular orbitals (6d-orbital (left) & 5f-orbital (right)) of singlet thorium at DFT(PBE0/def2-TZVP)-optimised structure. Natural orbitals generated with an isosurface of 0.035 a.u.

It is interesting that the singlet state shows significant occupation (∼0.8) of the 110 Th 5f as shown above in Table 4.20 as when this orbital is occupied in the triplet state it becomes a diffuse orbital. Figure 4.8, below, shows the difference in the 110 Th 5f orbital between the singlet and triplet states for the Th(II) complex. Whilst for the singlet 110 Th 5f is clearly a 5f σ orbital, in the triplet state the orbital appears diffuse indicative of a loosely bound electron. This indicates that the energy of the triplet state lies close to the ionisation energy of the Th(II) complex. It is also important to note that there is a much smaller relative energy difference between the singlet and triplet state of the Th(II) complex than there is for the Ce(II) complex which suggests that the 6d and 5f orbitals lie much closer in energy in Thorium than the 5d and 4f do in Cerium.

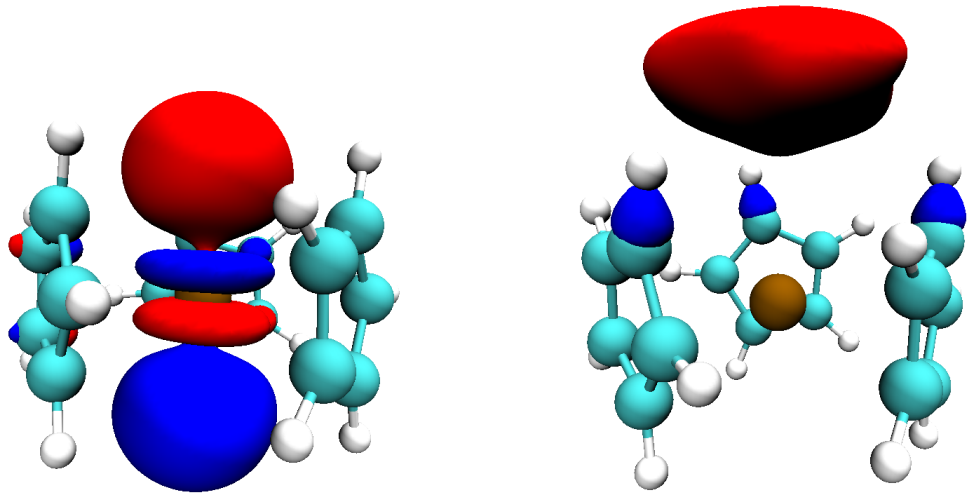

Figure 4.8: Th(II) 110 5f calculated using RASSCF(14,2,2;6,13,6) active space for the singlet (left) and triplet (right) spin states at DFT(PBE0/def2-TZVP)-optimised geometry. All isosurfaces generated at 0.35 a.u.

Pa(II)

Protactinium lies between Th and U in the periodic table, the ground state of the Pa(II) complex can therefore either be a doublet or a quartet. Figure 4.9 shows the orbitals that are 'strongly occupied' when using the RASSCF(15,2,2;6,13,6) active space and the natural orbital occupation numbers of the orbitals included in the active space are shown in Table 4.21 for both doublet and quartet spin states.

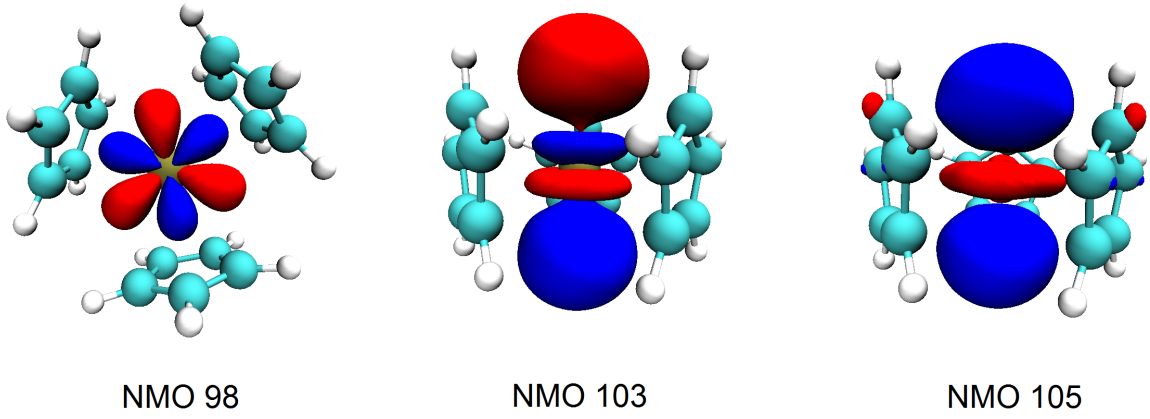

Figure 4.9: Occupied Pa(II) natural molecular orbitals calculated using RASSCF (15,2,2;6,13,6) active space for the quartet spin state at DFT (PBE0/def2-TZVP)-optimised geometry. All isosurfaces generated at 0.35 a.u.

From the RASSCF calculations using the (15,2,2;6,13,6) active space, the two most favourable electron configurations for Pa(II) are [Rn]$5f^16d^2$ (doublet) and [Rn]$5f^26d^1$ (quartet). It can be seen in Table 4.21 that the doublet electron configuration, where the 105 Pa 6d orbital is doubly occupied, is more energetically favourable than the quartet state, with an energy difference between these two states of 0.48 eV, this is relatively similar to the energy difference between the singlet and triplet states of the Th(II) complex, but importantly and interestingly lower. This suggests a relative destabilisation of the 6d orbital relative to the 5f orbital manifold moving from Th to Pa.

Natural Molecular Orbital (NMO)	Doublet	Quartet
98 **Pa 5f**	0.995	0.997
99 Cp $\pi*$	0.024	0.034
100 Pa 5f	0.024	0.034
102 Pa 6d	0.022	0.004
103 **Pa 5f**	0.090	0.998
105 **Pa 6d**	1.868	0.990
107 Pa 5f	0.010	0.020
Relative Energy (eV)	0.00	0.48

Table 4.21: Occupation numbers of natural orbitals included in the RAS2 subspace of the active space for $[Pa(II)Cp_3]^-$ for the doublet and quartet spin states with a natural orbital occupation number deviating from integer by greater than 0.02. Orbitals in bold are strongly occupied Protactinium d- and f-orbitals, shown in Figure 4.9, as calculated using the RASSCF(15,2,2;6,13,6) active space at $[Pa(II)Cp_3]^-$ DFT(PBE0/def2-TZVP) optimised structure. Also shown is the relative energy difference between the doublet and quartet states.

Looking at the natural orbital occupations presented in Table 4.21 it is clear that there is more significant occupation of the Pa metal orbitals included in the active space than there is for Thorium or Cerium, this suggests a lowering in the energy of the Pa orbitals.

The energy difference between the doublet and quartet states of the Pa(II) complex is a representation of the energetic cost of pairing two electrons in a 6d orbital against additionally filling another 5f orbital. This begins to give us insight into the energy gap between the 6d and 5f orbitals. The fact that both the ground states of Th(II) and Pa(II) complexes are predicted by RASSCF to be the lower of the two possible spin multiplicities, in addition to the fact that the energy gap between the two different spin multiplicities for the Pa(II) complex is lower than that of the Th(II) complex, which as expected suggests that going along the actinide series re-

sults in a lowering of the energy gap between the 6d and 5f orbitals. Should the trend continue it would be expected that higher spin multiplicities would become more energetically favourable.

Unfortunately there is no experimental data available for Pa(II) complexes to compare the ground state multiplicity against due to it's rarity and high level of radioactivity.

U(II)

The U(II) complex is the most computationally difficult of all the complexes modeled in this section as it has four electrons with which to fill orbitals in the RAS2 subspace. Although these four electrons can form a singlet, triplet or quintet spin state, only the quintet state has been investigated here using the RASSCF(16,2,2;6,13,6) active space due to the huge number of possible configurations for the singlet and triplet states as well as due to time constraints.

DFT(PBE0/def2-TZVP) ground state calculations have been performed on all three different spin states of the U(II) complex using the Turbomole 6.6 program, at the DFT(PBE0/def2-TZVP) optimised geometry. The DFT calculations completed predicted the singlet state to be much higher in energy (2.25 eV) whilst predicting that the quintet and triplet state to be close in energy. Further calculations were therefore completed using the CASSCF methodology on the triplet and quintet states, using a smaller active space than the RASSCF active space that has been used on previous actinide systems discussed in this section. This active space included just the 6d and 5f orbitals to form a CASSCF(4/12) active space. Agreeing with the energetics predicted by DFT, the CASSCF methodology with the (4/12) active space, also predicts the ground state to be the quintet spin state. It also, like DFT, predicts a relatively small energy gap between the triplet and quintet spin states, albeit a slightly larger energy difference (0.38 eV with CASSCF(4/12) compared with 0.26 eV with DFT(PBE0/def2-TZVP). The relative energy states of the singlet, triplet and quintet, as calculated by DFT and CASSCF with the (4/12) active space, are shown below in Table 4.22.

Spin State	CASSCF(4/12)	DFT (PBE0)
Singlet	-	2.25
Triplet	0.38	0.26
Quintet	0.00	0.00

Table 4.22: Relative energies of the spin states of $[U(II)Cp_3]^-$ calculated using CASSCF(4/12) and DFT(PBE0/def2-TZVP) at DFT(PBE0/def2-TZVP) optimised geometry. Energy values presented in eV.

Justification for examining only the quintet state with the RASSCF(16,2,2;6,13,6) active space has been derived from the fact that the singlet (as calculated by DFT) lies much higher in energy than either the triplet or quintet and that both DFT and CASSCF agree that the quintet is the ground state. Furthermore the quintet state has been shown experimentally to be the ground state of $U(II)Cp_3$ [19]. However looking at the configurations that compose the U(II) complex triplet state an important observation can be made. The U(II) triplet state, is primarily comprised of two relatively equally weighted states, one which can be approximated to $6d^2 5f^1 5f^1$ and the other $6d^1 5f^2 5f^1$ (i.e. doubly occupying a 6d or a 5f orbital). This is similar to what was observed for the Ce(II) singlet state and suggests that the 6d orbitals and 5f orbitals are close in energy.

Attention is now turned to the RASSCF(16,2,2;6,13,6) calculation on the quintet state. Figure 4.10 shows the 'strongly occupied' active space orbitals and can be approximated by an electron configuration of $[Rn]5f^3 6d^1$. The occupation numbers of the natural orbitals shown in Figure 4.10 as well as the rest of the orbitals included in the active space with significant occupation (greater than 0.02) are presented in Table 4.23.

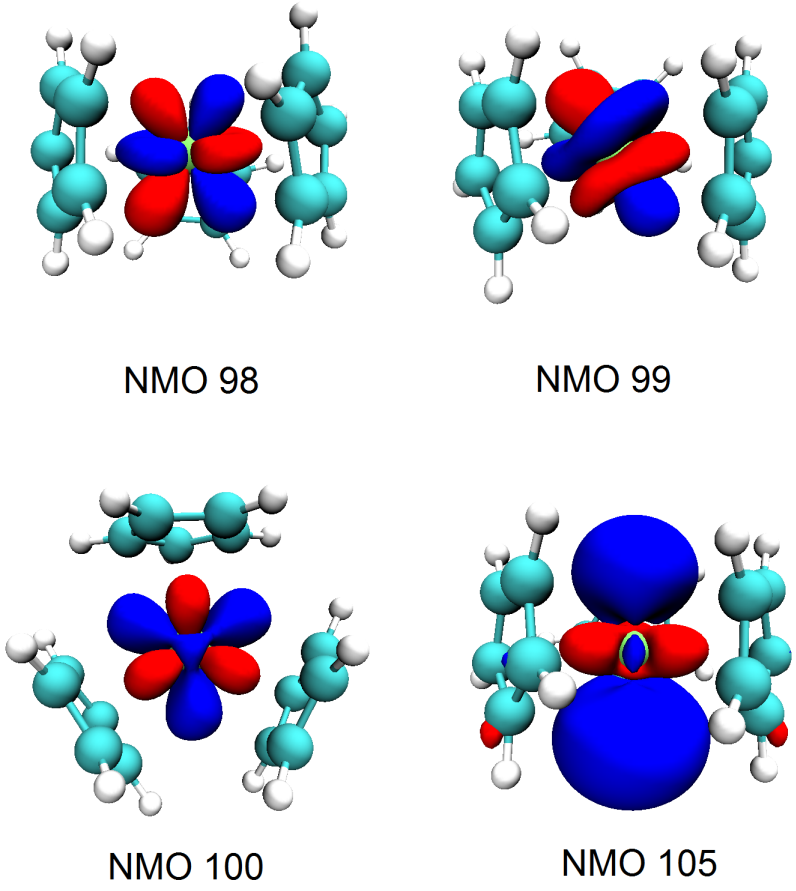

Figure 4.10: Strongly occupied U(II) natural molecular orbitals calculated using RASSCF (16,2,2;6,13,6) active space for the quintet spin state at DFT (PBE0/def2-TZVP)-optimised geometry. All isosurfaces generated at 0.35 a.u.

Natural Molecular Orbital (NMO)	Occupation
98 U 5f	0.989
99 U 5f	0.990
100 U 5f	0.994
103 U 5f	0.021
105 U 6d	0.987
106 U 5f	0.024
107 U 6d	0.024
108 Cp $\pi*$	0.037
109 Cp $\pi*$	0.036
110 Cp $\pi*$	0.032

Table 4.23: Occupation numbers of natural orbitals included in the RAS2 subspace of the active space for $[U(II)Cp_3]^-$ at the quintet spin state with occupations deviating from integer by greater than 0.02. Orbitals in bold are strongly occupied Uranium d- and f-orbitals, shown in Figure 4.10, as calculated using the RASSCF(16,2,2;6,13,6) active space at $[U(II)Cp_3]^-$ DFT(PBE0/def2-TZVP) optimised structure.

Table 4.23 shows the natural orbital occupations of the U(II) complex for the quintet spin state using the RASSCF(16,2,2;6,13,6) active space. It can be seen clearly in the table that U(II) can be approximated by an electron configuration of $[Rn]5f^36d^1$, with the strongly occupied orbitals all having occupations of 0.99 (rounded to 2dp). It can also be seen that the f-orbitals not considered to be 'strongly occupied' show non-negligible occupation of 0.02 suggesting weak multiconfigurational behaviour, this is similar to what was observed for the $[U(III)Cl_6]^{3-}$ complex in the previous section where although the strongly occupied orbitals had occupations of 2.00 there was also the presence of 'weakly occupied' orbitals with significant natural orbital occupations.

Comparison of An/Ln(II) Natural Orbital Occupations and relative energies

This subsection compares and contrasts the four divalent systems; $[Ce(II)Cp_3]^-$, $[Th(II)Cp_3]^-$, $[Pa(II)Cp_3]^-$ and $[U(II)Cp_3]^-$, investigated above. As above these will be referenced to here as Ce(II), Th(II), U(II) and Pa(II).

Table 4.24 below summarises the ground state approximated electron configurations and RASSCF-calculated energy gap between other spin states.

Complex	Approximated Metal Configuration	Spin	Relative energy difference (eV)
Ce(II)	$[Xe]4f^15d^1$	triplet	0.00
	$[Xe]4f^2/[Xe]5d^2$ *	singlet	2.87
Th(II)	$[Rn]6d^2$	singlet	0.00
	$[Rn]6d^1\ e^-$ **	triplet	0.67
Pa(II)	$[Rn]5f^16d^2$	doublet	0.00
	$[Rn]5f^26d^1$	quartet	0.48
U(II)	$[Rn]5f^36d^1$	quintet	0.00
	$[Rn]5f^26d^2$	triplet	0.26/0.38 ‡

Table 4.24: Approximated electron configuration of metal centre, ground state spin and relative energy as calculated by RASSCF(n,2,2;6,13,6) active space in eV (n=14-16) for the Ce(II), Th(II), Pa(II) and U(II) complexes. * Composed of equal weighting of $[Xe]5d^26f^0$ and $[Xe]5d^06f^2$. ** in Th(II) 5f orbital is formally unoccupied in singlet state but is a loosely bound electron in triplet state (as can be seen in Figure 4.8. ‡ DFT(PBE(def2-TZVP)/CASSCF(4/12) relative energies in eV.

Looking at the approximated metal configurations and relative energies in Table 4.24 for the actinide complexes investigated, it can be seen that there is a reversal in whether it is ener-

getically more favourable to doubly occupy a 6d-orbital over singly occupying a 5f-orbital after Pa. However this observation should be tempered with the fact that for the U(II) complex the relative energies have been calculated using DFT(PBE0/def2-TZVP) and CASSCF(4/12) rather than RASSCF(16,2,2;6,13,6). This reversal is to be expected as it is in keeping with what has been reported in the literature, that the 5f shell of the actinides increases in stability with the nuclear charge [154].

Table 4.25 below shows the natural orbital occupation numbers of the 'strongly occupied' metal orbitals in the Ce(II), Th(II), Pa(II) and U(II) complexes using the RASSCF active space.

Complex	Spin	Natural Orbital Occupation Numbers	Rel. Energy
Ce(II)	Singlet	1.04 4f, 0.95 5d	2.87
	Triplet	0.99 4f, 1.00 5d	0.00
Th(II)	Singlet	1.89 6d	0.00
	Triplet	1.00 5f, 0.99 6d	0.67
Pa(II)	Doublet	1.00 5f, 1.87 6d	0.00
	Quartet	1.00 5f, 1.00 5f, 0.99 6d	0.48
U(II)	Quintet	0.99 5f, 0.99 5f, 0.99 5f, 0.99 6d	-
	Triplet*	1.00 5f 1.00 5f 0.93 5f 1.06 6d	-

Table 4.25: Natural Orbital Occupations of 'strongly occupied' metal orbitals in $[An(II)Cp_3]^-$ complexes using RASSCF(n,2,2;6,13,6) active space (n=14-16). * indicates calculation completed using CASSCF(4/12) active space.

It can be seen in Table 4.25 that there is very little deviation from integer occupations of the f orbitals in the actinide complexes, with the exception of the U(II) triplet state complex. However in the Ce(II) complex for the singlet state the 4f orbital has a natural orbital occupation of 1.04, this can be explained by examining the configurations which comprise the ground state and show that the singlet state is actually composed as roughly a 50:50 combination of a $4f^2$

and $5d^2$ (resulting in natural orbital occupations of 1.04 and 0.95 respectively). This, as discussed previously, shows that occupation of the f-orbitals results in a lowering of the energy making them comparable to the energy of the d orbitals.

Interestingly, and as discussed previously, similar occupations are also observed for the U(II) complex in the triplet state where it is composed of two relatively equally weighted configurations, which can be approximated as $6d^2\ 5f^1\ 5f^1$ and $6d^1\ 5f^2\ 5f^1$. The fact that this is not observed for the lower spin states of the Th(II) and Pa(II) complexes is further evidence of the decreasing energy gap between the 5f orbitals and 6d orbitals going across the actinide series. However again it should be noted that the triplet state for the U(II) complex was simulated with a smaller CASSCF(4/12) active space.

4.5.6 QTAIM Analysis

It was shown in Section 4.4 that the QTAIM methodology can be used to examine bonding and covalency in lanthanide and actinide systems, therefore to further characterise these unique low oxidation state actinide and lanthanide complexes, the Quantum Theory of Atoms in Molecules (QTAIM) method, described in Section 2.8, has been utilised. This methodology has been used to contrast and compare the bonding amongst the (II) oxidation state complexes. From the QTAIM analysis in the previous section it was shown that there is a strong variation in covalency with oxidation state. With that in mind, in addition to investigation of the bonding in the (II) complexes of U and Th, the respective analogous complexes of U and Th in the (III) and (IV) states have also been investigated in this section.

Analysis of $[\mathbf{M(II)Cp_3}]^-$ complexes

Tables 4.26 and 4.27 below show the value of electron density at the bond critical point (ρ_{BCP}) and the value of the delocalisation index (δ(A,B)) respectively for the M-C and C-C bonds in the M(II) complexes that have been investigated with the RASSCF(n,2,2;6,13,6) active space. It is

important to note that whilst the δ(M,C) data has been calculated as an average of every M-C bond, the ρ_{BCP} data has been averaged over only a few data points as the QTAIM methodology does not identify a bond path between each respective metal centre and every carbon, discussed in Section 2.8.

Complex	ρ_{BCP}(M-C)			ρ_{BCP}(C-C)		
	Average	Highest	Lowest	Average	Highest	Lowest
^{1}Ce(II)	0.0301	0.0311	0.0292	0.3069	0.3091	0.3057
^{3}Ce(II)	0.0310	0.0316	0.0304	0.3073	0.3094	0.3060
^{1}Th(II)	0.0397	0.0442	0.0350	0.2981	0.3050	0.2912
^{3}Th(II)	0.0440	0.0442	0.0398	0.2987	0.3055	0.2919
^{2}Pa(II)	0.0395	0.0416	0.0375	0.3045	0.3057	0.3019
^{4}Pa(II)	0.0414	0.0432	0.0391	0.3051	0.3065	0.3021
^{5}U(II)	0.0356	0.0366	0.0350	0.3061	0.3080	0.3047

Table 4.26: Value of the electron density at the bond critical point of the M-C and C-C bonds (ρ_{BCP}(M/C,C)) of M(II) complexes at DFT(PBE0/def2-TZVP) optimised structures.

It can be seen in Table 4.26 that the values of ρ_{BCP}(M-C) between the two different spin states are very similar. However despite the values being very similar it can also be seen that the higher spin state consistently has a higher value of ρ_{BCP}(M-C), this is perhaps a result of more significant occupation of the d orbitals in the lower spin state which point along the molecular axis. Interestingly and conversely to that which was observed for U/Ce hexachlorides, the value of ρ_{BCP}(M-C) for all actinde complexes is higher than that for the lanthanide complex, $[Ce(II)Cp_3]^-$. This can perhaps be attributed to a combination of the electronegativity of the two different ligands and the differences in the valence f-orbitals of Ce and U. The chloride ligand is highly electronegative and attracts electron density more strongly than the Cp ligand does, however because of the poor shielding of the Ce 4f orbitals the valence electrons feel a strong effective nuclear charge which results in electron sharing to a similar degree as uranium

hexachloride.

Looking at the values of ρ_{BCP}(C-C) it can be seen that there is very little difference between the different complexes with a variation between the highest and lowest value of 3%.

Complex	δ(M-C)			δ(C-C)		
	Average	Highest	Lowest	Average	Highest	Lowest
^{1}Ce(II)	0.1534	0.1774	0.1326	1.2861	1.3291	1.2641
^{3}Ce(II)	0.1485	0.1680	0.1284	1.2909	1.3325	1.2732
^{1}Th(II)	0.2042	0.2546	0.1591	1.2798	1.3453	1.2299
^{3}Th(II)	0.1989	0.2366	0.1613	1.2848	1.3424	1.2408
^{2}Pa(II)	0.2126	0.2594	0.1849	1.2755	1.2932	1.2605
^{4}Pa(II)	0.2078	0.2420	0.1847	1.2809	1.3039	1.2619
^{5}U(II)	0.1855	0.2219	0.1614	1.2757	1.3133	1.2595

Table 4.27: Delocalisation indices of M-C and C-C bonds (δ(M/C,C)) of M(II) complexes at DFT(PBE0/def2-TZVP) optimised structures.

Table 4.27 shows the delocalisation indices (δ), a measure of the number of electrons shared between two atoms, of the M-C bonds as well as of the C-C bonds of the Cp ring. It can be seen in the Ce(II), Th(II) and Pa(II) complexes that the higher spin state (i.e. the state with more unpaired f-electrons) has a slightly lower value of δ(M,C) than the lower spin state does. This is understandable, particularly in the case of cerium, as the higher spin state has greater occupation of the f-orbitals which are often considered to be localised to the metal centre due to the poor shielding of the nuclear charge. Conversely to the pattern observed for δ(M,C), it can be seen that the value of δ(C,C) is slightly higher for the higher spin state, this suggests that there is less donation of electron density from the Cp ring to the metal centre for the higher spin state.

It is also apparent in Table 4.27 that there is a difference in the value of δ(M,C) between the actinide (II) complexes, Th, Pa and U, and the lanthanide (II) complex, Ce. The value of δ(Ce,C) is approximately 20-25% lower than that of δ(Th/Pa/U,C), this can be explained by the poorer shielding of the 4f orbitals than the 5f orbitals making them more core-like and therefore less involved in bonding. This is also in agreement with the data presented in Table 4.26 for ρ_{BCP}(M-C). However there is a difference between the trends observed for ρ_{BCP}(M-C) and δ(M-C) between the different spin states of the same complex. Whereas the value of ρ_{BCP}(M-C) is higher for the higher spin state, the value of δ(M-C) is lower for the higher spin state. Whilst often these two measures show the same trend this is not always the case and has been shown in the literature [refs]. This is because the value of ρ_{BCP} describes the magnitude of the electron density at the minimum point whereas the value of δ describes the number of electrons shared between the entirety of the bond, the previous being a topological property and the latter an integrated property.

The QTAIM analysis completed here on these divalent lanthanide and actinide complexes have shown the differences in covalency and bonding between the different spin states. Differences between the Ce complex and the actinide complexes have been highlighted whilst the similarities in the three different actinide complexes has also been shown.

Analysis of U/ThCp$_3$ Complexes

Attention is now turned to a discussion and comparison of covalency and bonding in [U/Th(II)Cp$_3$]$^-$, U/Th(III)Cp$_3$ and [U/Th(IV)Cp$_3$]$^+$ complexes which will be referred to hereafter as U/Th(II), U/Th(III) and U/Th(IV) respectively. Presented below in Tables 4.28 and 4.29 are the values of the electron density at the bond critical point (ρ_{BCP}) and the values of the delocalisation index (δ(A,B)) respectively for the M-C and C-C bonds of the U/Th(II-IV) complexes. QTAIM analysis has been performed on the RASSCF(n,2,2;6,13,6) converged wavefuctions of U/Th(II-IV).

Again it is important to note that whilst the δ(M,C) data has been calculated as an average of every M-C bond, the ρ_{BCP} data has been averaged over only a few data points as the QTAIM methodology does not identify a bond path between Th/U and every carbon.

Complex	Occ.	ρ_{BCP}(M-C)			ρ_{BCP}(C-C)		
		Average	Highest	Lowest	Average	Highest	Lowest
^{1}Th(II)	[Rn]$6d^2$	0.0397	0.0442	0.0350	0.2981	0.3050	0.2912
^{2}Th(III)	[Rn]$6d^1$	0.0401	0.0414	0.0389	0.3071	0.3101	0.3055
^{1}Th(IV)	[Rn]	0.0378	0.0386	0.0369	0.3079	0.3112	0.3048
^{5}U(II)	[Rn]$6d^1 5f^3$	0.0356	0.0366	0.0350	0.3061	0.3080	0.3047
^{4}U(III)	[Rn]$5f^3$	0.0396	0.0405	0.0374	0.3063	0.3115	0.3035
^{3}U(IV)	[Rn]$5f^2$	0.0433	0.0450	0.0418	0.3086	0.3124	0.3050

Table 4.28: Value of the electron density at the bond critical point of the M-C and C-C bonds (ρ_{BCP}(M/C,C)) of the U/Th(II-IV) complexes at DFT(PBE0/def2-TZVP) optimised structures.

Looking at the data in Table 4.28 it appears that increasing the oxidation state of the U centre increases the value of the electron density at the BCP. This increase in ρ_{BCP} can be, at least partly, attributed to a shortening of the U-C bond lengths with increasing oxidation state, as shown in Table 4.17. Nevertheless, even considering the shortening of the average U-C bond length, an increase in the value of ρ can be observed and is in agreement with the increase with uranium oxidation state seen for the uranium hexachlorides in Chapter 4.4. The data for Th in Table 4.28 however does not follow a trend with the average value of ρ_{BCP}(Th-C) roughly the same value for all three oxidation states. This can be partly attributed to the DFT-optimised bond lengths of the three thorium complexes being very similar.

Looking at the values of ρ_{BCP} for the C-C bonds of the Cp ring it can be seen that there is

very similar values between all of the U(II-IV) and Th(II-IV) complexes, with a range of 0.001 a.u. Although the change in ρ_{BCP} is very small, a pattern can be seen that with increased oxidation state of the metal centre there is an increase in the value of ρ_{BCP}.

Table 4.29, below, shows the delocalisation indices (δ) of the M-C bonds as well as of the C-C bonds of the Cp ring in the DFT-optimised structures of U(II-IV) and Th(II-IV) complexes.

Complex	Occ.	δ(M-C)			δ(C-C)		
		Average	Highest	Lowest	Average	Highest	Lowest
^{1}Th(II)	[Rn]$6d^2$	0.2042	0.2546	0.1591	1.2798	1.3453	1.2299
^{2}Th(III)	[Rn]$6d^1$	0.2065	0.2520	0.1750	1.2741	1.3036	1.2559
^{1}Th(IV)	[Rn]	0.1686	0.1812	0.1587	1.3268	1.3503	1.3029
^{4}U(II)	[Rn]$6d^1 6f^3$	0.1855	0.2219	0.1614	1.2757	1.3133	1.2595
^{3}U(III)	[Rn]$5f^3$	0.1846	0.2102	0.1605	1.2515	1.2603	1.2425
^{2}U(IV)	[Rn]$5f^2$	0.1896	0.2066	0.1764	1.2719	1.2956	1.2344

Table 4.29: Delocalisation indices of M-C and C-C bonds (δ(M/C,C)) of Th/U(II-IV) complexes at DFT(PBE0/def2-TZVP) optimised structures.

Comparing the values of the different Th oxidation states it can be seen that there is a similarity in the values of δ(Th,C) for the Th(II) and Th(III) complexes but a significant difference for the Th(IV) complex. This can be partly explained by the fact that Th(IV) has a closed shell electronic structure. This makes the bonding in the Th(IV) complex, where there are no d- or f-electrons, much more ionic than in the Th(III) or Th(II) complexes, where there are d electrons but with minimal interaction with the ligands, and so there is less sharing of electrons in the Th-C bond. This argument is supported by the fact that all three oxidation states of uranium, which all have at least one f-electron, have a very similar value of δ(U,C). As with the data for ρ_{BCP}(U-C), there is very little difference in the values of δ(U-C) between the different

oxidation states.

4.5.7 Conclusions

In this chapter the first computational analysis of divalent actinide complexes with the RASSCF and QTAIM methodologies have been performed. The differences in the stability of the f-orbitals between the lanthanide cerium complex and analogous actinide thorium complex has been demonstrated and shown that occupation of an f-orbital in Th(II) is unfavourable whilst in Ce(II) it is favourable.

Furthermore it has been shown that going along the actinide series from Th to Pa to U, the f-orbitals of the divalent complex lower in energy to the point where in the U complex it is more energetically favourable to singly occupy the f-orbitals rather than a d-orbital. Although this conclusion should be tempered with the fact that it was too computationally expensive to use the large RASSCF(16,2,2;6,13,6) active space and conclusions have been instead drawn from a smaller CASSCF(4/12) for the U complex. This is an area for further research that could be completed in future projects.

The QTAIM data for the divalent complexes has also highlighted the differences between the lanthanide Ce complex and the three actinide complexes in that the actinide complexes are shown to be more covalent in their bonding than the Ce complex. This is at odds with what was observed in Chapter 4.4 where the degree of covalency between the Ce and U complexes was shown to be very similar. However it should be noted that the results of this section are in line with the vast majority of literature reports which have investigated the differences in bonding between actinide and lanthanide complexes.

Furthermore when other oxidation states of Th and U of the same complex were investigated with the QTAIM methodology it was shown that there was very little variation in covalency

with oxidation state for Th, whilst increasing the oxidation state for U resulted in an increase in covalency (as determined by QTAIM in Tables 4.29 and 4.28).

This section has shown that the RASSCF methodology can be applied to larger f-element systems. Also having shown in this chapter how the RASSCF methodology can be reasonably applied to systems where this is a much smaller degree of interaction between the metal centre and the ligand, this thesis now returns full circle and the next step is to look at how this methodology can be applied to f-element porphyrin systems.

Chapter 5

Towards a Model of f-block Expanded Porphyrins

5.1 Overview

In Chapter 3 different transition metal porphyrin systems and their active spaces were investigated, ultimately it was seen that despite providing a good qualitative picture of the electronic structure, quantitative agreement was harder to come by because of the limitations in the number of orbitals that could be included realistically in the active space. Having then investigated actinide and lanthanide complexes in Chapter 4, where the degree of interaction between the ligand and metal is reduced (and hence less of a need to correlate more orbitals in the active space), this Chapter combines the work of previous two chapters and focuses on f-block complexed expanded porphyrins, and in particular Lutetium Texaphyrin (LuTex).

Where a porphyrin ring is composed of four connected pyrrole rings, expanded porphyrin rings can be composed of 5 pyrroles (or likewise) upwards. As mentioned above, this chapter focuses on texaphyrin, who get their name because the cavity can be arranged to resemble the star on the flag of Texas, this is shown along with the structure of texaphyrin below in Figure 5.1.

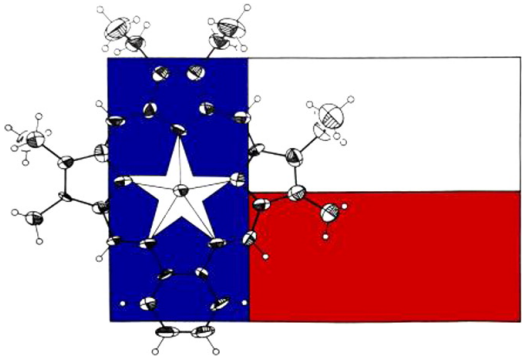

Figure 5.1: Texaphyrin Structure orientated around the Texas flag - Adapted from [8].

Because the texaphyrin ring contains five nitrogens rather than four it therefore has a larger cavity and so larger metal ions can be complexed. The practical uses of texaphyrins have been mainly medical; gadolinium texaphyrin (GdTex) has been shown to have applications as a contrast agent in medical imaging whilst lutetium texaphyrin (LuTex) has been used as a drug in photodynamic therapy (PDT) [155, 10, 129].

The latter of these two molecules, LuTex (the structure of which is shown in Figure 5.2), has been investigated and reported below using the CASPT2 methodology. As the texaphyrin ring is closely related to the porphyrin ring attempts have been made to apply a similar active space to those used in Chapter 3 on porphyrin systems to texaphyrin.

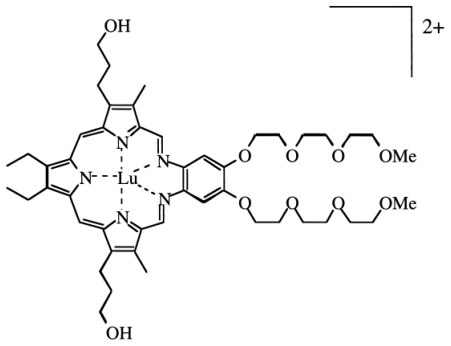

Figure 5.2: Experimental structure of Lutetium Texaphyrin (LuTex) Anion (Adapted from [9]).

5.2 Summary of previous works on Texaphyrins

The majority of texaphyrins have been developed by the Sessler group [**?**, 156, 8, 10, 157, 129] and have been synthesised with a variety of different metals complexed, including but not limited to manganese, gadolinium and lutetium [158, 127, 159, 157, 10, 156]. The general synthesis scheme of a texaphyrin is shown below in Figure 5.3.

The Sessler group have reported the synthesis and characterisation of many transition metal texaphyrins, including managanese texaphyrin. In particular they have have suggested the potential use of manganese texaphyrin (Mn(II)Tex) as a catalyst in the decomposition of peroxynitrate, an anion that has been reported to play a role in diseases such as amyotrophic lateral sclerosis (ALS) and cancer [158]. Magnetic moment measurements of Mn(II)Tex produced a magnetic moment of 6 μ_B which Groves *et al* attributed to the high spin state of Mn(II), this is in line with Mn(II)P in this work reported in Section 3.4.2. Furthermore Groves *etal* reported the result of UV-Vis experiments which showed that, like porphyrin ring systems, texaphyrins show a Q band and a Soret band excitation. The presence of a Q-like and Soret-like band have also been shown to exist in other transition metal texaphyrin systems, this has been reported by Sessler *et al* in 2002 [158].

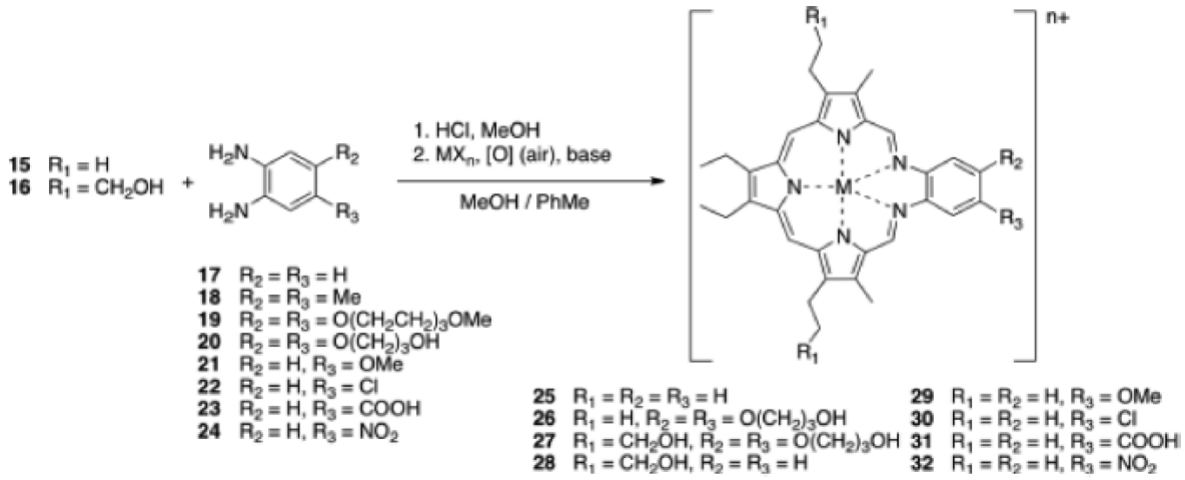

Figure 5.3: Schematic for synthesis of a texaphyrin macrocycle. Adapted from [8].

Reports in the literature have also shown the promise and potential of lanthanide texaphyrins as a photosensitising agent in photodynamic therapy (PDT). PDT is a method for kiling cancerous cells via the use of a photosensitising agent, which when exposed to a certain wavelength of light can excite singlet oxygen to the radical triplet oxygen which kills the cancerous cells. Lanthanide texaphyrins are obvious candidates as photosensitising agents because of their well defined band gap and similar energy gap to oxygen. Berns *et al* highlighted the potential use of a lutetium texaphyrin as a photosensitising agent in 1999 [160]. Their UV-Vis results showed a Q and Soret band at 1.68 and 2.70 eV respectively (converted from nm). Whilst the focus of this thesis is not medical, it should be noted that Berns *et al* commented that the lutetium texaphyrin complex studied showed a high potential for PDT.

Moving onto computational studies of texaphyrins; Cao and Dolg presented a series of Density Functional Theory calculations using the B3LYP *xc*-functional on lanthanum, gadolinium and lutetium texaphyrins (LaTex, GdTex and LuTex respectively) [161]. In their paper they examined both the structure and electronic excitation spectrum. Optimising the geometry of

the three texaphyrin structures they found that the three lanthanide ions sit in the cavity of the texaphyrin ring above the plane of the nitrogens. They calculated that there is a decreased distance from the mean plane of the nitrogens going from lanthanum to gadolinium to lutetium (0.73, 0.34 and 0.02 Årespectively), this is in line with the change in ion size of these three lanthanides. When the distance from the plane of the nitrogens are compared to experimental values Cao and Dolg showed that the experimental values are larger than those calculated with DFT, they attribute this to the experimental values having been determined from structures in solution where the lanthanide ion is additionally complexed with solvent molecules.

Cao and Dolg also investigated the electronic properties of LaTex, GdTex and LuTex. They found that for the three lanthanide complexes investigated there is effectively no change in the energies of the HOMO or LUMO of the texaphyrin ring when changing the lanthanide ion complexed and that the HOMO-LUMO energy gap is roughly 1.87 eV. Cao and Dolg's investigation of the excited states of the three lanthanide complexes with Time Dependent Density Functional Theory and the B3LYP *xc*-functional found, in line with experimental studies, a weak Q band and a strong intense Soret band. Their calculations predicted the intense Soret band at 2.71, 2.73 and 2.68 eV for LaTex, GdTex and LuTex respectively, a very small range which indicates that the lanthanide ion plays no part in the excitation of the Soret band. It also compliments their DFT findings that the HOMO-LUMO gap of these texaphyrin complexes is not affected by having a different lanthanide ion complexed.

Apart from the Dolg paper discussed above, the computational literature on LuTex is fairly sparse. As far as the author is aware there is no current studies on this complex using the CAS/RASSCF methodology.

5.3 Computational Details

Structures for LuTex were built with GaussView [66] and optimised with DFT (PBE0 [86]) using version 6.6 of the Turbomole program [67]. Calculations employed Ahlrichs-style basis sets of polarised triple-zeta quality (def2-TZVP) [68] and structures were constrained to C_s symmetry. Frequency analysis was also performed to ensure that minimum energy structures had been obtained.

CASSCF and RASSCF calculations were performed using the Molcas 8.0 code. CAS/RASSCF calculations have been performed on DFT(PBE0/def2-TZVP) optimised structures, as described above, and have employed relativistically contracted atomic natural orbital (ANO-RCC) basis sets [70] of polarised triple-zeta quality; (25s22p15d11f4g2h)/[8s7p4d3f2g] for Lu, (14s9p4d3f2g)/[4s3p2d] for C and N and (8s4p3d1f)/[3s2p] for H. Scalar relativistic effects have been included via the use of the 2nd order Douglas-Kroll-Hess Hamiltonian and the Cholesky decomposition has been used to reduce the computational cost of computing the two electron integrals. Like the DFT(PBE0/def2-TZVP)-optimisations the structure of LuTex has been constrained to C_s symmetry.

5.3.1 Description of Active Space

The orbitals included in the three active spaces employed in calculations were the same for both CASSCF and RASSCF calculations. Included were 16 electrons and 14 orbitals, shown in Figure 5.4, and has been based upon the CASSCF (16/14) active space employed in calculations on ZnP in Section 3.3.8. The similarities between ZnP and LuTex are obvious, both have a closed shell electronic structure with a metal complexed in the middle and it is expected that as a starting point the (16/14) active space should define the electronic excitations well. The orbitals included in the active spaces span the 69-75 a' and 50-56 a" irreps of C_s symmetry.

The three active spaces investigated for LuTex were a CASSCF(16/14), RASSCF(16,2,2;6,4,4)

and RASSCF(16,3,3;6,4,4). In the two RASSCF active spaces the "Gouterman"-like orbitals in the red box in Figure 5.4 were included in the RAS2.

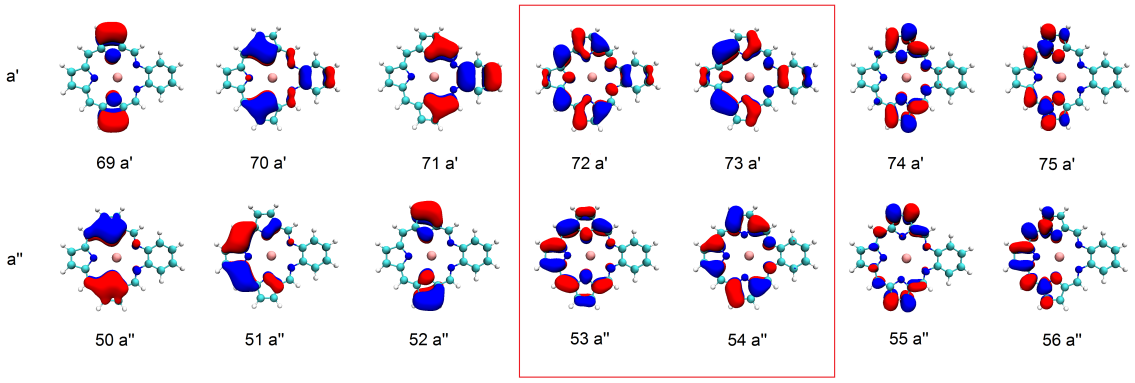

Figure 5.4: Orbitals (69-75 a' & 50-56 a") included in the CASSCF(16/14), RASSCF(16,2,2;6,4,4) and RASSCF(16,3,3;6,4,4) active spaces. The red box indicates orbitals included in the RAS2 of the two RASSCF active spaces. All orbitals generated with an isosurface of 0.03 a.u.

5.4 Results

5.4.1 Structure Optimisation

Table 5.1 gives the details of key coordinates in LuTex, calculated using DFT with the PBE0 *xc*-functional and def2-TZVP basis set, based upon the numbering scheme in Figure 5.5. For comparison, literature data of experimentally determined bond lengths and angles are also provided.

It can be seen from Table 5.1 that there is a difference between the experimental values and the DFT(PBE0/def2-TZVP)-optimised value of the Lu-N bonds of ∼0.05 Å. Although the difference in bond lengths is fairly significant, most of the difference can almost certainly be attributed to the fact that the experimental value has been measured from the solvated 8-co-ordinate [LuTex][NO_3][CH_3O] complex whilst the DFT geometry optimisations have been

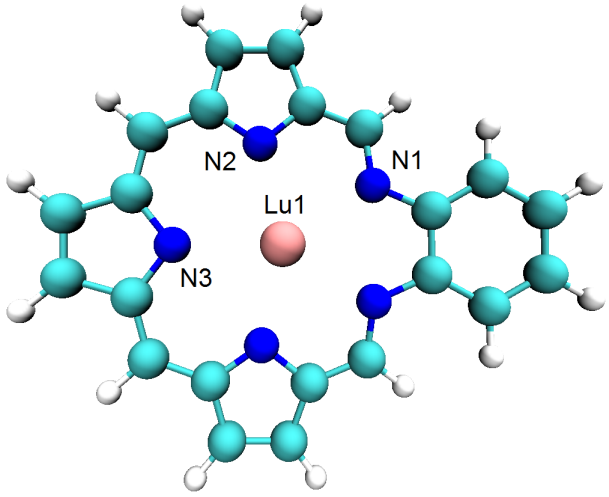

Figure 5.5: DFT-optimised (PBE0/def2-TZVP) structure of LuTex and labeling scheme used for Table 5.1.

Co-ordinate	PBE0	Experiment [157]
R(Lu1-N1)	2.375	2.428
R(Lu1-N2)	2.279	2.312
R(Lu1-N3)	2.365	2.421
A(N1-Lu1-N3)	160.1	-
A(N1-Lu1-N2)	68.4	63.5
A(N2-Lu1-N3)	74.8	72.8

Table 5.1: Key co-ordinates of optimised LuTex structure (DFT(PBE0/def2-TZVP)). R indicates bonds and are presented in Angstroms (Å), whilst A indicates angles and are indicated in °.

completed on the LuTex 2+ ion. This is a discrepancy that was also reported by Cao and Dolg in their paper on lanthanide texaphryins [161]. This same discrepancy is also seen in the difference in bond angles.

5.4.2 Analysis of Ground State RASSCF Wavefunction

The natural occupation numbers of the fourteen orbitals included in the three active spaces are shown in Table 5.2.

Natural Molecular Orbital	CASSCF(16/14)	RASSCF (16,2,2;6,4,4)	RASSCF (16,3,3;6,4,4)
69 a'	1.923	1.947	1.935
70 a'	1.970	1.982	1.976
71 a'	1.984	1.987	1.985
72 a'	0.217	0.196	0.211
73 a'	1.885	1.907	1.890
74 a'	0.070	0.049	0.059
75 a'	0.049	0.035	0.043
50 a"	1.975	1.985	1.979
51 a"	1.950	1.965	1.956
52 a"	1.926	1.948	1.937
53 a"	0.106	0.086	0.099
54 a"	1.843	1.832	1.835
55 a"	0.069	0.049	0.058
56 a"	0.036	0.025	0.030

Table 5.2: Occupation numbers of natural orbitals included in LuTex active space for the ground state $1\ ^1A'$.

Table 5.2 shows that application of all active spaces results in similar occupation numbers for each orbital, particularly when comparing the CASSCF(16/14) with the RASSCF(16,3,3;6,4,4) active spaces. It is also obvious from Table 5.2 that there is significant multiconfigurational character in the texaphyrin ring, evident by the natural occupation numbers differing from 2 or 0 by more than 0.02. In particular the "Gouterman-like" orbitals (72/73 a' and 53/54 a") show a large deviation from integer occupations.

Attempts were made to include the Lutetium f-orbitals into an expanded active space to form a RASSCF(30,2,2;6,14,4) active space. However, similar to that seen in Section 3.3.8 when attempts were made to include the Zn d-orbitals into the RASSCF(16,2,2;6,4,4) active space (to form a RASSCF(26,2,2;6,9,4)), the 4f-orbitals rotated out of the active space. When the Lu 4f-orbitals were forced into active space this produced a state with a higher energy than the one where they had rotated themselves out of the active space. Additionally the occupation numbers of all the 4f orbitals forced into the active space was 2.00. From this it can be concluded that the the Lu 4f-orbitals are core-like and can be considered to be non-bonding with the texaphyrin ring, therefore inclusion in the active space is unnecessary.

Comparison of LuTex with FBP and ZnP

As mentioned previously the texaphyrin ring is closely related to the porphyrin ring. The computational literature work available is far richer for porphyrin systems than it is texaphyrin systems, it makes sense therefore to make comparisons in this work between LuTex and ZnP, both systems with a closed electronic shell. Furthermore because it was shown in Section 3.3.13 that there is similarities between ZnP and FBP, comparisons between LuTex and FBP have also been included here.

Table 5.3 presents the natural orbital occupation numbers of the Gouterman orbitals of FBP (4 b_{2g}/b_{3g}, 5 b_{1u} and 2 a_u) and ZnP (5 b_{2g}/b_{3g}, 5 b_{1u} and 2 a_u) as well as the occupations of natural

orbitals in LuTex (72 a', 53 a'', 73 a' and 54 a'') which could be described as Gouterman-like, using a CASSCF(16/14) active space.

Orbital Symmetry Label (LuTex/FBP/ZnP)	LuTex	FBP	ZnP
72 a' / 4 b_{3g} / 5 b_{3g}	0.22	0.14	0.11
73 a' / 5 b_{1u} / 5 b_{1u}	1.89	1.89	1.91
53 a'' / 4 b_{2g} / 5 b_{2g}	0.11	0.12	0.12
54 a'' / 2 a_u / 2 a_u	1.84	1.88	1.90

Table 5.3: Comparison of natural orbital occupation numbers of "Gouterman" orbitals of ground state of LuTex, FBP and ZnP using CASSCF(16/14) active space.

It can be seen in Table 5.3 that the Gouterman orbitals have very similar natural orbital occupation numbers in LuTex, FBP and ZnP, this can be seen as a justification of using the same active space for all three systems. It also shows how closely related the electronic structure of poprhyrins are to expanded porphyrins. The biggest deviation between the three occurs for one of the "Gouterman LUMOs" (72 a', 4 b_{3g}, 5b_{3g}) which shows significantly more occupation in LuTex than it does FBP or ZnP. Interestingly the occupation of the "Gouterman HOMOs" are very similar (particularly between LuTex and FBP) which suggests the multiconfigurational character in these complexes is not simply confined to the Gouterman-like orbitals but in fact the whole texaphyrin ring, shown by the fact that the natural orbitals occupations of 72 a' and 54 a" added together is greater than 2.00.

5.4.3 Simulation of Excited States

Chapter 3 showed that using Time Dependent Density Functional Theory (TDDFT) with different xc-functionals produced different values for the vertical excitation energies. It was then shown that accurate values could be produced using the CASPT2(16/14) active space as well

as the RASPT2 derivatives. With this in mind and encouraged by the similarities between the porphyrin systems and LuTex ground state presented above, an investigation into the vertical excitation energies of LuTex with the active spaces has also been completed.

Table 5.4 shows the calculated vertical excitation energies of the seven lowest excited states as calculated by the three different active spaces; CASSCF(16/14), RASSCF(16,2,2;6,4,4) and RASSCF(16,3,3;6,4,4). Table 5.4 shows these calculated vertical excitation energies both with and without the addition of second order perturbation theory (PT2).

Method	1 A'	2 A'	3 A'	4 A'	1 A"	2 A"	3 A"	4 A"
CASSCF(16/14)	0.00	2.45	2.87	3.08	2.11	2.98	3.39	4.02
RASSCF(16,2,2;6,4,4)	0.00	2.70	3.27	3.85	2.28	3.63	3.94	4.37
RASSCF(16,3,3;6,4,4)	0.00	2.49	2.92	3.16	2.15	3.05	3.45	4.05
CASPT2(16/14)	0.00	2.59	2.81	2.97	1.82	2.74	3.21	3.83
RASPT2(16,2,2;6,4,4)	0.00	2.60	3.10	3.21	1.76	3.12	3.27	3.87
RASPT2(16,3,3;6,4,4)	0.00	2.55	2.78	2.90	1.75	2.69	3.10	3.76
Experiment [10] *	-	2.63	2.99	-	1.69	3.54	-	3.81

Table 5.4: Seven lowest calculated vertical excitation energies in eV of LuTex using three different active spaces; CASSCF (16/14), RASSCF (16,2,2;6,4,4) and RASSCF (16,3,3;6,4,4). Results are shown both with and without second order perturbation theory (PT2). Also shown are experimental values * Experimental values have been converted from nm.

Comparing the vertical excitation energies presented in Table 5.4 it can be seen that the energies calculated with the RASSCF(16,3,3;6,9,4) active space are closer in energy to the CASSCF(16/14) than those calculated using the RASSCF(16,2,2;6,9,4) are. This suggests that the transitions from the ground state to excited states contain a significant contribution from triplet and above excitations. This is an observation that was also made about the RASSCF

active space for the porphyrin systems. It can also be seen that the addition of second order perturbation theory does not change the values of the excitation energies massively, however significantly does bring them closer to experimental values.

Comparing the values calculated by the three different active spaces to aqueous phase experimental results shows that all three active spaces simulate the excitation energies well. The vertical excitation to the 2 A' state in particular is accurately predicted by all three active spaces with a maximum deviation of 0.08 eV for the RASPT2(16,3,3;6,9,4) active space. The values simulated using the CASPT2(16/14) active space are overlayed the experimental absorption spectrum below in Figure 5.6 to visualise the good agreement that is obtained.

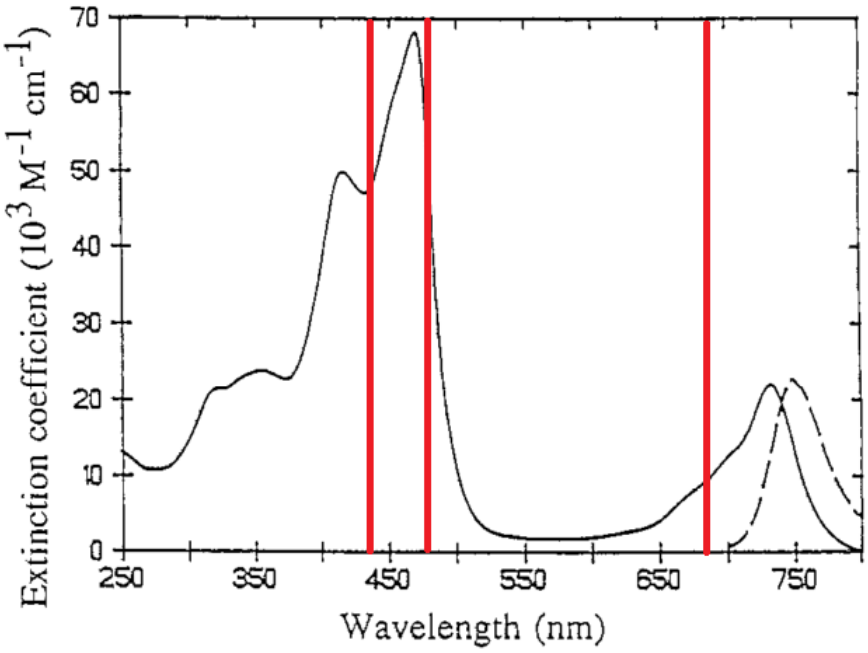

Figure 5.6: Experimental absorption spectrum of LuTex adapted from [10] with CASPT2(16/14) excitation energies overlayed in red.

5.5 QTAIM Analysis

Like with previous chapters the Quantum Theory of Atoms in Molecules methodology has been applied here to LuTex to investigate the bonding. Table 5.5 below shows the value of the electron density at the BCP (ρ_{BCP}) and the delocalisation index (δ) of the Lu-N bonds in LuTex.

Active Space	ρ_{BCP}(Lu-N)			δ(Lu-N)		
	Average	Max	Min	Average	Max	Min
CASSCF(16/14)	0.0604	0.0676	0.0552	0.2735	0.3007	0.2441
RASSCF(16,2,2;6,4,4)	0.0603	0.0675	0.0551	0.2763	0.3079	0.2447
RASSCF(16,3,3;6,4,4)	0.0603	0.0676	0.0552	0.2704	0.3040	0.2417

Table 5.5: Values of ρ_{BCP}(Lu-N) and δ(Lu-N) as calculated with the QTAIM methodology on the converged ground state wavefunction of three different active spaces; CASSCF(16/14), RASSCF(16,2,2;6,4,4) and RASSCF(16,3,3;6,4,4).

It can be seen in Table 5.5 that the values of both ρ_{BCP}(Lu-N) and δ(Lu-N) are almost identical when using the converged wavefunction of all three active spaces.

As has been discussed in previous sections, a value of ρ_{BCP} of under 0.1 is typically considered an ionic bond. It can therefore be seen in Table 5.5 that the Lu-N bond is very much an ionic bond. However it is interesting that this value of ρ_{BCP} is slightly higher than those published recently for $[LuBTP]^{3+}$ [162]. Bistriazolpyridine (BTP) is a ligand which has been investigated extensively [refs] as a potential ligand for the separation of nuclear waste. The fact that Lu-N bond, as determined by these results, is more covalent in LuTex than LuBTP suggests that texaphryin rings may be potential ligands for nuclear waste separation.

5.6 Conclusions and Future Work

In this chapter lutetium texaphyrin has been investigated with the CASSCF(16/14), RASSCF (16,2,2;6,4,4) and RASSCF(16,3,3;6,4,4) active spaces. The ground state wavefunction obtained using all three active spaces shows a considerable degree of multiconfigurational behaviour, with occupations of all orbitals included in the active spaces differing from integer values. As with what was observed for porphyrin systems in Chapter 3 the RASSCF(16,3,3;6,4,4) active space produces results close to those produced by using the CASSCF(16/14) active space. When the ground state natural orbital occupations for LuTex are compared to those obtained using the same active spaces for ZnP (a rough transition metal analogue) and FBP, remarkable similarities in occupations are observed.

To further justify the use of the 16 electron 14 orbital active spaces vertical excitation energies were also simulated for LuTex. It was found that when compared to an experimental absorption spectrum the vertical excitation energies predicted by the three active spaces, particularly the CASSCF(16/14), produce accurate excitation energies.

As far as the author is aware this is the first study of expanded porphyrins with the CAS/RASSCF methodology. This chapter has shown the similarities in electronic structure between texaphyrins and porphyrins, and more specifically that the 16 electron and 14 orbital active space that had been developed for porphyrin systems can be applied to LuTex. Furthermore as the lutetium orbitals have not been included in the active space it is not unreasonable to suggest that this active space could also be applied to other lanthanide texaphyrins systems such as gadolinium texaphyrin, this is one area for future work to build upon the work presented in this thesis.

In addition to an analysis of the CAS/RASSCF wavefunctions and excitation energies, QTAIM analysis has also been performed which has highlighted a potential application of the expanded

poprhyrins in nuclear waste separation. It has been discussed in the literature that the degree of covalency between the metal centre and ligand can drive the search for potential separation ligands [163, 138, 164, 165]. The QTAIM data presented in this chapter has shown that the Lu-N bond in LuTex is more covalent than one of the currently investigated ligands, BTP, as measured by the QTAIM indicators ρ_{BCP}(Lu-N) and δ(Lu-N). This is another area where future work can build upon the work presented here, the covalency of other lanthanide/actinide texaphyrin complexes should be investigated to determine the potential of texaphyrins (and other expanded porphyrins) as separation ligands.

Chapter 6

Concluding Remarks

This thesis has covered the use of the RASSCF methodology across several related chemical problems. Chapter 3 began with an investigation of the ground state of free base porphryin using Density Functional Theory (DFT) and a variety of different *xc*-functionals, all of which incorporated differing percentages of exact Hartree-Fock exchange ranging from 0% in the TPSS *xc*-functional to 50% in the BHLYP *xc*-functional. For free base porphyrin (FBP) it was found that results were consistent amongst the five different *xc*-functionals for ground state structure optimisations both simulated in the gas phase and in solution. Furthermore when compared to experiment it was shown that all *xc*-functionals reproduce experimental structures to a good degree of accuracy. Following structure optimisations of FBP, excited states were then calculated using the Time Dependent Density Functional Theory (TDDFT) methodology. The TDDFT results showed a slight variation with *xc*-functional used, however all *xc*-functionals reproduce the Q and B band excitations to a reasonable degree of accuracy.

Following the preliminary DFT and TDDFT calculations, Complete and Restricted Active Space Self Consistent Field (CAS/RASSCF) calculations were performed on FBP using a variety of active spaces to calculate the Q and B band excitations of FBP. These active spaces were based upon those reported in the literature. It was found that the smallest of the active spaces

investigated, a CASSCF(4/4) active space - including just the Gouterman orbitals, was too small and produced very large deviations from experiment. As the size of the active space was increased the accuracy of the simulated excitation increased. It was also seen that truncating the wavefunction by going from a CASSCF(16/14) active space to a RASSCF(16,3,3;6,4,4) decreased the accuracy of simulated excitations for FBP very slightly but dramatically decreased the computational cost.

To further justify and explore the use of the CAS/RASSCF methodology on porphyrin systems the next logical complexes to investigate were regular porphyrins, which like FBP have a closed electronic shell. The regular porphyrins; magnesium and zinc porphyrin, were investigated with the same five *xc*-functionals used for FBP to optimise structures (with DFT) and excited states (with TDDFT). Like what was observed for FBP, there is very little deviation in structures optimised with the different *xc*-functionals for MgP and ZnP. Again for the excited states there is a weak *xc*-functional dependence when calculating the Q and B band exitations for MgP and ZnP. When the active spaces used for FBP are applied to MgP and ZnP an almost identical pattern appears, the CASSCF(4/4) active space is far too small and leads to large deviations from experiment whilst the 16 electron and 14 orbital active space simulates excitation energies to a good degree of accuracy. For ZnP, which has a full 3d-shell, attempts were also made to include these d-electrons in the active space, however it was discovered that these were effectively core like and rotated themselves out of the active space.

The basis for the applicability of the RASSCF method in porphyrin systems was established with the results of FBP, MgP and ZnP described above. The real challenge in these calculations comes in simulating an irregular open shell transition metal porphyrin. Manganese porphyrin (MnP) was the primary focus because it has a half full d-shell and can have low, intermediate or high spin. When the MnP ground state was simulated with DFT using the five different *xc*-functionals it was found that there was a strong functional dependence on which

spin state was the ground state. It was seen that *xc*-functionals with higher percentages of HF exchange (BHLYP, PBE0 and B3LYP) predicted the ground state to be the high spin state (s=$^5/_2$) whilst those *xc*-functionals with lower percentages predict the intermediate spin state (s=$^3/_2$), experimentally it has been determined that manganese is high spin in MnP. This discrepancy does not occur when the CAS/RASSCF methodology is used regardless of the active space employed, even with the minimal CASSCF(9/9) active space. Interestingly when excited states are simulated for MnP using TDDFT more accurate results are obtained with the *xc*-functionals with lower percentages of Hartree-Fock exchange. Furthermore all of the active spaces investigated showed a significant deviation from experiment in the simulated B band of up to 1eV. However through the use of density difference plots it was shown that TDDFT appears to be simulating a different excitation to that which CAS/RASSCF was. Through examination of the natural orbital occupation numbers of the different CAS/RASSCF active spaces it was shown that the MnP B band excitation involves a change in the metal spin state, which can not be properly reproduced by TDDFT. When the ΔSCF method is used instead of TDDFT to simulate the vertical excitation energy of the B band it was shown that in fact the *xc*-functionals with higher Hartree-Fock exchange included predict more accurate excitation energies. This study on MnP has shown that whilst the RASSCF method can offer qualitative insight to the electronic structure of complex and multiconfigurational molecules, quantitative agreement is difficult to achieve without a large active space. Considering this, attention was moved to f-element complexes where the degree of interaction between ligand and metal is known to be lower than for transition metals, therefore the RASSCF methodology could be further investigated without being hindered by the computational cost of needing more orbitals included in the active space.

Chapter 4 began with a study of cerium and uranium hexachlrides, these molecules were chosen for investigation because recent experimental literature had suggested that the degree of covalency between cerium and uranium in these molecules was similar. In addition to this

they are small molecules meaning that a large active space can be considered here. Because of the small size and high symmetry geometry optimisations were performed at the RASSCF and RASPT2 level of theory in addition to DFT geometry optimisations. By inspection of the natural orbital occupations and visualisation of the orbitals it can be seen that there is increased multiconfigurational character with increased oxidation state. With the aid of the Quantum Theory of Atoms in Molecules (QTAIM) methodology the bonding in these cerium and uranium hexachlorides was further investigated and the degree of covalency quantified. It was seen in the ρ_{BCP}(M-Cl) data that there are very similar values obtained between the U(III) hexachloride complex and the Ce(III) hexachloride complex as well as between the U(IV) hexachloride complex and Ce(IV) hexachloride complex. Furthermore there is a clear trend in increased covalency in the bond with increased oxidation state of the metal. In agreement with the ρ_{BCP}(M-Cl) data is the δ(M-Cl) which also shows comparable covalency between the uranium and cerium complexes of the same oxidation state. The δ(M-Cl) data also shows, like the ρ_{BCP}(M-Cl) data that there is an increase in covalency with oxidation state of the metal. This study showed the use of the RASSCF methodology in f-block complexes and also how, with the aid of the QTAIM methodology, the bonding and covalency can be characterised and quantified.

Having shown the efficacy of the method with smaller f-block complexes, Chapter 4 then moved on to look at larger, more novel f-block complexes, namely cerium, thorium, protactinium and uranium triscyclopentene. The (II) oxidation state of all four complexes were investigated as well as the (III) and (IV) oxidation state of the uranium and thorium complexes. By examination of the natural orbital occupation numbers and the relative energy differences between different spin states of the (II) oxidation state, the differences between the lanthanide $[Ce(II)Cp_3]^-$ and the actinide analogue $[Th(II)Cp_3]^-$ could be seen. The major difference between the two complexes was shown to be the cerium complex favouring the triplet spin state whilst the thorium complex favouring the singlet spin state, this was attributed to the difference in energy between their respective d and f orbitals. It was also shown that there was a trend in

the relative energy difference of the actinide complexes for the (II) oxidation state going across the actinide series. Whilst the thorium and protactinium complex favoured a lower spin state, the uranium complex favoured a higher spin state. Again this trend can be attributed to a lowering in energy of the 5f orbitals going right across the actinide series. The bonding and covalency in these complexes was again quantified with the aid of the QTAIM methodology. It was seen that unlike what was observed in the hexachloride complexes there was a difference between the cerium complex and the actinide complexes, in the covalency of the metal-ligand bonds, this was seen in both the ρ_{BCP}(M-C) and δ(M-C) data. When the different oxidation states of the uranium and thorium complexes were compared it was seen that there was very little difference in covalency as measured by ρ_{BCP}(M-C) and δ(M-C) for thorium, this has been partly attributed to the three different oxidation states of thorium having very similar bond lengths. For uranium however, like what was observed for the hexachlorides, the QTAIM data for uranium shows increased covalency with increased oxidation state. Having shown the use of the RASSCF methodology on larger f-block complexes, this thesis turned back to the original area of investigation and looked at expanded porphyrin complexes.

Chapter 5 of this thesis looked at expanded porphyrins, and more specifically lutetium texaphyrin. Three of the same active spaces (CASSCF(16/14), RASSCF(16,2,2;6,4,4) and RASSCF (16,3,3;6,4,4)) that had been used on the regular porphyrins; FBP, MgP and ZnP, was also applied to LuTex. Attempts were also made to include the lutetium f-orbitals in the active space however this proved unsuccessful as it had been with attempts to include the zinc d-orbitals in the active space in Chapter 3. Inspection of the natural orbital occupation numbers revealed obvious multiconfigurational character with all orbitals deviating significantly from integer occupations. When the natural orbital occupations were compared to those obtained from the same active spaces for FBP and ZnP from Chapter 3 incredible similarities in the occupations were observed. The three active spaces were then used to simulate excitation energies, the simulated energies showed good agreement with experimental absorption spectra. Having shown

the multiconfigurational character in the texaphyrin ring, in addition to the the good agreement with experiment obtained for the excitation energies, this thesis has shown the potential applicability of the RASSCF method to expanded porphyrins. To further clarify the bonding QTAIM analysis was also completed which showed potential new applications for the expanded porphyrins as potential separation ligands.

Overall this thesis has shown the potential of the RASSCF methodology to deal with a variety of different chemical properties, particularly those where the popular density functional theory methodology fails. It has been shown how with the aid of other tools such as QTAIM the RASSCF methodology can be used for in depth investigation of the electronic structure and bonding of a variety of different complexes.

Chapter 7

Bibliography

[1] J. P. Perdew. Jacob's ladder of density functional approximations for the exchange-correlation energy. *AIP Conference Proceedings*, 577:1–20, 2001.

[2] M. K. Sabbe, M. Reyniers, and K. Reuter. First-principles kinetic modeling in heterogeneous catalysis: an industrial perspective on best-practice, gaps and needs. *Catalysis Science & Technology*, 2:2010, 2012.

[3] C. J. Cramer. *Essentials of Computational Chemistry - Second Edition*. Wiley, 2004.

[4] S. Akimoto, T. Yamazaki, I. Yamazaki, and A. Osuka. Excitation relaxation of zinc and free-base porphyrin probed by femtosecond fluorescence spectroscopy. *Chemical physics letters*, 309:177–182, 1999.

[5] Y. Parra, R. E. Ferrer, K. Montero, and M. Martínez. Spectroscopy of Quinoline Antimalarials Drugs Interactions with Fe(III)PPIX. *Thesis*, 2011.

[6] D. Dolphin. *The Porphyrins V3: Physical Chemistry*. Elsevier Science, 2012.

[7] S. T. Liddle. The renaissance of non-aqueous uranium chemistry. *Angewandte Chemie International Edition*, 54(30):8604–8641, 2015.

[8] C. Preihs, J. F. Arambula, D. Magda, H. Jeong, D. Yoo, J. Cheon, Z. H. Siddik, and J. L. Sessler. Recent developments in texaphyrin chemistry and drug discovery. *Inorganic Chemistry*, 52(21):12184–12192, 2013.

[9] M. S. Blumenkranz, K. W. Woodburn, F. Qing, S. Verdooner, D. Kesse, and R. Miller. Lutetium texaphyrin (lu-tex): a potential new agent for ocular fundus angiography and photodynamic therapy. *American Journal of Ophthalmology*, 129(3):353 – 362, 2000.

[10] J. L Sessler, W. C. Dow, D. O. Connor, A. Harriman, G. Hemmi, T. D. Modyb, R. A. Miller, F. Qing, S. Springs, K. Woodburn, and S. W. Young. Biomedical applications of Lutetium (III) texaphyrins as potential photodynamic therapy photosensitizers. *Journal of Alloys and Compounds*, 249:146–152, 1997.

[11] L Edwards and DH Dolphin. Porphyrins XVII. Vapor absorption spectra and redox reactions: tetraphenylporphins and porphin. *Journal of Molecular Spectroscopy*, 32:16–32, 1971.

[12] M. Gouterman. *The Porphyrins, Vol III.* Academic Press, New York, 1978.

[13] J. F. de Wet, M. R. Caira, and B. J. Gellatly. The crystal structures of hexahalouranates. II. Triphenylbenzylphosphonium hexachlorouranate(V). *Acta Crystallographica Section B*, 34(4):1121–1124, 1978.

[14] M. W. Löble, J. M. Keith, A. B. Altman, S. C. E. Stieber, E. R. Batista, K. S. Boland, S. D. Conradson, D. L. Clark, L. J. Pacheco, S. Kozimor, R. L. Martin, S. G. Minasian, A. C. Olson, B. L. Scott, D. K. Shuh, T. Tyliszczak, M. P. Wilkerson, and R. Zehnder. Covalency in Lanthanides. An X-ray Absorption Spectroscopy and Density Functional Theory Study of LnCl6x(x = 3, 2). *Journal of the American Chemical Society*, 137(7):2506–2523, 2015.

[15] E. Boss, C. Den Auwer, C. Berthon, P. Guilbaud, M. S. Grigoriev, S. Nikitenko, C. Naour, C. Cannes, and P. Moisy. Solvation of UCl62 anionic complex by MeBu3N+, BuMe2Im+, and BuMeIm+ cations. *Inorganic Chemistry*, 47(13):5746–5755, 2008.

[16] J. C. Taylor and P. W. Wilson. Neutron and X-ray powder diffraction studies of the structure of uranium hexachloride. *Acta Crystallographica Section B*, 30(6):1481–1484, 1974.

[17] N. Kaltsoyannis and P. Scott. *The f elements*. Oxford chemistry primers. Oxford University Press, 1999.

[18] R. R. Langeslay, M. E. Fieser, J. W. Ziller, F. Furche, and W. J. Evans. Synthesis, structure, and reactivity of crystalline molecular complexes of the [C5H3(SiMe3)2]3Th1 anion containing thorium in the formal +2 oxidation state. *Chemical Science*, 6(1):517–521, 2014.

[19] M. R. Macdonald, M. E. Fieser, E. Bates, J. W. Ziller, F. Furche, and W. J. Evans. Identification of the +2 Oxidation State for Uranium in a Crystalline Molecular Complex. *Journal of the American Chemical Society*, 135:13310–13313, 2013.

[20] G. Moore. Cramming more components onto integrated circuits. *Electronics*, 1965.

[21] D. Hartree. *Procession of Royal Society of London*, 113:621, 1928.

[22] F. Jensen. *Introduction to Computational Chemistry*. Wiley, 2007.

[23] D. Taylor. The pharmaceutical industry and the future of drug development. In *Pharmaceuticals in the Environment*, pages 1–33. The Royal Society of Chemistry, 2016.

[24] R. C. Ewing, W. J. Weber, and J. Lian. Nuclear waste disposalpyrochlore: Nuclear waste form for the immobilization of plutonium and minor actinides. *Journal of Applied Physics*, 95(11):5949–5971, 2004.

[25] N.A. Chapman and I.G. McKinley. *The geological disposal of nuclear waste*. Wiley, 1987.

[26] V. Poltev. *Molecular Mechanics: Method and Applications*, pages 259–291. Springer, 2012.

[27] G. R. Fowles. Solution of the schrdinger equation for the hydrogen atom in rectangular coordinates. *American Journal of Physics*, 30(4):308–309, 1962.

[28] M. Born and K. Huang. *Dynamical Theory of Crystal Lattices*. International series of monographs on physics. Clarendon Press, 1998.

[29] C. Trindle and D. Shillady. *Electronic Structure Modeling: Connections Between Theory and Software*. CRC Press, 2008.

[30] D.J. Griffiths. *Introduction to Quantum Mechanics*. Pearson international edition. Pearson Prentice Hall, 2005.

[31] P. A. M. Dirac. A new notation for quantum mechanics. *Mathematical Proceedings of the Cambridge Philosophical Society*, 35(3):416418, 1939.

[32] B. I. Dunlap, J. W. D. Connolly, and J. R. Sabin. On firstrow diatomic molecules and local density models. *The Journal of Chemical Physics*, 71(12):4993–4999, 1979.

[33] P Hohenberg and W Kohn. Inhomogeneous electron gas. *Physical review*, 155(1962), 1964.

[34] W Kohn and L J Sham. Self-Consistent Equations Including Exchange and Correlation Effects. *Physical Review*, 140(4A):A1133–A1138, 1965.

[35] C. Lee, W. Yang, and R. G. Parr. Development of the Colle-Salvetti correlation-energy formula into a functional of the electron density. *Physical Review B*, 37:785–789, 1988.

[36] W. Koch and M. C. Holthausen. *A Chemist's Guide to Density Functional Theory*, volume 3. Wiley, 2001.

[37] J. Tao, J. P. Perdew, V. N. Staroverov, and G. E. Scuseria. Climbing the density functional ladder: Nonempirical meta˘generalized gradient approximation designed for molecules and solids. *Physical Review Letters*, 91:146401, 2003.

[38] A. D. Becke. Density-functional thermochemistry. III. The role of exact exchange. *The Journal of Chemical Physics*, 98(7):5648, 1993.

[39] A. D. Becke. Completely numerical calculations on diatomic molecules in the local-density approximation. *Physical review. A*, 33(4):5–7, 1986.

[40] R. P. Feynman. Forces in molecules. *Physical Review*, 56:340–343, 1939.

[41] W. Kohn. Nobel Lecture: Electronic structure of matterwave functions and density functionals. *Reviews of Modern Physics*, 71(5):1253–1266, 1999.

[42] E. Runge and E.K.U Gross. Density-functional theory for time-dependent systems. *Physical Review Letters*, 52(12), 1984.

[43] M E Casida and M Huix-Rotllant. Progress in time-dependent density-functional theory. *Annual review of physical chemistry*, 63:287–323, 2012.

[44] M. Petersilka, U. Gossmann, and E. Gross. Excitation Energies from Time-Dependent Density-Functional Theory. *Physical Review Letters*, 76(8):1212–1215, feb 1996.

[45] E. K. U. Gross and W. Kohn. Local density-functional theory of frequency-dependent linear response. *Physical Review Letters*, 55:2850–2852, 1985.

[46] J. Grfenstein, E. Kraka, and D. Cremer. The impact of the self-interaction error on the density functional theory description of dissociating radical cations: Ionic and covalent dissociation limits. *The Journal of Chemical Physics*, 120(2):524–539, 2004.

[47] P. Mori-Snchez, A. J. Cohen, and W. Yang. Many-electron self-interaction error in approximate density functionals. *The Journal of Chemical Physics*, 125(20):201102, 2006.

[48] J. P. Perdew and A. Zunger. Self-interaction correction to density-functional approximations for many-electron systems. *Physical Review B*, 23(10):5048–5079, 1981.

[49] P. Malmqvist, A. Rendell, and B. Roos. The Restricted Active Space Self-Consistent-Field Method - Implemented with a Split Graph Unitary Group Approach. *The Journal of Physical Chemistry*, 94(14):5477–5482, 1990.

[50] J. Olsen, B. Roos, P. Jorgensen, and H. Jorgensen. Determinant based configuration interaction algorithms for complete and restricted configuration interaction spaces. *The Journal of Chemical Physics*, 89(4):2185–2192, 1988.

[51] P. R. Surján. *The Brillouin Theorem*, pages 87–92. Springer Berlin Heidelberg, 1989.

[52] F. Wei, G. S. Wu, W. H. E. Schwarz, and J. Li. Excited states and absorption spectra of uf6: A raspt2 theoretical study with spinorbit coupling. *Journal of Chemical Theory and Computation*, 7(10):3223–3231, 2011.

[53] R. Imai, T. Chen, and J. Simons. Direct calculation of density matrices: Natural orbitals and occupation numbers of model conjugated molecules. *International Journal of Quantum Chemistry*, 8(S8):323–333, 1974.

[54] V. Veryazov, P. Malmqvist, B. O. Roos, and S. Lund. How to select active space for multiconfigurational quantum chemistry? *International Journal of Quantum Chemistry*, 111(13):3329–3338, 2011.

[55] P.W. Atkins and R.S. Friedman. *Molecular Quantum Mechanics*. OUP Oxford, 2011.

[56] G. Ghigo, B. O. Roos, and P. Malmqvist. A modified definition of the zeroth-order hamiltonian in multiconfigurational perturbation theory (caspt2). *Chemical Physics Letters*, 396(1):142 – 149, 2004.

[57] G. Ghigo, B. O. Roos, and P. Malmqvist. A modified definition of the zeroth-order Hamiltonian in multiconfigurational perturbation theory (CASPT2). *Chemical Physics Letters*, 396(1):142–149, 2004.

[58] B. O. Roos and K. Andersson. Multiconfigurational perturbation theory with level shift - the Cr2 potential revisited. *Chemical Physics Letters*, 245(2):215–223, 1995.

[59] A. Kerridge. A RASSCF study of free base, magnesium and zinc porphyrins: accuracy versus efficiency. *Physical chemistry chemical physics : PCCP*, 15(6):2197–209, 2013.

[60] J. P. Zobel, J. J. Nogueira, and L. Gonzalez. The ipea dilemma in caspt2. *Chemical Science*, 8:1482–1499, 2017.

[61] R. F. W. Bader. *Atoms in Molecules: A Quantum Theory*. International Series of Monographs on Chemistry. Clarendon Press, 1994.

[62] R. F. W. Bader and H. Essn. The characterization of atomic interactions. *The Journal of Chemical Physics*, 80(5):1943–1960, 1984.

[63] Richard F. W. Bader. Bond paths are not chemical bonds. *The Journal of Physical Chemistry A*, 113(38):10391–10396, 2009. PMID: 19722600.

[64] C. F. Matta and R. J. Boyd. *An Introduction to the Quantum Theory of Atoms in Molecules*. Wiley, 2007.

[65] A. Kerridge. Oxidation state and covalency in f-element metallocenes (M = Ce, Th, Pu): a combined CASSCF and topological study. *Dalton transactions*, 42(46):16428–36, 2013.

[66] R. Dennington, T. Keith, and J. Millam. GaussView, 2009.

[67] TURBOMOLE V6.6 2010, a development of University of Karlsruhe and Forschungszentrum Karlsruhe GmbH, 1989-2007, TURBOMOLE GmbH, since 2007; available from `http://www.turbomole.com`.

[68] F. Weigend and R. Ahlrichs. Balanced basis sets of split valence, triple zeta valence and quadruple zeta valence quality for H to Rn: Design and assessment of accuracy. *Physical Chemistry Chemical Physics*, 7:3297–3305, 2005.

[69] V. Veryazov and R. Lindh. Molcas version 8.0. 2012.

[70] B. O. Roos, R. Lindh, P. Malmqvist, V. Veryazov, and P. Widmark. Main group atoms and dimers studied with a new relativistic ano basis set. *The Journal of Physical Chemistry A*, 108(15):2851–2858, 2004.

[71] M. Reiher. Douglas-Kroll-Hess theory: a relativistic electrons-only theory for chemistry. *Theoretical Chemistry Accounts*, 116(1):241–252, 2006.

[72] T. A. Keith. Aimall (version 17.01.25). *TK Gristmill Software, Overland Park KS, USA, 2017 (aim.tkgristmill.com).*

[73] A. R. Battersby, C. J. Fookes, G. W. Matcham, and E. McDonald. Biosynthesis of the pigments of life: formation of the macrocycle. *Nature*, 285(1):17–21, 1980.

[74] M. Gouterman. Spectra of porphyrins. *Journal of Molecular Spectroscopy*, 6(2):138–163, 1961.

[75] S. Karthikeyan and J. Y. Lee. Zinc-Porphyrin Based Dyes for Dye-Sensitized Solar Cells. *The Journal of Physical Chemistry A*, 117(42):10973–10979, 2013.

[76] Y. Xie, Y. Tang, W. Wu, Y. Wang, J. Liu, X. Li, H. Tian, and W. Zhu. Porphyrin cosensitization for a photovoltaic efficiency of 11.5%: A record for non-ruthenium solar cells based on iodine electrolyte. *Journal of the American Chemical Society*, 137(44):14055–14058, 2015.

[77] T. Higashino and H. Imahori. Porphyrins as excellent dyes for dye-sensitized solar cells: recent developments and insights. *Dalton Transactions*, 44:448–463, 2015.

[78] W. M. Campbell, K. W. Jolley, P. Wagner, K. Wagner, P. J. Walsh, K. C. Gordon, L. Schmidt-Mende, M. K. Nazeeruddin, Q. Wang, M. Grätzel, and D. L. Officer. Highly efficient porphyrin sensitizers for dye-sensitized solar cells. *The Journal of Physical Chemistry C*, 111(32):11760–11762, 2007.

[79] G. D. Sharma, D. Daphnomili, K. S. V. Gupta, T. Gayathri, S. P. Singh, P. A. Angaridis, T. N. Kitsopoulos, D. Tasis, and A. G. Coutsolelos. Enhancement of power conversion efficiency of dye-sensitized solar cells by co-sensitization of zinc-porphyrin and thiocyanate-free ruthenium(ii)-terpyridine dyes and graphene modified tio2 photoanode. *RSC Adv.*, 3:22412–22420, 2013.

[80] X. Sun, Y. Wang, X. Li, H. Agren, W. Zhu, H. Tian, and Y. Xie. Cosensitizers for simultaneous filling up of both absorption valleys of porphyrins: a novel approach for developing efficient panchromatic dye-sensitized solar cells. *Chemical Communications*, 50:15609–15612, 2014.

[81] D. Sundholm. Interpretation of the electronic absorption spectrum of free-base porphin using time-dependent density-functional theory. *Physical Chemistry Chemical Physics : PCCP*, 55:2275–2281, 2000.

[82] J. P. Perdew. Density-functional approximation for the correlation energy of the inhomogeneous electron gas. *Physical Review B*, 33(12):8822–8824, 1986.

[83] A. B. J. Parusel and A. Ghosh. Density Functional Theory Based Configuration Interaction Calculations on the Electronic Spectra of Free-Base Porphyrin, Chlorin, Bacteriochlorin, and cis- and trans-Isobacteriochlorin. *Journal of Physical Chemistry A*, 104:2504–2507, 2000.

[84] S. Grimme. Density functional calculations with configuration interaction for the excited states of molecules. *Chemical Physics Letters*, 259:128–137, 1996.

[85] L. Petit, A. Quartarolo, C. Adamo, and N. Russo. Spectroscopic properties of porphyrin-like photosensitizers: insights from theory. *The Journal of Physical Chemistry. B*, 110(5):2398–404, 2006.

[86] J. P. Perdew, M. Ernzerhof, and K. Burke. Rationale for mixing exact exchange with density functional approximations. *The Journal of Chemical Physics*, 105(22):9982, 1996.

[87] R. R. Valiev, V. N. Cherepanov, V. Y. Artyukhov, and D. Sundholm. Computational studies of photophysical properties of porphin, tetraphenylporphyrin and tetrabenzoporphyrin. *Physical chemistry chemical physics : PCCP*, 14(32):11508–17, 2012.

[88] M. Merchan, E. Orti, and B. O. Roos. Theoretical determination of the electronic spectrum of free base porphin. *Chemical Physics Letters*, 226, 1994.

[89] L. Serrano-Andres, M. Merchan, M. Rubio, and B. O. Roos. Interpretation of the electronic absorption spectrum of free base porphin by using multiconfigurational second-order perturbation theory. *Chemical Physics Letters*, 295(3):195–203, 1998.

[90] V. Sauri and L. Serrano-Andrés. Multiconfigurational second-order perturbation theory restricted active space (raspt2) method for electronic excited states: A benchmark study. *Journal of Chemical Theory and Computation*, 7(1):153–168, 2010.

[91] A. D. Becke. Density-functional exchange-energy approximation with correct asymptotic behavior. *Physical Review A*, 38(6):3098–3100, 1988.

[92] A. D. Becke. Density-functional thermochemistry. III. The role of exact exchange. *The Journal of Chemical Physics*, 98(7):5648, 1993.

[93] V. Staroverov, G. Scuseria, J. Tao, and J. P. Perdew. Tests of a ladder of density functionals for bulk solids and surfaces. *Physical Review B*, 69(7):075102, feb 2004.

[94] J. P. Perdew, A. Ruzsinszky, J. Tao, V. N. Staroverov, G. E. Scuseria, and G. I. Csonka. Prescription for the design and selection of density functional approximations: more

constraint satisfaction with fewer fits. *The Journal of Chemical Physics*, 123(6):62201, 2005.

[95] M. Gouterman. Spectra of porphyrins. *Journal of Molecular Spectroscopy*, 127:108–127, 1961.

[96] B. M. L. Chen and A. Tulinsky. Redetermination of the Structure of Porphine. *Journal of the American Chemical Society*, 94(12):4144–4151, 1972.

[97] D.R. Lide. *CRC Handbook of Chemistry and Physics, 98th Edition*. CRC HANDBOOK OF CHEMISTRY AND PHYSICS. Taylor & Francis, 2003.

[98] K. A. Nguyen and R. Pachter. Ground state electronic structures and spectra of zinc complexes of porphyrin, tetraazaporphyrin, tetrabenzoporphyrin, and phthalocyanine: A density functional theory study. *The Journal of Chemical Physics*, 114(24):10757, 2001.

[99] G. W. Canters, G. Jansen, M. Noort, and J. H. Van der Waals. High resolution Zeeman experiments on singlet, triplet, and quartet states of metalloporphines. *The Journal of Physical Chemistry*, 80(20):2253–2259, sep 1976.

[100] J. D. Keegan and A. M. Stolzenberg. Magnetic circular dichroism studies. 60. Substituent-induced sign variation in the magnetic circular dichroism spectra of reduced porphyrins. 1. Spectra and band assignments. *Journal of the American Chemical Society*, 104(16):2217–2220, 1982.

[101] G. A. Peralta, M. Seth, and T. Ziegler. Magnetic circular dichroism of porphyrins containing M = Ca, Ni, and Zn. A computational study based on time-dependent density functional theory. *Inorganic chemistry*, 46(22):9111–25, 2007.

[102] W Kohn, A. D. Becke, and R. G. Parr. Density functional theory of electronic structure. *The Journal of Physical Chemistry*, 100(96):12974–12980, 1996.

[103] A. Rosa, G. Ricciardi, O. Gritsenko, and E. J. Baerends. Excitation energies of metal complexes with time-dependent density functional theory. In Nik Kaltsoyannis and John McGrady, editors, *Principles and Applications of Density Functional Theory in Inorganic Chemistry I: Pt. 1 (Structure and Bonding)*, pages 49–115. Springer, Berlin, 2004.

[104] O. V. Gritsenko, P. R. T. Schipper, and E. J. Baerends. Approximation of the exchange-correlation KohnSham potential with a statistical average of different orbital model potentials. *Chemical physics letters*, 302:199–207, 1999.

[105] D Sundholm. Density functional theory study of the electronic absorption spectrum of Mg-porphyrin and Mg-etioporphyrin-I. *Chemical Physics Letters*, 317:392–399, 2000.

[106] M. Rubio, B. O. Roos, L. Serrano-Andrés, and M. Merchan. Theoretical study of the electronic spectrum of magnesium-porphyrin. *The Journal of Chemical Physics*, 110(15):7202, 1999.

[107] J. Seda, J. V. Burda, and J. Leszczynski. Study of electronic spectra of free-base porphin and Mg-porphin: comprehensive comparison of variety of ab initio, DFT, and semiempirical methods. *Journal of computational chemistry*, 26(3):294–303, feb 2005.

[108] K. Hirao. Multireference MøllerPlesset method. *Chemical physics letters*, 190(3):374–380, 1992.

[109] T. Hashimoto, Y. Choe, H. Nakano, and K. Hirao. Theoretical Study of the Q and B Bands of Free-Base, Magnesium, and Zinc Porphyrins, and Their Derivatives. *The Journal of Physical Chemistry A*, 103(12):1894–1904, mar 1999.

[110] F. Aquilante, P. Malmqvist, T. B. Pedersen, A. Ghosh, and B. O. Roos. Cholesky decomposition-based multiconfiguration second-order perturbation theory (CD-CASPT2): Application to the spin-state energetics of Co III(diiminato)(NPh). *Journal of Chemical Theory and Computation*, 4(5):694–702, 2008.

[111] M. Gouterman, L. K. Hanson, K. Gamal-Eddin, J. Buchler, K. Rohbock, and D. Dolphin. Porphyrins. xxxi. chemical properties and electronic spectra of d0 transition-metal complexes. *Journal of the American Chemical Society*, 97(11):3142–3149, 1975.

[112] C. W. Cady, R. H. Crabtree, and G. W. Brudvig. Functional models for the oxygen-evolving complex of photosystem ii. *Coordination Chemistry Reviews*, 252(3):444 – 455, 2008. The Role of Manganese in Photosystem II.

[113] E. J. Baerends and G. Ricciardi. A DFT/TDDFT interpretation of the ground and excited states of porphyrin and porphyrazine complexes. *Coordination Chemistry Reviews*, 230:5–27, 2002.

[114] W. Jentzen, I. Turowska-Tyrk, W. R. Scheidt, and J. Shelnutt. Planar Solid-State and Solution Structures of (Porphinato)nickel(II) As Determined by X-ray Diffraction and Resonance Raman Spectroscopy. *Inorganic Chemistry*, 35(12):3559–3567, 1996.

[115] S. R. Stoyanov, C. Yin, M. R. Gray, J. M. Stryker, S. Gusarov, and A. Kovalenko. Computational and experimental study of the structure, binding preferences, and spectroscopy of nickel(II) and vanadyl porphyrins in petroleum. *The Journal of Physical Chemistry. B*, 114(6):2180–8, 2010.

[116] K. Stavrev and M. C. Zerner. A theoretical treatment of the absorption and emission properties of Cu (II) porphyrin. *Chemical physics letters*, 233:179–184, 1995.

[117] Y. Umena, K. Kawakami, J. Shen, and N. Kamiya. Crystal structure of oxygen-evolving photosystem ii at a resolution of 1.9a. *Nature*, 473(7345):55–60, 2011.

[118] Y. Naruta, M. Sasayama, and T. Sasaki. Oxygen evolution by oxidation of water with manganese porphyrin dimers. *Angewandte Chemie*, 33(18):1839–1841, 1994.

[119] L. J. Boucher. Manganese porphyrin complexes. i. synthesis and spectroscopy of manganese(iii) protoporphyrin ix dimethyl ester halides. *Journal of the American Chemical Society*, 90(24):6640–6645, 1968.

[120] T.R. Cundari. *Computational Organometallic Chemistry*. Taylor & Francis, 2001.

[121] K. Andersson and B. O. Roos. Excitation energies in the nickel atom studied with the complete active space scf method and second-order perturbation theory. *Chemical Physics Letters*, 191(6):507 – 514, 1992.

[122] J. F Kirner, C. A. Reed, and W. R. Scheidt. Stereochemistry of Manganese Porphyrins. *Journal of the American Chemical Society*, 99(4):1093–1101, 1977.

[123] H. Kobayashi and Y. Yanagawa. Electronic spectra and electronic structure of iron (II) tetraphenylphorphins. *Bulletin of the Chemical Society of Japan*, 45(2):450–456, 1972.

[124] W. R. Scheidt and C. A. Reed. Spin-state/stereochemical relationships in iron porphyrins: implications for the hemoproteins. *Chemical Reviews*, 81(6):543–555, 1981.

[125] W. R. Scheidt. Trends in metalloporphyrin stereochemistry. *Accounts of Chemical Research*, 10(9):339–345, 1977.

[126] C. A. Reed, T. Mashiko, W. R. Scheidt, K. Sartalian, and G. Lang. High-Spin Iron(II) in the Porphyrin Plane. Structural Characterization of (meso-Tetraphenylporphinato)bis(tetrahydrofuran)iron(II). *Journal of the American Chemical Society*, 1027:2302–2306, 1980.

[127] J. Kim, D. Kim, M. Kang, H. Kim, J. Kim, E. Yu, and J. Jeong. Gadolinium-chlorin is potentially a new tumor specific mri contrast agent. *Archives of Pharmacal Research*, 29(3):188, 2006.

[128] P. Caravan, J. J. Ellison, T. J. McMurry, and R. B. Lauffer. Gadolinium(iii) chelates as mri contrast agents: structure, dynamics, and applications. *Chemical Reviews*, 99(9):2293–2352, 1999. PMID: 11749483.

[129] J. L. Sessler, W. C. Dow, D. O'Connor, A. Harriman, G. Hemmi, T. D. Mody, R. A Miller, F. Qing, S. Springs, K. Woodburn, and S. W. Young. Biomedical applications

of lutetium texaphyrins as potential photodynamic therapy photosensitizers. *Journal of Alloys and Compounds*, 249(1):146 – 152, 1997.

[130] J. G. Bunzli and C. Piguet. Taking advantage of luminescent lanthanide ions. *Chemical Society Reviews*, 34:1048–1077, 2005.

[131] E. Skovran and N. C. Martinez-Gomez. Just add lanthanides. *Science*, 348(6237):862–863, 2015.

[132] R. Thirunakaran, A. Sivashanmugam, S. Gopukumar, and R. Rajalakshmi. Cerium and zinc: Dual-doped LiMn2O4 spinels as cathode material for use in lithium rechargeable batteries. *Journal of Power Sources*, 187(2):565 – 574, 2009.

[133] M. Sasidharan, N. Gunawardhana, M. Inoue, S. Yusa, M. Yoshio, and K. Nakashima. La2O3 hollow nanospheres for high performance lithium-ion rechargeable batteries. *Chemical Communications*, 48:3200–3202, 2012.

[134] N. Kaltsoyannis. Does covalency increase or decrease across the actinide series? Implications for minor actinide partitioning. *Inorganic chemistry*, 52(7):3407–13, 2013.

[135] G. R. Choppin. Comparative solution chemistry of the 4f and 5f elements. *Journal of Alloys and Compounds*, 223(2):174 – 179, 1995.

[136] G. R. Choppin. Complexation kinetics of f-elements and polydentate ligands. *Journal of Alloys and Compounds*, 225(1):242 – 245, 1995. Proceedings of the 2nd International Conference on f-Elements.

[137] I. Kirker and N. Kaltsoyannis. Does covalency really increase across the 5f series? a comparison of molecular orbital, natural population, spin and electron density analyses of ancp3 (an = th-cm; cp = [small eta]5-c5h5). *Dalton Transactions*, 40:124–131, 2011.

[138] M. L. Neidig, D. L. Clark, and R. L. Martin. Covalency in f-element complexes. *Coordination Chemistry Reviews*, 257(2):394 – 406, 2013.

[139] A. Kerridge. f-orbital covalency in the actinocenes (An=Th-Cm): multiconfigurational studies and topological analysis. *RSC Advances*, 4(24):12078–12086, 2014.

[140] R. Beekmeyer and A. Kerridge. Assessing Covalency in Cerium and Uranium Hexachlorides: A Correlated Wavefunction and Density Functional Theory Study. *Inorganics*, 3:482–499, 2015.

[141] M. Gregson, E. Lu, F. Tuna, E. J. L. McInnes, C. Hennig, A. C. Scheinost, J. McMaster, W. Lewis, A. J. Blake, A. Kerridge, and S. T. Liddle. Emergence of comparable covalency in isostructural cerium(iv)- and uranium(iv)-carbon multiple bonds. *Chemical Science*, 7:3286–3297, 2016.

[142] S. Vancoillie, H. Zhao, V. T. Tran, M. Hendrick, and K. Pierloot. Multiconfigurational Second-Order Perturbation Theory Restricted Active Space (RASPT2) Studies on Mononuclear First-Row Transition-Metal Systems. *Journal of Chemical Theory and Computation*, 7(12):3961–3977, dec 2011.

[143] P. Löwdin. Quantum theory of many-particle systems. i. physical interpretations by means of density matrices, natural spin-orbitals, and convergence problems in the method of configurational interaction. *Phys. Rev.*, 97:1474–1489, Mar 1955.

[144] M. W. Schmidt and M. S. Gordon. The construction and interpretation of MCSCF wavefunctions. *Annual Review of Physical Chemistry*, 49(1):233–266, 1998.

[145] A. Kerridge. Quantification of f-element covalency through analysis of the electron density: insights from simulation. *Chemical Commununications*, 53:6685–6695, 2017.

[146] P. Mori-Sánchez, A. M. Pendás, and V. Luana. A classification of covalent, ionic, and metallic solids based on the electron density. *Journal of the American Chemical Society*, 124(49):14721–14723, 2002.

[147] S. J. Grabowski, W. A. Sokalski, E. Dyguda, and J. Leszczyński. Quantitative classification of covalent and noncovalent h-bonds. *The Journal of Physical Chemistry B*, 110(13):6444–6446, 2006.

[148] M. J. Tassell and N. Kaltsoyannis. Covalency in ancp4 (an = th-cm): a comparison of molecular orbital, natural population and atoms-in-molecules analyses. *Dalton Transactions*, 39:6719–6725, 2010.

[149] M. Alikhani. On the chemical bonding features in boron containing compounds: a combined QTAIM/ELF topological analysis. *Physical chemistry chemical physics : PCCP*, 15(30):12602–9, 2013.

[150] F Cortesguzman and R Bader. Complementarity of QTAIM and MO theory in the study of bonding in donor?acceptor complexes. *Coordination Chemistry Reviews*, 249(5-6):633–662, mar 2005.

[151] M. E. Fieser, M. R. MacDonald, B. T. Krull, J. E. Bates, J. W. Ziller, F. Furche, and W. J. Evans. Structural, Spectroscopic, and Theoretical Comparison of Traditional vs Recently Discovered Ln2+ Ions in the [K(2.2.2-cryptand)][(C5H4SiMe33)3Ln] Complexes: The Variable Nature of Dy2+ and Nd2+. *Journal of the American Chemical Society*, 137:369–382, 2015.

[152] R. Coates. Oxidation State Ambiguities in Cerium Organometallics - A Computational Approach. *Thesis*, pages 1–149.

[153] R. C. Alig, Z. J. Kiss, J. P. Brown, and D. S. McClure. Energy Levels of Ce2+ in CaF2. *Physical Review*, 186(2):276–284, 1969.

[154] S. Cotton. *Lanthanide and Actinide Chemistry*. Inorganic Chemistry: A Textbook Series. Wiley, 2013.

[155] S W Young, K W Woodburn, M Wright, T D Mody, Q Fan, J L Sessler, W C Dow, and R A Miller. Lutetium texaphyrin (PCI-0123): a near-infrared, water-soluble photosensitizer. *Photochem Photobiol*, 63(6):892–897, 1996.

[156] J L Sessler, T D Mody, G W Hemmi, and Lynch V. Synthesis and Structural Characterization of Lanthanide (III) Texaphyrins. *Inorganic chemistry*, (32):3175–3187, 1993.

[157] J. L. Sessler, T. D. Mody, G. W. Hemmi, and V. Lynch. Synthesis and structural characterization of lanthanide(iii) texaphyrins. *Inorganic Chemistry*, 32(14):3175–3187, 1993.

[158] R. Shimanovich, S. Hannah, V. Lynch, N. Gerasimchuk, T. D. Mody, D. Magda, J. L. Sessler, and J. T. Groves. Mn(II)Texaphyrin as a Catalyst for the Decomposition of Peroxynitrite. *Journal of the American Chemical Society*, 123(15):3613–3614, 2001.

[159] D. I. Rosenthal, P. Nurenberg, C. R. Becerra, E. P. Frenkel, D. P. Carbone, B. L. Lum, R. Miller, J. Engel, S. Young, D. Miles, and M. F. Renschler. A phase i single-dose trial of gadolinium texaphyrin (gd-tex), a tumor selective radiation sensitizer detectable by magnetic resonance imaging. *Clinical Cancer Research*, 5(4):739–745, 1999.

[160] M. J. Hammer-Wilson, M. Ghahramanlou, and M. W. Berns. Photodynamic activity of lutetium-texaphyrin in a mouse tumor system. *Lasers in Surgery and Medicine*, 24(4):276–284, 1999.

[161] Xiayon Cao and Michael Dolg. Density functional studies on lanthanide (iii) texaphyrins (ln-tex2+, ln = la, gd, lu): structure, stability and electronic excitation spectrum. *Molecular Physics*, 101(15):2427–2435, 2003.

[162] I. Fryer-Kanssen, J. Austin, and A. Kerridge. Topological study of bonding in aquo and bis(triazinyl)pyridine complexes of trivalent lanthanides and actinides: Does covalency imply stability? *Inorganic Chemistry*, 55(20):10034–10042, 2016.

[163] L. E. Roy, N. J. Bridges, and L. R. Martin. Theoretical insights into covalency driven f element separations. *Dalton transactions*, 42(7):2636–42, 2013.

[164] F. W. Lewis, L. M. Harwood, M. J. Hudson, M. G. B. Drew, J. F. Desreux, G. Vidick, N. Bouslimani, G. Modolo, A. Wilden, M. Sypula, T. Vu, and J. Simonin. Highly efficient separation of actinides from lanthanides by a phenanthroline-derived bis-triazine ligand. *Journal of the American Chemical Society*, 133(33):13093–13102, 2011. PMID: 21770458.

[165] H. H. Dam, D. N. Reinhoudt, and W. Verboom. Multicoordinate ligands for actinide/lanthanide separations. *Chemical Society Reviews*, 36:367–377, 2007.